Solar Wind Particle Populations at 1 AU: Examining their Origins in Advance of the Solar Orbiter Mission

Allan Ross Macneil

A dissertation submitted in partial fulfillment
of the requirements for the degree of
Doctor of Philosophy
of
University College London.

Department of Space and Climate Physics
University College London

September 2018

I, Allan Ross Macneil, confirm that the work presented in this thesis is my own. Where information has been derived from other sources, I confirm that this has been indicated in the work.

Abstract

The three studies presented in this thesis aim to understand the properties of solar wind particle populations in the context of their origins at the Sun. The observations used begin with *in situ* plasma measurements, and extend to remote sensing of solar wind sources. This approach is motivated by the upcoming Solar Orbiter mission, which will use similar techniques at <0.3 au to address the question of how the Sun creates and controls the heliosphere.

The first study compares energetic properties of suprathermal solar wind electrons, the 'halo' and 'strahl', against the inferred electron temperature of their source. From the weak nature of the resulting correlations we conclude, in contrast to earlier results, that a relationship with electron temperature may exist in the corona, but that usually no strong signatures remain in these distributions at 1 au.

The second study examines the origin of "intermediate" transitional heavy ion charge states in solar wind rarefactions. Linking *in situ* measurements of these regions with extreme ultraviolet solar observations, they are found to originate near trailing coronal hole boundaries. This result and a simple solar wind model suggest that it is the intrinsic properties at these boundaries which are the primary cause of the intermediate ionisation, as opposed to interplanetary mixing. The technique used to link these observations is also critically evaluated and improvements are suggested.

The final study compares solar wind associated with a coronal hole-quiet Sun boundary, to solar wind associated with the same coronal hole later bordering an active region. Changing features found in a range of *in situ* parameters are compared in the context of source region mapping. We put forward suggestions for mechanisms of solar wind production which could produce such changes.

Impact Statement

The work contained in this thesis stands to have a beneficial impact both inside and outside of academia. Regarding academic impact, each study in this thesis addresses a key aspect of one of the pivotal questions in heliophysics: What is the origin of the solar wind? This thesis thus makes critical contributions to a body of work by the heliophysics community. Academic dissemination of this work has taken the form of one publication in an academic journal, as well as presentations at several national and international conferences and workshops.

Further academic impact stems from the testing of a widely-applied technique for mapping solar wind observations to their source in Chapter 5. Evaluating the accuracy of this technique for a particular type of solar wind, we make vital recommendations to improve it for future studies. This work thus stands to benefit the large group of researchers who apply this method in their own work.

Impact both inside and outside of academia is generated through contributions to the Solar Orbiter mission. Solar Orbiter is a European Space Agency mission which aims to explore the Sun-heliosphere connection and origins of the solar wind. The work in the research chapters of this thesis is highly relevant to Solar Orbiter, and will contribute to the science returns of the mission. Results in Chapters 5 and 6 illuminate potential challenges to Solar Orbiter in achieving its science goals. In Chapter 7 several studies are proposed which can only be carried out using data from the Solar Orbiter mission. Material in this thesis has also been presented at 4 Solar Orbiter-themed meetings.

The UK is playing a significant role in the Solar Orbiter mission. This involvement capitalises on the UK subscription to ESA ($\sim$ £300 million in 2018) by providing significant benefit to UK industry. The prime contractor is Airbus in Stevenage, whose contract is worth $>$ £300 million. Construction of the spacecraft bus and select instruments which is taking place in the UK is also of major benefit to a range of smaller contractors and institutions. UCL in particular is involved with

instrument building, operations, and scientific aspects of Solar Orbiter. The work in this thesis will contribute to the success of the mission, and thus to these broader impacts.

Finally, the work in this thesis is relevant to the science behind space weather. Space weather describes solar phenomena which can have major impacts on terrestrial life and infrastructure. Space weather is listed on the UK government's National Risk Register of Civil Emergencies (available at `https://www.gov.uk/government/collections/national-risk-register-of-civil-emergencies`). The solar wind defines the Earth's local plasma environment and as such is the prime driver of space weather at Earth. Efforts towards explaining the solar wind's origins and nature, such as in this thesis, are thus crucial to the development of forecasting tools which aim to predict space weather events, and limit its impact on humanity across the globe.

Acknowledgements

The full list of people who have in some way helped me reach this point is likely longer than this thesis. Thank you therefore to anyone opening this page to see if you have been acknowledged - I hope that this catch-all sentence prevents any disappointment.

My first and biggest thanks go to my supervisors, Chris Owen and Rob Wicks. Your guidance, insight, and encouragement were crucial throughout the past three years. Chris, thanks for having in-depth meetings with me even with a thousand more pressing matters to deal with, and for always identifying that one thing I don't understand. Thanks too for teaching me to recognise when a project is done; or needs to be. Rob, thanks for always considering my well-being during the more difficult times of my PhD.

I am very grateful to all the members of the Space Plasma group. Andrew Fazakerley, Jonny Rae, Colin Forsyth and Daniel Verscharen: thanks for taking the time to engage and help with my work; especially at student discussions when I would do most of my complaining. Thank you to the postdocs who have given me something to aspire towards: Licia Ray, Zhonghua Yao, Simon Thomas, Jasmine Sandhu, George Nicolaou and Marina Georgiou. Thanks to the students who have all been inspiring officemates in their own way: Lloyd Woodham, Honghong Wu, Frankie Staples and Michaela Mooney. Special thanks to Nadine Kalmoni and Georgie Graham, who I was lucky enough to spend nearly all of my PhD with. Nadine, thanks for your advice, and helping me keep things in perspective. Georgie, thanks for being there every day to talk about physics, cartoons, frogs, or whatever was needed to keep me going.

Thanks to the members of the Solar group for patiently teaching me about the Sun, and for giving me a desk. Special thanks to Louise Harra, Deb Baker, and Dave Long for your contributions to my work, as well as your guidance and encouragement in an unfamiliar field. Thanks too to the G01 students: Alex James, Jack

Jenkins, and Jenny O'Kane, for keeping me in the group chat when I left, and for living life a quarter-mile at a time.

I am thankful to all of the members of the Planetary group. In particular, thanks to Geraint Jones for some very helpful references and discussion, Will Dunn for your inspirational talks, and to Roger Stabbins for your enthusiasm.

I also owe a debt of gratitude to many of the staff and students at MSSL. Thanks to all the staff in the main office for helping me with an array of problems. Thanks to Gethyn Lewis for advice on spacecraft potential. Thanks to Philippa Elwell and Daisuke Kawata for all your help and support. Thanks to Damron Macleod for fixing my laptop. Thanks to Chris Brockley-Blatt for finding me when I was lost in Paris. Thanks to the imaging group for adopting me at EGU. Thanks to Dave Williams and Andrew Walsh for buying me many ill-advised drinks at conferences.

Thank you to my housemates in Maple Grove for providing me a place of refuge from work. Luke Pratley, thanks for teaching me heaps of New Zealand slang. Ollie Price, thanks for thinking up puns with me, and for your (occasionally brutal) honesty. Magnus Woods, thanks for being as great a friend as anyone could ask for. Also, thank you for your Simpsons DVDs.

Special thanks to Mollie Joyce for supporting me while I wrote this thesis. Keeping me sane for the past 5 months was not easy, and I'm forever grateful for that.

Thanks finally to all my family, and my parents. Dad, thanks for believing in me. Mum, thanks for pointing me in the right direction long before I could find it myself.

I would also like to acknowledge the Science and Technology Facilities Council for financial support of my PhD studies.

Contents

List of Figures

List of Tables

List of Abbreviations

3DP	3-Dimensional Plasma analyser (Wind)
ACE	The Advanced Composition Explorer
AIA	Atmospheric Imaging Assembly (SDO)
AR	Active Region
AU	Astronomical Unit
CH	Coronal Hole
CHB	Coronal Hole Boundary
CHBL	Coronal Hole Boundary Layer
CIR	Corotating Interaction Region
CME	Coronal Mass Ejection
CR	Carrington Rotation
DoY	Day of Year
EAS	Electron Analyser System
EESA	Electron Electrostatic Analyser (Wind-3DP)
EIS	Extreme-Ultraviolet Imaging Spectrometer (Hinode)
ESA	European Space Agency
EUI	Extreme Ultraviolet Imager (Solar Orbiter)
EUV	Extreme Ultraviolet
FIP	First Ionisation Potential
FOV	Field of View
GOES	Geostationary Operational Environmental Satellite system
HCS	Heliospheric Current Sheet
HIS	Heavy Ion Sensor (Solar Orbiter)
HMF	Heliospheric Magnetic Field
HMI	Helioseismic and Magnetic Imager (SDO)

ICME	Interplanetary Coronal Mass Ejection
ICS	Intermediate Charge State
IMF	Interplanetary Magnetic Field (also: HMF)
L1	1st Lagrangian Point
LOS	Line of Sight
MFI	Magnetic Field Investigation (Wind)
MHD	Magnetohydrodynamics
NASA	National Aeronautics and Space Administration
NOAA	National Oceanic and Atmospheric Administration
PA	Pitch Angle
PAS	Proton and Alpha Sensor (Solar Orbiter)
PFSS	Potential Field Source Surface
PHI	Polarimetric and Helioseismic Imager (Solar Orbiter)
QS	Quiet Sun
QSL	Quasi-Separatrix Layer
$R_\odot$	Solar radius
SDO	Solar Dynamics Observatory
SEP	Solar Energetic Particle
SPICE	The extreme ultraviolet imaging spectrograph for Solar Orbiter
SW	Solar Wind
SWA	Solar Wind Analyser (Solar Orbiter)
SWE	Solar Wind Experiment (Wind)
SWEPAM	Solar Wind Electron, Proton and Alpha Monitor (ACE)
SWICS	Solar Wind Ion Composition Spectrometer (ACE, Ulysses)
UV	Ultraviolet
VDF	Velocity Distribution Function

Chapter 1

Introduction

The origin of the solar wind, the supersonic outflow of plasma from the Sun, is one of the great unknowns in the domain of heliospheric physics. The processes by which it is accelerated, escapes from magnetically closed regions of the Sun, and is imparted with a range of plasma and compositional properties, are all still unknown. These questions of how the Sun creates the solar wind can be grouped under the umbrella of the "Sun-heliosphere connection". Knowledge of these topics is invaluable because the solar wind defines the local space environment of both our planet and others in the solar system. Further, the solar wind is the only stellar wind which we are able to directly observe, and so presents the best opportunity to understand the environments which surround other stars.

For observational studies into the Sun-heliosphere connection, it is naturally desirable to link the domains of the Sun and the solar wind. The goal is then to observe solar wind source locations and properties simultaneously with resultant *in situ* solar wind properties. Establishing solar wind properties which reflect unique signatures of source region properties and processes is one approach to establishing this link. Another is to map the propagation of the solar wind from the Sun to the observer, such that remote sensing of the source region can be employed. In both

cases, making this link reliably is not trivial.

The research contained in this thesis aims to connect the Sun to the solar wind at 1 au, to understand different aspects of its origins. We do so both by employing *in situ* signatures of source region properties and processes, and by combining remote sensing and *in situ* observations through solar wind mapping.

Solar Orbiter (Müller et al., 2013) is an upcoming ESA mission scheduled for launch in 2020. One of its major goals is to further knowledge of the Sun-heliosphere connection, by better-establishing the observational link between the two domains. To do so, the spacecraft is equipped with a suite of both *in situ* and remote sensing instruments, and will orbit the Sun with a perihelion of $\sim 0.28\,\mathrm{au}$. Solar Orbiter will thus combine observations of the more-pristine solar wind in the inner-heliosphere with detailed observations of solar wind source regions. Solar Orbiter will also make the first observations of the Sun's polar magnetic field, through an inclined orbit which will reach 25° from the ecliptic. The recently launched Parker Solar Probe is another *in situ* heliospheric mission which will explore solar wind origins. It will investigate the acceleration mechanisms of the wind at distances $< 10\,\mathrm{R}_{\odot}$.

A strong motivator for the work in this thesis is to prepare for Solar Orbiter. By examining solar wind origins using current instruments and techniques, we aim to identify specific opportunities to further knowledge of this topic using Solar Orbiter. We also wish to highlight what potential challenges we might face in doing this.

The remainder of this chapter contains the information necessary to contextualise the original research work in this thesis. First, we will lay the physical groundwork by defining and describing the properties of a plasma. Second, the Sun and particularly its atmosphere, the corona, will be introduced. Finally, working outwards from the Sun, we introduce the solar wind; its bulk properties, magnetic field, and

particle populations.

1.1 Plasma Physics

Plasma is frequently described as the fourth state of matter; an ionised gas made up of a non-negligible fraction of unbound positively and negatively charged particles. Thus, in addition to those forces which apply to a neutral gas, matter in this state is subject to both external and self-generated electromagnetic forces.

Although the study of such previously-unnamed ionised gases was already underway (e.g., Debye and Hückel, 1923), the term "plasma" was first coined by Irving Langmuir (1928). He used the term to describe a "region containing balanced charges of ions and electrons". While Langmuir never elucidated in his own work, separate accounts of this naming both indicate his intention to draw parallels with the other type of plasma - that which is a component of blood (Tonks, 1967; Mott-Smith, 1971). The latter account reports on Langmuir's direct comparison between the manner in which blood plasma carries red and white blood cells, and how this new plasma was observed to carry energetic electrons and ions.

Plasma can be created in the lab, but also occurs naturally in the atmospheres of Earth and other planets, in astrophysical bodies, and in interplanetary and interstellar space. This section will provide a more rigorous definition of a plasma, and then outline some of the key physics which arises and the systems used to describe it. First, some concepts necessary to inform the rest of the discussion will be introduced.

1.1.1 Electromagnetism

A plasma is sensitive to electric and magnetic fields as it contains unbound charged particles. Descriptions of physical processes in plasma therefore first require the use of concepts in electromagnetism. Some key equations are listed and described

below.

Maxwell's equations describe the relationships between electric and magnetic fields and their sources. For a charged particle population in vacuum, they are expressed in differential form as follows (Maxwell, 1863):

$$\nabla \cdot \mathbf{E} = \frac{\rho_\mathrm{q}}{\varepsilon_0} \tag{1.1a}$$

$$\nabla \cdot \mathbf{B} = 0 \tag{1.1b}$$

$$\nabla \times \mathbf{E} = -\frac{\partial \mathbf{B}}{\partial t} \tag{1.1c}$$

$$\nabla \times \mathbf{B} = \mu_0(\mathbf{J} + \varepsilon_0 \frac{\partial \mathbf{E}}{\partial t}) \tag{1.1d}$$

$\mathbf{E}$ and $\mathbf{B}$ are the electric and magnetic fields, respectively; ρ_q is net charge density, ε_0 is the vacuum permittivity, μ_0 is the vacuum permeability, and $\mathbf{J}$ is current density.

These fields act on charged particles via the Lorentz force; the force on a particle of charge q and velocity $\mathbf{v}$ due to electric and magnetic fields:

$$\mathbf{F} = q(\mathbf{E} + \mathbf{v} \times \mathbf{B}) \tag{1.2}$$

The motion of charged particles due to the Lorentz force results in changes to the electric and magnetic fields, which then act differently on the particles and so on. This coupling of fields and particles is a source of complexity in the study of plasmas.

Field Lines

A field line is a conceptual line in space which is used to describe vector fields. At each point along its length, it is aligned with the vector field direction. An example of a vector field and corresponding field lines is shown in Figure 1.1. In plasma physics specifically, the concept of electric and particularly magnetic field lines is

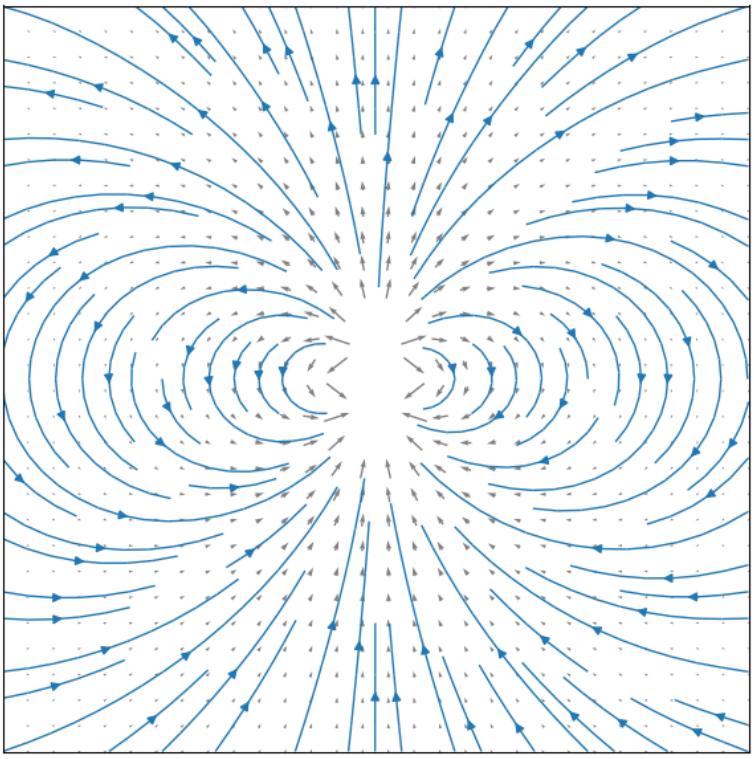

Figure 1.1: Grey vector arrows and corresponding sections of field lines for a dipolar field. Arrows show the direction and magnitude of the magnetic field vector at positions along an evenly spaced grid. Field lines are drawn in blue. The field lines are drawn arbitrarily and are assigned an arbitrary length. As such, they represent field line sections rather than full magnetic field lines which must be closed.

very useful. Many processes in plasma depend on whether their action is parallel or perpendicular to the local magnetic field, and charged particles are guided or controlled by magnetic field lines. A magnetic field does not have sinks or sources, as a result of Equation 1.1a, and so all full magnetic field lines necessarily take the form of closed loops. Figure 1.1 represents a magnetic field, however we choose to start and stop drawing sections of field lines at an arbitrary length, as this allows us to illustrate more individual field lines overall. Doing so also stresses that any number of field lines can be drawn based on a given vector field.

While the choice of which field lines to draw can be made arbitrarily, as in Figure 1.1, field lines can also be drawn such that they take on further significance. Figure 1.2 draws field lines for a dipolar magnetic field such that they close (or reach the

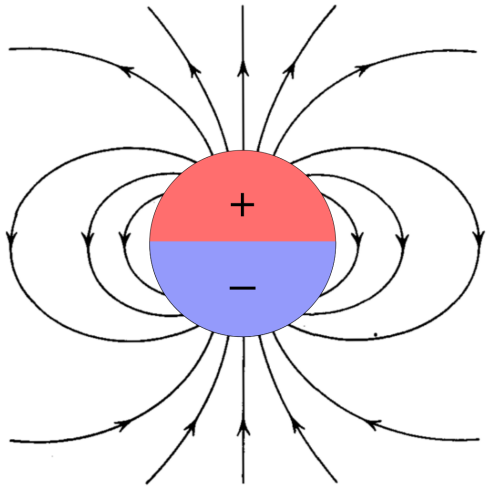

Figure 1.2: Dipolar magnetic field represented through magnetic field lines. Field lines are either closed (both ends return to the source body), or reach the boundary of the figure. The field lines are also drawn such that their 'density' is proportional to magnetic field strength. Adapted from Jackson (2012).

boundary of the figure), and their density (number of field lines in a volume) is proportional to magnetic field strength. Magnetic field lines are most commonly drawn in such a way.

Magnetic Flux Tubes

As a consequence of Equation 1.1b, we may define the concept of a magnetic flux tube. $\nabla \cdot \mathbf{B} = 0$ states that the total magnetic flux through a closed surface must be zero. If we define a tube made up of field lines, such that at no points do the field lines intersect the walls of the tube, then to conserve flux it must follow that the total flux through any cross-section of the tube is constant; $BA = \text{const}$. The field strength along a flux tube may increase or decrease, but only if the area, A, decreases or increases correspondingly.

1.1.2 Characteristic Scales and Frequencies

To rigorously define a plasma, we must first understand some important scales and frequencies. In an ionised gas containing an equal number of protons and electrons which are distributed uniformly, the addition of an extra charge will cause protons and electrons to experience a coulomb potential due to the new charge imbalance. The protons and electrons are compelled to move in this potential, with electrons

moving far faster due to their low mass. (Protons and other ions in a plasma are frequently approximated as stationary.) The electrons move to cancel the unbalanced charge, such that the coulomb potential due to the new particle is attenuated with distance. Particles distant from the charge imbalance experience a reduced coulomb potential as other charges have moved to balance this out. The electrostatic potential, ϕ, experienced by a charge a distance r from the new particle, of charge q, is then

$$\phi = \frac{q}{4\pi\varepsilon_0 r} \mathrm{e}^{-r/\lambda_D} \tag{1.3}$$

where the exponential decay is defined by λ_D; the Debye length. The Debye length defines the characteristic length at which a shielded potential is a factor of $1/\mathrm{e}$ smaller than its unshielded counterpart. The formula for the Debye length is described in Equation 1.4 (Parks, 1991):

$$\lambda_D^2 = \frac{kT_e\varepsilon_0}{n_e q_e^2} \tag{1.4}$$

where n_e is the electron number density, T_e is the electron temperature, ε_0 is the vacuum permittivity, and k is the Boltzmann constant. The Debye length increases with electron temperature, as more energetic electrons are less affected by electrostatic potential and so can not be held as close to a charge imbalance to shield it. It decreases with number density as a greater number of charges in the region mean more are available for shielding.

When electrons move as a result of a charge imbalance, the ions remain approximately static. However, as with a stretched spring or pendulum, the electrons which are accelerated will overshoot the equilibrium position; resulting in oscillation. The frequency of this oscillation is characteristic to the properties of the plasma, and is

known as the electron plasma frequency ω_{pe} (Baumjohann and Treumann, 1997):

$$\omega_{pe} = \sqrt{\frac{n_e e^2}{m_e \varepsilon_0}} \tag{1.5}$$

Neutral gases maintain thermal equilibrium via collisions between particles. In an ionised gas, pairs of charged particles can interact via coulomb collisions; changes in particle trajectory caused by electrostatic attraction or repulsion. Collisions are traditionally defined by the cross-section of the particles, however as electrostatic forces act at range, this is not the case for coulomb collisions. One may define the occurrence of a 'collision' as only those interactions for which the energy of the interaction is greater than or equal to the mean kinetic energy of the particles: $e^2/4\pi\varepsilon_0 r \geq kT$ (Meyer-Vernet, 2007). Only these interactions perturb the motion of the particles significantly. At the limit of equality, the maximum radius at which a collision may occur can be defined:

$$r_L \equiv \frac{e^2}{4\pi\varepsilon_0 kT} \tag{1.6}$$

r_L is called the Landau radius, and from it a collisional cross-section for coulomb interaction can be defined as $\sigma_C = \pi r_L^2$. It is important to note that while collisions become more frequent with increasing temperature in a neutral gas, the temperature term in Equation 1.6 means that coulomb collisions actually become less frequent with temperature.

1.1.3 The Plasma Criteria

For matter to be classified as a plasma, it must meet three conditions. These can be expressed in many ways, but the list below is adapted from Baumjohann and Treumann (1997).

1. A plasma must be **quasi-neutral**. Quasi-neutrality is the condition that while small charge concentrations can exist, the system overall must 'appear' neutral. The net amount of positive charge must thus approximately cancel the amount of negative charge. Local charge imbalance is permitted, so long as it is masked from the main population by Debye shielding. Thus the first criterion requires that the characteristic shielding length (the Debye length λ_D) must be far smaller than the size of the system, L: $\lambda_D \ll L$.

2. A plasma must exhibit **collective behaviour**. Debye shielding is a collective behaviour by which quasi-neutrality is preserved, and one can define a sphere with radius equal to the Debye length, which has a number of particles $N \approx n\lambda_d^3$. To satisfy that collective behaviour of the plasma exists, enough particles must exist within a Debye sphere to perform shielding: $n\lambda_d^3 \gg 1$.

3. A plasma must only experience **infrequent collisions**. Collisions must not have a large effect on the plasma, otherwise it will cease to be dominated by collective effects and will begin to act as a gas. As described above, plasma particles exhibit a characteristic oscillation in response to the disturbance of quasi-neutrality at the plasma frequency, ω_{pe}. In an electron-proton plasma, the protons are effectively static relative to the electron motion due to their mass difference. To maintain the condition that collisions do not dominate the plasma, electrons must be able to perform many oscillations within the average time between two collisions with neutrals, τ_n: $\omega_{pe}\tau_n \gg 1$.

1.1.4 Single Particle Motion

There are numerous descriptions which are useful to gain an understanding of plasma properties. These range from descriptions of single particles, to the plasma as a statistical distribution of particles, to the plasma as a magnetised fluid. The single particle description makes assumptions to avoid consideration of the collective

plasma effects. Systems under this description are required to have a strong external magnetic field, such that self-generated magnetic fields are negligible. The plasma is also required to have a low density, such that inter-particle interactions, such as collisions, are negligible. An important result from the single particle description is the gyration of ions and electrons about the magnetic field direction. The $\mathbf{v} \times \mathbf{B}$ term in Equation 1.2 expresses a force perpendicular to a particle's velocity and the field. In the case of a uniform background magnetic field, the changing components of $\mathbf{v} \perp \mathbf{B}$ lead to particle motion which describes a periodic circular path, in the plane perpendicular to the field, with frequency ω_g; known as the gyrofrequency (Baumjohann and Treumann, 1997).

$$\omega_g = \frac{qB}{m} \tag{1.7}$$

r_g, the gyroradius, is the radius of this gyration, and depends on the gyrofrequency and the particle's velocity component perpendicular to $\mathbf{B}$, $v_\perp$.

$$r_g = \frac{mv_\perp}{qB} \tag{1.8}$$

The positive charge of a proton means it gyrates clockwise, as viewed by an observer whom the field is directed towards, while an electron gyrates anticlockwise in the same configuration. It should be noted that due to their lower masses, electrons have far greater gyrofrequencies and smaller gyroradii than ions.

Particles with velocity components both parallel and perpendicular to $\mathbf{B}$ will follow helical paths directed along the magnetic field. Figure 1.3 sketches such a helical path projected onto a plane x-z, where z is parallel to $\mathbf{B}$. Since the perpendicular motion is constrained to gyration, the centre of the particle's gyrating motion (the so-called guiding centre) will follow the magnetic field at the parallel speed $v_\parallel$. The pitch angle, α, of the particle defines the angle between velocity components

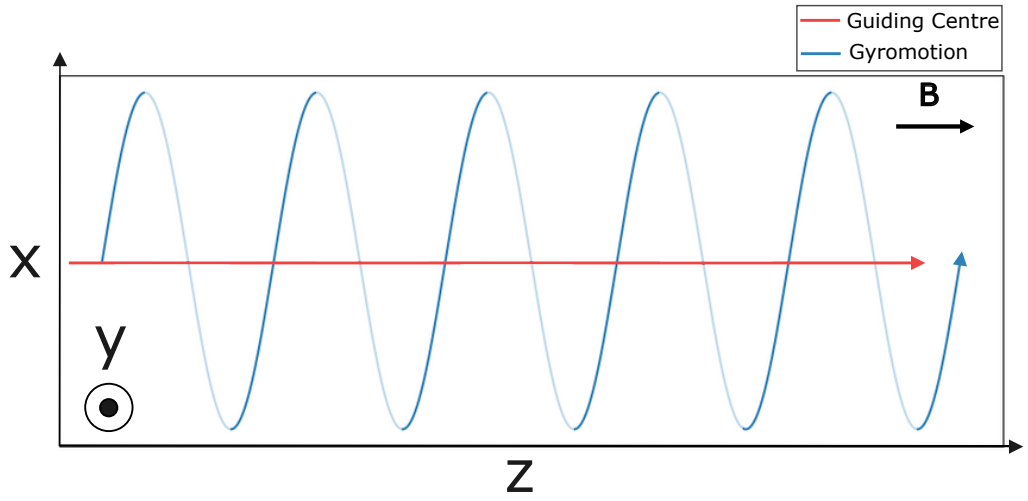

Figure 1.3: A schematic of the gyromotion of a charged particle with both parallel and perpendicular velocity components along the magnetic field. The field is parallel to z, and the motion is shown in the x-z plane.

perpendicular and parallel to the magnetic field.

$$\alpha = \arctan \frac{v_\perp}{v_\parallel} \tag{1.9}$$

The guiding centres of particles can be caused to move in the plane perpendicular to **B** (or 'drift') by external forces or spatial variations in the background magnetic field. The general description of drifts is that forces on the particle perpendicular to **B** modulate the radius of the gyromotion, such that the guiding centre of the gyration drifts relative to the field. The generic equation for this motion given a force **F** is (Baumjohann and Treumann, 1997):

$$\mathbf{v}_{\text{drift}} = \frac{\mathbf{F} \times \mathbf{B}}{qB^2} \tag{1.10}$$

F can be produced by external sources; electric fields apply a force of $q\mathbf{E}$ to the particles, gravitational fields apply a force of $-m\mathbf{g}$. Drifts can also result from variations in the magnetic field such as gradients and curvature of the field.

It should be noted that the charge dependence in Equation 1.10 means that drifts

generally create currents, as the direction of the drift is different for ions and electrons. The so-called $\mathbf{E} \times \mathbf{B}$ drift describes the drift due to the force from an electric field $\mathbf{E}$. Since $\mathbf{F} = q\mathbf{E}$ for such a force, the charge terms cancel in Equation 1.10. $\mathbf{E} \times \mathbf{B}$ drift therefore does not generate currents.

The First Adiabatic Invariant

There are invariants which can apply to the motion of charged particles in a magnetic field, so long as the changes in the field and plasma are slow, compared to the other timescales of the plasma (i.e., the changes are adiabatic). For the purposes of this thesis, we describe only the first. This is the magnetic moment, μ, defined as:

$$\mu = \frac{1}{2}\frac{mv_{\perp}^2}{B} \tag{1.11}$$

m is the particle mass, B is magnetic field strength, and $v_{\perp}$ is the perpendicular velocity component of the particle, as it gyrates about the field. The numerator thus describes the portion of kinetic energy which is a result of perpendicular velocity only. The invariance of μ has the consequence that as particles move into regions of increased (decreased) magnetic field strength, their perpendicular velocity will increase (decrease) accordingly.

1.1.5 Kinetic Theory

The effectiveness of single particle approaches is limited when collective effects are non-negligible. In such cases calculating the motion of each individual particle due to the influence of all other particles in the system becomes impractical. Kinetic theory describes the particles in a plasma in a statistical fashion using a distribution function, f, which describes the probability of a particle having position, $\mathbf{r}$, and velocity, $\mathbf{v}$, at a point in time, t. The $\mathbf{r}$-$\mathbf{v}$ space is known as "phase space" and so the distribution $f(\mathbf{r}, \mathbf{v}, t)$ is known as phase space density at time t (Parks, 1991).

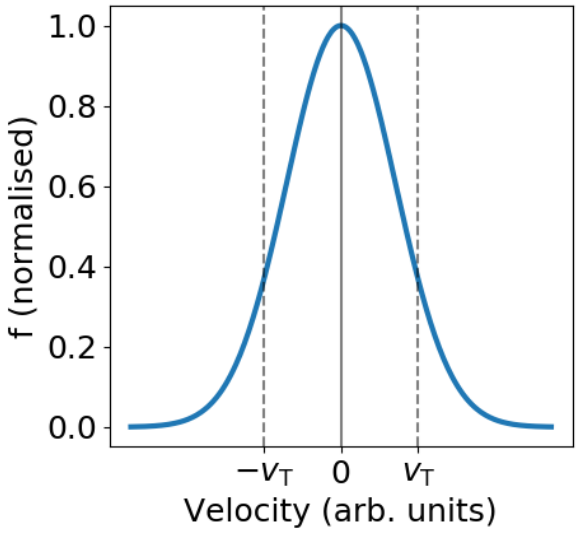

Figure 1.4: An example of a 1-dimensional Maxwellian distribution function, f, plotted against velocity. f is normalised such that its maximum is 1. Velocity is plotted in arbitrary units, with thermal velocity $\pm v_T$; the velocity corresponding to the equality $mv_T^2/2 = kT$ labelled.

The quantity $f(\mathbf{r},\mathbf{v},t)\,d\mathbf{r}\,d\mathbf{v}$ is then the number of particles at time t which exist in the position range $\mathbf{r}$ to $\mathbf{r}+d\mathbf{r}$ and velocity range $\mathbf{v}$ to $\mathbf{v}+d\mathbf{v}$. When positional and temporal variation in the population are not being considered, such as for a single spacecraft measurement of the plasma (see Chapter 3), f reduces to the velocity distribution function (VDF); $f(\mathbf{v})$.

As for a neutral gas, a plasma population in thermal equilibrium can be described by a Maxwellian velocity distribution. Equation 1.12 is one means of writing the Maxwellian distribution function for an isotropic plasma (Baumjohann and Treumann, 1997).

$$f(v) = n\left(\frac{m}{2\pi kT}\right)^{3/2} \mathrm{e}^{-\varepsilon/kT} \tag{1.12}$$

$\varepsilon = \frac{1}{2}mv^2$ is the kinetic energy of a particle with velocity v, and kT is the average thermal energy of all particles in the distribution. The Maxwellian distribution is described only by number density and temperature. Figure 1.4 shows an example of a 1-dimensional Maxwellian distribution plotted as a function of velocity.

Due to the effects of magnetic fields in plasmas, distributions are often anisotropic. This results in the plasma being better described as a bi-Maxwellian, which is a

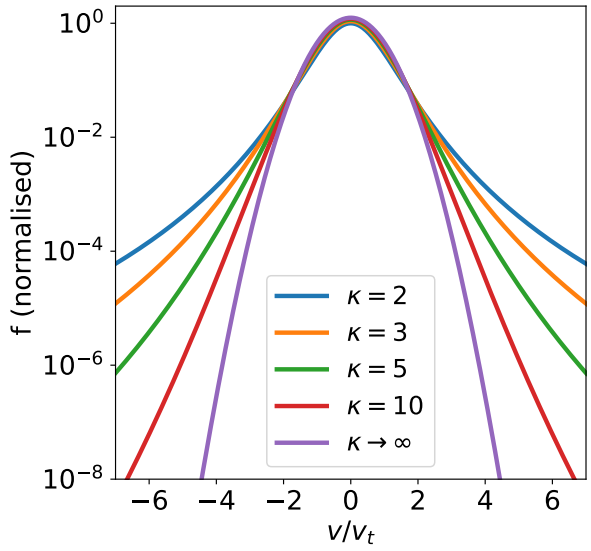

Figure 1.5: Several normalised 1-dimensional kappa distribution functions, f, plotted logarithmically against velocity. Velocity is plotted as a fraction of v_T; the velocity corresponding to the equality $mv_T^2/2 = kE_0$. At greater values of κ the distribution more closely resembles a Maxwellian distribution.

Maxwellian distribution with two characteristic temperatures:

$$f(v_\perp, v_\parallel) = \frac{n}{T_\perp T_\parallel^{1/2}} \left(\frac{m}{2\pi k}\right)^{3/2} \exp\left(-\frac{mv_\perp^2}{2kT_\perp} - \frac{mv_\parallel^2}{2kT_\parallel}\right) \tag{1.13}$$

$T_\parallel$ corresponds to velocity components parallel to the magnetic field; $v_\parallel$, and $T_\perp$ corresponds to those perpendicular; $v_\perp$. Plasma distributions will have anisotropies in temperature; $T_\perp/T_\parallel \neq 1$, in many situations.

Another common distribution function used in particular to describe space plasmas is the kappa distribution (Baumjohann and Treumann, 1997),

$$f(E) = n\left(\frac{m}{2\pi\kappa E_0}\right)^{3/2} \frac{\Gamma(\kappa+1)}{\Gamma(\kappa-1/2)} \left(1 + \frac{E^*}{\kappa E_0}\right)^{-(\kappa+1)} \tag{1.14}$$

where Γ represents the gamma function, E is particle energy, E_0 is mean particle energy, and E^* is the shift-energy of the particle, which allows the distribution to be centred around any energy to account for drift velocities. At low values of κ, $f(E)$ describes a distribution with an extended high-energy tail, which is responsible for a larger fraction of the total distribution as κ decreases. The kappa distribution tends to a Maxwellian as $\kappa \to \infty$ (Livadiotis and McComas, 2013). 1-dimensional

examples of kappa distributions for various values of κ are plotted in Figure 1.5.

Bulk physical properties are desired to fully understand the nature of plasma populations. These can be obtained by taking "moments" of the distribution's VDF. The nth moment of a VDF is the integral of the function over all velocity components weighted by $\mathbf{v}^n$ (Parks, 1991). To account for distribution with a bulk motion, $\mathbf{v}$ is offset by the bulk velocity $\mathbf{v}_b$. The first three moments (zeroth to second) as described in Baumjohann and Treumann (1997) are listed below.

$$n(\mathbf{r},t) = \int f(\mathbf{r},\mathbf{v},t)\, d^3\mathbf{v} \tag{1.15a}$$

$$\mathbf{v}_b(\mathbf{r},t) = \frac{1}{n}\int \mathbf{v} f(\mathbf{r},\mathbf{v},t)\, d^3\mathbf{v} \tag{1.15b}$$

$$\underline{\underline{P}}(\mathbf{r},t) = m\int (\mathbf{v}-\mathbf{v}_b)(\mathbf{v}-\mathbf{v}_b) f(\mathbf{r},\mathbf{v},t)\, d^3\mathbf{v} \tag{1.15c}$$

The zeroth and first-order moments yield number density and the bulk velocity, which have been described already. The second-order moment gives the pressure tensor $\underline{\underline{P}}$. In an isotropic plasma, 1/3 the trace of $\underline{\underline{P}}$ gives the iostropic pressure, $P = nk_BT$. In an anisotropic plasma the diagonal gives the anisotropic pressure terms. The off-diagonal terms represent shear stresses on the plasma.

1.1.6 Magnetohydrodynamics

When describing a plasma on large scales, it is often not necessary to know the full distribution function to sufficiently understand the system. Thus, the variation of moments of the velocity distributions in time and space are all that is required. Magnetohydrodynamics (MHD) describes the plasma as a single conducting fluid. This captures the evolution of the plasma as a gas which is sensitive to, and generates, electromagnetic fields. MHD thus relates bulk moments of the plasma to

electric and magnetic fields.

Since it deals in bulk properties of the plasma, such as density and temperature, rather than full distributions, MHD effectively averages over the motions of individual particles in time and space. It can only be safely applied when describing a plasma system in which the characteristic time and length scales are larger than the so-called "kinetic scales" of the plasma, such as gyroradii, mean-free-paths, and gyrofrequencies of its ions and electrons.

A plasma must contain positive and negative particles (usually protons and electrons), and so to describe it fully would require a fluid approach which describes two (or more) fluids. Often for simplicity however, a single-fluid approximation is applied to MHD.

Rather than considering the plasma fluid at a fixed point in space, it is often more useful to consider a volume element of the fluid, co-moving with the local flow. Changes in properties thus take the form of changes in time which are local to the volume element, and changes which occur as the volume element changes its position. We thus mathematically define the derivative of a given parameter a using the "advective derivative":

$$\frac{da}{dt} = \frac{\partial a}{\partial t} + \mathbf{v} \cdot \nabla a \tag{1.16}$$

The Mass Continuity Equation

As is typical for neutral fluids, in the absence of sinks or sources we describe an MHD fluid as having conservation of mass. The mass continuity equation states that change in the mass contained within a volume element can only occur as a result of mass flow into or out of that volume:

$$\frac{\partial \rho}{\partial t} + \nabla \cdot (\rho \mathbf{v}) = 0 \tag{1.17}$$

ρ is the mass density in the given volume element in space. In the single fluid approximation, the velocity vector $\mathbf{v}$ and density ρ describe the mean velocity, and total density, of the combined protons and electrons.

The Momentum Equation

We wish to express the change in velocity of a fluid element as a result of all of the forces which act upon it; producing an equation of motion for the fluid. If we include gravitational, gas pressure, and Lorentz forces, then the equation of motion for an isotropic single fluid plasma is:

$$\rho \frac{d\mathbf{v}}{dt} = \rho \left(\frac{\partial}{\partial t} + \mathbf{v} \cdot \nabla \right) \mathbf{v} = \rho \mathbf{g} - \nabla P + \rho_{\mathrm{q}} \mathbf{E} + \mathbf{J} \times \mathbf{B} \tag{1.18}$$

This is the MHD momentum equation. $\mathbf{g}$ is gravitational acceleration, P is the isotropic gas pressure, and the remaining right-hand terms are the Lorentz force. The electric-field term is only non-zero in the case of a non-zero charge density ρ_q; which constitutes a departure from quasi-neutrality. Depending on the system being described, many of the forces on the right hand side of the equation can be approximated to zero, allowing a simpler description.

Ohm's Law

The current density in an unmagnetised, isotropic, and slowly varying ($\mathbf{J} \sim$ constant) plasma is related to the electric field:

$$\mathbf{J} = \sigma \mathbf{E} \tag{1.19}$$

where $\sigma = (ne^2/m_e \nu_{ei})$ is the conductivity of the plasma (Meyer-Vernet, 2007). This conductivity describes the effect of coulomb collisions (ν_{ei} is the ion-electron collision frequency) hampering the oppositely-directed flows of electrons and pro-

tons produced by an electric field. However, equation 1.19 is a simplified version of Ohm's law for a plasma.

Now considering effects of magnetic fields, and removing all assumptions, we can write the generalised Ohm's law:

$$\mathbf{E} + \mathbf{v}_i \times \mathbf{B} - \eta \mathbf{J} = \frac{\mathbf{J} \times \mathbf{B}}{q n_e} - \frac{\nabla \cdot \underline{\underline{P_e}}}{q n_e} - \frac{m_e}{q} \frac{d\mathbf{v}_e}{dt} \tag{1.20}$$

where $\mathbf{v}_i$ and $\mathbf{v}_e$ are ion and electron velocity respectively, $\eta = 1/\sigma$ is the resistivity (the reciprocal of conductivity), and $\underline{\underline{P_e}}$ is the electron pressure tensor. The left hand terms are the electric and magnetic field contributions to the current through the Lorentz force, and the current itself. The right hand terms from left to right are known as the Hall term, electron pressure term, and electron inertia term.

If we neglect the right hand terms of Equation 1.20 (assuming isotropy and slow variations) we arrive at a simplified Ohm's law for a magnetised, collisional, plasma:

$$\mathbf{J} = \sigma(\mathbf{E} + \mathbf{v} \times \mathbf{B}) \tag{1.21}$$

which applies in the case of collisional MHD; where σ is finite. In contrast, ideal MHD describes non-collisional regimes, where $\sigma \to \infty$ (since $\nu_{ei} \to 0$). Now Ohm's law becomes:

$$\mathbf{E} = -\mathbf{v} \times \mathbf{B} \tag{1.22}$$

Equation of State

An equation of state is required to close the MHD equations by relating pressure and mass density. Common in space plasmas is the assumption of an adiabatic fluid:

$$P = K\rho^{\gamma} \tag{1.23}$$

where K is a constant and γ is the adiabatic index, which depends on the degrees of freedom of the fluid. For an isotropic Maxwellian plasma, $\gamma = 5/3$ (Parks, 1991). Another common equation of state is that of an isothermal fluid:

$$P = C\rho \tag{1.24}$$

where C is also a constant.

Magnetic Reynolds Number and Frozen-in Flux

The equations shown above, when combined with Maxwell's equations, describe the behaviour under single-fluid, conductive, MHD. We now outline some important results which arise from these equations for this thesis and space plasmas in general.

Applying Ohm's law (Equation 1.21) and Maxwell's Equations 1.1c and 1.1d, in the frame of a moving plasma with velocity $\mathbf{v}$, one obtains an expression for the change in magnetic field (Parks, 1991):

$$\frac{\partial \mathbf{B}}{\partial t} = \frac{\nabla^2 \mathbf{B}}{\mu_0 \sigma} + \nabla \times (\mathbf{v} \times \mathbf{B}) \tag{1.25}$$

$\nabla^2 \mathbf{B}/\mu_0\sigma$ is a magnetic diffusion term; the rate at which the magnetic field moves from regions of high to low magnetic field strength. The term $\nabla \times (\mathbf{v} \times \mathbf{B})$ is the magnetic convection term; the magnetic field evolution component which is dictated by plasma flow.

The magnetic Reynolds number, R_M, describes the ratio of the influence of diffusion over convection terms in Equation 1.25. By approximating ∇ as $1/L$ (where L is the characteristic scale length of $\mathbf{B}$) and $\partial/\partial t$ as $1/t$ (where t is the characteristic time scale of $\mathbf{B}$ changes), the ratio of timescales for diffusion, t_D, and transport

$t_T (= v/L)$, can be calculated.

$$R_M = \frac{t_D}{t_T} = \mu_0 \sigma L v \tag{1.26}$$

For $R_M \gg 1$, diffusive timescales are far longer than those for transport, and so the plasma velocity influences the evolution of magnetic field far more than diffusion, and the second term in Equation 1.25 dominates. For $R_M \ll 1$ the opposite is true. In a perfectly conducting plasma (ideal MHD), $\sigma = \infty$, so $R_M \gg 1$. In ideal MHD the magnetic field evolves only as a result of the plasma motion, and it can be shown (see Parks, 1991) that the "frozen-in" condition for the plasma applies. This condition states that the flux of magnetic field through an imaginary closed surface co-moving with the plasma flow is constant; and also that packets of plasma which are found on a given magnetic field line will not leave that field line. Under frozen-in flux, we can consider particles to follow magnetic field lines (or be confined to flux tubes), or magnetic field lines to be defined by the trajectories of particles.

Plasma Beta

Neglecting gravity and external electric fields in the momentum equation (Equation 1.18), the change in momentum is controlled by the gradient of thermal pressure P and the magnetic force term $\mathbf{J} \times \mathbf{B}$. Substituting $\mathbf{J}$ from Equation 1.1d, again neglecting electric fields, the latter term can be expressed as follows:

$$\mathbf{J} \times \mathbf{B} = [(\mathbf{B} \cdot \nabla)\mathbf{B} - \nabla B^2/2]\mu_0^{-1} \tag{1.27}$$

Consider first the term $\nabla B^2/2\mu_0$. Functionally this is analogous to a pressure, and so we define it as the 'magnetic pressure':

$$p_B = B^2/2\mu_0 \tag{1.28}$$

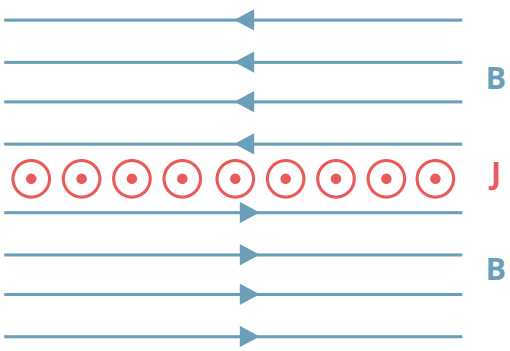

Figure 1.6: An illustration of a current sheet generated by oppositely-directed field lines. The field lines are infinitely long. The right-left antiparallel field (blue) generates current directed out of the page (red).

The ratio of the thermal pressure of the plasma to the magnetic pressure is called the plasma beta or β:

$$\beta = \frac{P}{B^2/2\mu_0} \tag{1.29}$$

β describes the competition between particles and field to control the overall motion of the plasma. When frozen-in flux applies, for $\beta \gg 1$ the particle flow dominates the magnetic field, whereas for $\beta \ll 1$ the magnetic field evolution dominates the motion of the plasma.

Magnetic Tension

Returning to Equation 1.27, we consider now the term $(\mathbf{B}\cdot\nabla)\mathbf{B}$. This term is zero in the case of a straight field line. When this is not the case, this term makes a contribution to $\mathbf{J}\times\mathbf{B}$, such that a bent magnetic field may generate a force on the plasma which opposes that bending. This is analogous to the effect of tension on a string, and so we name this term the 'magnetic tension'.

Current Sheets

From Equation 1.1d, a magnetic field with non-zero curl must be associated with currents which are perpendicular to the plane of the curl. If we now consider a functionally infinite plane (the plane may end at some location outside of the considered boundaries) across which magnetic field direction reverses, then a current must exist within the plane; oriented as shown in Figure 1.6. This current feature is

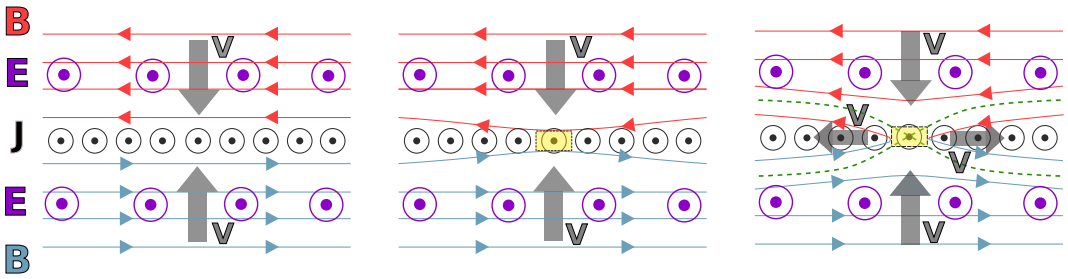

Figure 1.7: A simple schematic of reconnection for antiparallel field lines, with snapshots in time going from left to right. Left: A current sheet (black) is found at the interface between oppositely directed (red and blue) magnetic fields. A background electric field is shown in purple. Middle: The field lines are brought together by $\mathbf{E} \times \mathbf{B}$ drift, resulting in a thin region where magnetic diffusion is permitted (yellow box). Right: The field lines reconnect after being allowed to diffuse. Previously isolated field lines are now connected. The magnetic tension in the new topology causes the field and plasma to flow outwards perpendicular to the original inward flow. A pair of separatrices are shown in green.

1-dimensional, and in principal infinitely thin, and so is known as a "current sheet".

1.1.7 Magnetic Reconnection

Magnetic reconnection is a change in the topology of a magnetic field, which can be understood as a change in connectivity of one or more pairs of field lines. One important consequence of this is that two plasma populations, previously confined to separate field lines by frozen-in flux, are allowed to mix as a result of the change in connectivity.

A schematic of the basic reconnection process is shown in Figure 1.7. Two separate plasma populations are shown, associated with magnetic fields which are antiparallel (as in the figure) or have strong shear between them across the central current sheet. The field lines are associated with the two plasma populations, and frozen-in flux applies ($R_M \gg 1$). In the presence of a uniform electric field, these two populations are brought together by oppositely-directed $\mathbf{E} \times \mathbf{B}$ velocity drifts on either side of the current sheet (grey arrows in the figure). The continual driving together of plasma and frozen-in magnetic flux causes energy buildup in the form of a more intense, narrower current sheet. In the middle panel of the figure, the field lines are

driven together to the point where the characteristic scale, L, of the current sheet becomes small enough that $R_M \ll 1$ (Equation 1.26). Thus in a small region at the interface of the two fields, frozen-in flux may break down, and magnetic field can diffuse through the plasma. This region is thus known as the "diffusion region". Through this diffusion, the magnetic field on one side of the current sheet reconnects with the field on the other and so reaches a lower energy state. When the field moves out of the diffusion region it again freezes-in to the plasma. In the right panel of the figure, this process has taken place, such that magnetic field lines now connect across the current sheet between the two initially separate populations. The new field lines are highly kinked, and so magnetic tension forces lead to fast outflow of plasma from the reconnection site.

The above description illustrates a highly-idealised, active, reconnection configuration, in which a current sheet forms between antiparallel fields. Here, two "separatrices" cross at the magnetic null (shown in replacegreenpurple in the figure). A separatrix is a surface where there is a discontinuity in magnetic connectivity. The shape of the separatrix leads to the name "X-point" reconnection for this configuration.

In three dimensions, even field lines which are not antiparallel will produce current sheets, and may ultimately reconnect, if there is a strong shear between field lines. Thus reconnection is generally possible if there is some antiparallel component between the field lines. Reconnection in this case can be termed "component reconnection".

1.1.8 Waves and Fluctuations in a Plasma

A host of wave types may exist in a plasma, operating from kinetic (small) scales to larger MHD scales. These waves have the capacity to scatter particle trajectories, accelerate and heat populations through damping and resonances, and transport en-

ergy between locations. Here we describe just a small subset of plasma waves, and their effects.

As already described, magnetic tension forces oppose the distortion of field lines; acting as a restoring force in response to perturbations. These restoring forces can thus lead to waves. When the magnetic field is frozen into the plasma, waves which propagate along a field line must also displace the frozen-in particles. Therefore a wave can only propagate at the speed to which the magnetic field can accelerate the plasma. This speed is known as the Alfvén speed, v_A, and is found by equating the total kinetic energy density of the plasma, $\rho v^2/2$, to the energy density of the magnetic field, $B^2/2\mu_0$ (Alfvén, 1942), giving

$$v_A = \frac{B}{\sqrt{\mu_0 \rho}} \tag{1.30}$$

A transverse magnetic wave in an MHD plasma will propagate at this speed and is known as an Alfvén wave. Other modes of MHD waves also exist, including compressive longitudinal waves. These are known as magnetosonic waves as their restoring force includes the effect of pressure gradient of the plasma particles. In the specific case where they propagate perpendicular to the background magnetic field direction, magnetosonic waves travel at the magnetosonic speed c_{ms}:

$$c_{ms}^2 = c_s^2 + v_A^2 \tag{1.31}$$

where c_s is the sound speed.

Electromagnetic (EM) waves can propagate in a plasma, but are affected by the medium. Many different wave modes are viable, which exhibit different dispersion relations. When there is a background magnetic field, waves of different polarities, and of frequencies comparable to or less than a given particle gyrofrequency, are affected differently by that species of gyrating particle. For example, waves with fre-

quency below the electron gyrofrequency, and which are polarised in the same sense as the gyrating electrons, obey a dispersion relation by which higher-frequency wave components propagate faster than lower-frequency components. Thus, for a broadband wave of this type emitted at some location, the higher-frequency components arrive at an observer before the lower. The observer experiences a wave of decreasing frequency with time, and so these types of waves are known as "whistler-mode waves".

Wave-Particle Interactions

All individual charged particles in a plasma will in some fashion interact with an electromagnetic wave or fluctuation, in the sense that their velocity will likely be altered by the Lorentz force. Waves and fluctuations in a plasma thus have the capacity to alter particle populations, by adding or removing kinetic energy. Particularly in plasmas with a low collisional frequency, waves which are produced and later dissipated by interacting with particles act to allow those particles to communicate with one another in place of collisions.

We consider a circularly-polarised electromagnetic wave, propagating in the opposite direction to a charged particle. The wave frequency and particle gyrofrequency may be in phase, or nearly in phase, given the appropriate Doppler shift. This is known as the wave and particle being at resonance. In the frame co-moving with the particle, a perfect resonance causes the particle to experience an electric field which is not fluctuating. Particles which are not quite at resonance because their parallel velocity is less than the wave phase velocity are accelerated by the wave, up to the wave phase speed. Particles with parallel velocity which is greater than the phase speed are decelerated. In the former case wave energy is transferred to the particle, while in the latter the wave gains energy from the particle. We note that the above argument also applies if the shifted wave frequencies are an integer factor

of the gyrofrequency. The resonance condition can thus be written:

$$\omega - k_{\|} V_{\|} = n\Omega \tag{1.32}$$

where ω is the wave frequency, $k_{\|}$ is the parallel component of the wave vector, $V_{\|}$ is the parallel component of the particle velocity, n is a positive or negative integer, and Ω is the particle gyrofrequency.

For a Maxwellian distribution of particles interacting with a wave with resonance condition given by Equation 1.32, the particles in the distribution with parallel velocity within a range $[V_{\|} - \Delta v, V_{\|} + \Delta v]$ will interact strongly and gain or lose energy. Examining the positive sector of Figure 1.4, it is clear that in a Maxwellian distribution the number of particles in any sub-range $[V_{\|} - \Delta v, V_{\|}]$ is always greater than that in the higher range $[V_{\|}, V_{\|} + \Delta v]$, for $V_{\|} > 0$. Thus, more particles are accelerated than decelerated, regardless of the value of the wave phase velocity. Thus the distribution is heated, and the wave is damped. This process is known as 'Landau damping'.

The damping of waves is not necessarily guaranteed for any generic particle distribution. A distribution which contains a beam (or 'bump') may ultimately lose energy to the wave, depending on the wave phase velocity. This process then excites the wave, and is known as inverse Landau damping.

Distributions which are liable to excite waves as above are unstable, and the process of excitation is known as an instability. A further example of an instability is the electron "two-stream" instability. The configuration for this instability is a main thermal electron population, plus a high-energy beam. When the drift velocity of the beam exceeds the thermal velocity of the main population, the instability can be triggered. This leads to the excitation of waves which may go on to interact further.

Plasma Turbulence

Turbulence is a phenomenon which occurs in both neutral and magnetised (plasma) fluids. It describes fluctuations across length-scales. Turbulent fluctuations take the form of a collection of eddies across a range of scales, known as the inertial range. Length-scales above the upper-limit of the inertial range are generally where driving occurs; the energy is injected in the system through mechanical work. Within the inertial range, energy is transported from higher to lower length-scales in a cascade; larger eddies give way to smaller ones. At scales smaller than the inertial range, the energy is dissipated.

In neutral fluids, energy dissipation occurs due to the viscosity of the medium. The cascading energy carried in the turbulent fluctuations thus ultimately heats the fluid. The process of dissipation in magnetised fluids is far more complex; plasmas are often non-collisional, and the length-scales at which the fluid description breaks down for ions and electrons are far apart. This remains a topic of active research. For the purposes of this thesis, we simply note that the energy of the fluctuations is dissipated at small scales, such that it is transferred into the kinetic energy of individual particles; increasing the temperature of the distribution.

1.1.9 Plasma Ionisation and Charge States

Ionisation is necessary to create a plasma from a neutral gas. In a plasma environment with high density and temperature, and low flux of incoming radiation, ionisation and recombination of species are dominated by collisions of ions with free electrons. Collisional ionisation occurs when an electron collides with an ion or neutral, resulting in the loss of bound electrons. If the evolution of the plasma is slow enough, then an equilibrium state can be reached whereby for each ionisation state, the rate of ionisation/recombination into that state is balanced by the rate of

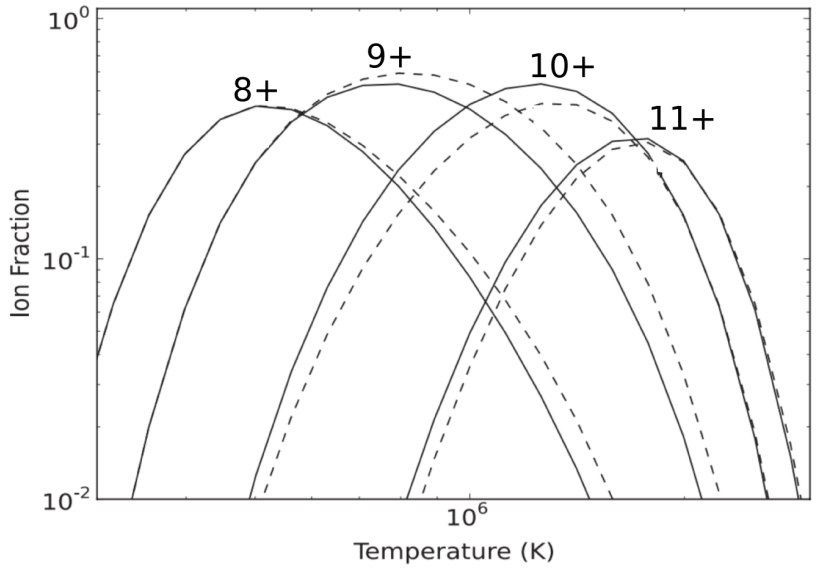

Figure 1.8: Fraction of Fe ions in ionisation states Fe^{8+}–Fe^{11+} (labelled using only charge numbers) as a function of electron temperature, in collisional equilibrium. Abundances are calculated using the CHIANTI database (Dere et al., 1997; Landi et al., 2013) of ionisation and recombination coefficients. The solid lines use rates calculated from version 7.1 of the database (Landi et al., 2013), while the dashed lines use the earlier version 6 (Dere et al., 2009). Figure adapted from Landi et al. (2013).

ionisation/recombination out of it. This is known as collisional equilibrium. The kinetic energy available to the electron population to perform ionisation will increase with increasing temperature; at higher temperatures, higher ionisation states become available. To illustrate this, Figure 1.8 plots the fraction of Fe in states Fe^{8+}–Fe^{11+} as a function of electron temperature. The fractions are calculated from the CHIANTI database (Dere et al., 1997; Landi et al., 2013) under the assumption of collisional equilibrium. At increasing temperatures Fe is distributed into higher ionisation states.

At collisional equilibrium we can calculate the relative densities of two adjacent ionisation states, the "charge state ratio" n_{i+1}/n_i, using ratios of ionisation and recombination rate coefficients:

$$\frac{n_{i+1}}{n_i} = \frac{C_i(T_e)}{R_{i+1}(T_e)} \tag{1.33}$$

C_i is the coefficient for the rate of ionisation for ions of charge state i to charge state $i+1$, while R_{i+1} is the equivalent coefficient for recombination from state $i+1$ to i, and T_e is the electron temperature. Each ion species is thus partitioned into ionisation states as a function of T_e.

1.1.10 Plasma Radiation

As with neutral atoms, electron transitions in ions lead to the emission or absorption of radiation. We are particularly interested in this phenomenon as it occurs at the Sun. By observing radiation we can thus remotely infer structure and properties of the plasma environment. Transitions of bound electrons from a high to low (low to high) energy state results in (from) the emission (absorption) of a photon. The energy (and thus wavelength) of the associated photon is equal to the difference in energy between the states. A given neutral atom thus has a spectrum associated with it, made up of the transitional lines for its characteristic energy states.

The transitions which are available for positive ions are different to those for the corresponding neutral atoms of the same species. The spectrum associated with an element in a given ionisation state is denoted by a roman numeral, starting from I referring to the atomic state. The spectrum of Fe which has been ionised through the removal of 5 electrons for example is thus referred to as Fe VI.

The intensity of emission of a spectral line is linearly dependent on the density of its corresponding ion. Because of the dependence of the relative ion abundances on temperature, the relative intensities of emission lines from the plasma also depend on the electron temperature. In the case that the mechanism for emission itself is excitation by electron collisions, followed by spontaneous emission, then the intensity also scales with n_e^2, where n_e is the electron number density (Golub and Pasachoff, 2010). The relative intensities of emission lines can thus be used to infer density, temperature, and composition information on the emitting plasma, under

certain assumptions.

Zeeman Splitting

The magnetic field of an emitting plasma is an invaluable parameter to diagnose. The presence of a magnetic field causes the splitting of spectral lines, as the energies of usually-degenerate electron spin states become split. This is known as the Zeeman effect. When the magnetic field is aligned with the line of sight the line splits into two components. Each line is offset either side of the original spectral line, by a wavelength proportional to the magnetic field strength. The polarisation of the split components gives information on the polarity of the line-of-sight magnetic field.

1.2 The Sun and Corona

The Sun is a star of mass $\sim 2 \times 10^{30}$ kg and radius $\sim 7 \times 10^{5}$ km (Meyer-Vernet, 2007). Its influence dominates the solar system through gravitation, electromagnetic radiation, energetic particle radiation, and plasma outflows and their associated magnetic fields. The core of the Sun is the site of nuclear fusion which provides the energy for this electromagnetic and particle radiation. The Sun possesses a magnetic field, which is at times approximately dipolar (solar minimum), and at times far more complex (solar maximum). The Sun is the source of the solar wind; a radial flow of plasma which escapes from it in all directions. The solar wind, and the Sun's magnetic field which it carries, creates a 'bubble' in interstellar space. This is the region of the Sun's influence in the interstellar medium, and is known as the 'heliosphere'.

1.2.1 Structure of the Sun

Given the goal of this thesis to understand the origins of the solar wind, we do not concern ourselves here with details of the Sun's structure below its visible surface; the photosphere. It suffices to say that below the photosphere, convective motions driven by energy generated through fusion in the core cause plasma to rise buoyantly to photospheric heights, ultimately feeding material into the regions above. Flows of plasma below the photosphere generate the solar magnetic field, through a dynamo process (for a detailed review of the solar dynamo, see Charbonneau, 2010).

The photosphere is commonly referred to as the "surface" of the Sun, as below it the mean free paths of absorption and re-emission for photons are very low (optically thick), and above it they tend to infinity (optically thin). Photospheric emission temperatures are around 5000 K (Athay, 2012). Since the photosphere is the height at which plasma can radiate heat, it is the site at which upwardly-convecting plasma cools, and subsequently falls back down below the surface. This cycle takes place over granular cells which have scales of ~ 1 Mm. Magnetic flux emerges from the photosphere in concentrated regions, but rapidly expand to fill the available volumes at greater heights. Regions of highly-concentrated flux appear dark, as the strong magnetic field prevents convective motions from supplying new, hot plasma (Hale, 1908). These cool, low-density, regions are known as sunspots. The convective motions of the photosphere move the footpoints of field lines which extend above it, adding complexity to the field topology in the solar atmosphere. The magnetic field of the photosphere can be measured through Zeeman splitting since these concentrated regions contain strong fields, and the photosphere is optically thick.

The Sun rotates differentially as can be observed at the photosphere by e.g., tracking sunspots as pioneered by Carrington (1863). Near its rotational equator, the sidereal (relative to background stars) period is around 25 days, while towards the poles

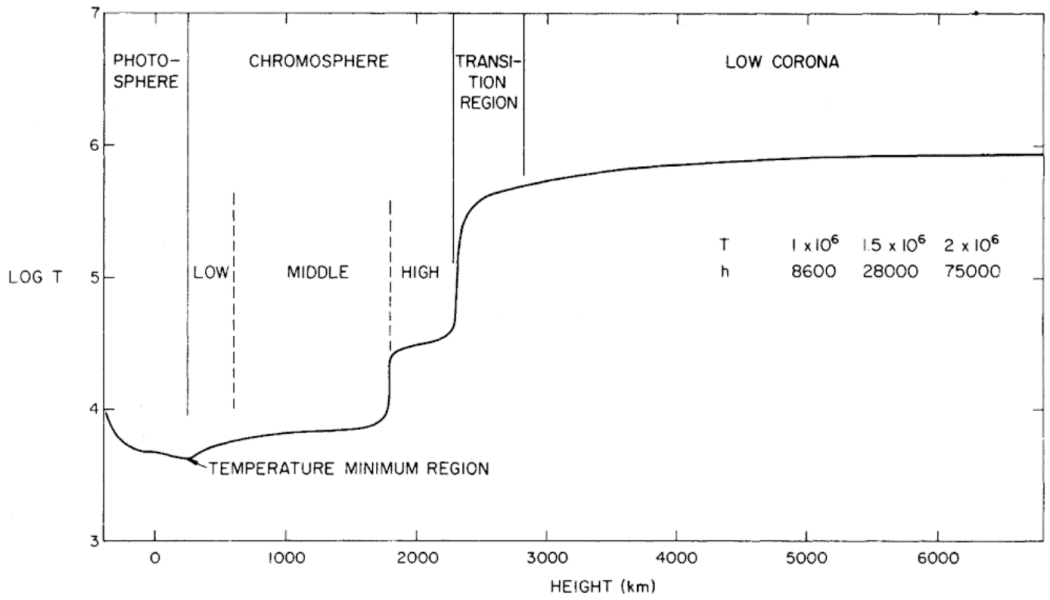

Figure 1.9: Profile of modelled solar ion temperature (as $\log(T)$) from the photosphere to the low corona as a function of height. A selection of temperatures (in K) at heights which exceed the x-axis range are also printed. Figure from Athay (2012).

the period is around 35 days (Schrijver and Siscoe, 2009). This differential rotation moves the footpoints of field lines which extend above the photosphere, again leading to increased complexity in their topology. We shall see later that solar rotation leads to the spiral geometry of the heliospheric magnetic field, and the interaction of streams in the solar wind. A "Carrington rotation" is one equatorial rotation of the Sun, as viewed from Earth. The length of a Carrington rotation is thus the synodic solar rotation period, which is ~ 27 days (Carrington, 1863).

Figure 1.9 shows a plot of the temperature of the Sun with height above the photosphere. Directly above the photosphere lies a region known as the chromosphere. Around 2500 km thick, the chromosphere exhibits lower densities, and higher temperatures than the photosphere. The increase over photospheric temperatures is around a factor of 3–4, to $\sim 2 \times 10^4$ K. Between the chromosphere and the corona the temperature rapidly increases to $\sim 10^6$ K (typical coronal temperatures) in a thin layer known as the transition region. The mechanisms by which energy is transferred to heat the plasma, leading to these high coronal temperatures, are still

unknown. This open question is known as the "coronal heating problem" and is one of the longstanding mysteries of heliophysics. In the corona, the temperature eventually levels-off, before gradually decreasing with height (not shown in figure).

1.2.2 The Corona

The corona is the Sun's atmosphere. It is optically thin, and extends from its lower edge at the chromosphere, to its upper edge where it forms the solar wind. There is no hard boundary between the corona and the solar wind, and so the solar wind is often thought to be a part of the extended corona. Typically when describing the corona, authors refer to heights on the order of a few solar radii.

Plasma number densities in the corona are $\sim 10^8\,\mathrm{cm}^{-3}$, while magnetic fields are on the order of 1–10 G (Meyer-Vernet, 2007). Given the aforementioned temperature of $\sim 10^6\,\mathrm{K}$, plasma beta in the corona is expected to be ≤ 1, so that the magnetic field evolution either dominates or is at least comparable to the plasma motion. Moving radially outwards, further into the corona and eventually the solar wind, we find that β drops off with distance.

The Coronal Magnetic Field

The magnetic field in the corona extends up from footpoints in the photosphere. Field lines rapidly expand out of the concentrated channels of the photosphere; filling the volume of the corona. The magnetic field in the corona can be classified as "closed" or "open". Closed magnetic field lines have both footpoints rooted in the photosphere. Closed fields thus take on a loop structure of finite length, and when filled with material are known as "coronal loops". Open magnetic field lines on the other hand have only one footpoint rooted in the photosphere, while the other stretches off into the heliosphere. To satisfy $\nabla \cdot \mathbf{B} = 0$, these field lines do in fact close; they may extend to the edge of the heliosphere, and meet the photosphere

Figure 1.10: Diagram of interchange reconnection adapted from Crooker et al. (2002). Magnetic field lines before reconnection are drawn on the left, and following reconnection are drawn on the right.

again as open flux of the opposite polarity. The field is "open" insomuch as it extends outside of the domain of the corona itself.

The coronal magnetic field has yet to be measured directly. The field is weak in comparison to the photospheric magnetic field, and so cannot be measured through Zeeman splitting.

Reconnection of Coronal Magnetic Fields

The 3-dimensional nature of the corona means that reconnection can occur in numerous configurations; both with and without a magnetic null (Schindler et al., 1988). Reconnection in the presence of a null normally occurs somewhere along a separatrix (Démoulin, 2007). Without a null, component reconnection may still take place in the presence of a "quasi-separatrix layer" or QSL (Priest and Démoulin, 1995). QSLs define thin volumes which field line connectivity changes at a rate greater than some threshold; not necessarily discontinuously.

A type of reconnection which applies particularly to coronal and heliospheric magnetic fields is "interchange reconnection' (Crooker et al., 2002). A schematic of this process, adapted from Crooker et al. (2002), is shown in Figure 1.10. This process describes reconnection between an initially closed loop and an open magnetic field line, as in the left panel of the figure. The result, as shown in the right panel, is a change of connectivity for the open magnetic field, and the formation of a new, smaller, closed loop at the Sun.

Coronal Plasma

Plasma which is confined to coronal loops is heated, likely by mechanisms related to general coronal heating (Reale, 2014). The confinement of the plasma leads to the energy being retained. Loop plasma can thus reach temperatures of 2–3 MK. Models for loops in the quiet Sun predict that maximum loop temperature should positively correlate with the height of the loop (Rosner et al., 1978). We also expect loops to carry more material than open field lines, since it is fed from the base of the loop but unable to escape into the heliosphere. The plasma in the corona thus exists at multiple different temperatures, or is "multi-thermal", due to the many different open field regions, loops, and loop properties which are present there.

Coronal Emission

Since the corona is optically thin, observations of coronal emission are in fact superpositions over the line-of-sight (LOS) between the observer and the photosphere. The intensity of emission is proportional to the integrated density of material in this LOS, squared (Golub and Pasachoff, 2010). Discerning structure in the corona is thus somewhat ambiguous due to projection effects. Since the occurrence of emission of different spectral lines by material in the corona is highly sensitive to temperature, imaging the corona in different wavebands allows observers to discern material which is emitting at different temperatures. The structure of the corona can thus be imaged as loops of different temperature. Combining images at various wavelengths allows observers to somewhat overcome issues due to projection effects.

Active Regions

An active region is an area of strong magnetic field. A dipolar on-disk active region is shown with different observational methods in Figure 1.11. In the photosphere,

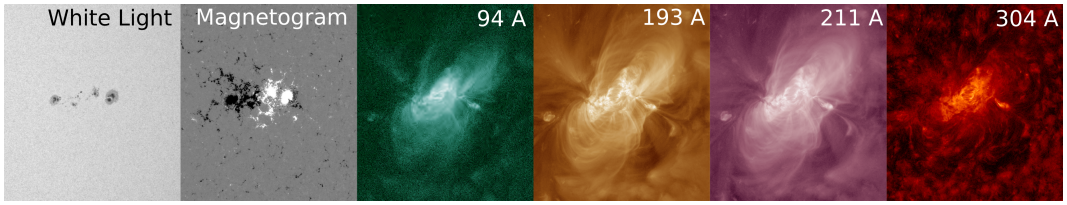

Figure 1.11: A dipolar active region (NOAA 12699) shown in different wavelengths, and in a magnetogram. The left right panels are from SDO-HMI. The white light image clearly shows sunspots at the loop footpoints on the photosphere. The magnetogram shows regions of concentrated positive (white) and negative (black) magnetic flux at the photosphere. EUV observations of the corona (first 4 panels) are from SDO-AIA - wavelengths are labelled on each panel. Loops containing plasma of different temperature are visible in the EUV panels, and are visibly different sizes. Loop footpoints coincide with areas of most concentrated magnetic flux.

visible in the white light observations in the left-most panel, the magnetic footpoints associated with active regions typically are visible as sunspots. The strong field is apparent in the magnetogram (black is inward LOS field, white is outward LOS field) to the right of this panel. In the corona, active regions typically manifest as groups of particularly bright loops in extreme ultraviolet (EUV - panels 3–6 of the figure) and x-ray wavelengths (not shown). At their simplest, the magnetic topology of active regions is dipolar, and the two opposite-polarity regions are connected by these loops. Active regions also exist in multi-polar states.

Active regions have a life-cycle which spans from emergence to dispersion. Emergence occurs as strong concentrations of magnetic flux begin to penetrate upwards through the photosphere. Once all flux has emerged, the decay process of the AR begins as small sub-regions of flux migrate away from the main concentrated regions, breaking the latter down. From their emergence to the breakdown of the associated sunspot, active region lifetimes are around 30–60 days (Bray and Loughhead, 1964).

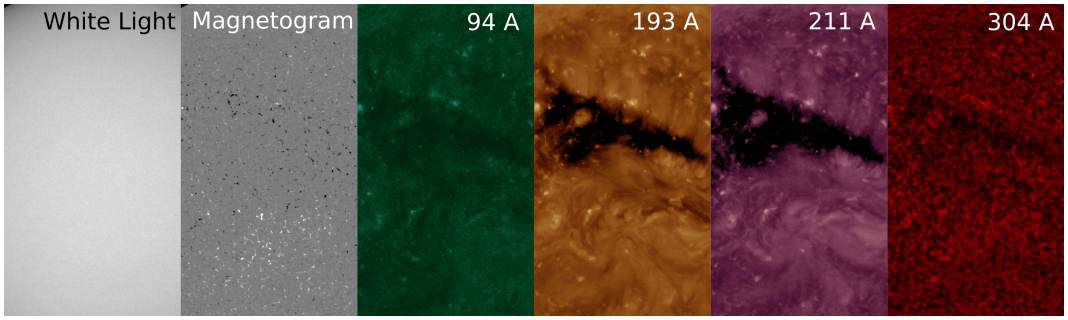

Figure 1.12: A coronal hole shown in different wavelengths and in a magnetogram. The format is identical to Figure 1.11. There are no sunspots visible in the white light imagery, and no strongly concentrated flux regions in the magnetogram. The magnetogram shows the coronal hole is primarily unipolar. The coronal hole is particularly dark in 193 Å and 211 Å.

Coronal Holes

Coronal holes are regions of the corona which are defined by 1. Reduced emission in the EUV and x-ray and, 2. Open magnetic flux. An example of a coronal hole is shown in Figure 1.12. The dimness of the coronal hole is most obvious in the 193 Å and 211 Å bands in the figure. Open flux can only be inferred by magnetic extrapolation. However from the lack of sunspots in the white light panel, and the flux and polarity in the magnetogram panel, coronal hole magnetic fields are not highly-concentrated, and are primarily unipolar. In contrast to the photosphere below, coronal holes are observed to rotate approximately rigidly; moving at near the equatorial rotation rate across all latitudes (e.g., as reviewed by Nash et al., 1988).

Coronal holes have long been thought to be the source of the 'fast' solar wind (e.g., Wilcox, 1968; Krieger et al., 1973). To act as a solar wind source, at least some open flux must be rooted in coronal holes. Figure 1.13 shows a schematic of magnetic field associated with coronal holes at different heights from the interpretation of Cranmer (2009). The open flux is found to be interspersed between low-lying ($< 1.5 \times 10^4$ km), cool ($< 8 \times 10^5$ K), closed loops, as in Panel (b) of the figure (Feldman et al., 1999). The dimness of coronal holes is the result of material there

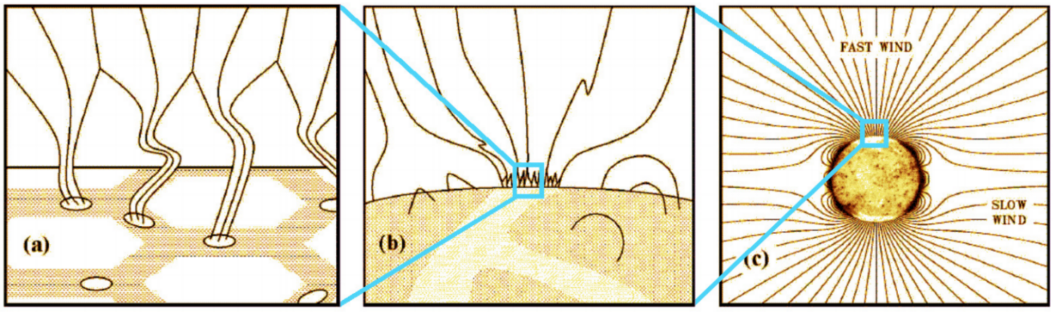

Figure 1.13: Diagram of the expansion of coronal hole magnetic field at different scales, taken from the review by Cranmer (2009). Panel (a) shows the flux emerging from funnels in the photosphere and expanding to fill the available volume. Panel (b) shows further expansion as flux elsewhere closes down. Panel (c) shows the global picture, with a coronal hole each in the north and south poles expanding to fill the extended corona and heliosphere.

being rapidly freed from these small loops to escape into the solar wind, rather than being confined and heated in larger loops. This also explains the observation that coronal holes possess a lower electron temperature than the closed-field corona.

As shown in Panels (b) and (c) of Figure 1.13, the magnetic field of coronal holes expands super-radially as it fills the available volume which exists in the regions above closed loops. The coronal holes in Panel (c) of the figure have magnetic fields which expand to fill the entire heliosphere, despite their original size spanning only around 60° each.

The Quiet Sun

The quiet Sun refers to closed-field regions on the Sun which are not active regions; they lack the appropriately strong, and coherent, concentrations of magnetic flux. Quiet Sun surrounds the coronal hole in Figure 1.12. In EUV observations of the corona, the quiet Sun appears as dim (although brighter than coronal holes) and diffuse structures, some of which are the magnetic footpoints of large loops (Golub and Pasachoff, 2010). As with coronal holes, low-lying loops also exist in the quiet Sun. These are, however, found to be somewhat larger (4×10^4–4×10^5 km) and hotter ($\sim 1.5 \times 10^6$ K) than their coronal hole counterparts (Feldman et al., 1999).

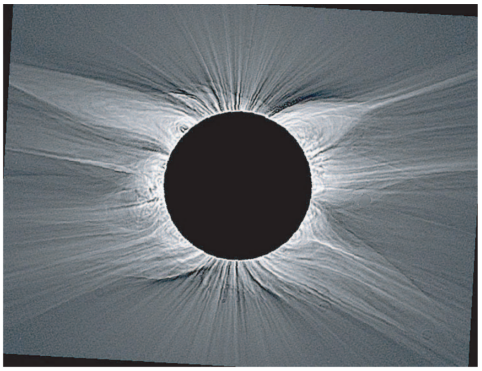

Figure 1.14: Eclipse image from Wang et al. (2007). Streamers and pseudostreamers are shown off the limb.

The Streamer Belt

A streamer is a large, closed, magnetic structure, which appears as a bright loop when viewed off the limb of the Sun. The loop connects opposite-polarity regions. Streamers are clearly visible in the eclipse image of Figure 1.14 from Wang et al. (2007). The streamer belt describes the typically equatorial region in which large groups of streamers are found. These streamers typically separate large polar coronal holes. Since magnetic polarity inverts over the streamer belt, a current sheet (in fact, the *heliospheric* current sheet, see below) must be embedded within it. Pseudostreamers are structures which have a similar appearance to streamers, however they do not separate opposite-polarity regions.

1.2.3 CMEs, Flares, and SEPs

A flare is a transient event in which a local region of the corona and chromosphere is rapidly heated. A flare is the result of the release of energy stored in a solar magnetic field which has become stressed through twisting. Flares are classified by the intensity of the resulting emission as observed at 1 au. This classification is B, C, M, or X, corresponding to intensity thresholds of 10^{-7}, 10^{-6}, 10^{-5}, and $10^{-4}\,\mathrm{W\,m^{-2}}$ respectively, across the X-ray wavelength range 1–8 Å (Bornmann et al., 1996). A number following each class indicates the intensity within that range, e.g., a C2.8 flare has intensity of $2.8 \times 10^{-6}\,\mathrm{W\,m^{-2}}$.

Nanoflares are a subset of flares which occur at very small scales, and release far smaller quantities of energy than typical flares (see observations by e.g., Porter et al., 1995). They are so small that they are very difficult to observe above background emission. They are thought to continually occur, however, and thus make a potentially significant energy contribution to coronal plasma.

Typically associated with, although not necessarily caused by, flares are coronal mass ejections (CMEs). CMEs are transient events in which mass, in a closed magnetic structure, is expelled outwards from the corona. CMEs are often visible off the solar limb out to many $R_\odot$, indicating their enhanced density over the background solar wind. Coronal mass ejections normally originate from eruptions in active regions, and so become more frequent during peaks in solar activity.

Solar energetic particle (SEP) populations are high-energy ($\sim$ 10 keV–GeV) ions and electrons which are accelerated and released at, or near, the Sun into the heliopshere. Acceleration can result directly from the energy released from flaring. Acceleration can also take place at the shocks which often form at the front of outward travelling CMEs. The former case is thought to be responsible for 'impulsive' SEP events, while the latter results in 'gradual' events. SEPs may make their way into the heliosphere along open magnetic field lines. As a result of their high energies, SEP events are hazardous for spacecraft and humans in space.

1.2.4 Coronal Composition

Predominantly, the composition of the corona is hydrogen ($\sim 91\%$) and helium ($\sim 9\%$) ions (Meyer, 1985). Heavier elements constitute $< 1\%$ of the coronal plasma. The relative abundances of all these elements, and their charge states, define the 'composition' of the coronal plasma. This composition is important as it propagates into the solar wind, and can be used as an identifier of coronal origin. Abundance in particular serves this purpose through a phenomenon known as the first ionisation

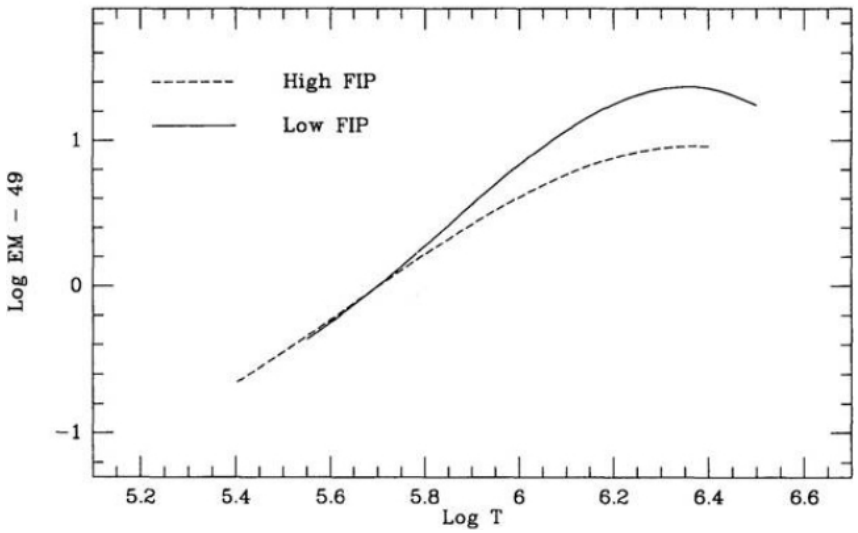

Figure 1.15: Plot showing fits to the emission of lines associated with high FIP ($> 10\,\mathrm{eV}$) and low FIP ($< 10\,\mathrm{eV}$) elements, as a function of the characteristic line temperature. At photospheric temperatures ($\log(T) < 6$) the emission is comparable, but at coronal temperatures ($\log(T) > 6$) emission from low FIP elements are enhanced. Adapted from Laming et al. (1995).

potential (FIP) effect.

The FIP effect describes the discrepancy between elemental abundances of species between the photosphere and corona. The coronal abundance of certain elements, those with a first ionisation potential below $\sim 10\,\mathrm{eV}$ (low-FIP), are enhanced relative to the photosphere. There is no such enhancement for elements with FIP above $\sim 10\,\mathrm{eV}$ (high-FIP). This is the FIP effect, or FIP bias, in coronal abundance (Meyer, 1985).

Figure 1.15, adapted from Laming et al. (1995), demonstrates the FIP effect through solar emission from high and low-FIP ions. The emission measure (EM; related to the number density of the emitting ions) for high and low FIP species is similar at photospheric temperatures ($\log(T) < 6$), but diverges at temperatures corresponding to coronal material ($\log(T) > 6$), with emission from low-FIP ions being enhanced. This is evidence of the increased abundance of low-FIP elements in the corona (e.g., Laming, 2015).

FIP biasing is most pronounced in the closed corona, quiet Sun and active regions (bias levels of around 2–5), but is relatively unseen in coronal holes, which feature close to photospheric abundance (e.g., Brooks and Warren, 2011). The FIP effect thus appears to be related in some way to closed magnetic loops.

Research into the cause of the FIP effect is still ongoing. The main school of thought is that waves which propagate both up and down closed field lines (but which can only propagate *up* open field lines) lead to the heating of ions, but not neutrals, below the transition region (e.g., Schwadron et al., 1999). Higher temperature populations are able to exist at greater heights along the loop. Low-FIP elements are ionised at lower heights than high-FIP elements; closer to the region of ion heating. Low-FIP ion populations become hotter than high-FIP, and are thus are able to propagate up into the corona more readily, enhancing their coronal abundance. The bias towards low-FIP elements in the corona is therefore a 'real' enhancement, rather than a depletion of high-FIP elements.

1.2.5 The Solar Cycle

As a result of the solar dynamo, solar activity (EUV and x-ray emission, number of flares and CMEs, total solar irradiance) varies on an approximately 11-year cycle. This cycle was first observed through a periodicity in sunspot number (Schwabe, 1844). The cycle begins at a minimum of activity, before rising to a maximum, and then declining back towards a new minimum. Over the course of one cycle, the polarity of the dipolar component of the solar magnetic field is inverted. Thus to return to the original state in fact takes ~ 22 years. Away from solar minimum, the solar magnetic field takes on more higher-order components.

At solar minimum, the corona generally features two large coronal holes, one at each pole, and largely closed field at lower ecliptic latitudes. This dipole is slightly tilted with respect to the Sun's rotational axis. Active regions are also uncommon

during minimum. At solar maximum, coronal holes are found across all latitudes, and typically persist for only a few solar rotations before undergoing significant reconfiguration (Cranmer, 2009). Active regions are numerous, and activity often associated with them (flaring, CMEs) occurs more often. The solar wind is sensitive to the presence, and distribution with latitude, of different coronal structures, and therefore also varies during the solar cycle.

1.3 The Solar Wind and The Heliosphere

The solar wind is the constant supersonic stream of plasma which escapes from the Sun. Due to frozen-in flux, it carries with it the Sun's magnetic field, and the plasma and field combined create the heliosphere - the region of interstellar space dominated by the Sun's magnetic field. The solar wind is largely collisionless, high-beta, and has $R_M > 1$, so magnetic flux is frozen into the plasma (Meyer-Vernet, 2007). The speed of the solar wind is such that it is both supersonic and, beyond a few tens of $R_\odot$, super-Alfvénic (its velocity is greater than the local Alfvén speed). The rotation of the Sun leads to a periodicity in the solar wind, as sources at the Sun recur at Earth orbit each rotation. This section will provide background on the origins and evolution of solar wind particles and magnetic field, both theoretically and as observed throughout the heliosphere.

1.3.1 Models of Solar Wind Expansion

The first prediction of how the solar wind might flow is attributed to Parker (1958). This work correctly predicted the supersonic nature of the solar wind using a fluid description. We shall discuss both fluid and kinetic solar wind models below.

Fluid Approach

Parker's model relies on the outward pressure gradient between the dense corona and outer space competing only against the inward force of the Sun's gravity. The MHD momentum equation (Equation 1.18) thus reduces to

$$\rho(\mathbf{v}\cdot\nabla)\mathbf{v} = -\nabla P + \rho\mathbf{g} \tag{1.34}$$

This expression relies on simplifying assumptions of an isotropic pressure, negligible electromagnetic effects ($\mathbf{E} \to 0$, $\mathbf{J}\times\mathbf{B} \to 0$), negligible effects of electrons and heavier ions, and a steady ($\partial\mathbf{v}/\partial t = 0$) and uniform flow. Space is assumed to effectively be a vacuum, such that for radius $r \to \infty$, pressure $P \to 0$. To supply a pressure sufficient gradient to produce an outward flow, a temperature distribution with height is used, which to exist in reality requires additional heating of the coronal plasma (which is known to occur - Section 1.2.2). Under these conditions a radial solar wind flow is produced, in which the solar wind accelerates with increasing r, while density, temperature and magnetic field strength all decrease. A key prediction of Parker's model is the supersonic nature of the solar wind; a result of the density gradient produced by gravity. The flow begins as subsonic in the low corona, but exceeds the sound speed and becomes supersonic at a height known as the critical point: r_c.

The drop-off of n and B, and increase of v, with r results in the solar wind bulk speed eventually exceeding the Alfvén speed (Equation 1.30). The radius at which this occurs is known as the Alfvén critical point, typically lying at around 10–30 $\mathrm{R}_\odot$ (Weber and Davis Jr, 1967).

Kinetic Approach - Exospheric Model

The first kinetic model of the solar wind was developed by Chamberlain (1960). This class of so-called "exospheric models" explain the solar wind through evaporation of coronal plasma. Treated individually, particles in the corona at height r_0, can escape the Sun's gravity if they reach the escape velocity

$$v_{\mathrm{esc}} = \sqrt{\frac{2GM_{\odot}}{r_0}} \tag{1.35}$$

where G is the gravitational constant and $M_{\odot}$ is the solar mass. Considering only thermal velocity, $v_{\mathrm{th}} = \sqrt{2kT/m}$, if coronal protons and electrons are at temperature equilibrium ($T_p = T_e$) then $v_{\mathrm{th},e} \gg v_{\mathrm{th},p}$ since $m_e \ll m_p$. As a result of this, for a Maxwellian distribution, the number of electrons with $v > v_{\mathrm{esc}}$ is far greater than the number of protons. This discrepancy results in a charge imbalance, producing a radial electric field. The field applies an outward force to the protons, allowing a greater proportion to escape the Sun's gravitational field. To maintain the quasi-neutrality of the corona, the outward flux of electrons must then be approximately equal to the flux of protons (neglecting heavier ions). This constrains the electric field which is created by the charge separation, and the flow of the solar wind.

1.3.2 The Interplanetary Magnetic Field

Coronal magnetic field is dragged outwards as the solar wind escapes as a result of frozen-in flux. In the solar wind, the magnetic field is known as the interplanetary magnetic field (IMF) or heliospheric magnetic field (HMF). The IMF corresponds to open flux from the corona, and thus can be either positive or negative in its polarity (directed outwards or inwards).

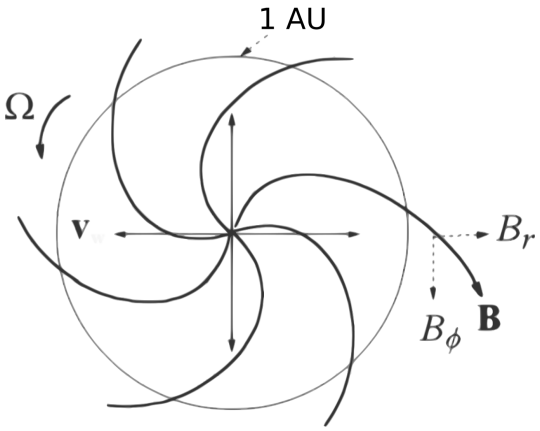

Figure 1.16: Schematic representation of the interplanetary magnetic field in the ecliptic plane, as viewed from the north pole. The direction of solar rotation, Ω, the solar wind flow **v**, magnetic field vector **B**, and components B_r and B_ϕ are all indicated. The field exhibits the Parker spiral geometry described in the text. Image adapted from Meyer-Vernet (2007).

The Parker Spiral

A schematic representation of the IMF, as a slice in the ecliptic plane, is shown in Figure 1.16, adapted from Meyer-Vernet (2007). We see that close to the Sun, the IMF is approximately radial, as the supersonic solar wind pulls it radially outwards. With sufficient time (i.e., distance travelled by the solar wind), solar rotation drags the footpoint of the magnetic field around azimuthally. while the field outside of the corona is still carried outwards. In this simplified case, the IMF becomes wound into an Archimedean spiral, as is clear at greater heliospheric distances in the figure. The spiral obeys the expression

$$\frac{B_\phi}{B_r} = \frac{-\Omega r \sin\theta}{v_r} \tag{1.36}$$

where v_r is the radial component of the solar wind bulk velocity, B_r and B_ϕ are the respective radial and azimuthal component of the magnetic field, Ω is the mean solar rotation speed, and θ is the heliospheric latitude of the observer (Parker, 1958). The spiral is thus more (less) tightly wound with increasing (decreasing) r, decreasing (increasing) v_r, and nearer (further) from the ecliptic plane. For solar wind speeds of $\sim 450\,\mathrm{km\,s^{-1}}$, $B_\phi/B_r \approx -1$ at 1 au. The Parker angle, the angle between the two, is thus $\sim 45°$.

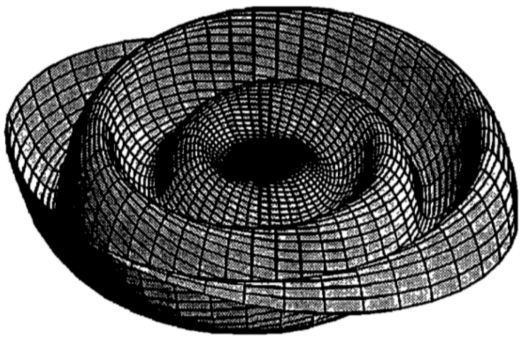

Figure 1.17: Representation of the heliospheric current sheet, shown out to 10.5 au. The sheet is non-planar as a result of the dipole tilt of the solar magnetic field. A spacecraft in the ecliptic will thus cross the HCS twice per solar rotation. Figure from Smith (2001).

The Heliospheric Current Sheet

Current sheets separate oppositely directed magnetic fields. During solar minimum, when the magnetic field is approximately dipolar, a singular large current sheet in the streamer belt separates the two polarities. This current sheet is thus known as the heliospheric current sheet (HCS), a schematic of which is shown at solar minimum in Figure 1.17. As in the figure, the HCS is typically not flat. A spacecraft sampling solar wind in the ecliptic plane during solar minimum is expected to cross the current sheet twice over the course of a solar rotation, as a result of the tilt of the dipolar field. As the solar cycle progresses, the HCS becomes more warped and complex, as sources of open flux begin to emerge at lower latitudes. More crossings are expected during solar maximum due to the increased warping of the sheet.

1.3.3 Properties and Sources of the Solar Wind

The solar wind is often described as bimodal. It is grouped into 'fast' or 'slow' based on the bulk speed of the plasma, as it flows radially out from the Sun. The bimodality of the wind is then typically explained through there broadly being two classes of solar wind source; fast solar wind is associated with largely open field source regions, and slow solar wind is associated with closed source regions.

The classification of solar wind purely by its bulk speed is likely an oversimplification. Despite this, much of the vocabulary surrounding solar wind research still

revolves around the fast-slow dichotomy. We therefore describe here the solar wind in the classic bimodal sense. For both types, we shall outline the characteristic properties, and rough origins at the Sun. Further, we describe transient interplanetary coronal mass ejections, as these make up a significant portion of the plasma which can be encountered in the heliosphere.

Fast Solar Wind

There is no universally agreed-upon cutoff in velocity between fast and slow solar wind. Meyer-Vernet (2007) for example quotes a characteristic fast solar wind velocity at 1 au of $750\,\mathrm{km\,s^{-1}}$. The lower limit for solar wind to be considered fast is usually $\sim$ 500–600 $\mathrm{km\,s^{-1}}$, depending on the authors, and can extend up to $> 800\,\mathrm{km\,s^{-1}}$. The density of electrons in the fast wind is given by Meyer-Vernet (2007) as $2.5\,\mathrm{cm^{-3}}$ at 1 au, which is relatively low compared to the slow wind.

The flow in the fast wind is relatively steady, with fluctuations in velocity, magnetic field, and other parameters largely being a result of Alfvénic turbulence (turbulence in which fluctuations in the magnetic field correlate with those in velocity). This is suggestive of fast streams being released from a singular structure, through a continuous outflow. Coronal holes meet this criteria well, and have long been thought to be the source of the fast solar wind (Krieger et al., 1973).

As a consequence of the latitudinal coronal hole distribution changing through the solar cycle, fast solar wind is primarily confined to high latitudes during solar minimum. However, the dipole tilt, super-radial expansion of open magnetic field lines, and low-latitude coronal hole extensions result in fast solar wind still being observable in the ecliptic plane during solar minimum (although often at reduced speeds).

The distribution of fast solar wind over the solar cycle is summarised in Figure 1.18, adapted from McComas et al. (2003), which shows solar wind velocity and IMF polarity over a range of ecliptic latitudes as measured by the Ulysses spacecraft.

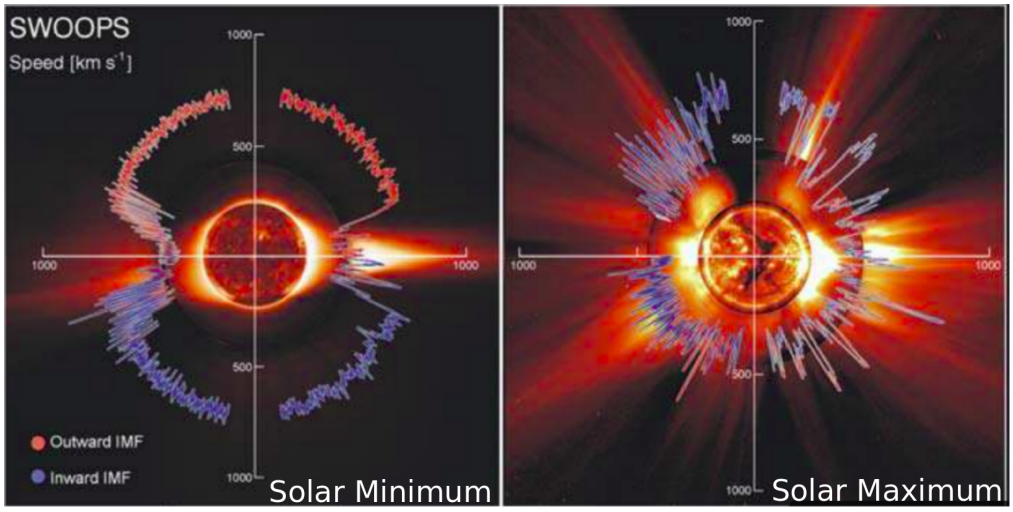

Figure 1.18: A set of plots which show solar wind velocity and magnetic field orientation for two latitudinal scans of the Ulysses spacecraft. The plots are polar, such that the angle between the x-axis and the line shows the latitude of the spacecraft out of the ecliptic plane. The radial position of the line shows the measured solar wind bulk speed at that latitude, while the colour shows the orientation of the IMF as either outward or inward. The left panel shows a scan taken during solar minimum, while the right shows a scan taken during solar maximum. Adapted from McComas et al. (2003).

The left panel shows data measured during solar minimum, while the right shows data during maximum. At minimum, solar wind of velocities $> 500\,\mathrm{km\,s^{-1}}$ rarely occurs at ecliptic latitudes. Likewise, velocities of $< 500\,\mathrm{km\,s^{-1}}$ are rarely observed far from the ecliptic plane. The simple dipolar nature of the field is also clear. Meanwhile, the right panel shows that during solar maximum, streams of different velocity are present at all latitudes, as are inward and outward directed IMF. As well as showing the distribution of fast solar wind, this figure also demonstrates the complexity of the corona and heliosphere in general at solar maximum.

Slow Solar Wind

The slow solar wind contrasts with the fast in many of its *in situ* properties. At 1 au, typical slow wind speeds are $\sim 400\,\mathrm{km\,s^{-1}}$ and number densities $\sim 7\,\mathrm{cm^{-3}}$ (Meyer-Vernet, 2007). Slow solar wind speeds may extend down to the order of $< 300\,\mathrm{km\,s^{-1}}$ (e.g., Sanchez-Diaz et al., 2016).

While the fast solar wind is largely steady, the slow solar wind is highly variable in its properties (Schwenn, 1990). This hints at a variable and sporadic source mechanism. The slow solar wind falls between the fast streams which are associated with coronal holes; regions of largely open flux (Krieger et al., 1973). This and compositional evidence suggest that the slow wind originates in, or is at least associated with, magnetically closed regions (Geiss et al., 1995b). Closed origins are problematic however, as flux which is not open does not extend into the heliosphere by definition. Slow wind origins is one of the primary unanswered questions in solar wind research. We shall consider current research on the topic in Chapter 2.

Interplanetary Coronal Mass Ejections

Interplanetary coronal mass ejections (ICMEs) are CMEs which propagated out into the heliosphere. These represent transient events over the background solar wind. The magnetic field of an ICME is typically connected at both ends to the Sun initially, but may disconnect at one end or both ends during propagation. The list by Richardson and Cane (2010) catalogues ICMEs which have been encountered in near-Earth space. From this list, the bulk velocities associated with ICMEs range upwards from $\sim 200\,\mathrm{km\,s^{-1}}$ to extremes of $\sim 2000\,\mathrm{km\,s^{-1}}$. Typical ICME speeds are around $500\,\mathrm{km\,s^{-1}}$.

1.3.4 Solar Wind Structure

Globally, the solar wind is highly structured, as a result of the different solar wind types and sources described above. The so-called 'sector-structure' of the solar wind refers to the opposite magnetic polarity which is found above and below the HCS, which repeats each rotation.

Persistent coronal holes lead to fast solar wind streams which also recur with each solar rotation, creating structure in solar wind plasma parameters. Further, the rota-

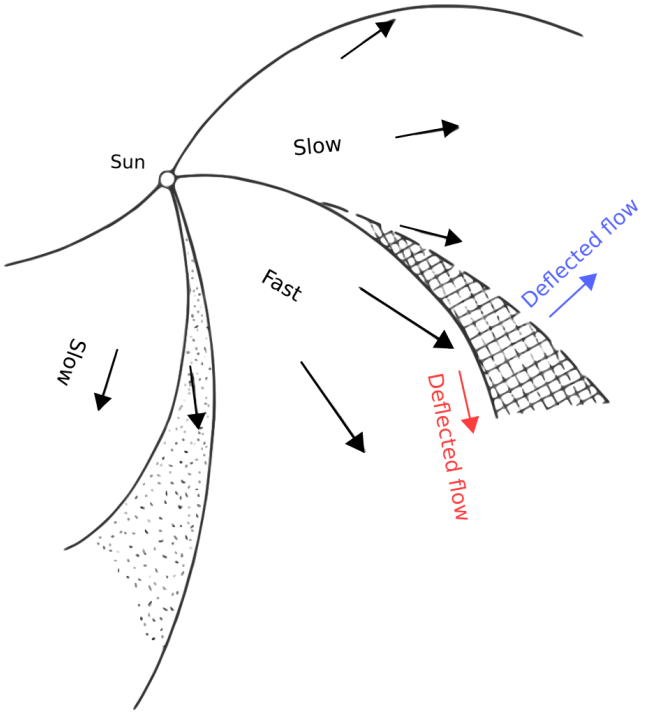

Figure 1.19: Representation of a typical solar wind stream structure. Solar wind bulk flows are shown with black arrows. Two slow streams are separated by a fast stream, with the locations of the edges of the streams shown by solid black lines. At the leading edge of the fast stream a CIR forms, indicated by the hatched area. At the trailing edge of the fast stream, a rarefaction forms, indicated by the dotted area. At either side of the CIR, the direction of the deflection to the bulk flow is indicated by a coloured arrow. The red arrow shows the fast stream deflection while the blue arrow shows the slow. Adapted from Parker (1965).

tion of the Sun causes solar wind from different source regions to be released into the heliosphere at the same longitude and latitude in the sidereal frame. Instances occur whereby fast wind streams follow slow (and vice-versa) as the solar wind propagates radially outward. This results in interactions between the streams.

In the case of fast solar wind following slow, a compression forms. The compression region is known as a corotating interaction region (CIR, Smith and Wolfe, 1976) or sometimes a stream interaction region (SIR, Owens and Forsyth, 2013). A CIR is exemplified by the hatched area in Figure 1.19, adapted from Parker (1965). CIRs are characterised by a rapid, sometimes discontinuous, velocity increase, and enhanced density and magnetic fields. The initially fast and slow streams are kept separate as a result of frozen in flux, which prevents mixing of distinct solar wind populations. In a similar manner to the magnetic field, the stream interaction region describes an Archimedean spiral (as in the figure). The solar wind plasma is deflected away from the interaction region due to the pressure gradient (Gosling, 1975). The directions of the deflected velocity components in each stream are indi-

cated on Figure 1.19.

In the case of slow solar wind following fast, the fast stream propagates out into the heliosphere more rapidly, leaving a rarefaction between the two streams. A rarefaction is shown in the dotted area of Figure 1.19. The resulting pressure gradient accelerates the slow wind and decelerates the fast. Rarefactions are characterised by smoothly decreasing velocity, and depressed plasma density and magnetic field strength. We briefly note that compressions and rarefactions can also form on either side of an ICME, depending on its propagation speed and the speeds of the surrounding streams.

As is shown in Figure 1.19, interaction regions develop and expand as the solar wind propagates outwards. Close to the Sun, the stream boundary will be nearly tangential to the radial flow of the solar wind, but as the solar wind propagates further into the heliosphere it takes on a more spiral-like geometry.

1.3.5 Solar Wind Protons and Alpha Particles

The dominant ion populations in the solar wind are protons ($\sim 95\%$ of ions by number) and alpha particles ($\sim 5\%$) (Meyer-Vernet, 2007). The remainder is made up of heavier ions which constitute $< 1\%$ of the number density. The dynamic pressure of the solar wind is primarily supplied by protons and alphas. Similarly, the direction of the bulk velocity is dominated by these two species.

Alpha particles have long been observed to flow differentially relative to the protons (e.g., Formisano et al., 1970; Marsch et al., 1982; Steinberg et al., 1996). This flow is along the field, in the anti-sunward direction. The speed of the flow relative to the bulk is proportional to the local Alfvén speed (e.g., Berger et al., 2011). Differential streaming is found to typically be enhanced in fast solar wind streams.

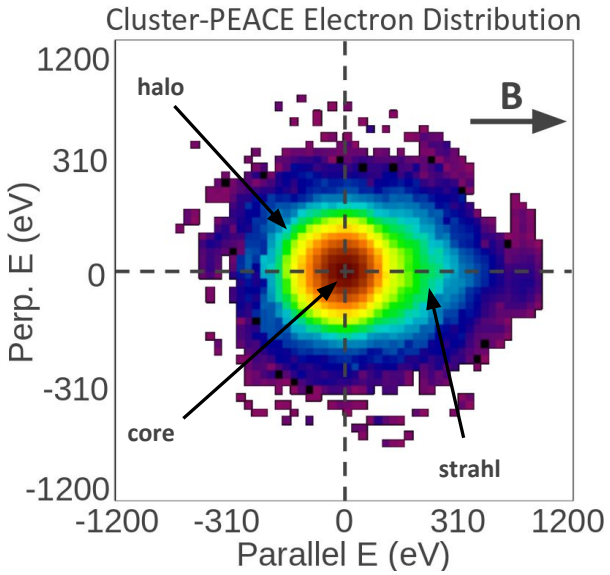

Figure 1.20: 2-dimensional plot of a sample electron VDF observed by the Cluster spacecraft adapted from Viñas et al. (2010). The distribution is shown in the frame of the solar wind. The x and y axes are magnitude of the energy calculated from the parallel and perpendicular velocity components respectively, but with the sign of the velocity preserved (e.g., $E_{\parallel} = 0.5 m_e v_{\parallel} |v_{\parallel}|$). No colourbar is supplied in the original plot, and so this figure is used for illustrative purposes only. The VDF generally decreases as we move radially from the origin. The core population is located near the origin, primarily in red. The halo population is most clearly shown in the yellow, green, and cyan colours, in the anti-parallel sector (where it is not obscured by the strahl). The strahl population is seen in the enhancement of the VDF in the parallel sector.

1.3.6 Solar Wind Electrons

Solar wind electrons are commonly described as consisting of three distinct populations (Pierrard et al., 2001): a thermal core, allowed to become anisotropic by lack of collisions; a near-isotropic and suprathermal halo; and a strongly field-aligned suprathermal strahl. A more energetic and even less dense fourth population, dubbed the superhalo, has been reported at energies above $\sim 1\,\mathrm{keV}$ (Lin et al., 1995). Figure 1.20, adapted from Viñas et al. (2010), shows a labelled example of these three main populations as observed by the Cluster spacecraft. We shall describe each population in detail below.

Core Electrons

The electron core is the primary electron population in the solar wind, possessing around 90–95% of the electron number density (Maksimovic et al., 2005; Stverak et al., 2009). The core propagates approximately with the bulk solar wind. The core is well-described by a bi-Maxwellian, as in Pilipp et al. (1987), indicating that it is approximately thermalised. Typical core temperatures (averaged perpendicular and parallel) are $\sim 10\,\mathrm{eV}$ at 1 au.

Suprathermal Electrons

The halo and strahl are both suprathermal populations; they exist as VDF enhancements over the expected values for a Maxwellian distribution (e.g., a purely-core distribution) at high energies. Combined, the halo and strahl electrons make up 5–10% of the total solar wind electrons (Maksimovic et al., 2005; Stverak et al., 2009). The origins of, and relationship between, the halo and strahl populations are a topic of active research, which shall be discussed in Chapter 2.

The strahl is a beam of electrons, aligned with the interplanetary magnetic field, generally propagating along the field away from the Sun. This is visible in Figure 1.20 as a VDF enhancement in the direction parallel to the magnetic field, which is not present in the antiparallel direction. The direction suggests that in this example the IMF itself was directed anti-sunward. Strahl electrons become distinct from the quasi-isotropic populations at energies of around 100 eV, and are present at energies of up to a few keV. The presence of an electron beam is expected, as a result of the conservation of the first adiabatic invariant, μ (Equation 1.11). As the IMF field strength falls off with radial distance, so too must the perpendicular velocity component $v_\perp$. The electrons which propagate in the anti-sunward direction thus 'focus' into a beam centred parallel to the field. Conversely, suprathermal electrons which are propagating sunward experience an increase in $v_\perp$. There is therefore no

equivalent sunward beam.

While strahl is more typically prominent in fast solar wind streams than slow, the halo is common to both (Rosenbauer et al., 1977). The halo is a quasi-isotropic population, and so is often described using a Maxwellian or bi-Maxwellian distribution, with its own temperature and density values, despite the fact that it is not strictly 'thermal'. This description for the halo implies that in the core energy ranges there is a superposition of core and halo electrons. This is largely a semantic issue, as there is no actual distinction between these populations for the individual electrons in a given energy range.

1.3.7 Solar Wind Minor Ions

Ionised species in the solar wind which are heavier than He do not have a strong effect on the dynamics of the solar wind. These species are thus referred to as 'minor' or 'heavy' ions, and account for $< 1\%$ of solar wind ions (Bochsler, 2007). Despite their limited influence on solar wind dynamics, solar wind minor ions are particularly useful in conveying information on the origins of the solar wind in the corona out into the heliosphere.

Elemental Abundance

Commonly-observed minor species include C, N, O, Ne, Na, Mg, Al, Si, S, Ar, Ca, Cr, and Fe (as summarised by Bochsler, 2007). The most abundant of these is oxygen, followed by carbon. These elemental abundances are controlled by the abundance of the different species at the solar wind source region. By calculating relative abundances in the solar wind, typically relative to oxygen, it is thus possible to infer abundance information about the corona, at the location where a given parcel of solar wind plasma originates. The relative abundances of elements should not change as the solar wind propagates outward, since frozen-in flux prevents the

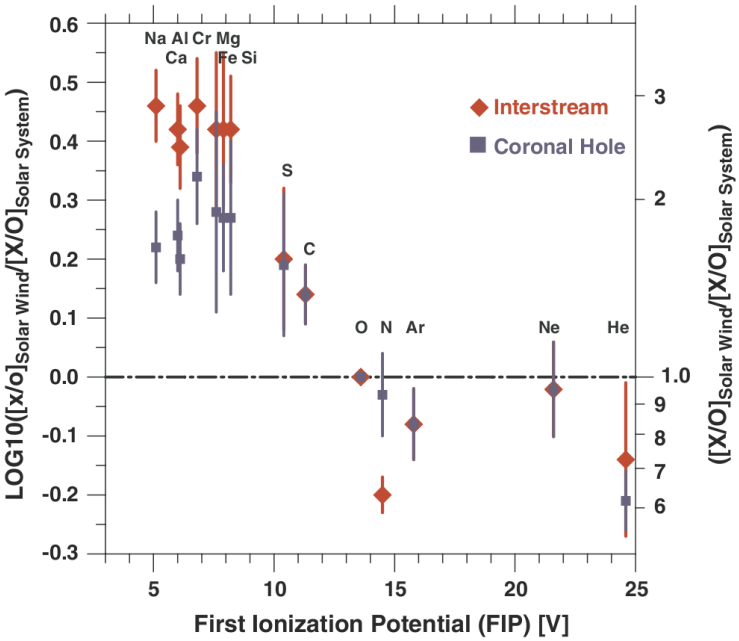

Figure 1.21: Plot of ion abundances, relative to oxygen, against ion first ionisation potential. Measurements from both coronal hole and 'interstream' (non-coronal hole) solar wind types are shown in grey and red respectively. The axes indicate the level of abundance divided by the 'solar system' (photospheric) abundance. Figure from Bochsler (2007).

mixing of separate populations. Abundance measurements can thus aid in identifying the source region, as in the corona relative elemental abundances are subject to the FIP effect (Section 1.2.4) which varies from source region to source region.

The expectation that solar wind abundance reflects that of the source appears to be true, as the *in situ* FIP effect is usually lessened in fast wind from coronal holes, and strengthened in slow wind. An example of this is shown in Figure 1.21, taken from Bochsler (2007). The figure shows the abundance of different species in the solar wind relative to oxygen, divided by the relative 'solar system' abundance (which is also the expected photospheric abundance) and plotted against each species' FIP. Both coronal hole (fast wind) and 'interstream' (non-coronal hole; slow wind) measurements indicate an enhancement in low-FIP elements relative to solar system values. Interstream wind is however enhanced by around twice as much as coronal hole wind; a relationship similar to that observed between the FIP biases of quiet Sun and coronal holes remotely. However, we note from the figure that the abso-

lute values of FIP bias for coronal hole and interstream solar wind are not in full agreement with those expected for their respective source regions (coronal holes are expected to have a FIP bias of ~ 1, while quiet Sun FIP biases are expected to range from 2–5).

Ionisation

Heavy ions in the solar wind can be fully or partially ionised. The distribution of ionisation states (or charge states) of heavy ions can be determined through *in situ* measurements, and constitute another valuable property which is indicative of coronal conditions. Ionisation in the corona is dominated by electron collisions, as described in Section 1.1.9. At a given location in the corona then, assuming that collisional equilibrium is in effect, ions are distributed into ionisation states depending on the ambient electron temperature, as exemplified in Figure 1.8. Density ratios of adjacent ionisation states (charge state ratios) can then be calculated from rate coefficients as in Equation 1.33, and depend on the coronal electron temperature only.

Since the solar wind is largely non-collisional, at some height in the corona collisional equilibrium must no longer apply. Figure 1.22, adapted from Bochsler (2007), displays the modelled ionisation states for Mg with height in an expanding corona. As the electron temperature increases with heliocentric distance, Mg is distributed into higher charge states. This continues until a critical height, indicated by the dashed line, at which collisions effectively cease. The charge states thus remain characteristic of the electron temperature at the height where collisions ended. Mg ions above the critical height in the figure remain in the same distribution of states, despite the drop-off of electron temperature. If no other ionisation or recombination processes are viable, then the ions will in fact remain in these charge states indefinitely as the plasma propagates through the solar wind. This process is known as

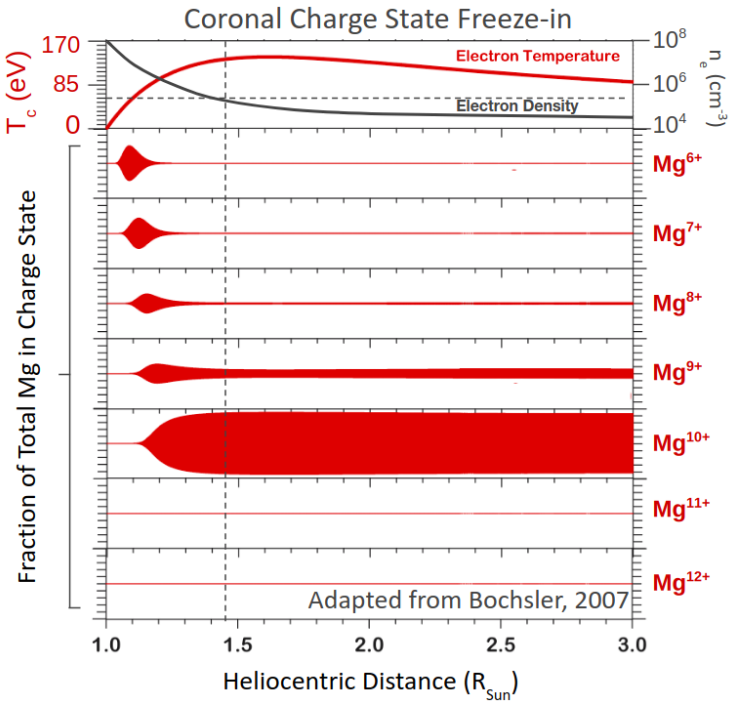

Figure 1.22: Plot of modelled coronal parameters and normalised densities of a subset of Mg charge states against heliocentric distance. The top panel shows the evolution of coronal electron temperature and number density. Each other panel shows the evolution of a given charge state of Mg. The width of the line indicates the fraction of Mg which inhabits each charge state, with the full width of the panel being 100%. The dashed line shows the approximate location where electron density drops below the threshold for ionisation equilibrium. At heights below this, the Mg charge states are distributed according to the electron temperature. Above, Mg is frozen into its distribution of charge states, which is predominantly Mg^{9+} and Mg^{10+}. Adapted from Bochsler (2007).

the 'freezing-in' of heavy ion charge states (Hundhausen et al., 1968b)[1]. Measuring charge state ratios in the solar wind allows us to calculate the electron temperature at the location of freeze-in (the "freeze-in height" where collisions ceased) using Equation 1.33. This value is known as the "freeze-in temperature". Each species in the corona will have a unique collisional cross-section (reflected in the ionisation rate coefficients found in e.g., Dere et al., 1997; Landi et al., 2013), and as such freeze into their charge states at different heights; producing different freeze-in temperatures.

[1]Freeze-in in this context is not related to the concept of frozen-in magnetic flux introduced in Section 1.1.6. We shall take care throughout this thesis to be explicit about which of these two similar terminologies is being applied at a given time.

Some of the simplifying assumptions in the argument for charge state freeze-in above do not hold in reality. Research of ionisation beyond these assumptions was first carried out by Owocki et al. (1983), and is still ongoing. The freeze-in temperature implied from a given ion may not necessarily represent a real electron temperature imprinted at some singular height in the corona. Current research into the ionisation process in the corona is primarily modelling-based, and shall be discussed further in Chapter 2.

Differential Streaming of Minor Ions

As is the case for alpha particles, heavy ions too stream differentially at a speed related to the local Alfvén speed (observed by e.g., Berger et al., 2011). As such, it appears that differential streaming is caused by preferential acceleration of minor ions, but is limited to v_A by some instability (e.g., Verscharen et al., 2015). All *in situ* observations of minor ion and alpha particle streaming at present have been carried out *in situ*, at distances $\gtrsim 0.3\,\mathrm{au}$. At $1\,\mathrm{R}_\odot$, the plasma is approximately at rest, and so the onset of differential streaming occurs above this, with the ions ultimately reaching a streaming speed on the order of v_A at some unknown distance $< 0.3\,\mathrm{au}$.

Minor ion differential streaming is aligned with the local magnetic field direction. As such, although minor ions flow faster than the bulk solar wind, they are expected to remain on the same flux tube as they propagate through the heliosphere. This can be understood by splitting the ion velocity, $\mathbf{v}_i$, into components; $\mathbf{v}_i = \mathbf{v}_b + \mathbf{v}_s$, where $\mathbf{v}_b$ is the radial solar wind bulk velocity and $\mathbf{v}_s$ is the minor ion streaming velocity, which is parallel to the magnetic field, $\mathbf{B}$. Under frozen in flux, the bulk plasma moves at $\mathbf{v}_b$, and 'drags' the magnetic field along with it. Since $\mathbf{v}_s$ does not have a component which is perpendicular to $\mathbf{B}$, the components $\mathbf{v}_i \perp \mathbf{B}$ and $\mathbf{v}_b \perp \mathbf{B}$ are equal. The heavy ions which flow at $\mathbf{v}_i$ thus do not move across the field relative to

the bulk, and so both bulk plasma and minor ion populations remain on the same flux tube throughout propagation.

Source Region Tracers

Abundance and ionisation states are considered to be effective "tracers" of the solar wind source and its properties (Bochsler, 2007). From Figure 1.21 we saw that solar wind from coronal holes, usually the fast solar wind, is associated with low FIP biasing, while wind from closed field sources, usually the slow solar wind, is associated with high FIP biasing. Similarly, we note that coronal holes are typically associated with lower electron temperatures than quiet Sun or active regions, and so their associated solar wind is thus identifiable through lower degrees of ionisation. Meanwhile, solar wind from closed field regions is associated with stronger ionisation.

Like composition, solar wind properties such as velocity, density, and magnetic field strength are all initialised in the corona. However these properties are dynamic, and so may evolve away from the coronal state as the solar wind expands. Based on the differential streaming argument above, we expect that the composition (be it relative abundances or charge state ratios) of heavy ions which is associated with a given field line cannot be altered. This is because heavy ion populations cannot mix across the field, and so their relative concentrations, which define the composition, are preserved. As a result of this, composition also does not change as the solar wind propagates. Heavy ions are therefore more effective source region tracers than dynamic solar wind properties.

Despite their more rapid propagation, heavy ions should act as tracers for the source of the bulk solar wind which is measured simultaneously to them. In other words, a time lag is not necessary when comparing spacecraft measurements of heavy ions and bulk plasma properties. This is again due to the above argument that ions will

remain on the same field line throughout their propagation. So long as the source region in which the field line is rooted does not change, the same composition of ions is continually supplied at the base of the field line, and so composition is preserved along its length. This argument does not hold for cases in which the solar wind source region, which a given field line is rooted in, changes with time, and begins releasing ions of a different composition into the solar wind at the base of the field. In Chapters 2 and 5 we discuss and then carry out research which investigates such cases, and thus whether composition is truly a reliable tracer.

Chapter 2

Solar Wind Origins

In the previous chapter we introduced key concepts in the study of the solar wind and its origins at the Sun. In this chapter, which takes the form of a literature review, we outline developments in this field upon which the research in this thesis is built. First, we describe current theories on the origins of the slow solar wind. Next, we discuss studies which concern heavy ion charge states, one of the primary *in situ* tracers of coronal properties, and what information we can expect to be conveyed by these signatures in the solar wind. We then outline work which considers the origins of a particular component of the solar wind; suprathermal electrons. This leads to a consideration of what coronal and heliospheric signatures these electrons might be able to carry into the solar wind. Moving towards the origins of solar wind which is associated with specific structures, both in the corona and the heliosphere, we present research on the origins of solar wind within rarefaction regions. Of particular interest is the cause of the compositional signatures which manifest there. Finally, we describe research on the solar wind associated with active regions; one of the classes of structure often linked to the slow solar wind.

2.1 Sources of the Solar Wind

From their contrasting dynamic and compositional properties, it seems apparent that the fast and slow solar wind should have different origins. Although there are still unknown elements to both, the current state of research considers the understanding of fast wind origins to be more complete than slow. In this section we describe research pertaining to each in turn.

2.1.1 Sources and Properties of the Fast Wind

As indicated by early observations by Krieger et al. (1973), coronal holes (CHs) are thought to be the source of the fast solar wind. The acceleration process for fast solar wind, which lead to it being faster than slow wind, is not yet known with certainty. Contemporary theories of the properties of the fast solar wind thus attempt to explain how these properties are imparted in coronal holes.

The speed of the fast solar wind is very likely a consequence of the fact that it originates in open flux regions of the corona. Wang and Sheeley Jr (1990) demonstrate the empirical relationship that solar wind speed is inversely proportional to the so-called 'expansion factor' of open magnetic flux tubes at the wind's origins. This expansion factor, f_s, describes the rate at which modelled coronal open flux expands between the photosphere and the outer edge of their model, which they call the source surface, at distance R_{ss}. It takes the form $f_s = (\mathrm{R}_\odot/R_{ss})^2[B(\mathrm{R}_\odot)/B(R_{ss})]$. For normal radial expansion, $f_s = 1$, while for superradial expansion, $f_s > 1$. As a corollary to the f_s-speed relationship, it follows that solar wind from the centre of coronal holes should be the fastest, as the flux tubes there undergo the least expansion. Further, larger coronal holes should then produce wind of higher maximum speeds.

A schematic explanation for the f_s-speed relationship is that flux tubes which ex-

pand more severely must spread whatever energy is supplied at their base over a larger area. If the energy input at the base of each flux tube is comparable, this results in less energy being available for acceleration in more strongly-expanding fields.

Broadly, two classes of models for the acceleration of solar wind from coronal holes exist; those which transport and distribute energy through waves and turbulence, and those which rely on the energy released from interchange reconnection between the open flux and closed loops (see the review by Cranmer, 2009). In wave-turbulence models, Alfvén waves driven by convective motions in the photosphere propagate upwards; turbulence develops and energy is dissipated, heating and accelerating the plasma. The expansion factor of the magnetic field controls the evolution of the Alfvén speed, which ultimately produces the velocity-expansion factor relationship described above (Cranmer et al., 2007). Cranmer et al. (2007) also model the charge state freeze-in process for the expansion of wind heated in this way, and find that charge state correlates positively with expansion factor; in agreement with observations by Wang et al. (2009).

In reconnection models, interchange reconnection occurs between open flux and closed loops, liberating energy which heats and accelerates the plasma. Small closed loops are observed low-down in coronal holes (e.g., Dowdy et al., 1986), so interchange reconnection can occur within coronal holes themselves. Fisk (2003) develops a model based on these principles, in which emerging closed loops undergo interchange reconnection with open field lines at their base. The footpoints of the open field lines are thus displaced, and work involved in moving the upper portion of the magnetic field line in response to this displacement heats the coronal plasma. Further, heavy ion charge states, a function of electron temperature, relate to the height of the loops which are opened (Gloeckler et al., 2003), due to the loop height-temperature relation (Section 1.2.2).

2.1.2 Sources and Properties of the Slow Wind

The origins of the slow solar wind are considerably more uncertain than the fast. Slow wind compositional properties such as charge states and abundance (e.g., Geiss and Bochsler, 1985), and the presence of the HCS (which is typically embedded in the streamer belt, as noted in the previous chapter) suggest that it originates from closed magnetic field regions of the Sun. Any model which hopes to fully explain the slow wind must thus explain how the slow wind could emerge from such locations. Models must also explain the lower bulk speed, high variability, angular extent (as much as $\sim 30^\circ$ away from the HCS, Zhao et al., 2009) and other characteristics of the slow wind. Here we describe three prominent classes of slow solar wind models.

Expansion factor models (e.g., Withbroe, 1988; Wang and Sheeley Jr, 1990; Wang et al., 1997) explain the origins of the slow wind as essentially the same as the fast. If the slow wind originates at the edges of coronal holes, then the rapidly expanding magnetic field leads to low bulk speeds and high charge states, given the empirical relationship of these properties with expansion factor. The actual physical process for producing the slow wind thus falls to either the waves and turbulence, or loop-opening solar wind models described in the previous section. There are problems with this description however. For example, the often non-steady nature of the slow wind is unaccounted for, as whatever mechanism is producing it should be the same as that which produces the comparatively steady fast wind.

Interchange models share some similarities with the reconnection model for the fast solar wind. Fisk et al. (1998); Schwadron et al. (1999) argue that the slow wind could escape along open field lines which have moved diffusively into quiet Sun (QS) regions. This motion is enabled by repeated interchange reconnection; starting in the coronal hole. The resulting properties of the slow wind emerge from

the fact that larger, hotter loops are available to be opened in the quiet Sun than in the coronal hole. This model accounts for the variability of the slow wind since these reconnection processes are necessarily dynamic. A distinguishing factor between this class of model, and the loop-opening case of the above expansion factor model, is that here the diffusive motion of open magnetic field lines allows the slow wind to originate from locations far-removed from the coronal hole boundary. Edmondson et al. (2010) present results modelling the evolution of open flux, arguing that the diffusion of open flux far into closed-field regions does not necessarily occur. This is a problem for interchange models, since field lines must diffuse far into the quiet Sun regions in order to explain the angular extent of the slow wind.

The tops of streamers, which are located at the base of the HCS, constitute a separatrix, and so reconnection there is likely. Reconnection can release plasma into the heliosphere as demonstrated in modelling by e.g., Endeve et al. (2004); contributing to the solar wind. This description does not account for the slow wind's angular extent, as it predicts that it can only be released from the tops of streamers and not throughout the quiet Sun. The model by Antiochos et al. (2011) applies similar principles, but extends the locations at which reconnection can occur. The model posits that at the photosphere, all like-polarity coronal holes are in fact connected by thin, magnetically open, corridors. This suggestion is consistent with modelling by Antiochos et al. (2007). The field lines rooted in these open corridors rapidly expand with height in the corona, creating a QSL (see Section 1.2.2) associated with each edge of the corridor, where reconnection might occur. The convective motions in the photosphere have a strong effect on the topology of such a thin structure, and so the corridor is constantly evolving, with interchange reconnection at the QSLs facilitating the motion of the open flux and releasing closed-field plasma into the heliosphere. Further, closed-closed reconnection can occur as it does at the separatrix in streamer tops, releasing blobs of plasma. These processes create a variable and

extended slow solar wind. The complexity of the photospheric motions and magnetic field causes the resulting QSLs to be numerous and also complex - forming a 'web'. This model is therefore named the 'separatrix-web' or 'S-web' model.

The different theories on the origins of the slow solar wind are clearly varied, however identifying which is valid, or at least dominant over the others, with observations is difficult. Compositional signatures are important, but as we shall discuss below the precise mechanisms by which these are generated are also not fully grasped. Mapping solar wind observations back to the Sun leads to large uncertainties, as we shall see in Chapter 3, and anyway the necessary models of the coronal magnetic field which this mapping employs cannot yet describe these complex processes of solar wind production. In the rest of this section, we describe some of the specifics of the origins of certain solar wind particles, and other regions of solar wind which have not yet been discussed.

2.2 Heavy Ion Charge States

2.2.1 The Origins of Solar Wind Ionisation Signatures

In Chapter 1, we provided a simplified view of how solar wind heavy ions come to be distributed by charge state. We also outlined the argument for these ions acting as tracer species of coronal properties, and thus as powerful tools in understanding solar wind origins. In this section we briefly describe recent work on the ionisation processes in the corona, and discuss how this may affect the role of charge states as tracers in the solar wind.

Much detailed modelling of ionisation has been carried out in the studies Cranmer et al. (2007); Landi et al. (2011, 2012a,b, 2014); Landi and Lepri (2015). These studies all model the charge states in the corona, for plasma which is flowing out into the solar wind. Given inputs of electron temperature, density, and velocity

profiles, rates of ionisation and recombination are calculated for each charge state, across the range of coronal heights. The evolution of each charge state as it flows out through the corona can thus be calculated. This is a far more detailed approach than the simple picture described in Section 1.3.7, as it no longer assumes ionisation equilibrium, and allows for different charge states of the same species to freeze-in at different heights.

A key result from the above class of model, presented by Landi et al. (2012b), is that the rate of outward expansion causes a given parcel of plasma to travel through a temperature scale height, before ionisation equilibrium can be reached. Since the ions are flowing up from the cooler transition region, they begin at charge states which are cooler than equilibrium states for coronal temperatures. In many species, collisions then cease before the ion charge states are enhanced to represent the true coronal temperature. This leads to the freeze-in temperature implied by a given charge state (the calculation of which assumes equilibrium) being systematically lower than the true coronal temperature at the freeze-in height. Further, the freeze-in temperature ultimately ends up being dependent on the full temperature profile of the corona, below the freeze-in height, as opposed to only at this height.

The studies Landi et al. (2011); Landi and Lepri (2015) investigate which species of ion acts as the best tracer of source region properties. Landi et al. (2011) compare the freeze-in process for the commonly-used charge state ratio O^{7+}/O^{6+}(frequently applied, as oxygen is the most abundant species in the solar wind, in studies such as Zurbuchen, 2002; Zhao et al., 2009) to carbon charge state ratios C^{6+}/C^{5+} and C^{6+}/C^{4+}. The model outputs using fast solar wind parameters suggested that the freeze-in of individual carbon charge states C^{4+}, C^{5+}, C^{6+} occurs within the range of heliocentric distances 1.2–1.6 $R_\odot$ (C^{4+} at $\sim 1.2\,R_\odot$, C^{5+} at $\sim 1.35\,R_\odot$, and C^{6+} at $\sim 1.6\,R_\odot$). Meanwhile oxygen charge states O^{5+}, O^{6+}, O^{7+} freeze-in over the range $\sim$ 1–1.6 $R_\odot$ (O^{5+} at $\sim 1.25\,R_\odot$ O^{6+} at $\sim 1.0\,R_\odot$ and O^{7+} at at $\sim 1.6\,R_\odot$).

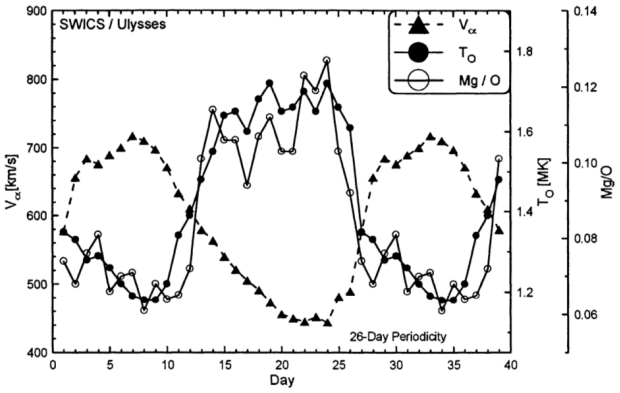

Figure 2.1: 26-day superposed epoch analysis results for solar wind velocity, oxygen freeze-in temperature and Mg/O plotted against time from Geiss et al. (1995a). The data are plotted over 40 days so that both the leading and trailing boundaries of the fast stream are clear. In the rarefaction (days 9–20) the compositional parameters change far more sharply than velocity.

The coronal electron temperature thus evolves most significantly over the course of freezing-in of the different oxygen charge states, since the largest temperature increase occurs between 1.0 and 1.2 $R_\odot$. This result implies that a freeze-in temperature derived from carbon charge states should be more-closely representative of a true coronal electron temperature, at a single height in the corona, than one from oxygen charge states, which instead represents a combination of a broad range of temperatures at different heights.

Further, Landi and Lepri (2015) tested the effect of photoionisation, another process neglected in the freeze-in description of Section 1.3.7, for a range of solar wind heavy ions. They introduced ionising radiation, derived from observations across different points in the solar cycle, into their modelled ionisation and recombination rates. Particularly at times of strong radiation (solar maximum) the upper charge states of C, O and N were all found to be subject to enhancements due to photoionisation, with oxygen being affected significantly more strongly than carbon ratios. Again the authors recommend the use of a carbon charge state ratio, in particular C^{6+}/C^{4+}, instead of the more widely-applied O^{7+}/O^{6+}.

2.2.2 Application of Charge States as Coronal Tracers

Despite the above drawbacks applying charge state ratios (particularly the commonly used O^{7+}/O^{6+} ratio) as tracers of the solar wind source, they have been widely-applied in the literature, and their utility has been frequently demonstrated. Geiss et al. (1995a) perform a superposed epoch analysis (the averaging of data over multiple Carrington rotations) on solar wind bulk velocity, charge state (oxygen and carbon), and abundance (Mg/O and Fe/O) data from the Ulysses spacecraft between 1992 and 1993. Results of this are shown in Figure 2.1. The boundary between solar wind streams as seen in the compositional data is far sharper than the boundary seen in the bulk velocity; particularly in the rarefaction (the region of decreasing velocity). It appears that charge states and abundance of ions adhere more closely to the initial coronal boundaries than velocity; evidence in support of the resilience of these parameters to solar wind transport effects as discussed in Section 1.3.7.

O^{7+}/O^{6+} is also found to be a better tracer of coronal origin than velocity alone in the more modern work of Ko et al. (2014). They found, amongst other results, that in the declining period of solar cycle 23, while wind from both the northern and southern polar coronal holes exhibited the same wind speed, there was a notable discrepancy in their corresponding O^{7+}/O^{6+} values. This indicates that O^{7+}/O^{6+} is a characteristic of the source region, which performs better not only in identifying boundaries as above, but also in identifying unique properties of the source regions.

The key points we wish to highlight from these studies are thus: 1. Heavy ion charge states are not uniquely related to coronal electron temperature in a simple way. Broadly however, they do serve as indicators of source regions with distinct freeze-in properties, be they temperature, density, or expansion rate. 2. When possible, carbon charge states should be considered over the more traditional oxygen charge states, due to a mix of freeze-in and photoionisation effects.

2.3 Origins and Evolution of Suprathermal Electrons

In Section 1.3.6 we introduced the populations of solar wind electrons; core, halo, strahl and super halo. In this section, focusing on halo and strahl populations, we review past research as to how these populations originate and evolve as they propagate through the heliosphere. This is important from the perspective of understanding physical processes in the corona and the solar wind, as well as in applying measurements of halo and strahl to diagnose properties at the solar wind source. Here we focus primarily on the energy content of halo and strahl electrons, how this might relate to the coronal properties, and how it evolves during propagation through the heliosphere. Additionally, we discuss the application of the strahl in particular to yield information on the topology of the interplanetary magnetic field.

2.3.1 Formation in the Corona

The origins of the distinct strahl and halo electron populations in the solar wind are not well understood. Evidence has been found that a suprathermal tail can exist in the solar wind using exospheric models (e.g., Lie-Svendsen et al., 1997) which ultimately require a seed suprathermal electron population to exist in the corona. Pierrard et al. (1999) use *in situ* electron VDF measurements from WIND (see Chapter 3) to provide boundary conditions to their model of electron VDFs which originate at $4\,R_{\odot}$. Their results too suggest that an electron VDF which includes suprathermal electrons at 1 au must correspond to one which also included suprathermal electrons in the corona. The relative strength of the suprathermal tail is predicted to be considerably weaker in the corona than at 1 au, and the effect of coulomb collisions in influencing the distribution for slow wind electrons is predicted to be more significant than for fast wind.

Using a Kappa function (Equation 1.14) to model the ionising electron population in the corona, Ko et al. (1996) simulated the charge state distributions of coronal ions given different core electron temperatures and values of κ. They thus predict, based on solar wind oxygen and carbon ionisation measurements, a weak suprathermal tail ($\kappa \geq 5$) should exist in the corona. At such levels it is not expected that the influence of collisions with these electrons on ionisation equilibrium would be very significant. In a related study, Esser and Edgar (2000) invoked additional ionisation by suprathermal electrons to explain an established discrepancy between freeze-in temperatures measured *in situ*, and estimates of coronal electron temperature derived from coronal emissions (Sections 1.1.10 and 3.3.1). They claimed that the sensitivity of the dominant charge state ratios to T_h/T_c (the ratio of modelled electron halo temperature to the core temperature) varied strongly based on species, with O^{7+}/O^{6+} proving most sensitive. A range of halo temperatures were thus thought to be necessary to meet the observed ionisation states for different species *in situ*.

In contrast, Laming (2004) proposed an explanation of the above compositional-spectral temperature discrepancy via extra heating of the coronal thermal electrons by waves, in place of suprathermal electrons. The author notes that remote estimates of coronal temperature using O VI line diagnostics should be sensitive to suprathermal influence. However, these lines do not appear to show evidence of this in practice, casting doubt on the predictions of the existence of a significant suprathermal electron population in the corona.

Che and Goldstein (2014) present a model for halo formation in the corona via an instability process which is related to nanoflares. As in the work of Lin (1997), they postulate that nanoflares accelerate electrons in the coronal base to beams with energies on the order of keV. These beamed electrons then travel upwards in the corona, where they trigger an electron two-stream instability (Section 1.1.8) with the thermal electron population. This results in a redistribution of energy, as discussed in

Che et al. (2014), involving a transfer of energy from the nanoflare-triggered electron beam to the core electron population, and the ultimate formation of an isotropic electron halo population. Modelling both as Maxwellians, the final core-halo temperature ratio then obeys the relation:

$$\frac{T_h}{T_c} \approx \frac{n_c}{n_h}\frac{1-C_T}{C_T} + 4 \tag{2.1}$$

where T_h and T_c are the halo and core temperatures respectively, n_h and n_c are the halo and core densities, and C_T is the fraction of kinetic energy which is transferred to the core electrons. For values of C_T approaching 1, this describes a proportionality between the core and halo electron temperatures in the corona. The authors argue that this feature is preserved out to the solar wind as the coulomb collision rate is insufficient to scatter halo electrons to form a single thermal distribution before reaching the low-density region of the corona. It should also be noted that the predicted height of formation of the electron halo is 1–1.1 $R_\odot$; below typical ion freeze-in heights in Section 2.2.1. This suggests that the VDF of suprathermal electrons in the corona may have a relationship with the charge states of minor ions, due to their common dependence on the coronal core electron temperature. As ion charge states are not influenced by dynamic processes in the solar wind, a relationship between these charge states and suprathermal electron VDFs persisting at 1 au would indicate that these electrons have propagated out to 1 au relatively unaltered themselves.

2.3.2 Evolution in the Heliosphere

We shall now discuss the changes undergone by suprathermal electron populations as they propagate out through the heliosphere. Maksimovic et al. (2005) and Stverak et al. (2009) showed that the relative density of the halo population increases with heliocentric distance at the apparent expense of the strahl. They thus infer that the

strahl is scattered into the halo continuously. Owens et al. (2008) estimated the degree of scattering necessary in such a case to counteract the effect of magnetic focusing during solar wind expansion and thus presented an explanation to the observed pitch angle widths of strahl. Modelling by Vocks et al. (2005) predicts that this scattering is caused by wave-particle interactions, notably with whistler waves. Seough et al. (2015) put forward an alternative explanation for the observed strahl pitch-angle widths involving asymmetric pitch-angle scattering of the halo caused by the core-halo drift (in which the mean velocity of the halo is offset from that of the core, as observed by e.g., Feldman et al., 1975).. They predict that the strahl is the unscattered field-aligned portion of the halo which results from this asymmetry. Both of the above descriptions would mean that the halo and strahl are linked intrinsically; halo electrons are scattered into the strahl population and/or strahl electrons are scattered into the halo Such scattering could potentially distort solar wind electron VDFs to the point at which an initial relationship with heavy ion charge states is no longer apparent at 1 au.

Results from a study by Hefti et al. (1999) using solar wind ion and electron observations suggest that there is an influence from the coronal source evident in the *in situ* suprathermal electrons at 1 au. Combining heavy ion data from the SWICS instrument on the ACE spacecraft with electron data from the 3DP instrument on WIND, these authors reported a relationship to exist between properties of the electron suprathermal tail and the charge state ratio O^{7+}/O^{6+}. In particular, the energy content of the suprathermal tail was characterised by defining an effective suprathermal temperature (hereafter T_{eff}) using the VDF derived from WIND electron measurements. This temperature is derived by differentiating the equation for a single Maxwellian distribution:

$$T_{\text{eff}} = \frac{-1}{k(d\ln f/dE)} \tag{2.2}$$

where k is the Boltzmann constant, f is the electron VDF, and E is energy. For a

pure Maxwellian distribution, $d\ln f/dE$ would be constant with energy. However, as observed suprathermal electrons do not follow a perfect Maxwellian, particularly at higher energies, this T_{eff} calculated with observational data in fact varies with energy.

Applying this calculation for T_{eff} at a number of energies (300, 500 and 800 eV) to solar wind data at a boundary between two slow-fast wind transitions, a correlation between T_{eff} (at a given energy) and O^{7+}/O^{6+} was investigated by Hefti et al. (1999). The authors restrict themselves to two periods in the solar wind observations where the wind speed has just increased significantly between streams, and find that O^{7+}/O^{6+} varies similarly to T_{eff}. This leads them to conclude that suprathermal electrons at 1 au retain information about their coronal source as ionisation states do. However, the study is limited to only two short ($\sim$ 5 day) intervals in the ACE and WIND datasets. As such, this relationship is yet to be more generally verified. In Chapter 4 we attempt to do so; improving on the methodology and extending the study to consider separately the halo and strahl, over many years of observation.

2.3.3 Electrons as Probes of Heliospheric Magnetic Topology

As was first established observationally by Kahler and Lin (1994), the beamed nature of strahl electrons can be applied to diagnose the topology of the IMF. Since the strahl propagates anti-sunward along the field, a field line which is directed anti-sunward (sunward) in the corona will at all points along it have strahl flowing in the parallel (anti-parallel) direction. Kahler and Lin (1994) applied this knowledge to infer the 'true' polarity of the IMF during instances when its local orientation was not definitively sunward or anti-sunward. Their illustration of this is shown in Figure 2.2. In case A, all of the field lines are anti-sunward when they leave the Sun, but a portion become locally inverted or 'kinked'. In the drawn time series, an in-

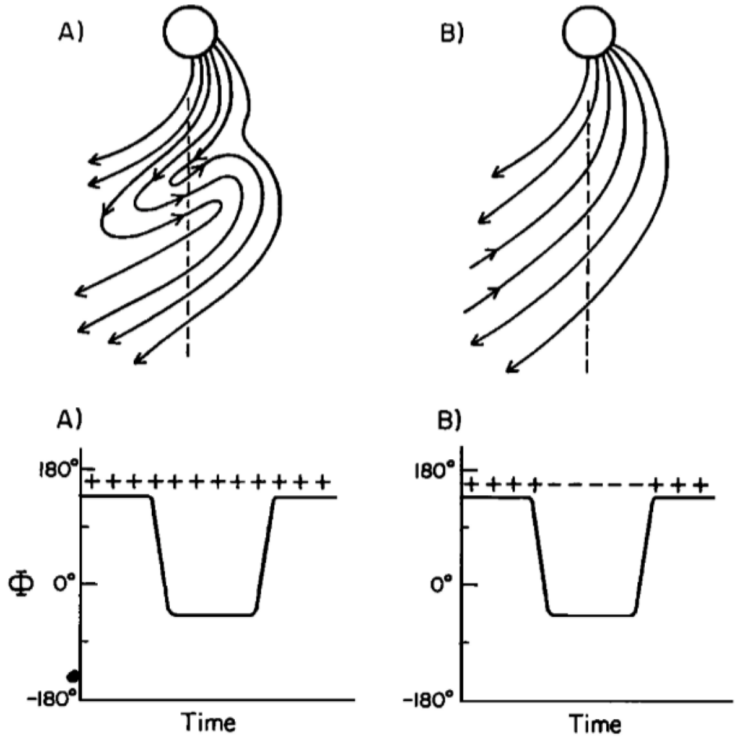

Figure 2.2: Schematic of two IMF configurations from Kahler and Lin (1994). The top panels show IMF field lines in the ecliptic plane. The dashed line shows the effective path of a spacecraft through the field. The bottom panels show illustrative time series which would be the result of these topologies at the spacecraft. The IMF azimuthal direction is labelled Φ, while the strahl alignment is shown as '+' for parallel to the magnetic field and '-' for antiparallel. The two configurations represent field which is initially anti-sunward but becomes kinked (A) and field which is both sunward and anti-sunward, and is unkinked (B). These configurations produce similar time series in Φ but can be distinguished by the strahl alignment.

version of the field is seen in the azimuthal angle of the magnetic field, but strahl alignment remains parallel to the magnetic field direction throughout. In case B, there are both anti-sunward and sunward field lines. The magnetic field orientation in the time series acts identically to A, but now the strahl streams antiparallel to the field during the magnetic field inversion. The authors observed several such kinks in a set of *in situ* solar wind observations.

Kinks in the IMF may originate from a handful of processes, including interchange reconnection, as was shown in Figure 1.10 in Section 1.2.2. The combination of *in situ* magnetic field and strahl measurements can in fact be used to identify a number

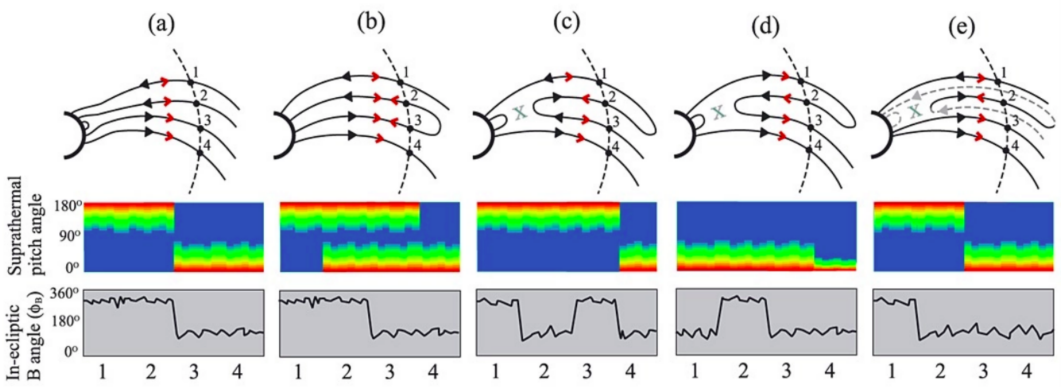

Figure 2.3: Diagram of five different IMF configurations (a–e), and resultant *in situ* suprathermal electron spectrogram and magnetic field angle time series from Owens et al. (2013). Top panels show example magnetic topology in the ecliptic plane. Black arrows show magnetic field direction, red arrows show strahl beam direction, and the dashed line shows a spacecraft slice through the field. Greyed-out dashed lines show magnetic field which lies out of the ecliptic plane. An 'X' marks where reconnection has taken place. The ordering of field lines as observed by the spacecraft are numbered 1–4. Middle panels show illustrative electron pitch angle distributions as a spectrogram. The strahl beam is shown as an enhancement (red, yellow, green) over the background (blue). Bottom panels show the azimuthal magnetic field angle; $\sim 315°$ is anti-sunward flux while $\sim 135°$ is sunward.

of IMF configurations, as summarised in Figure 2.3, from Owens et al. (2013). The figure shows five different configurations, with the expected suprathermal electron and magnetic field orientation data. The configurations are: (a) open field lines of opposite polarities, (b) open field field lines of opposite polarity separated by a closed loop, (c) open field lines with a kink (as in Figure 2.2 A) separating opposite polarities, (d) open field lines with a kink separating like polarities, (e) open field lines with a kink, where some field lines lie out of the ecliptic plane. We note in particular that in (b) a closed loop in the IMF is identified through the strahl flowing in both directions. This signature is known as 'bidirectional' strahl. It can apply in cases of closed loops in the ambient solar wind, and also for ICMEs in which both magnetic footpoints are rooted in the Sun. In (d) there is a narrower strahl beam present at point 4 in the time series; a result of reduced strahl scattering when travelling a shorter distance along the IMF. Several of these configurations are associated with instances of reconnection at the Sun, and so the strahl electrons

also act as a remote signature of reconnection.

2.4 Solar Wind at Fast-Slow Interfaces

The boundaries between fast and slow solar wind, and fast and slow solar wind sources, are key in understanding the origins of the solar wind. It is at these locations where the wind transitions in type, and so differences are expected to be most apparent. The proper identification of these boundaries *in situ* is also crucial to classify regions of the solar wind by source. At the Sun, the boundaries of coronal holes are one of the candidate slow wind regions, per expansion factor models (Wang and Sheeley Jr, 1990), and open-closed boundaries in general are sites of solar wind production in interchange (Fisk et al., 1999) and S-web (Antiochos et al., 2011) models. Here we present research on the (primarily compositional) properties and origins of solar wind around stream boundaries; particularly for rarefactions where the plasma is not compressed.

In discussing the superposed epoch analysis of Geiss et al. (1995a) (Figure 2.1) we noted above that the transition from low to high T_O (oxygen freeze-in temperature calculated from O^{7+}/O^{6+}) and Mg/O in the rarefaction of the fast solar wind stream is far sharper than the corresponding transition in velocity from fast to slow. This makes intuitive sense, as the formation of a rarefaction leads to a large region of velocity transition (Section 1.3.4) which should not affect the transition in composition. The transition in composition however is not discontinuous; T_O changes from low to high temperatures over the course of $\sim$ 3–4 days, while Mg/O does so in closer to 6. The time resolution of the data used here limits the clarity of the apparent transitions. We expect that a discontinuous boundary in source region properties at the Sun should result in a discontinuous boundary in charge state and abundance *in situ* as a consequence of frozen-in flux. Since Geiss et al. (1995a) and others (e.g., McComas et al., 2002) do not observe a discontinuous transition we must

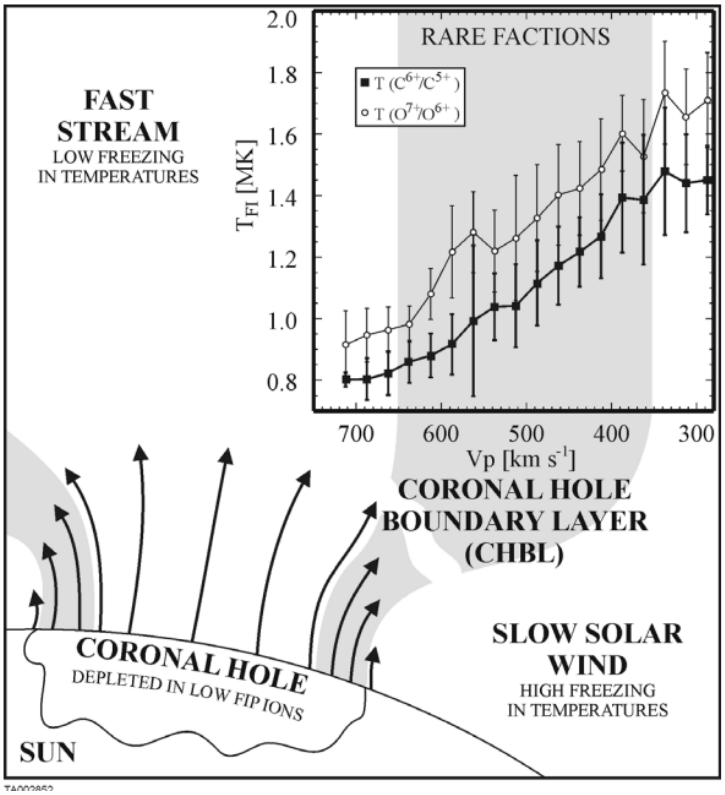

Figure 2.4: Diagram showing origins of the fast, slow and CHBL solar wind, with compositional properties labelled, from McComas et al. (2002). Inset is a representation of the expected anti-correlation between freeze-in temperatures (inferred from O^{7+}/O^{6+} and C^{6+}/C^{5+}) and solar wind speed in the CHBL.

conclude that either: 1. There is some source region with intrinsically intermediate/transitional properties between fast and slow sources. 2. Fast and slow streams might be magnetically connected. We discuss research on these topics below.

Expansion factor solar wind models necessarily predict that towards the edge of coronal holes there should be a decrease in solar wind speed, as well as an increase in charge states. For some region then charge states should inhabit values which are intermediate between the fast and slow solar wind values. McComas et al. (2002) explain the composition of rarefactions in this way; a region of transitional properties at the edge of the coronal hole named the "coronal hole boundary layer". The CHBL predicted by McComas et al. (2002) is shown in Figure 2.4. While ion charge states are thought to be intermediate, these authors argue that the CHBL

should feature photospheric (low-fractionation) elemental abundances, as matches their *in situ* observations. Wang et al. (2009) predict the existence of a similar wind source at the boundaries of coronal holes, but instead associate observed intermediate values of fractionation with it. We note that from the data shown in this study, these authors' definition of 'intermediate' may be very similar to the photospheric values attributed to the CHBL by McComas et al. (2002).

Borovsky and Denton (2016) perform a study of a collection of rarefactions in the solar wind, identifying features in the charge states within them. In addition to a discontinuous 'jump' in charge state, a gradual transition is frequently observed. We note that the authors primarily identify this feature through superposed epoch analysis, which is likely to smooth-out discontinuities in all *in situ* parameters. The *in situ* transition is explained as a gradual transition from small, cooler loops in coronal holes feeding plasma into the solar wind through interchange reconnection, into larger, hotter, loops doing so towards the coronal hole boundary. These gradual *in situ* transitions are also observed by e.g., Zurbuchen et al. (1999) in contrast to Geiss et al. (1995a).

Other possibilities for the origins of these intermediate/transition regions of composition in rarefactions exist. One such alternative is the mixing of plasma between the distinct fast and slow solar wind streams, at some location between the Sun and the observer. For this to occur, a magnetic connection needs to exist between solar wind streams along which plasma can mix. Schwadron (2002) models how the differential rotation of the photosphere causes footpoints of open magnetic fields to rotate at below the solar rotation rate. In the frame corotating with the solar equator, open flux footpoints (at non-zero latitudes) are thus dragged eastward around the Sun. This results in a so-called "sub-Parker spiral" IMF structure, in which the spiral configuration is less tightly-wound (more radial) than is implied by Equation 6.1 using rigid rotation. This radial magnetic field has been observed by e.g., Murphy

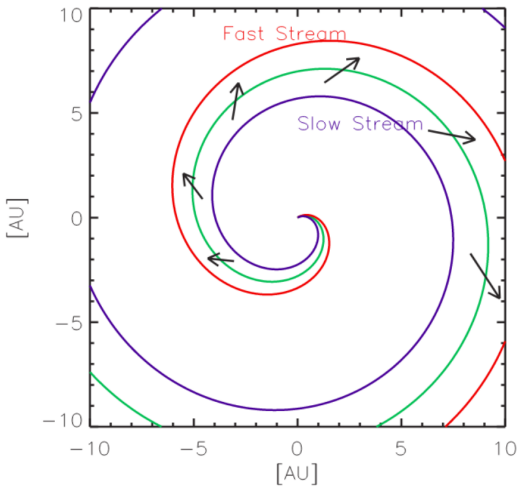

Figure 2.5: Schematic of sub-Parker spiral field in a rarefaction from Murphy et al. (2002), drawn out to 10 au. Streamlines are shown as solid-coloured lines, denoting the fast edge (red), slow edge (blue) and centre (green) of the rarefaction only. Black arrows show the IMF direction at select locations within the rarefaction. The field is significantly more radial than the Parker spiral configuration, and thus crosses the stream boundary in the centre of the rarefaction.

et al. (2002), who particularly noted its existence in rarefactions between fast and slow streams. Key to the study by Schwadron et al. (2005), who model composition in this configuration, is that this footpoint motion carries flux over coronal hole boundaries in the corona; changing the source region connectivity of the magnetic field. This creates a magnetic connection across the associated stream boundary in the solar wind. A diagram from Murphy et al. (2002) which illustrates this in solar wind rarefactions is reproduced here in Figure 2.5. The magnetic field in the figure is more radial than in the Parker spiral case defined by Equation 6.1, which would align the field with the streamlines. The magnetic field thus threads the fast-slow boundary embedded in the centre of the rarefaction region. Plasma in the originally fast portion of the rarefaction is thus connected to a slow wind source.

Schwadron et al. (2005) model *in situ* ion charge states in the context of the sub-Parker spiral IMF. The authors model the solar wind in a 2-dimensional MHD framework. The model spans from $30\,R_\odot$ (the presumed Alfvén critical point) to 5 au (the approximate distance of Ulysses observations with which they compare their results) and considers the solar wind at a latitude of 75° from the ecliptic (the approximate latitude of the Ulysses observations). The motion of the magnetic field footpoints from a fast to slow source region causes high charge state oxygen ions to be released onto field lines which downstream are associated with low charge state

ions. Minor ion differential streaming then causes these high charge state ions to catch up to bulk solar wind which was previously associated with low charge states (see Section 1.3.7). This leads to a mixed region of high and low charge state in the rarefaction, wherever differentially streaming oxygen ions have crossed the stream boundary. The authors set the differential streaming rate to be equal to the local Alfvén speed. The authors compare the results of this model at 5 au to the superposed epoch analysis of Geiss et al. (1995a) shown in Figure 2.1. They find that the extent of the mixed region (around 25°, or 1.8 days) accounts for around 1/3 of the duration of the intermediate composition region in the rarefaction. They explain the remainder using an intrinsically-intermediate CHBL which is introduced at the inner boundary, between the purely fast and slow sources.

In Chapter 5, we carry out a study on the origins of rarefaction solar wind as measured at L1 by ACE. We do so with the aim of discerning whether the intermediate charge state signatures there are predominantly an effect of some mixing process (such as that above) or in fact an intrinsic property of the source region only (such as at the CHBL).

2.5 Solar Wind from Active Regions

In Section 2.1 we introduced sources of the solar wind relating to coronal hole and quiet Sun sources. In addition to this, evidence has been found that solar wind, in particular slow wind, can also be released from active regions (ARs). The role of active regions in solar wind production is unique, in that active regions are distinct from both the quiet Sun and coronal holes in structure and composition, and conceivably should therefore also be distinct in solar wind release mechanism. Further, active regions are of high interest more generally throughout solar physics and heliophysics, due to their association with flares and eruptions. In this section we describe the current state of research on active region-associated solar wind. First,

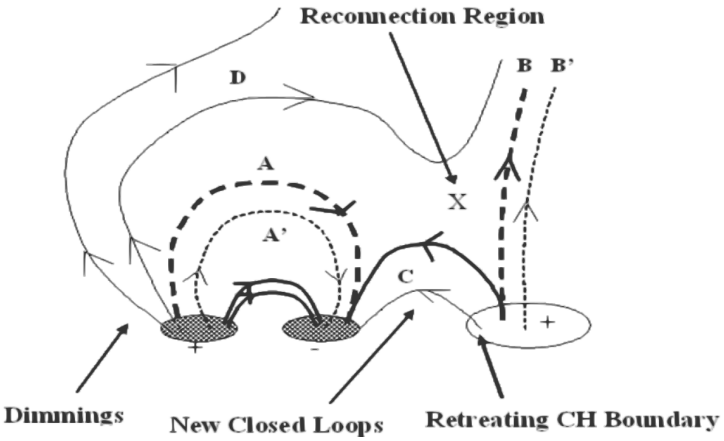

Figure 2.6: Schematic of active region-coronal hole interchange reconnection from Baker et al. (2007). Observational features are labelled along the bottom of the image. The location for reconnection is located between the negative active region and positive coronal hole field. Magnetic fields are labelled. A: active region loops; B: coronal hole open flux; C: new closed loops at the boundary; D: newly-opened fields at the eastward active region footpoint.

we detail the relevant background information of active region properties. We then describe the evidence for solar wind flowing out of active regions. Finally, we introduce a host of candidate processes for active region solar wind to be produced.

2.5.1 Active Region Interactions

As regions of highly-concentrated magnetic flux, active regions interact strongly with surrounding coronal structures. As active regions emerge, and their coronal loops grow, the probability of reconnection with neighbouring magnetic fields increases. Typically slow and continuous (van Driel-Gesztelyi and Green, 2015), this reconnection changes magnetic topology surrounding the active region. This is in contrast to the rapid reconnection associated with flares.

Active region reconnection with open magnetic flux is of particular interest from a solar wind origins standpoint. For example, Baker et al. (2007) observe the emergence of an active region to the east of a coronal hole. The coronal hole boundary is observed to recede away from the active region; evidence of interchange reconnection between the active region and coronal hole. The authors' schematic of this

process is reproduced in Figure 2.6. The active region is oriented such that its leading polarity and the coronal hole polarity are opposite; thus antiparallel reconnection can take place. Open flux is transferred to the trailing active region footpoint; plasma from this region may then escape into the solar wind.

2.5.2 Active Region Composition

Elemental abundance (primarily in the form of FIP bias) is a key compositional signature for solar wind source identification. Feldman and Widing (2003) review the FIP bias levels in different structures in the corona. In addition to the bias of 3–4 in the quiet corona, and ~ 1 in coronal holes, they describe FIP bias in active regions. Active region abundance is found to be highly-variable, spanning from photospheric to coronal values depending on the active regions and the loops being observed therein. The authors note that FIP biases of up to 7 can also be observed with higher spatial resolution, when finer loops in the active region can be observed. The mean FIP bias over many active regions reveals an average of ~ 2, however given the variability noted above this value is not likely to be representative.

Active region FIP bias was studied by Widing and Feldman (2001) as a function of time using the Mg/Ne relative abundance with Skylab. Studying 4 active regions, the authors found the highest FIP bias regions were often located in the small loops in the "core" of the active region. Close to emergence, all active regions featured photospheric composition (FIP bias ~ 1). Following this, each active region increased in FIP bias to coronal levels of 4–5 over ~ 2 days. The bias increased further to values of ~ 7 over the course of 3–5 days. One of the likely causes of variability in active region abundance is thus active region age. Feldman and Widing (2003) argue further that the FIP bias of a structure in general, and thus also solar wind released from that structure, is also a function of age.

A young active region studied by Baker et al. (2013) using Hinode-EIS (Section

3.4.2) was found to have FIP bias of 2–3 at the footpoints of active region loops. This was attributed not only to the active region's young age, but also to interchange reconnection between the active region and a neighbouring coronal hole; allowing mixing of active region and coronal hole plasma. Observable portions of the loops themselves featured weakly-enhanced FIP bias of ~ 1.5. This is evidence that active region loops are the location of enhanced fractionation which increases with active region age; beginning at the footpoints before spreading upwards. This study is further evidence that active regions are locations of highly variable plasma composition, in terms of abundance.

2.5.3 Observations of Solar Wind from Active Regions

Since active regions in the corona are magnetically closed, and from the studies described above are often highly fractionated, solar wind from active regions is typically thought to contribute to the slow wind rather than the fast. Remote observations suggesting that solar wind can escape from active regions came into prominence with Hinode-EIS. Studies by Sakao et al. (2007); Harra et al. (2008) observed continuous outflows from the edge of an active region through Doppler velocity measurements. Through PFSS modelling (Section 3.5) apparent open field lines were located at the boundary between the active region and a nearby coronal hole; close to the upflow locations. The results suggested that the outflows were in fact plasma escaping into the solar wind. Full confirmation of this conclusion was in this case not possible through complementary *in situ* observations, however.

Observations by Brooks and Warren (2011) provided *in situ* confirmation of active region solar wind which was lacking from the studies of Sakao et al. (2007); Harra et al. (2008). These authors observed solar wind with a high degree of fractionation, several days after observing highly fractionated abundances remotely in outflowing regions at the edge of an active region with Hinode-EIS. Given the solar wind travel

time to 1 au, this was considered compelling evidence for the direct observation of active region outflow *in situ*. We note that the highly-fractionated plasma being located near an *outflowing* region is key here, due to the strong spatial variability in active region plasma composition. This study as well as those of Sakao et al. (2007); Harra et al. (2008), and earlier work by e.g., Kojima et al. (1999), suggest solar wind escapes from the edges of active regions; at loop footpoints of one polarity, rather than loop tops.

A host of other studies have linked *in situ* solar wind observations to active region sources. Neugebauer et al. (2002) applied the two-step backmapping procedure (Section 3.6) mapping solar wind streams back to active region sources. Such streams were found to exhibit moderately lower speeds, higher charge states, and also greater variability in composition and plasma parameters than those from coronal holes.

Statistical studies by Kilpua et al. (2016); Fu et al. (2017) also identified solar wind from active regions (amongst other sources) using different mapping techniques, and studied their properties. Kilpua et al. (2016) studied solar wind only during solar minimum, while Fu et al. (2017) studied streams over a solar cycle, and separated results according to cycle phase. Discrepancies between these two studies are probably a result of different mapping approaches, and study periods. Kilpua et al. (2016) find that mean active region-linked solar wind bulk velocity lies between that of coronal hole and quiet Sun wind, while exhibiting a wider spread. Fu et al. (2017) meanwhile find, even at solar minimum, that the velocity of active region wind is very similar to quiet Sun wind. Kilpua et al. (2016) find a moderate enhancement in both charge state ratio C^{6+}/C^{4+} and (FIP bias proxy) abundance ratio Fe/O in active region wind over quiet Sun wind (both of which are greater than coronal hole wind). Fu et al. (2017) only clearly find this enhancement in Fe/O, while their chosen charge state, O^{7+}/O^{6+}, is enhanced only during solar minimum. In these studies

there is large spread present in all parameters; reaffirming that active region solar wind is variable; likely a result of the variability in the active regions themselves, and the associated solar wind release process. The expectation that active regions make some contribution to what is observed *in situ* as slow solar wind appears to be confirmed by these studies.

2.5.4 Solar Wind Release Mechanisms

It seems clear that active regions do in fact release solar wind, the *in situ* properties of which are somewhat known. We now outline some potential physical mechanisms through which solar wind is expected to escape from active regions.

Active Region Loop Expansion

One candidate solar wind mechanism is the expansion of active region loops. This expansion has been observed to continually occur by Uchida et al. (1992), and has been observed recently at distances of $>12\,R_{\odot}$ by Morgan et al. (2013). At these distances the loops themselves should be considered a part of the solar wind. Gopalswamy et al. (2013) point out that *in situ* these loops should be distinct from ICMEs in that due to the lack of a flaring, their charge states should be lower than typical ICME charge states. The possibility of disconnection of these loops at one or both ends via interchange reconnection makes confirmation of this source mechanism challenging. Bidirectional strahl, the usual signature for closed loops in the heliosphere, will not be present in such cases.

Interchange Reconnection

Interchange reconnection is often invoked to describe how AR plasma might escape into the solar wind, and is found to commonly occur at active regions; particularly at coronal hole boundaries (e.g., Baker et al., 2007). Reconnection is a favourable mechanism to explain the usually variable and sporadic nature of AR solar wind

observed *in situ*. The process readily explains the presence of open flux at active region footpoints inferred by Sakao et al. (2007); Harra et al. (2008) (see Figure 2.6). In the contrasting case of expanding loops, we would expect both loop footpoints to be open to the heliosphere, whereas here only one footpoint is required. Baker et al. (2009) showed that AR upflows typically occur at QSLs and magnetic nulls. Interchange reconnection at the CH-AR boundaries would be likely to occur along such structures, and allow plasma to escape into the solar wind, explaining these upflows, and those seen by Sakao et al. (2007); Harra et al. (2008). Fazakerley et al. (2016) found evidence of solar wind flows associated with multiple CH-AR boundaries over one Carrington rotation. Bipolar, tripolar, and quadrupolar ARs were included in this study. Given the relative polarities of the ARs and CHs present on the Sun at this time, they inferred solar wind to escape through a range of different interchange reconnection configurations. They found evidence of solar wind from all present active regions, except for the lone active region which was not adjacent to a coronal hole.

Multi-Step Reconnection

Even without the presence of a coronal hole boundary adjacent to the AR, reconnection at QSLs and magnetic nulls can be invoked to explain solar wind originating in ARs. Culhane et al. (2014) observed in situ solar wind to be associated with an AR, despite the AR being apparently confined beneath the magnetic field of the streamer belt. This particular case was later explained by Mandrini et al. (2014) through a multi-step reconnection process, with at least one instance of closed-closed reconnection, followed by reconnection at a high-altitude null point ($0.15\,R_\odot$ above the photosphere) itself open to the heliosphere. It is thus possible for active regions to make contributions to the solar wind through complex reconnection chains.

Chapter 3

Instrumentation and Methods

In this chapter we describe the spacecraft, measurements, and techniques which are used to produce and analyse the data in this thesis. The first 4 sections describe the principles of *in situ* plasma observations; the spacecraft from which *in situ* data are obtained for this thesis; the techniques for determining coronal properties from remote sensing observations; and then the solar observing missions from which data are obtained for this thesis. The latter 2 sections describe models and techniques which are employed in the analysis of Chapters 5 and 6.

3.1 *In Situ* Solar Wind Plasma Observations

Due to its low density, the most effective way to measure the solar wind is through directly probing the plasma environment using spacecraft. In this way, electromagnetic fields and particle populations can be sampled at point locations.

Single-point measurements have a major limitation in that a lone spacecraft cannot discern between spatial and temporal variations in a plasma (i.e., the $\partial/\partial t$ and $(\mathbf{v}\cdot\nabla)\mathbf{v}$ terms in Equation 1.16). In the solar wind, the typical assumption is that variation is dominated by spatial changes advected by the plasma flow. Further, the majority of spacecraft in the solar wind move very slowly relative to its bulk flow

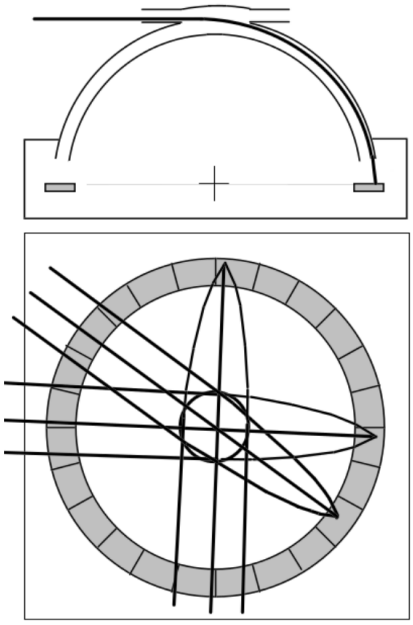

Figure 3.1: Schematic representation of a top hat electrostatic analyser. Black lines show the paths of detected particles, while detector plates are shown in grey. The top panel shows the analyser from the side, showing the channel through which incoming particles are deflected. The bottom panel shows the analyser looking down on the plane in which the detectors lie. From Paschmann and Daly (1998).

speed, and so observe it essentially without aberration from the spacecraft velocity. Time series measured by spacecraft thus largely represent radial profiles of the advecting solar wind.

3.1.1 Characterising Plasma Populations

To fully describe properties of a plasma at a spacecraft's location, we must begin with measurements of individual particles. Measuring particle energies and trajectories allows for a velocity distribution to be constructed statistically. Further information can be obtained through measuring particle charge and mass; critical to identify particle species for composition measurements. The way in which these parameters are measured by different spacecraft is described in Section 3.2. Once a velocity distribution has been obtained, moments can be calculated by converting moment equations (e.g., Equations 1.15a–1.15c) from continuous integrals into discrete summations.

Electrostatic Analysers

Electrostatic analysers are a type of particle detector. Here we describe a particular class of electrostatic analyser; top hat analysers. Top hat analysers function by selectively measuring particles within a given energy range. They also determine particle direction of motion at the sensor aperture, such that a 2 or 3-dimensional velocity distribution can be computed. A schematic of a top hat analyser is shown in Figure 3.1. The basic geometry of the analyser consists of two nested hemispheric plates, with a 'top hat' aperture, which allows particles of approximately tangential velocity to enter through the top, as in the upper panel of the figure. Particles can thus enter the detector from 360° in the detector plane, which is shown in the top-down view of the lower panel of the figure, and are then deflected by an applied electric field between the plates. The field strength is tuned such that particles which are outside of the desired energy-per-charge (E/q) range collide with the walls of the instrument, while those within the desired range are able to pass exactly between them. Those which pass through the instrument reach a detector and are counted.

Detector surfaces are arranged in a circular fashion, shown on the bottom panel of the figure, such that particle incident angle is recorded in an angular bin, based on which detector it strikes. To measure a particle distribution, the deflecting electric field strength is varied with time, allowing particles in different energy ranges to be measured. A counts vs. (E/q) distribution for multiple arrival directions is thus built up. Knowing, or assuming, the species which is being measured, this distribution can be converted into a VDF for that species. To complement the top hat analyser and produce a full-sky 3-dimensional velocity distribution, spacecraft mounted with these instruments often spin. This changes the range of allowed incident angles with time, such that a near-4π coverage is obtained.

Faraday Cups

Another type of particle detector is the Faraday cup. Faraday cups are relatively simple particle instruments which collect and count charged particles over a wide solid angle. Particle energy is determined through a modulating potential, allowing entrance of particles of only a select energy in time.

3.1.2 Spacecraft Charging

Spacecraft charging describes the phenomenon whereby there is a charge imbalance across all, or part, of a spacecraft. The spacecraft potential, Φ, describes the electrostatic potential of the spacecraft. This is one value, assuming uniform charge distribution, or a complicated function if there is differential charging. Differential charging occurs in the case of a non-conductive spacecraft.

In the solar wind, photoionisation by solar ultraviolet (UV) radiation is the dominant process by which spacecraft become charged. This leads to typical positive spacecraft potentials of $\sim$ 10–15 V (Lavraud and Larson, 2016). The UV flux on a spacecraft at a fixed heliocentric distance is relatively constant, and so the potential itself is most sensitive to the ambient plasma density and temperatures.

A non-zero Φ deflects charged particles, changing their properties as measured by the spacecraft, or preventing them from being measured at all. Positive spacecraft potentials, typical in the solar wind, accelerate electrons towards the spacecraft, and decelerate ions. Energies of detected ambient electrons are thus uniformly increased by $q\Phi$.

Correcting electron distributions for spacecraft charging requires some estimate of the spacecraft potential. This can be obtained from an electric field instrument, if one is present on the spacecraft. If not, then estimates can be made through more sophisticated means, by examining features of the particle distributions themselves

(see Lavraud and Larson, 2016, and references therein).

3.1.3 Measuring Electromagnetic Fields

Also crucial to understanding the solar wind environment are *in situ* measurements of the electromagnetic fields by spacecraft. Magnetic field data are important for to understand particle distributions, due to e.g., anisotropies which align with the field.

Fluxgate Magnetometers

Fluxgate magnetometers are commonly used for measuring magnetic fields in space plasmas. They typically consist of three orthogonally mounted "fluxgates", each measuring the magnetic field in a single direction. To reliably measure the interplanetary magnetic field, instead of that generated by the spacecraft, magnetometers are usually mounted on the ends of long booms.

A fluxgate consists of a pair of coils wrapped around a magnetically-permeable ring core. The coils are wrapped such that the first (coil 1) generates a magnetic field in the core, which stands to induce a current in the second (coil 2) which is wrapped around it. The winding of the second coil is normal to the direction of the external field being measured. An alternating current is driven in coil 1, inducing oppositely-directed magnetic fields in the two halves of the core. With no external field, the induced field in the two sides of the core are equal and opposite throughout the entire cycle (they are driven in and out of saturation at the same time) and so the current in coil 2 is identical to the input current in coil 1. With an external field, the core-half in which the induced field is aligned with the external field is driven into saturation more rapidly than the core-half in which the induced field is in opposition. A non-cancelling magnetic field therefore exists when either coil-half is not in saturation, and so a variable current is thus induced in coil 2 which is

different from that in coil 1. The strength and phase of this difference depends on the external field's strength and polarity.

3.2 *In Situ* Plasma Missions

In this section we give information on the spacecraft from which *in situ* plasma measurements are obtained for this thesis. All *in situ* data are publicly available from NASA's Space Physics Data Facility (SPDF) maintained by the Heliophysics Science Division at Goddard Space Flight Center. The data can be acquired from the repository at `https://cdaweb.sci.gsfc.nasa.gov`.

3.2.1 The Wind Spacecraft

Wind is a NASA mission (Ogilvie and Desch, 1997) launched in 1994 with the primary aim of measuring the near-Earth solar wind. The spacecraft initially had a variable orbit, measuring the magnetosphere and the near-lunar environment, as well as the solar wind. From 2004 until the time of writing, Wind has orbited the 1st Lagrangian point (L1) and measures the solar wind continuously. The spacecraft spins with a period of 3 s in approximately the ecliptic plane.

Wind carries a suite of instruments which measure gamma rays, electromagnetic fields, plasma waves, and charged particles. Below we list the instruments on Wind which were used in the research for this thesis.

MFI

The Magnetic Fields Investigation (MFI) measures the interplanetary magnetic field (Lepping et al., 1995). It consists of a pair of fluxgate magnetometers, each mounted on booms on opposite sides of the spacecraft. Public vector magnetic field data is available at $\sim$ 0.09-s, 3-s, 1-min, and 1-hour resolution.

3DP

The 3-Dimensional Plasma Analyser (3DP) instrument on WIND measures 3-dimensional distributions of electrons and protons using 4 electrostatic analysers (2 per species, collectively covering 3 eV–30 keV), and 2 solid state telescopes which measure electron energies up to 400 keV and protons up to 6 MeV (Lin et al., 1995). Studies in this thesis employ only electron measurements, and at energies where only the electrostatic analysers are required.

The two electron electrostatic analysers, EESA-L and EESA-H, are top hat analysers which measure electrons at low (5–1100 eV, EESA-L) and high (100 eV–30 keV, EESA-H) energies. EESA-L has a 180° field-of-view in one plane, while EESA-H has 360°. As a result, EESA-L sweeps the full sky every spacecraft spin, while EESA-H does so every half-spin. The analysers sweep through their respective energy ranges in 32 or 64 energy steps (mode-dependent) and each energy is measured with a resolution of $\Delta E/E \sim 0.3$.

EESA-L and EESA-H data are also publicly available in the form of 2-dimensional pitch angle distributions, which have been computed from the full-sky measurements above, in combination with MFI magnetic field data. Pitch angle distributions consist of differential number flux measurements (in units $\mathrm{cm^{-2}\,sr^{-1}\,eV^{-1}\,s^{-1}}$) at 8 pitch angles. The angles change depending on the magnetic field direction, but typical values are ∼15°, 35°, 57°, 80°, 102°, 123°, 145°, and 165°. The pitch angle data are available at ∼ 24-s time resolution.

SWE

The Solar Wind Experiment (SWE) measures solar wind electrons and ions using a suite of sensors (Ogilvie et al., 1995). The sensor suite consists of a pair of Faraday cups, a vector electron and ion spectrometer, and a special strahl sensor. In this

thesis, only solar wind ion moments derived from the Faraday cups are employed.

SWE Faraday cups observe in a cone of half-angle 60°. The two cups are placed on the top and bottom of the spacecraft, on opposite sides, such that as it rotates a 3-dimensional scan is performed. The wide acceptance angle allows the Faraday cups to perform a full scan in 1 s, which is faster than a rotation period.

Ion moments are publicly available from the SWE Faraday cup at 92-s resolution. These moments include proton and alpha number densities, 3-dimensional velocities, and parallel and perpendicular temperatures.

3.2.2 The ACE Spacecraft

The Advanced Composition Explorer (ACE) is a NASA mission which measures the solar wind (Stone et al., 1998). Launched in 1997, its primary objective was to measure the composition of energetic particles in the heliosphere. ACE is still in operation at the time of writing.

ACE orbits L1 allowing it to measure solar wind directly upstream of the Earth. The spacecraft spins with a period of 12 s to assist in the angular coverage of its plasma instruments. The spin axis is approximately aligned with the sunward direction.

Magnetic Fields Experiment

The ACE Magnetic Fields Experiment (Smith et al., 1998) consists of a pair of flux-gate magnetometers which are located on the ends of booms, mounted on opposite solar panels. Each of these measures the interplanetary magnetic field. Publicly available data include magnetic field vectors on time resolutions ranging from 1-s to 1-hour.

SWEPAM

The Solar Wind Electron Proton and Alpha Monitor (SWEPAM) is designed to measure bulk solar wind conditions from the three most common solar wind particle species (McComas et al., 1998). Electrons and ions are measured separately with two spherical-section electrostatic analysers. These analysers operate with similar principles to the top hat style analysers described previously, but are not designed to measure 360° of planar coverage simultaneously.

The ion electrostatic analyser (SWEPAM-I) produces full, 3-dimensional, proton and alpha plasma measurements every 64 s. Publicly available data include bulk solar wind velocity, proton number density, and proton temperature, at either 64 s or 1 hour resolution. Electron measurements from SWEPAM-E are not used in this thesis.

SWICS

The Solar Wind Ion Composition Spectrometer (SWICS) measures energy, mass and charge of common solar wind ions with masses ranging from H to Fe; determining their ionisation, isotopic states, and other properties (Gloeckler et al., 1998). ACE-SWICS is the flight spare of the SWICS instrument on the Ulysses spacecraft (Gloeckler et al., 1992).

The instrument functions by collimating incident particles which are then selected by energy over mass ratio (E/q) using a deflecting electrostatic field (as for electrostatic analysers). Ions are then accelerated using a potential drop of $\sim 30\,\mathrm{kV}$. Following this acceleration, the ions enter a time-of-flight system which measures their velocity. The ions then strike a solid state detector which measures their kinetic energy. These measurements provide sufficient information to solve for the input ions' mass, charge and energy.

SWICS sweeps its electrostatic field over a period of $\sim 13\,\mathrm{min}$, through an E/q range of $0.11\text{–}66.7\,\mathrm{keV\,Q^{-1}}$. Publicly available data take the form of compositional and plasma properties, the former being of primary interest in this thesis. For the period 1998–2011, available data include charge state ratios O^{7+}/O^{6+}, C^{6+}/C^{4+}, C^{6+}/C^{5+}; iron relative abundance Fe/O; and average charge states $\langle Q(Fe)\rangle$, $\langle Q(Si)\rangle$, $\langle Q(Mg)\rangle$, $\langle Q(C)\rangle$ at 1-hour time resolution. The same period includes abundances C/O, He/O, Ne/O, and full charge state distributions for C, O, Ne, Mg, Si, and Fe at 2-hour resolution. 12-min resolution data are reportedly available from the SWICS team, but not used here, as they are subject to greater uncertainty from counting statistics. For the period 2012–present, a more limited set of parameters is available from SWICS as a result of hardware degradation. These include C^{6+}/C^{5+}, O^{7+}/O^{6+}, O^{8+}/O^{6+}, $\langle Q(Fe)\rangle$, and Fe/O on 2-hour time resolution.

3.3 Remote Sensing Solar Observations

Chapters 5, and particularly 6, make use of remotely sensed solar observations, in combination with *in situ* measurements of the type described above. In this section we introduce the missions which provide these remote sensing observations. First, however, we describe some techniques through which coronal properties may be inferred from such observations.

3.3.1 Inferring Plasma Properties in the Corona

In Sections 1.1.10 and 1.2.2 of Chapter 1 we discussed plasma emission from the corona. The combined emission of all material from the photosphere-upwards results in a solar spectrum. The spectrum consists of a continuum, over which emission and absorption lines are superposed. Coronal emission is primarily in EUV, and is dominated by the emission lines of select elements. Analysis of detailed

measurements of these lines can reveal properties of the plasma.

The LOS bulk velocity of the emitting plasma can be inferred from the Doppler shift of the emission line. The velocity can be calculated from the expression

$$f = f_0\left(1 + \frac{v}{c}\right) \tag{3.1}$$

where f_0 is the (known) unshifted frequency, f is the observed frequency, v is the LOS velocity of the material and c is the speed of light.

Emission lines are broadened by many factors, including LOS velocities which are not part of the bulk. LOS velocities include thermal motions, where the velocity distribution leads to a distribution of frequencies of the emission about the central frequency. The temperature of the emitting ions is thus related to the width of the line. Temperature can be estimated independently from line width (if it is assumed that ions and electrons are in thermal equilibrium) by measuring the relative intensities of spectral lines (see Sections 1.1.9 and 1.1.10) to provide an electron temperature, T_e.

Typically, measured line widths suggest an ion temperature, T_o, which is greater than T_e; the lines are broader than expected. One source of excess broadening is non-thermal velocity ($v_{\rm nt}$). This is additional motion of the plasma, which is neither bulk nor thermal in nature. $v_{\rm nt}$ is any motion beyond that which is explained by T_e:

$$v_{\rm nt} = [2k_B(T_o - T_e)/m_i]^{1/2} \tag{3.2}$$

where k_B is the Boltzmann constant, and m_i is the mass of the emitting ion. Non-thermal motions might include wave activity and plasma turbulence. Flows which are on subpixel scales for a given instrument, and thus become integrated together into the line profile, also contribute to $v_{\rm nt}$. Enhancements and fluctuations in $v_{\rm nt}$

have also been linked to motions associated with reconnection events (Harra et al., 2001).

In Section 1.1.10 we noted that line intensity is proportional to the density of electrons, and the abundance of the associated ion, integrated along the line of sight. The relative abundance of an ion can thus be inferred from the intensity ratio of a pair of lines, usually with some correction factor for each ion's efficiency of radiation.

3.4 Solar Remote Sensing Missions

In this section we describe the missions from which remote sensing data are obtained for use in this thesis. These data are all publicly available from different sources which are listed as required.

3.4.1 The Solar Dynamics Observatory

The Solar Dynamics Observatory (SDO) is a NASA mission launched in 2010 (Pesnell, 2015). SDO provides near-continuous observations of the Earth-facing corona and photosphere, which are enabled by the spacecraft's inclined-geosynchronous orbit. Below we describe the two instruments, AIA and HMI, from which data are obtained for this thesis, and the relevant data products. Both HMI and AIA data can be obtained from the Joint Science Operations Center (JSOC) through a range of means, including through procedures included in the SolarSoft IDL package.

The Atmospheric Imaging Assembly

The Atmospheric Imaging Assembly (AIA) instrument (Lemen et al., 2011) measures emission from the corona in EUV and UV wavelengths. It measures full-disk EUV in 7 bands centred on the lines Fe XVIII (94 Å), Fe VIII, XXI (131 Å), Fe IX (171 Å), Fe XII XXIV (193 Å), Fe XIV (211 Å), He II (304 Å), and Fe XVI

(335 Å). The EUV lines correspond to a range of emission temperatures 6×10^4 K–2×10^7 K. It also measures emission at additional wavelengths ~ 1600 Å, ~ 1700 Å, and ~ 4500 Å.

AIA consists of 4 Cassegrain telescopes, 3 of which are responsible for measuring 2 of the EUV bands each, while one measures the remaining EUV band and the 3 UV and visible bands. Exposures for each band last 0.5–3 s, resulting in a cadence of 10–12 s for the return of images in 8 bands (7 EUV + 1 UV or visible band). The CCD has 4096×4096 pixels, each corresponding to $0.6''$. However the resolution for the instrument is in fact $\sim 1.5''$, as a result of the optics.

The Helioseismic and Magnetic Imager

The Helioseismic and Magnetic Imager (HMI) measures the polarisation of the Fe I (617.3 nm) line (Scherrer et al., 2012; Schou et al., 2012). From this, line-of-sight (LOS) and vector magnetograms of the photospheric magnetic field can be produced by analysis of Zeeman splitting. HMI also measures Doppler motions to perform helioseismology studies. The magnetograms are of primary interest for this thesis.

HMI collects light through a refracting telescope. As with AIA, the image resolution of the HMI CCD is 4096×4096 pixels. Each pixel corresponds to an angular size of $\sim 0.5''$. The telescope is however diffraction-limited at $0.91''$. Polarisation information is obtained through a series of polarisers which are mounted on the optical bench. HMI provides full-disk Doppler, LOS magnetogram, and photospheric continuum images at 45 s resolution. Vector magnetograms are returned either every 90 or 135 s.

3.4.2 Hinode

The Hinode satellite (Kosugi et al., 2007) is a Japan Aerospace Exploration Agency (JAXA) mission launched in 2006. It is operated in collaboration with the National Astronomical Observatory of Japan (NAOJ), the UK Science and Technology Facilities Council (STFC), NASA, the European Space Agency (ESA) and the Norwegian Space Centre (NSC). The spacecraft carries three telescopes for solar observations; the X-Ray Telescope (XRT), Solar Optical Telescope (SOT) and Extreme Ultraviolet Imaging Spectrometer (EIS). EIS data are employed in Chapter 6 of this thesis and this instrument will now be introduced.

The Extreme Ultraviolet Imaging Spectrometer

EIS (Culhane et al., 2007) is an imaging spectrometer which measures spectra in the bands 170–210 Å and 250–290 Å. It was built by a consortium led by UCL/MSSL. Imaging spectrometers produce spectral images (images where each pixel has an associated spectrum) of a given field-of-view. They do this through a process known as "rastering". Spectra are obtained in a slice or "raster" using a thin slit. Imaging through the slit produces an image with one spatial (along the slit) and one spectral dimension. The slit is shifted stepwise along the desired FOV in a direction normal to its length, making a new raster at each position. The rasters are then combined side-by-side, producing a spectral image of the full FOV.

The rastering process requires exposure time for each raster, and also time to change slit positions (both on the order of seconds). The result is that spectral images typically require several minutes to build up. EIS uses 4 widths of slit ($1''$ and $4''$ slits, and larger $40''$ and $266''$ slots) to allow for longer or shorter exposure times. Using the slots, larger FOVs can be imaged at high-cadence, but at the expense of spatial resolution and some spectral purity.

The spectra obtained from EIS can be used to infer properties of the emitting chromospheric and coronal plasma. These include Doppler velocities, non-thermal velocities, temperatures and relative abundances (see Section 3.3.1). The data are publicly available to be browsed and obtained from the MSSL EIS archive (`http://solarb.mssl.ucl.ac.uk/SolarB/SearchArchive.jsp`).

3.4.3 Geostationary Operational Environmental Satellites

The Geostationary Operational Environmental Satellite (GOES) Programme comprises a series of satellites which largely perform Earth observations for meteorological purposes. A joint NASA and National Oceanic and Atmospheric Administration (NOAA) programme, the first GOES satellite was launched in 1975. The currently operational satellites are GOES-15 and GOES-16.

The GOES-XRS (X-ray Sensors) measure solar X-ray flux in bands of 0.5–4 Å and 1–8 Å. The latter band corresponds to that from which flares are classified (see Section 1.2.3). Each XRS consists of four apertures; two for each of the bands above. For each band, one aperture is large (81 mm^2) and designed for maximum sensitivity, while the other is small (4.5 mm^2) and is designed to measure flares. The apertures open into cavities, at the end of which photodiodes measure the X-ray photons.

GOES X-ray data are available as continuous flux measurements, or alternatively as a flare list. This list includes flare time, classification, and attributed active region - if available. It can be found in the NOAA repository at `https://www.ngdc.noaa.gov/stp/space-weather/`. The GOES flare list is used to examine active region activity in Chapter 6.

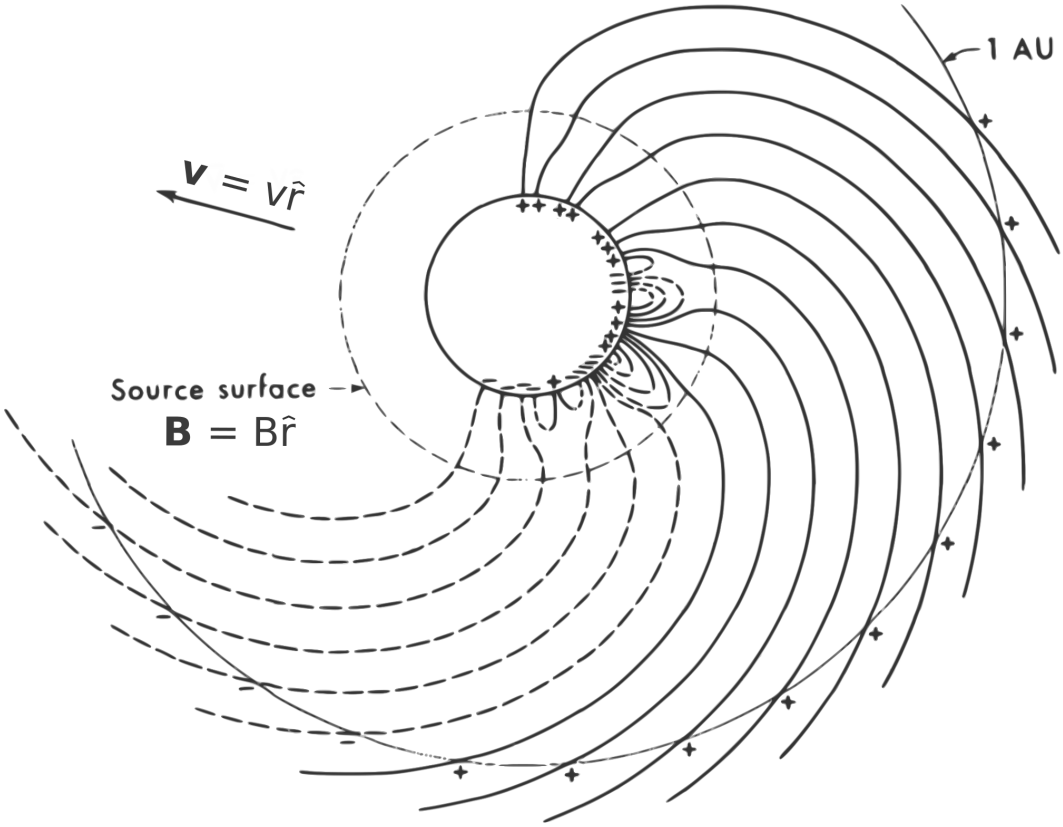

Figure 3.2: A schematic of PFSS model magnetic field lines adapted from Schatten et al. (1969). The Sun and heliosphere is viewed from the ecliptic north pole, and field lines in the ecliptic plane are drawn from the photosphere, through the source surface, to beyond 1 au. Magnetic field lines which reach the source surface are constrained to be radial at that height, and beyond it follow the Parker spiral.

3.5 Potential Field Source Surface Models

Unlike the photosphere, the optically thin nature of the corona renders remote sensing measurements of its magnetic field impossible. Instead, if we wish to estimate the coronal magnetic field, modelling must be employed. In Chapters 5 and 6 we require information on the coronal magnetic field, and so we use one particular class of model; the potential field source surface (PFSS) model. In this section we discuss the theory and application of these models, as well as their advantages and drawbacks in describing the coronal field.

PFSS models were first employed to describe the coronal magnetic field by Schatten

et al. (1969), whose schematic we adapt to illustrate the model in Figure 3.2. They model the field between a pair of spherical shell boundaries. The inner boundary is at the photosphere, where the field can be defined observationally using magnetogram data. The outer boundary is located at a theoretical "source surface". The model assumes that the magnetic field between the photosphere and source surface is dominant over the plasma (low β), and thus modelling plasma parameters becomes unnecessary. Above the source surface, the assumption changes to the plasma dominating over the field (high β). A further critical assumption is that all magnetic field is constrained to be radial at the source surface, since the expanding solar wind drags the field outwards. Magnetic field lines which do not close before reaching the source surface height are presumed to be open to the heliosphere, and so beyond the source surface follow a Parker spiral configuration. The radius of the source surface, R_{ss}, is a free parameter of the model. While Schatten et al. (1969) employed a source surface radius of $R_{ss} = 1.6\,R_{\odot}$, contemporary studies typically choose a radius of 2.5–3.25 $R_{\odot}$ (e.g., Riley et al., 2006). This choice of radius is very influential over the resulting modelled field, as it determines the amount of open flux; lower source surface heights lead to more field lines which are open. The optimal range 2.5–3.25 $R_{\odot}$ has in fact been verified through maximising the agreement between *in situ* measurements and PFSS-modelled open flux (e.g., Hoeksema et al., 1983).

PFSS models also assume the current-free assumption. For a current-free field, $\mathbf{J} = 0$. If displacement current from Equation 1.1d is also neglected, we produce $\nabla \times \mathbf{B} = 0$. It follows that $\mathbf{B}$ can then be described as the gradient of a scalar potential field: $\mathbf{B} = -\nabla\phi$, and from Equation 1.1b:

$$\nabla^2 \phi = 0 \tag{3.3}$$

Equation 3.3 can be solved numerically using boundary conditions such as those

above. Doing so results in a unique global coronal magnetic field solution, which represents the minimum energy state for the magnetic field configuration between the two boundaries.

PFSS Limitations

A magnetic field model produced through PFSS assumptions is limited in the structures and processes it can describe. Since the field can carry no currents, and represents the minimum energy state, reconnection processes cannot be modelled. The modelled field can however be used to identify QSLs, as in e.g., van Driel-Gesztelyi et al. (2012). Further, magnetically complex regions, such as active regions, where the twisting of magnetic field leads to the storage of energy, cannot be fully described (Wiegelmann and Sakurai, 2012).

PFSS models cannot include realistic time-evolution of the coronal field since they represent the minimum energy configuration. Time-dependent effects resulting from e.g., plasma motions or flux emergence at the photospheric inner boundary will simply result in the non-realistic, instantaneous, shifting of the field to the new lowest-energy state.

Defining the Inner Boundary

A global estimate of photospheric magnetic flux is required to provide an inner boundary for a global PFSS model. However, at present, all available observations of the photospheric field are approximately along the Earth-Sun line. These observations must be propagated through time to produce maps of the photospheric field across the entire solar surface. Such maps are known as synoptic magnetograms. Most simply, they can be produced by combining the central meridian sections of consecutive magnetograms over an entire Carrington rotation. Synoptic magnetograms constructed in this way using SDO-HMI data are available from

the Joint Science Operations Center (JSOC, `http://hmi.stanford.edu/data/synoptic.html`). These magnetograms make no attempt to account for evolution of the photospheric magnetic flux over the course of a Carrington rotation. More sophisticated approaches make an effort to do so through the use of flux transport models (Schrijver and DeRosa, 2003; Arge et al., 2010). These models allow the unobserved photospheric flux to evolve through a range of processes while still incorporating the most up-to-date observations.

Testing PFSS Model Outputs

Testing the accuracy of PFSS model outputs is not trivial, since the coronal magnetic field cannot be directly observed. Schatten et al. (1969); Wang and Sheeley Jr (1995) and others have found favourable comparisons between *in situ* measured magnetic flux, and PFSS model open flux. We note that as these tests only consider the open flux, they can not speak to the accuracy of the configuration of any closed loops. Riley et al. (2006) compare a range of properties of a magnetic field resulting from a PFSS approach to those resulting from a more complex MHD model. They find that the PFSS model performs reasonably, so long as it is restricted to describing the large-scale corona, during periods when temporal changes in photospheric flux are negligible. When comparing the magnetic field associated with an active region, however, they find that many features present in the MHD model do not appear using PFSS.

Despite the intrinsic limitations for PFSS approaches to fully describe the coronal magnetic field, they are nevertheless widely applied by the community. This is a result of the relatively-low computational resources needed to produce a global model, and the simplicity of the assumptions involved. We now outline one particular application of PFSS models; describing the global coronal magnetic field to identify solar wind source regions as part of a mapping procedure used in this

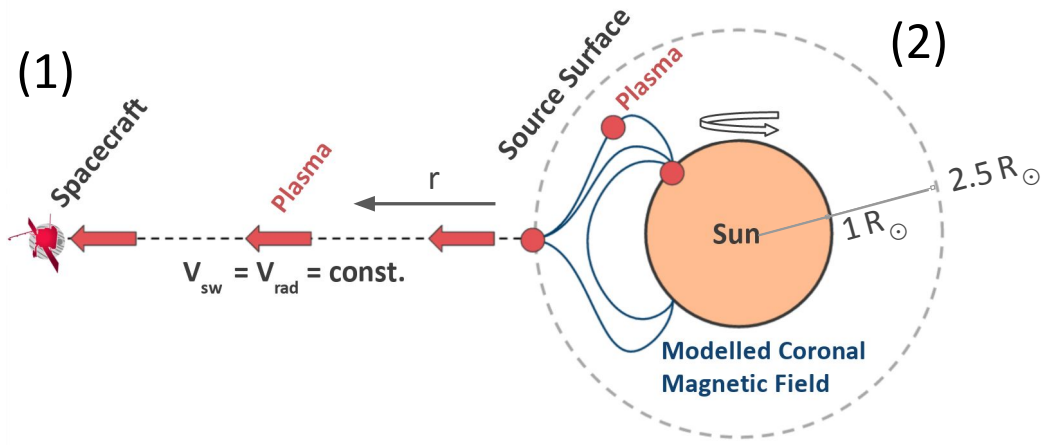

Figure 3.3: Schematic of the outwards solar wind propagation which is assumed in the 2-step backmapping procedure. Solar wind observed *in situ* is traced back from the spacecraft to a coordinate at the source surface. Below the source surface, a small number of coronal magnetic field lines are drawn, to illustrate the closing down of field below the source surface, and the opening of field lines which reach it. Corotation is assumed in this region. From its mapped source surface coordinate, the plasma is then traced back along the nearest open field line to 1 $R_{\odot}$.

thesis.

3.6 The Two-Step Backmapping Procedure

In Chapters 5 and 6 we describe analysis results in which we trace solar wind measured at L1 back to the Sun, so that we may combine both *in situ* and remote sensing measurements to identify its origins. We apply the two-step backmapping method (also called ballistic backmapping) to accomplish this. A schematic of the assumed solar wind propagation for the technique is shown in Figure 3.3. By first assuming a constant, radial solar wind propagation, the procedure maps solar wind plasma back to the source surface radius of a PFSS magnetic field model. It then maps to the photosphere or low-corona by tracing the path of the plasma along open field lines produced by the model (details in Section 3.5) on the basis of a concurrent magnetogram. The mapped source location at the photosphere thus corresponds to the magnetic footpoint of the solar wind plasma measured *in situ*, barring the occurrence of reconnection during solar wind propagation. In the literature, these

locations are often referred to as solar wind 'footpoints'. To distinguish these from the footpoints of the coronal magnetic field in general, and to account for the possibility of reconnection, in this thesis we instead describe these locations as solar wind 'sourcepoints'. This technique has been used by a range of authors (e.g., Neugebauer et al., 1998; Zhao et al., 2009; Ko et al., 2014; Culhane et al., 2014; Fu et al., 2015; Fazakerley et al., 2016; Heidrich-Meisner et al., 2016) and is commonly applied to produce mapped solar wind sourcepoint locations at the photosphere with relatively low computational requirements. In this section we shall describe the implementation of the backmapping technique, as applied in the studies contained in this thesis, in detail.

3.6.1 Ballistic Solar Wind

We perform ballistic constant-velocity backmapping to convert from *in situ* data as a function of time at ACE, located at L1 (heliocentric distance ~ 1 au), to a function of Carrington heliographic latitude and longitude at the source surface at $2.5\,R_\odot$. The ballistic portion of this mapping was first employed by Nolte and Roelof (1973). Beginning from heliographic latitude, θ_{sc}, and longitude, ϕ_{sc}, coordinates of the spacecraft at the measurement time, we use the Sun's sidereal rotation rate to calculate the longitude coordinate at r_0, the distance at which the solar wind plasma was released.

$$\phi_{r0} = \phi_{sc} + \Delta\phi \tag{3.4}$$

As Carrington longitude decreases with time, this expression ensures $\phi_{r0} > \phi_{sc}$. We define $\Delta\phi$ as:

$$\Delta\phi = \Omega_\odot \Delta t \tag{3.5}$$

$\Omega_\odot$ is the solar sidereal angular rotation rate; $\Omega_\odot = 2\pi/T_\odot$, where $T_\odot = 25.38$ days is the sidereal rotation period. Δt is the solar wind travel time from the hypothetical location at which the solar wind plasma transitions from full-corotation to no coro-

tation. r_0 is the "release radius" of the solar wind, as below this point plasma is held at the longitude of its source. For our purposes, r_0 is taken to be the source surface radius, as below the source surface we assume that the plasma follows the coronal magnetic field, and so rotates rigidly with the corona. Thus $r_0 = r_{ss} = 2.5\,\mathrm{R}_\odot$ and so $\phi_{r0} = \phi_{ss}$. In the study by Nolte and Roelof (1973), r_0 was taken to be the low corona, as they did not make use of a coronal magnetic field model.

The standard two-step mapping procedure assumes that the solar wind propagates between r_0 and the spacecraft (located at r_{sc}) at a constant velocity v_{sc}; that measured at the spacecraft. We define the time lag Δt_c as the time for this propagation:

$$\Delta t_c = \frac{\Delta r}{v_{\mathrm{sc}}} = \frac{r_{\mathrm{sc}} - r_0}{v_{\mathrm{L1}}} \tag{3.6}$$

It is assumed that the solar wind propagates radially above r_0, and so changes in Carrington latitude for the backmapping need not be considered. Figure 3.4 shows the results of applying this ballistic technique to a portion of solar wind studied in Chapter 5. The *in situ* measured velocities are shown as a function of heliographic longitude at L1 in the top panel, and at the source surface in the bottom panel. All velocity features map to a greater longitude at the source surface than that which they appear at *in situ*, but to different degrees depending on the solar wind speed. This leads to a warping of many features, as seen in the figure, in which the longitude shift of select features are indicated with arrows.

Arguably the most crucial effect which warps the *in situ* features is that, in rarefactions, faster solar wind streams overlap with slower streams in ϕ_{ss}. This occurs since the method does not account for stream interactions, and so cannot represent the acceleration and deceleration processes which take place in rarefactions (see Chapter 1, Section 1.3.4). Regions where this overlap has occurred are often referred to as "dwells". Such a dwell is labelled in Figure 3.4.

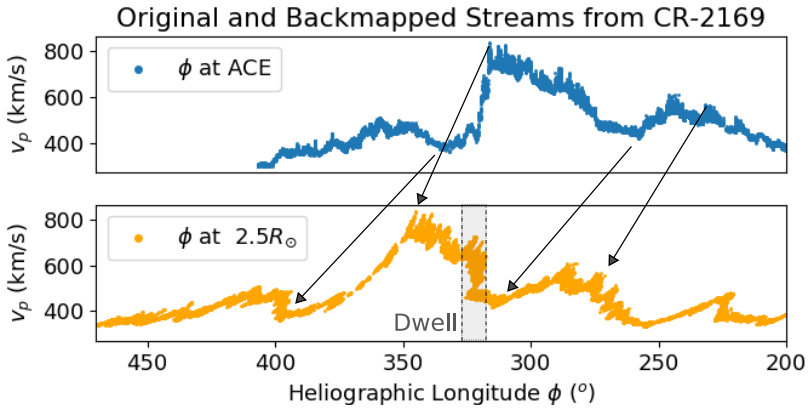

Figure 3.4: Plot of velocity against heliographic longitude for a solar wind stream before and after backmapping to 2.5 $R_\odot$. Longitude decreases from left to right as this orients the data in the same manner as a time series. As the data spans two Carrington rotations, we extend the longitude above 360°. An example of a dwell is labelled for the mapped data. Arrows show indicate the change in longitude for select features of the stream between ACE and 2.5 $R_\odot$.

As detailed by Nolte and Roelof (1973), the validity of the constant velocity approximation also hinges on the key assumption that the error in mapping caused by neglecting solar wind acceleration (e.g., such as that predicted by the model of Parker, 1957) cancels with the error from also disregarding corotation of the plasma beyond the photosphere (at distances where we expect the coronal magnetic field still dominates over the plasma flow). In comparison with the "true" connection longitude, neglecting the former shifts the mapped measurements to lower ϕ_{ss}, as it decreases ballistic propagation time. This is because interplanetary acceleration causes the solar wind's average speed over its propagation to the spacecraft, $\bar{v}$, to be less than that measured by the spacecraft: $\bar{v} < v_{sc}$. Meanwhile, neglecting the latter shifts the mapped measurements to higher ϕ_{ss}, as the distance travelled by the plasma without being "locked" to its source region longitude by corotation is greater, leading to a longer effective propagation time. The cancellation of these two errors results in an error estimate for this method derived by Nolte and Roelof (1973) of $\leq 10°$ longitude.

If the two offsets to ϕ_{ss} do not cancel as described above, then the Nolte and Roelof

(1973) estimate of error ceases to be valid. The estimate is derived by assuming a solar wind acceleration profile which is an approximation by Burlaga (1967) to the Parker (1958) model:

$$v(r) = Kr^{1/4} \tag{3.7}$$

where r is heliocentric distance, $v(r)$ is the solar wind bulk velocity, and K is a constant. Further, they estimate that corotation should cease at heliocentric distances of 0.1–0.25 au. Given this, and the acceleration profile of Equation 3.7, the majority of solar wind acceleration is expected to occur before corotation ends. Neugebauer et al. (1998) meanwhile, estimate that corotation of the solar wind should drop off at distances in the range 2.5–3.25 $R_\odot$, as is the PFSS model assumption, which would mean that significant acceleration of the wind in fact occurs after corotation has stopped. This is supported by their results from applying the backmapping technique, in which they find a systematic increase (westward shift) in ϕ_{ss} is necessary to align the *in situ* measured polarity of solar wind with that of PFSS open magnetic flux. This longitude shift is equivalent to an increase in travel time Δt.

In Chapter 5 we test whether increasing Δt improves the accuracy of the mapping. Given the results of Neugebauer et al. (1998), there is a reasonable expectation that this may be the case. We calculate a new travel time, Δt_a, based on the travel time applicable to a solar wind accelerating under Equation 3.7. Nolte and Roelof (1973) derive this time for plasma following this acceleration profile from $r = 0$ to $r = r_{sc}$:

$$\Delta t_a = \frac{4 r_{sc}}{3 v(r = r_{sc})} \approx \frac{4}{3} \Delta t_c \tag{3.8}$$

We note that the resulting solar wind travel time under this acceleration is simply a factor of Δt_c.

3.6.2 Application of the PFSS Model

We use the PFSS software available with the Solarsoft IDL package from Lockheed Martin Solar and Astrophysics Lab (LMSAL) to obtain and interpret models of the coronal magnetic field. This package can be used to download and extract data from pre-computed PFSS models from the LMSAL Forecaster (found at `http://www.lmsal.com/forecast`). The software calculates magnetic field lines from the outputs of these models. The models in question are computed from synoptic maps of photospheric flux which are produced by combining LOS magnetogram data from SDO-HMI with a flux transport model (for details on this, see Schrijver and DeRosa, 2003). The source surface of these models is located at $2.5\,R_\odot$.

We use the PFSS model to identify the source coordinates, at $1\,R_\odot$, of plasma which we have traced from ACE to $2.5\,R_\odot$. This is shown as the 2nd step in Figure 3.3; given θ_{ss} and ϕ_{ss} coordinates at a given time at the source surface, we follow open field lines from the PFSS model down to a latitude and longitude at the photosphere: $\theta_{\rm ph}$ and $\phi_{\rm ph}$. The PFSS model assumption is that the field must be open and radial at the source surface of $2.5\,R_\odot$, and no regions on the surface may exist in a "vacuum" with no field. Thus, any [θ_{ss}, ϕ_{ss}] coordinate on the surface will have a valid [θ_{ph}, $\phi_{\rm ph}$] to which it is related. There is thus no need to interpolate our coordinates onto some nearest-open-flux location at the source surface, beyond the interpolation onto the grid of the model.

The PFSS models are updated at 6-hour intervals to incorporate the newest synoptic magnetograms at their inner boundary. For each *in situ* data point, we employ the PFSS model which uses the photospheric flux map closest in time to its backmapped release time from the Sun.

We do not include any time-lag for plasma to move along the PFSS field line between the photosphere and the source surface. Under the corotation assumption,

plasma in the corona is dominated by the magnetic field, and thus in the backmapping process its final mapped source region from $2.5\,R_\odot$ is entirely described by the magnetic topology in the corona, and is not dependent on the time taken to travel from 1 to $2.5\,R_\odot$. Further, we assume that for steady solar wind sources, such as the coronal holes which we are primarily interested in for Chapters 5 and 6, their evolution in the corona is slow enough that their magnetic connectivity should not change significantly over the time taken for plasma to traverse this distance.

3.6.3 Limitations of the Technique

Some limitations associated with the two-step backmapping technique are as follows. The first is the occurrence of dwells, as described in Section 3.6.1. Two or more *in situ* solar wind measurements which map to dwells at the source surface can not be separated from each other when mapping is then extended down to the photosphere. Dwells are a key issue in the results of both Chapters 5 and 6 as both studies focus on the solar wind in rarefactions. We shall address their impacts in the discussion sections of these chapters.

Second, a quantification of uncertainty in mapped sourcepoint location is difficult to produce. As described previously, the $\pm 10^\circ$ error in ϕ_{ss} derived by Nolte and Roelof (1973) does not necessarily appear to hold true. Further, the translation of this uncertainty in ϕ_{ss} to $\phi_{\rm ph}$ depends strictly on the magnetic topology produced by the PFSS model. The expansion of field lines between 1 and $2.5\,R_\odot$ means that separations of a few degrees on the source surface might result in separations of many tens of degrees at the photosphere, after tracing down the field lines. Equally, they may also result in separations which are very small. Qualitatively, we expect the errors in $\phi_{\rm ph}$ (and $\theta_{\rm ph}$) to be greatest when the mapped region at the source surface is near a boundary which separates two distinct regions of open flux at the photosphere. This is an inescapable issue for any attempts at source region

identification, as the expansion of magnetic field lines is a real phenomenon in the coronal magnetic field.

Finally, the potential field approximation cannot fully describe the magnetic field configuration as it exists in the corona. The PFSS field is calculated based only on the most up-to-date photospheric magnetic flux map and the field is assumed to relax into the lowest energy state available given these boundary conditions. As a result, the PFSS has no "memory" of its previous states (each output is only a function of the current input data). Without including time-dependence (e.g., in a model which allows for currents to facilitate the field evolving realistically) the effects of footpoint motion (important in Chapter 5 and in e.g., Schwadron and McComas, 2005; Schwadron et al., 2005) cannot be accounted for, as there is no scope for continuity of the field with time. In addition, the effects of reconnection (important in Chapter 6) cannot be modelled directly in a PFSS framework beyond identification of QSLs.

We find that the open flux topology of the corona can change quite noticeably over the 6 hour period between PFSS model runs. At times this results in some consecutive data points mapping to source regions many tens of degrees apart at $1\,R_{\odot}$. This sensitivity illustrates the importance of updating the PFSS model as often as possible, but also implies that errors in ϕ_{ss} and θ_{ss} from the ballistic mapping could have significant knock-on effects on ϕ_{ph} and θ_{ph}.

Chapter 4

How Coronal are Solar Wind Suprathermal Electrons?

This chapter is based on the published work "Tests for coronal electron temperature signatures in suprathermal electron populations at 1 au", Macneil et al. (2017).

4.1 Introduction

Solar wind plasma populations leaving the Sun can be expected to have properties that reflect conditions of their source regions. However during the course of the wind's propagation out to 1 au and beyond, internal dynamic processes may develop within the solar wind plasma. These cause many of the solar wind properties to be altered to the extent that the signatures of their solar source, including proton temperature (Freeman, 1988) and bulk speed (Schwenn, 1990), are no longer clear. Thus solar wind *in situ* properties which do retain signatures of their coronal source are invaluable when attempting to understand the origins of the solar wind. One such property is described in Chapter 1; the degree of ionisation of heavy ion species in the solar wind provides a well-established means by which the temperature of its coronal source may be inferred, even when observed at 1 au (Hundhausen et al.,

1968a). In this chapter, we consider another possible source region signature which may be present in suprathermal solar wind electrons at 1 au.

In Section 2.3 we described the ongoing research into the coronal origins and heliospheric evolution of halo and strahl electron populations. To summarise, there is evidence that solar wind suprathermal electron populations have their origins in the corona. In particular, Che and Goldstein (2014) model the formation of paired electron core and halo populations, where the core electron temperature T_c is proportional to the halo temperature T_h. Studies by Maksimovic et al. (2005); Owens et al. (2008); Stverak et al. (2009); Seough et al. (2015) suggest that the halo and strahl are of the same origins. Specifically, the strahl forms initially through adiabatic focusing of the halo, and then scattering processes maintain the two populations (Section 2.3.1); the seed population for both is the coronal halo. Temporarily ignoring scattering, the formation of a strahl population through adiabatic focusing would preserve the initial relationship between T_c and the energy content of the suprathermal electrons described above, due to conservation of energy. Scattering processes may erode this relationship to varying degrees, depending on the processes themselves, and the frequency of events. On the basis of these studies, one could expect that, directly above the region of solar wind formation, a clear relationship between the energy content of the suprathermal electrons and heavy ion charge states might exist. The low-collisional nature of suprathermal electrons in the solar wind suggests the possibility that they may retain these coronal signatures, and therefore a relationship with the ions, out to 1 au. Indeed, a study by Hefti et al. (1999) showed limited examples in which this relationship held, but this has not yet been tested to confirm this is generally the case. The field-aligned strahl electrons may be most likely to retain such coronal information, as their far more rapid propagation through the heliosphere should subject them to less scattering (e.g., Owens et al., 2008).

In this study, we attempt to examine the possible preservation of a coronal electron temperature signature in suprathermal electrons (both halo and strahl) at 1 au by evaluating their possible relationship with charge states of heavy ions sampled contemporaneously at L1. We first attempt this by addressing limitations of the Hefti et al. (1999) method by fitting the entire core and halo/strahl range of energies using a Maxwellian+kappa fit, and compare parameters drawn from these fits to the O^{7+}/O^{6+} charge state ratio. Further, we isolate the strahl portion of the electron distribution, and take partial moments of these to test for any relationship of the strahl at 1 au with the electron temperature of its source. We use the suprathermal electron parameters produced through these methods in a statistical analysis over a large dataset, to robustly explore the nature and repeatability of this possible relationship. We do so with the view that a clear relationship is indicative of an observational agreement with the description in the previous paragraph, while a weak relationship is indicative either that this description is not accurate, or the relationship has been heavily altered en route to 1 au, in either the corona or solar wind.

4.2 Data

We use ion charge state data from ACE-SWICS (Gloeckler et al., 1998) and electron flux data from WIND-3DP (Lin et al., 1995) to approximate simultaneous observations of solar wind heavy ions and suprathermal electrons as closely as possible (see Chapter 3 for details on these instruments). The time period considered covers 1998–2011, during which both satellites spent the majority of their time orbiting L1. Additional magnetic field measurements are taken from the WIND-MFI instrument. We use only the oxygen charge state ratio O^{7+}/O^{6+} for the purpose of this study, to maintain continuity with the work of Hefti et al. (1999). We have examined several of the results using instead carbon charge state C^{6+}/C^{5+}, and find no discrepancies large enough to affect our ultimate conclusions.

From WIND-3DP, we derive electron distribution functions from differential electron flux spectra measured by EESA-L ($\sim$5 eV$-$1 keV commonly at $\sim$30 s cadence) and EESA-H ($\sim$100 eV$-$30 keV commonly at $\sim$98 s cadence). In this study we use the pitch angle (PA) distribution data ($\sim$15°, 35°, 57°, 80°, 102°, 123°, 145° and 165° relative to the magnetic field direction). We use the magnetic field vector, **B**, produced by the WIND Magnetic Field Investigation (Lepping et al., 1995) to convert the pitch angles such that they span from the direction of electron propagation along the field line which is anti-sunward (that is, the common strahl direction) to sunward. These shall henceforth be referred to as PA bins 1 to 8, and the VDFs which are derived from the fluxes in these bins as f_1 to f_8. Bin 1 is the anti-sunward bin which will most commonly contain strahl, while bin 8 will contain strahl in the less common case of a sunward beam. To minimise computation time, these distributions are averaged to the same time resolution as the 1-hour SWICS heavy ion data.

The WIND spacecraft is subject to positive charging on the order of $5-15$ V. Estimates of spacecraft potential, Φ, are available in the "WI_ELM2_3DP" dataset on CDAWeb. A positive potential provides a fixed additional energy to all detected solar wind electrons. The potential also accelerates photoelectrons towards the spacecraft, which appear only at energies below that corresponding to Φ (to within the energy resolution of the detector). To remove the photoelectrons and correct the energies measured, we shift the energy bins down by a value equal to Φ. Data from any bins which are thus assigned a negative energy are considered photoelectrons and removed from the analysis. Note however that the suprathermal electron parameters calculated here in all cases concern electrons too high in energy to be contaminated by a photoelectron population. This energy range is also high compared to Φ, which means that the suprathermal electrons are not significantly altered by the acceleration due to the positive potential. We thus continue our analysis un-

der the assumption that any possible inaccuracies in the reported value of Φ are insufficient to alter our ultimate conclusions.

During the chosen period 1998–2011, suitable data are sometimes sporadic due to the orbit of WIND taking it away from L1. In particular, gaps exist due to this in the data taken before 2005. We have chosen time periods where WIND spends several days at a time near L1 with which to carry out this study. Data were used only when WIND's orbital position data indicated that it was within $100\,R_E$ of L1. To maximise the compatibility of the data from the two spacecraft, solar wind proton bulk velocity measurements taken from ACE-SWICS were compared with those from WIND-SWE. Cross-correlation was performed on the proton velocity data from both WIND and ACE to reveal what time-lag was present between the two spacecraft. The calculated time lags were always smaller than the 1-hour time resolution of the SWICS composition data available, and so no corrective time-shifting was performed on the data. We thus consider ACE and WIND to be sampling the same packets of solar wind for the majority of periods used in this study, to within the resolution limits of the data.

4.3 Methodology

4.3.1 Charge State Ratio

We choose the data product of oxygen charge state ratio O^{7+}/O^{6+} as the primary *in situ* tracer of coronal temperature. Figure 4.1 shows a plot of the oxygen freeze-in temperature, T_O, as calculated from SWICS measurements of O^{7+}/O^{6+} collected throughout 2007, derived by solving Equation 1.33 for T_e. We do so using lookup tables of ionisation fractions as a function of electron temperature from the CHIANTI database (Dere et al., 1997; Landi et al., 2013), which can be rearranged to find the temperature corresponding to a given charge state ratio. From the figure we

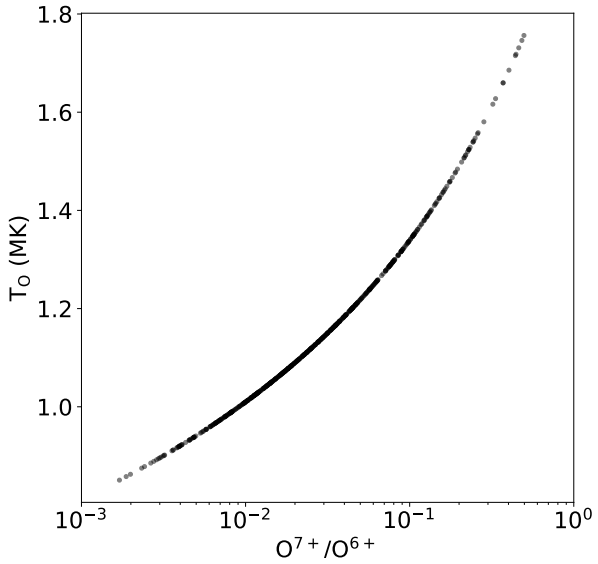

Figure 4.1: Plot of oxygen freeze-in temperature T_O against the corresponding oxygen charge state ratio O^{7+}/O^{6+}, from which it is calculated, taken from SWICS during the year 2007. Note that O^{7+}/O^{6+} is plotted on a logarithmic scale, demonstrating that linear variations in T_O correspond to order-of-magnitude variations in O^{7+}/O^{6+}.

see that variations in O^{7+}/O^{6+} over an order of magnitude correspond to variations of $< 50\%$ in the oxygen freeze-in temperature. We also note the range of O^{7+}/O^{6+} observed, which approaches three orders of magnitude.

We take steps to ensure that plasma associated with interplanetary coronal mass ejections (ICMEs) is excluded from our analysis. To do so we follow the method of Elliott et al. (2012); identifying as ICME times all of the intervals indicated by the Richardson and Cane list (Richardson and Cane, 2010), with additional time 15 hours before and 6 hours after the interval, to account for associated compressions and timing uncertainties. Any periods which fall within these criteria are not included in the analysis of subsequent sections.

4.3.2 Core + Suprathermal Fits

We fit the WIND electron data to a core-halo consisting of the sum of a Maxwellian and kappa function, as was found to be suitable in Maksimovic et al. (2005) and Stverak et al. (2009). We do this in both parallel and perpendicular directions without removal of strahl electrons from the parallel VDFs. As a result, fits made parallel to the field will include both halo and strahl electrons within a single kappa function, which should ideally be used only to describe one population. The potential

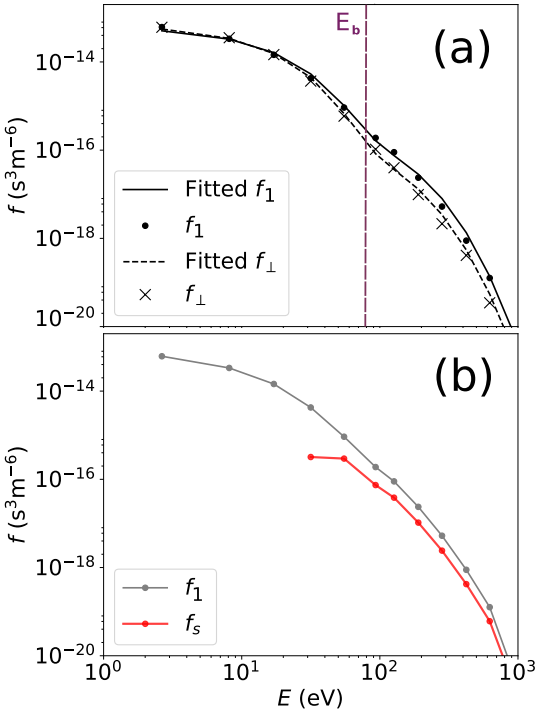

Figure 4.2: Example electron distribution functions calculated from time-averaged WIND-3DP flux data. Both (a) and (b) plot $f(E)$ on logarithmic axes. Spacecraft potential corrections have been applied to each. (a) shows data overlaid with fitted curves as described in the text. f_1 is enhanced over $f_\perp$ due to the presence of the strahl population at energies $>\sim 100$ eV. An estimate of the break-point energy E_b is shown in purple. (b) shows an example f_s distribution calculated as described in the text. Also shown is the corresponding f_1 distribution. f_s makes up a significant portion of f_1 at energies > 100 eV. f_s drops off rapidly below this energy, and is non-physical below 30 eV as it is numerically negative.

consequences of this for the results will be discussed in Section 4.5. In terms of kinetic energy, $W = \frac{1}{2}m_e v^2$, the kappa function used is the same form as in Equation 1.14 in Chapter 1:

$$f(W) = n_e \left(\frac{m_e}{2\pi\kappa W_0}\right)^{3/2} \frac{\Gamma(\kappa+1)}{\Gamma(\kappa-1/2)} \left(1+\frac{W}{\kappa W_0}\right)^{-(\kappa+1)}$$

Here, n_e is electron number density; m_e is the electron mass; $W_0 = k_b T(1-3/2\kappa)$; κ is a dimensionless value ≥ 1.5; and T is the temperature defined by the 2nd moment of the distribution, and is independent of κ (Livadiotis and McComas, 2013). This formulation can also be modified to allow for the distribution to shift up or down in energy by applying a uniform offset to W. WIND-3DP EESA-L and EESA-H data are combined to give the full electron distribution between $\sim$5 eV and 1.5 keV; the approximate energy range spanned by the core-halo-strahl populations. Energies above this range may contain the super-halo population (Lin et al., 1995). We fit the electrons to the VDFs in two pitch-angle directions separately: f_1, the bin closest to parallel, and $f_\perp = (f_4 + f_5)/2$, which averages the two bins either side of 90°.

We attempt to fit the core and suprathermal populations independently. For example, we make effort to ensure that the suprathermal number density could not be decreased at the expense of an increase in the core number density during fitting. This is motivated by the premise of the study; that while the core electron population may not be expected to reach 1 au unaltered from its coronal state, it is more reasonable to think that the suprathermal populations might. We therefore take care not to allow influence of "non-coronal" distributions (the core) on our potentially "coronal" parameters (those which describe the suprathermals). We apply a similar method to that in Stverak et al. (2009) to achieve this. We first estimate the break-point energy between the core and suprathermal populations (hereafter E_b). This is taken to be the energy at which each population makes equal contribution to the combined VDF. For the case in which both distributions were Maxwellian, each would form a straight line in log-linear space (f log; E linear). The break-point would then occur when the two lines intersect. An example of where we would expect the break-point energy to lie is labelled in Fig. 4.2. We note that in the log-log space of the figure, the break can be seen as a shoulder in the distribution. We find that the fitted kappa tail of the combined suprathermal distribution is very rarely smaller than $\kappa = 6$, and so at lower energies the halo is anyway closely approximated by a Maxwellian. We fit the core and halo portions of the VDF each to a straight line; discounting the contributions from energy bins between 40–150 eV in order to avoid energies at which we may expect the break to lie. The energy at which the fitted lines meet is then calculated, and used as the break-point energy for that VDF. The uncertainty in E_b, σ_b, is estimated from the error in the fitted parameters from each line.

Once a break-point has been found, we perform the fits for each population independently of each other, as in Maksimovic et al. (2005). To ensure that there is no contribution of one population to the fitting of the other, the core is fitted to

a Maxwellian between the limits $0 < E < (E_b - \sigma_b)$ and the suprathermals to a kappa function within the limits $(E_b + \sigma_b) < E < 1.5\,\mathrm{keV}$. This method results in a possible overestimate of the core density of approximately 2–5% due to the halo contribution in that energy range (Maksimovic et al., 2005).

For a given pitch angle bin, the core is fitted with two parameters for the Maxwellian density (n_c) and temperature (T_c). The suprathermals are fitted with three parameters which in a typical kappa distribution represent density ($n_{\text{h-s}}$), temperature ($T_{\text{h-s}}$) and kappa (κ). We have denoted these parameters as h-s, as they describe a combined suprathermal population of both halo and strahl. When referring specifically to the perpendicular suprathermal population, we exclude the 's' from this notation, as we expect contribution from the halo only (e.g., perpendicular suprathermal temperature; $T_{\text{h}\perp}$). These parameters are calculated for each bin as though they contain independent distributions. Usually we would employ bi-Maxwellian and bi-kappa distributions to produce parallel and perpendicular temperatures and one common density. However, any strahl electrons complicate this method, as they exist predominantly in the anti-sunward direction but not the sunward. The fits to the VDF for each pitch angle bin are thus assigned separate temperature and density parameters which are not constrained to be identical for all pitch angles. This means that a value of $n_{\text{h-s}}$ for a given direction represents the number density of the distribution were it integrated across all pitch angles as though it were isotropic. Attempting to derive the strahl number density with the calculation $n_s = n_{\text{h-s1}} - n_{\text{h}\perp}$ would then overestimate n_s, as the strahl is narrow in pitch angle. It is not strictly accurate, then, to describe these parameters as true temperature or density measurements of the suprathermal populations. Instead we refer to these as "proxy" suprathermal temperature and density (or proxy temperature and proxy density) through the remainder of the chapter.

Figure 4.2 (a) gives an example of the fitting method for the anti-sunward distribu-

tion, f_1, and the perpendicular distribution, $f_\perp$. The fits rapidly diverge from the data above 1 keV as these energies are not included in the fitting process to exclude the superhalo population. For this reason these example plots are cut off at 1 keV. The increase in f_1 over $f_\perp$ in the strahl energy range ($\sim E > 100$ eV) is clear, and we find that the fitting algorithm primarily accounts for this with an increase in $n_{\text{h-s1}}$.

If the strahl is present in the solar wind at a given time, then it should be primarily contained in the kappa fit to f_1. The halo is thus best described using the fits to f_8 and $f_\perp$, as the fits for these are not expected to encompass strahl electrons and instead will only describe the assumed near-isotropic halo. The parameters arising from the fit to f_1 are a result of a combined strahl and halo population, and so do not necessarily describe either to a satisfactory degree. To test for coronal signatures carried by the strahl electrons alone, the strahl must be isolated from the halo.

4.3.3 Strahl Characterisation

The strahl population is more difficult to characterise than the core or halo. Some authors (Maksimovic et al., 2005; Tao et al., 2016) have calculated numerical moments directly from isolated strahl populations. However, the methods for isolating strahl velocity distribution functions (VDFs) can be limited as they are derived from subtracting distributions from different pitch angle bins, over a limited energy range, leading to potentially large uncertainty in the moment. These strahl moments are also subject to assumptions about the extent of the strahl in pitch angle, which can only be estimated to within the angular width of a given measurement pitch angle bin. Alternatively, fitting a model function to isolate strahl components (as in Stverak et al., 2009, where a truncated kappa function was fitted) may circumvent the issue of energy cut-offs. However, any model functions used are rather ad-hoc below the typical energy at which the core/halo populations begin to dominate the strahl. We choose to directly calculate numerical moments to avoid these mod-

elling issues. We follow most closely the method of Tao et al. (2016) as their study concerns the same WIND-3DP dataset.

The strahl angular width is assumed to be less than 45°, and so contained entirely within PA bins 1 and 2. While Tao et al. (2016) subtract from this the mean distribution taken from f_3–f_8, taking this average does not address that these bins can not be expected to contain identical VDFs due to halo anisotropy. As bins 1 and 2 are close to the parallel direction, we subtract from these the corresponding data in bins 7 and 8 which, in the case that a bi-kappa function models the halo accurately, should best remove the halo contribution to the near-anti-sunward VDF. The resulting VDF, which we label f_s, describes the excess electrons in the anti-sunward direction which represent the strahl. This method assumes that the effect of any anisotropy in the halo on f_s is negligible. Figure 4.2 (b) shows an example of f_s plotted with the anti-sunward distribution f_1 from which it is calculated. We see that a significant portion of f_1 is made up of the strahl electrons in f_s in the energy range $0.1\,\mathrm{keV} \leq E \leq 1\,\mathrm{keV}$. Numerically, f_s frequently becomes negative, and thus unphysical, at variable energies below 100 eV, where it is obscured by the core/halo.

The strahl can be characterised by taking proxy-moments of f_s. Again following Tao et al. (2016), we may do so by numerically integrating f_s within the energy range $0.1-1.5\,\mathrm{keV}$. The reason for doing this is to exclude core, halo and super-halo electrons from the moment calculation. Due to the hard boundary on the numerical integration, these values shall hence be referred to as "partial moments". This is appropriate as they do not account for all of the electrons represented by f_s. We distinguish these from the above proxy temperatures and densities as they are calculated over a fixed energy range.

For the purpose of this study, we calculate only the mean energy of strahl electrons,

E_s, through the second partial moment of the distribution:

$$E_s = \frac{1}{n_s} \sum_{v(100\,\mathrm{eV})}^{v(1.5\,\mathrm{keV})} 2\pi(1-\cos 45^\circ) f_s(v) \frac{1}{2} m v^4 \Delta v \tag{4.1}$$

where $2\pi(1-\cos 45^\circ)$ and v^2 are included as a result of the integration in spherical coordinates. Calculating this over a constant and finite energy range should be treated with some caution, as fluctuations in the electron populations could cause the extent of the strahl to vary about these limits.

When comparing E_s to O^{7+}/O^{6+} we do not assign a time lag despite the strahl's more rapid propagation to 1 au down the magnetic field line. If the strahl beam's bulk velocity is aligned with the IMF at all stages during its propagation, then the strahl observed at 1 au simultaneously to the bulk solar wind must be from the same source region in the corona. Applying a time lag would thus instead lead to comparing strahl to ion data from different source regions. This is only the case if we assume that no scattering of the strahl takes place which would alter the guiding centre of the electrons. We note also the implicit assumptions that the freezing-in temperature of oxygen at the solar wind source has not changed significantly, and that there is no change in connectivity of the IMF, over the travel time of the oxygen ions themselves. These assumptions may be more likely to hold true for coronal hole sources than for the slow solar wind source regions, which tend to be more chaotic and variable than the fast wind.

4.4 Results

We first compare time series of O^{7+}/O^{6+} with proxy suprathermal temperatures $T_{\text{h-s1}}$ and $T_{\text{h}\perp}$. Figure 4.3 shows time series of solar wind bulk proton speed v_p (from SWICS), oxygen charge state O^{7+}/O^{6+}, and temperatures $T_{\text{h-s1}}$ and $T_{\text{h}\perp}$ taken during 2008 (a) and 2009 (b) over $\sim$16 days. These time periods have been chosen

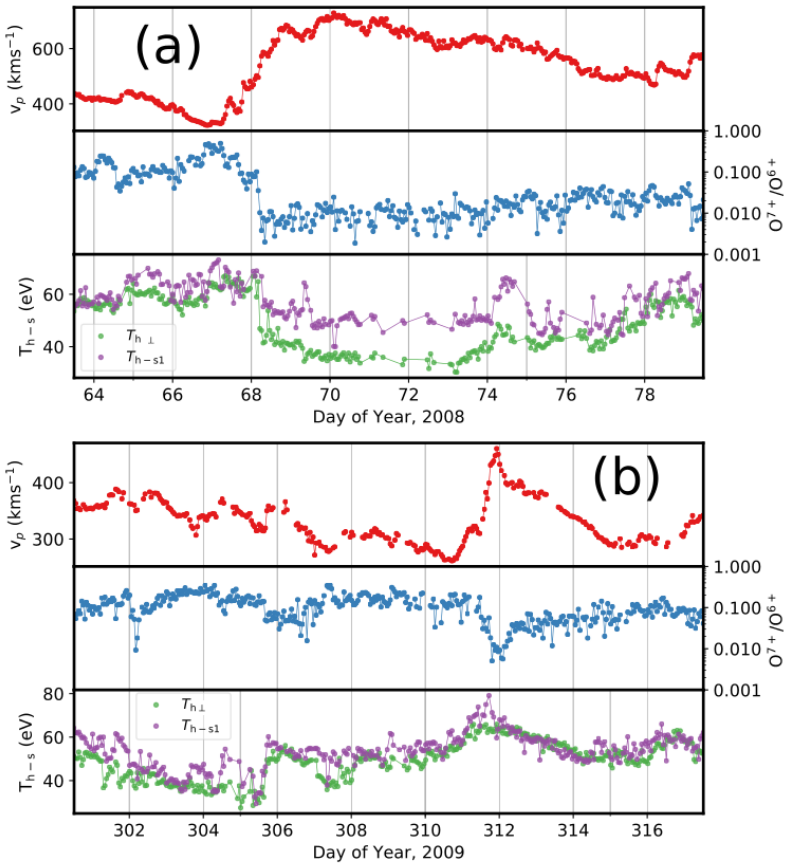

Figure 4.3: Time series data taken from portions of 2008 (a) and 2009 (b). Panel 1 shows solar wind proton speed as measured by the ACE spacecraft. Panel 2 plots the oxygen charge state ratio O^{7+}/O^{6+} on a logarithmic scale. O^{7+}/O^{6+} varies counter to v_p as is expected. Panel 3 plots the pair of proxy suprathermal temperatures $T_{h\perp}$ and $T_{h\text{-}s1}$. These vary synchronously, with $T_{h\text{-}s1}$ tending to moderately higher values. We note that both temperatures appear to track well with O^{7+}/O^{6+} in case (a), but in case (b) appear to vary oppositely with it.

to best contrast the possible relationships between these parameters, which depend on the heliospheric conditions at the time. We observe that both $T_{h\text{-}s1}$ and $T_{h\perp}$ appear to evolve in agreement with O^{7+}/O^{6+} in (a) but in (b) evolve oppositely. Viewing the data this way, it is immediately apparent that there can be no consistent tendency for our proxy suprathermal temperature to either correlate or anti-correlate with O^{7+}/O^{6+}. Other time periods can also be found where no apparent positive or negative relationship is clear.

Next, we plot proxy suprathermal temperatures against O^{7+}/O^{6+} directly, to bring

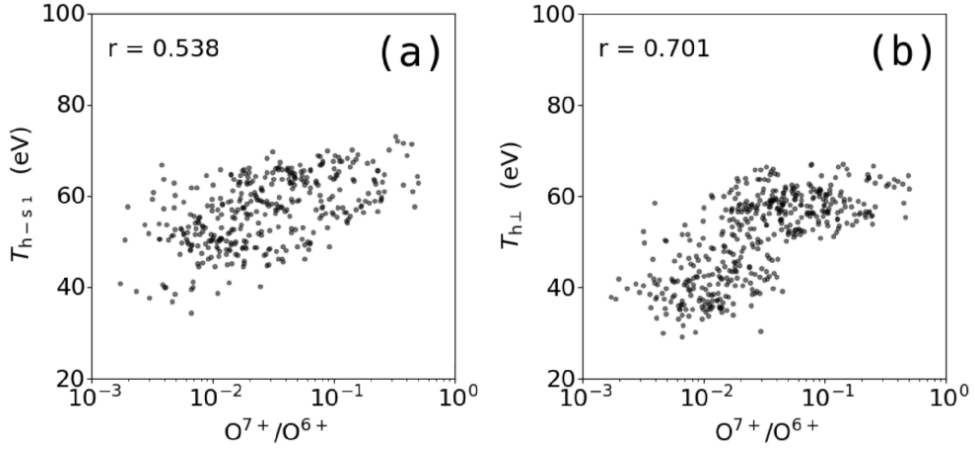

Figure 4.4: Scatter plots of (a) $T_{\text{h-s1}}$ and (b) $T_{\text{h}\perp}$ against O^{7+}/O^{6+} for Carrington rotation 2067. Pearson linear correlation coefficients are printed on the plots. Both have moderate and positive values of r, with $T_{\text{h}\perp}$ having a slightly stronger correlation. $T_{\text{h-s1}}$ is also systematically higher than $T_{\text{h}\perp}$ by around 5–10 eV.

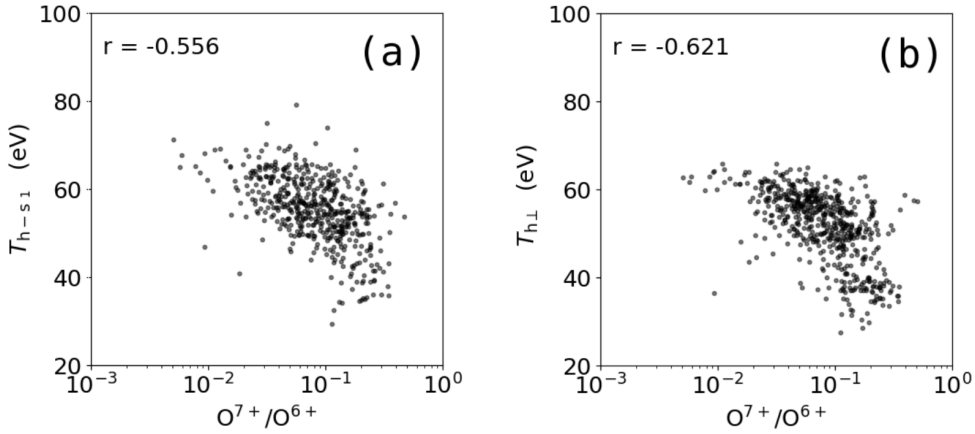

Figure 4.5: Scatter plots of (a) $T_{\text{h-s1}}$ and (b) $T_{\text{h}\perp}$ against O^{7+}/O^{6+} for Carrington rotation 2089. Pearson linear correlation coefficients are printed on the plots. Both have moderate and negative values of r, with $T_{\text{h}\perp}$ having a slightly stronger correlation. $T_{\text{h-s1}}$ is also systematically higher than $T_{\text{h}\perp}$ by around 5–10 eV.

to light which, if any, relationship it has with O^{7+}/O^{6+}. Analysing scatter plots of T_{h-s} against O^{7+}/O^{6+}, and producing associated correlation coefficients allows for a more robust analysis of the nature of any possible relationship between the two than is possible with time series data alone. We compare data over the timescales of Carrington rotations as this allows as close to a full, instantaneous, sample of all of the solar wind in the ecliptic at 1 au as possible. This minimises any effects from

drifting O^{7+}/O^{6+} relative to E_s or $T_{\text{h-s}}$ from any temporal factors on the Sun, in our correlation calculations. Figures 4.4 and 4.5 show the result of plotting $T_{\text{h-s1}}$ and $T_{\text{h}\perp}$ against O^{7+}/O^{6+} for Carrington rotations 2067 (day 52–80, 2008; end of declining phase of the solar cycle) and 2089 (day 286–315, 2009; beginning of rising phase of the solar cycle), respectively. Note that while the times in Fig. 4.3 (b) overlap with CR-2089, (a) does not overlap with CR-2067. Pearson linear correlation coefficients are calculated between each temperature and $\log_{10}(O^{7+}/O^{6+})$. Corresponding p-values for these correlations, and those shown in Figs. 4.5 and 4.6, have all been found to tend to zero, and so are not displayed on the plots themselves. We use the logarithm of O^{7+}/O^{6+} as it varies over orders of magnitude for linear changes in freeze-in temperature, as shown in the previous section. $T_{\text{h}\perp}$ exhibits a positive relationship ($r = 0.701$) with O^{7+}/O^{6+} during CR-2067, and a negative one ($r = -0.621$) during CR-2089. $T_{\text{h-s1}}$ varies similarly, although it has smaller magnitude in r for both Carrington rotations shown. Thus for isolated time periods, and indeed whole Carrington rotations, it is possible to find both somewhat convincing positive and negative relationships. This agrees with the relationships inferred from the time series data in Fig. 4.3. We note that the $T_{\text{h}\perp}$-O^{7+}/O^{6+} relationship shows signs of being split into a pair of populations during CR-2067; for high and low $T_{\text{h}\perp}$. This does not appear to be the case for $T_{\text{h-s1}}$, or for either of the relationships during CR-2089.

Turning to the electrons identified as forming the strahl populations, we now plot E_s against O^{7+}/O^{6+} in the same format in Figs. 4.6 (a) and (b); for Carrington rotations 2067 and 2089. The former period exhibits a mild positive correlation, with E_s varying over a range of approximately 20 eV, similarly to $T_{\text{h}\perp}$ in the same time period. During the latter period, there is no strong positive or negative correlation, although the E_s values show a similar range of variation as those in Carrington rotation 2067. We also do not observe any apparent grouping of points during CR-

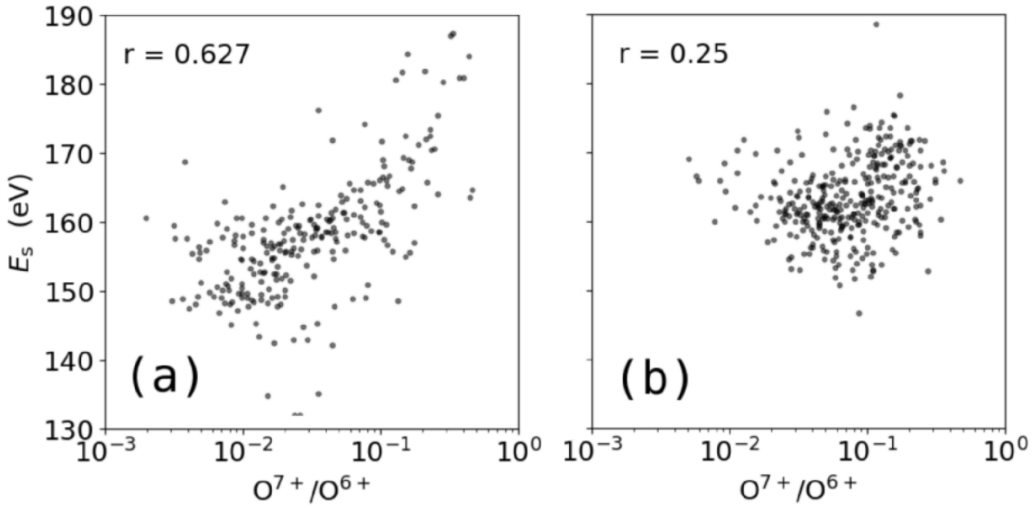

Figure 4.6: Scatter plots of E_s against O^{7+}/O^{6+} for Carrington rotations (a) 2067 and (b) 2089. Pearson linear correlation coefficients are printed on the plots. A weak positive relationship appears in (a) ($r = 0.627$) which is absent in (b).

2067 as we did for $T_{\mathrm{h}\perp}$.

Observations Over a Solar Cycle

To explain the observation of both periods of positive and negative correlations between O^{7+}/O^{6+} and proxies for the suprathermal temperature, we now consider the data over multiple Carrington rotations. We group the available data in time, based on the phase of the solar cycle, which we define simply by using quartiles of the monthly sunspot number, acquired from the SILSO World Data Center. Our $T_{\mathrm{h}\perp}$, $\kappa_\perp$, E_s and O^{7+}/O^{6+} data from the lower and upper quartile time periods (2006–2010 and 1999-2003, approximately solar minimum and maximum respectively) are shown in the left and right columns of plots in Fig. 4.7. Data from the remaining two middle quartiles (corresponding to the rising and declining phases of the cycle) are shown combined in the central column. We note that there is a large portion of missing data in the upper quartile time period owing to the orbit of WIND. This period falls primarily over the time range for the sunspot maximum, leaving only around 1 year's worth of data available for that quartile in total.

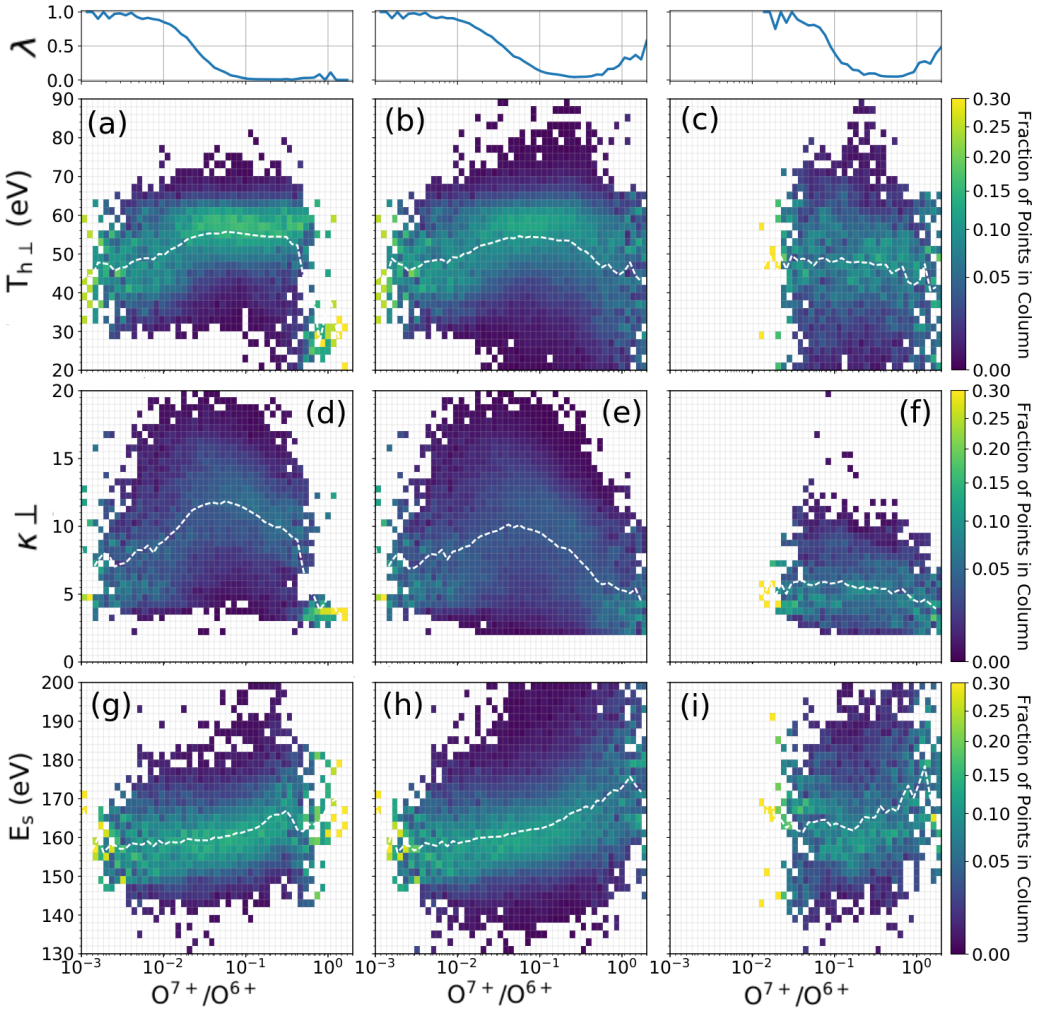

Figure 4.7: Histogram plots for $T_{h\perp}$ (a–c), $\kappa_\perp$ (c–f) and E_s (g–i) against O^{7+}/O^{6+}. (a,d,g) are composed of data taken during the lower quartile period of sunspot number, (b,e,h) the middle two, and (c,f,i) the upper. The plots are normalised for each box by the number of points in that bin of O^{7+}/O^{6+}. For each column of plots, the small top panel above shows λ; the fraction of solar wind samples above 500km s^{-1} (fast solar wind) per bin of O^{7+}/O^{6+}. For $T_{h\perp}$, we note a weak upward trend in (a) which is not found in (c); likely as O^{7+}/O^{6+} in (c) does not extend to sufficiently low values. (b) shows a similar increase in $T_{h\perp}$ at low O^{7+}/O^{6+} values as (a) does, and also a drop-off at high O^{7+}/O^{6+} values as in (c). $T_{h\perp}$ extends down to the pre-defined limit of halo temperature, indicating likely drop-outs of the halo at large O^{7+}/O^{6+}. For $\kappa_\perp$, in both (d) and (e) we observe a broadly spread upwards trend in the low-O^{7+}/O^{6+} regions (< 0.02), which then inverts to become a downwards trend at higher values. In (f), we see only high-O^{7+}/O^{6+} values and see that they decrease gradually. There is a degree of agreement between these trends and those of $T_{h\perp}$ above. For E_s, a weak upward trend is found in (g), which appears to sharply fall off at higher O^{7+}/O^{6+} (> 0.2). This may be due to a lack of samples at high O^{7+}/O^{6+}, however. (i) also shows a weak positive trend, but this is far less smooth as (i) is made up of fewer samples than (g) or (h). (h) shows a continuous positive trend through all available O^{7+}/O^{6+} samples. The trend increases more sharply as O^{7+}/O^{6+} increases.

To contextualise the types of solar wind which are represented in these plots by solar wind speed as well as O^{7+}/O^{6+}, for each column we define λ as the fraction of solar wind samples in each bin of O^{7+}/O^{6+} which can be considered "fast" ($v > 500\mathrm{km\,s^{-1}}$). We plot λ against O^{7+}/O^{6+} as the top panel of each column. This shows in each case that the low (high)-O^{7+}/O^{6+} portions of each period contain $> 80\%$ fast (slow) wind, with intermediate sections at mid-range values. We note, however, that with increasing solar activity (moving left to right) we see a trend for the transition from fast to slow to occur at higher O^{7+}/O^{6+} values. Further, we attribute the up-turn in λ at high-O^{7+}/O^{6+} to be a result of the high-speed solar wind which is associated with compositionally hot active regions.

Each main panel in Fig. 4.7 (labelled a to i) plots a derived electron parameter (on the y axis) against O^{7+}/O^{6+} as a 2D histogram which has been normalised by the number of data points in each column of O^{7+}/O^{6+}. In this way, the colour of each box describes the probability of measuring that value of y given the corresponding O^{7+}/O^{6+} value. This normalisation is applied to account for discrepancies in the number of samples at the extremes of O^{7+}/O^{6+}, which tends to be skewed strongly towards higher values. A dashed white line in each plot traces the weighted mean y for each bin of O^{7+}/O^{6+}.

The data acquired during periods of quiet Sun in Fig. 4.7 (a) displays a weak upwards trend for $T_{\mathrm{h}\perp}$ with O^{7+}/O^{6+}, which climbs primarily between $O^{7+}/O^{6+} = 0.002$–0.02; levelling out and falling off at $O^{7+}/O^{6+} > 0.1$. This is most clearly visible in the mean line, as the spread of the data in $T_{\mathrm{h}\perp}$ is very broad. The large spread in the data means that any correlation coefficient calculated from it would be very small. The histogram appears to be split into two clusters, in the bottom left and bottom right of the plot, at around $O^{7+}/O^{6+} = 0.02$. This corresponds to around 70% fast solar wind.

The data acquired near solar maximum in Fig. 4.7 (c) do not exhibit an upwards

trend or clustering, in contrast to the lower quartile data. However in this case the data do not extend to below $O^{7+}/O^{6+} = 0.02$, which is near the cut-off for the clustering and upwards gradient observed in (a). This is likely due to the properties of solar wind streams which existed at these times; possibly in combination with sampling issues brought about by WIND's orbit. Nevertheless a downwards trend around higher O^{7+}/O^{6+} values still seems apparent. $T_{h\perp}$ overall appears to be lower on average than in (a), with a wider spread that may be due to a lack of samples taken for this period.

Figure 4.7 (b) contains the same plot as above for the remainder of the $T_{h\perp}$ data, covering mid-levels of activity. The left section of the plot appears to mimic the relationship found in (a), while the right mimics that found in (c). This suggests that these relationships may be dependent mostly on the availability of high and low O^{7+}/O^{6+} solar wind at low-latitudes.

In Fig. 4.7 (d–f) we plot $\kappa_\perp$ against O^{7+}/O^{6+} for different solar cycle periods. Overall this parameter exhibits far more spread than we see in $T_{h\perp}$. We find that in the low-O^{7+}/O^{6+} section, $\kappa_\perp$ increases with increasing charge state, whereas it falls with increasing charge state in the high-O^{7+}/O^{6+} section. This is similar to the change in $T_{h\perp}$ in 4.7 (a) and particularly (b). Further, we see $\kappa_\perp$ decline with O^{7+}/O^{6+} in (f), as $T_{h\perp}$ does in (c). For all periods of the solar cycle these two parameters, which both primarily describe the halo population, exhibit similar trends with O^{7+}/O^{6+}. We note that this result appears to agree with Tao et al. (2016), who reported correlation during fits to the halo population between the temperature and κ.

We find similar results for E_s in Fig. 4.7 (g–i) as we do for $T_{h\perp}$, with some distinctions. A positive correlation with O^{7+}/O^{6+} can be seen when sufficiently low values of O^{7+}/O^{6+} are sampled, as is evident from the white line which illustrates the mean in (g). However, at times when these low values are not sampled in the

solar wind the upward trend appears to continue. The increasing trends found here are associated with a similar wide spread in underlying values to those in $T_{\mathrm{h}\perp}$. We find in (h) the strongest positive trend in E_s with $\mathrm{O}^{7+}/\mathrm{O}^{6+}$. Particularly, in the upper range of $\mathrm{O}^{7+}/\mathrm{O}^{6+}$ (> 0.1) there is a moderate increase in E_s.

Returning to calculations of correlation coefficient, we repeat the calculation of r for our suprathermal electron parameters against $\log_{10}(\mathrm{O}^{7+}/\mathrm{O}^{6+})$, for each Carrington rotation within the available dataset. The results of this are shown in Fig. 4.8. Panel (a) serves to contextualise the correlation data in the rest of the plot. The dashed black line shows the monthly sunspot number, showing that the full dataset spans the time of approximately one solar cycle. The first half of the data occurs around solar maximum, and the second around minimum. The histogram shows in red the occurrence of interplanetary coronal mass ejections (ICMEs) detected at 1 au, taken from the Richardson and Cane (2010) ICME list. Greyed-out boxes show periods when absence of WIND data has prevented analysis. The period with fewest ICMEs appears to correspond to the period of maximum positive correlation for $T_{\mathrm{h}\perp}$, around 2007–2008. This also coincides with the declining phase of cycle 23 indicated by the sunspot number, with a slight offset in time. Apart from this trend, there does not appear to be a direct correspondence with ICME activity and the correlation of $\mathrm{O}^{7+}/\mathrm{O}^{6+}$ with any of the suprathermal electron parameters on a per-Carrington rotation basis.

The variation in r with time is shown in panel (b) of Fig. 4.8 for $T_{\mathrm{h}\perp}$ only. Filled-in points indicate correlation coefficients with a corresponding p-value of less than 0.05; a typical cut-off for significance. The square of a Pearson correlation coefficient, r^2, can be interpreted as the fraction of variation in the data which is described by the assumption that the two variables from which r is calculated are linearly dependant. We plot $r \cdot |r|$ for the correlation of $T_{\mathrm{h}\perp}$ ($T_{\mathrm{h\text{-}s1}}$) with $\mathrm{O}^{7+}/\mathrm{O}^{6+}$ in panel (c) (panel (d)) of Fig. 4.8. This expresses the value of r^2 between the parameters, while

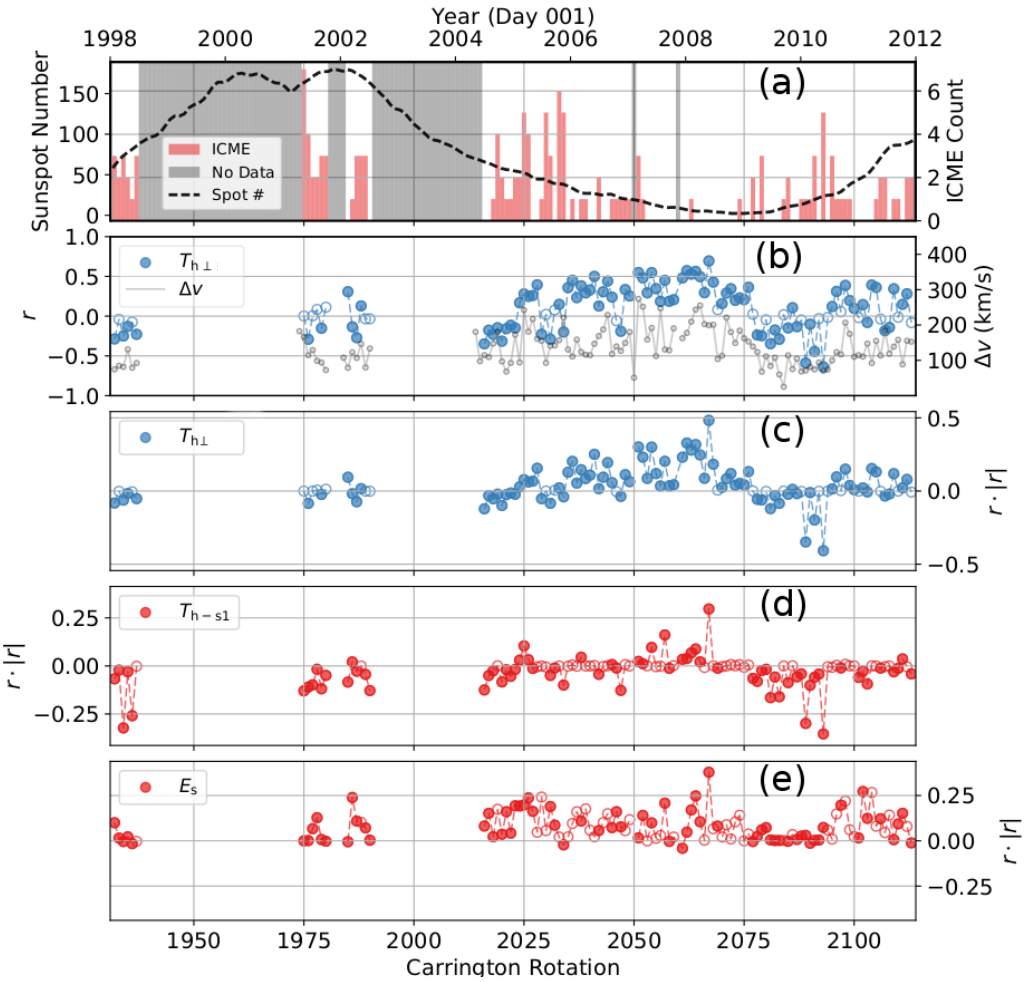

Figure 4.8: Linear correlation data for suprathermal electron parameters with O^{7+}/O^{6+}, as calculated over single Carrington rotations against time. Also shown is supporting solar and heliospheric data. Time is shown as years on the top axis and Carrington rotation number on the bottom. All correlation data (r or $r \cdot |r|$) are shown as a filled in point only when the corresponding p-value is < 0.05, otherwise it is outline-only. Panel (a): Monthly sunspot number is plotted as a dashed line. A sunspot maximum followed by a minimum can be seen over the course of the observations. Also plotted is a histogram of the number of ICME detections at L1 from the Richardson and Cane list (Richardson and Cane, 2010). Greyed-out boxes correspond to gaps resulting from a lack of WIND electron data. The time for the minimum in ICMEs leads that of sunspot minimum by 1–2 years. This period has some agreement with that of strongest $T_{h\perp}$-O^{7+}/O^{6+} correlation in 2007–2008. Panel (b): The left axis plots the correlation coefficient r calculated for the pairing $T_{h\perp}$-O^{7+}/O^{6+}. The right axis plots the value Δv, which describes the range of the velocity data sampled as a difference of upper and lower quartiles (detailed in text). There is some apparent tracking between these two parameters, notably in the period following 2006. Panel (c): $r \cdot |r|$ for the correlation coefficient between $T_{h\perp}$ and O^{7+}/O^{6+}. The fractional dependence of the two parameters on each other is clearly less that 20% for most Carrington rotations. A notable exception to this is the period of enhanced positive correlation around the time 2007-2008. Panel (d): The same plot as Panel (c), with $T_{h\perp}$ replaced by $T_{h\text{-}s1}$. The magnitude of $r \cdot |r|$ is almost uniformly smaller than for $T_{h\perp}$. Panel (e): $r \cdot |r|$ for the linear correlation r calculated for E_s with O^{7+}/O^{6+}. For most Carrington rotations there is a weak, positive, relationship. There are no notable Carrington rotations in which there is a negative relationship.

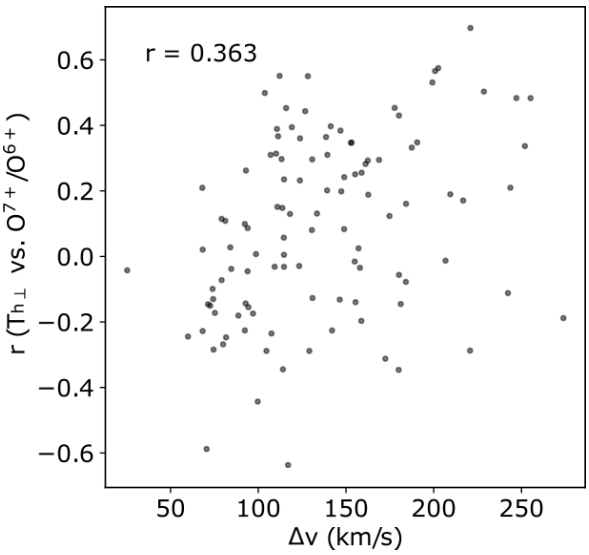

Figure 4.9: Plot of the correlation coefficient r, calculated between $T_{h\perp}$ and O^{7+}/O^{6+} for each Carrington rotation, against the measure of spread in velocity Δv. There is a weak positive trend between the two.

still preserving the sign of r. With this parameter we easily observe that, for the majority of Carrington rotations, there is very little dependence of halo temperature on O^{7+}/O^{6+}, as r^2 rarely exceeds 25%. Panel (c) shows $r \cdot |r|$ exceeds a positive correlation with dependency of 25% during some Carrington rotations in 2007–2008; the period of fewest ICMEs noted above.

To quantify the extent to which a full sample of the available solar wind conditions have been captured for a given Carrington rotation, we define Δv as the lower quartile value of the solar wind speed subtracted from the upper. This provides a description of the range of velocities covered by the data, which will be smaller when solar wind streams exhibit a narrow spread of velocities, or when a portion of the data corresponding to one velocity regime is missing. To test if there is a relationship between the degree of correlation and Δv, we plot the two directly against each other in Fig. 4.9. Any apparent tracking in Panel (b) only amounts to a small correlation coefficient of 0.363; which is essentially no correlation. While calculating the correlation coefficient of data which consist of a group of correlation coefficients is not statistically sound, visual inspection of the scatter plot itself supports that the degree of correlation observed between $T_{h\perp}$ and O^{7+}/O^{6+} is not very sensitive to the range of available solar wind speeds.

Panel (e) of Fig. 4.8 shows $r \cdot |r|$ calculated for the correlation coefficient of E_s with O^{7+}/O^{6+}. As with the other parameters, any relationship represented by these values of r is very weak, as r^2 never exceeds 0.5, and the values are typically smaller than even those for $T_{\mathrm{h}\perp}$. The most extended period where r is positive appears to fall between 2004 and 2008; the declining phase of cycle 23, which is slightly longer than the extended positive period for $T_{\mathrm{h}\perp}$. There is no comparable period of negative correlation, although there is a period of extended near-zero correlation which appears to correspond to the period of most negative correlation for both $T_{\mathrm{h}\perp}$ and $T_{\mathrm{h\text{-}s1}}$ around the rising phase of cycle 24.

4.5 Discussion

4.5.1 Coronal Temperature Signatures at 1 au

We first note that all correlation coefficients and apparent trends between O^{7+}/O^{6+} and derived suprathermal electron properties in the data which have been shown in Section 4.4 only imply, at best, weak relationships. Correlation coefficients which accompany the scatter plots in Figs. 4.4-4.6 and feature in the long-term analysis of Fig. 4.8 only correspond to values of r^2 which rarely exceed 10%. As described in Section 4.4, this value describes the fraction of variation in the data which can be explained by the two sharing a linear relationship. Likewise, while there is frequently a positive trend in the mean lines in the histograms in Fig. 4.7, the large spread in the data is indicative of the weakness of the overall increasing trend. Caution must be used when trying to explain or draw conclusions from such weak correlations, but perhaps more reasonably we can attempt to explain the weakness itself, and the variation therein. The weakness of the T_{h-s} and E_s relationships with O^{7+}/O^{6+} could suggest that the suprathermal electron populations have lost almost all characteristics relating to coronal temperature signatures before they reach 1 au. Alternatively,

this could mean that these signatures are not set in the corona in the way predicted by Che and Goldstein (2014), and summarised in Section 4.1, i.e., with more energetic suprathermal electron populations being formed in regions with higher core electron temperature, at the correct height to map to the oxygen freeze-in height. In this section we explore how the evidence may be interpreted in each case.

The following discussion focuses on $T_{\mathrm{h}\perp}$, which we believe is a better representation of the halo temperature than $T_{\mathrm{h\text{-}s1}}$, while our parameter E_s will be used to provide information about the isolated strahl. The observation in Fig. 4.4, and in later plots, that $T_{\mathrm{h\text{-}s1}}$ tends to be greater than $T_{\mathrm{h}\perp}$, is most likely due to the presence of the strahl electrons in f_1. The strahl is well-described as a beam of electrons. The effect of adding such a beam, with a relative velocity drift, to the halo is to create a new combined distribution which is enhanced around the beam energy. Thus a kappa fit to this distribution returns a temperature which is enhanced over that for the halo alone, as long as the central strahl energy is sufficiently displaced from the central halo energy. The size of the temperature increase depends strongly on the number density of the strahl. Given these complications in interpreting $T_{\mathrm{h\text{-}s1}}$, we do not consider it further in this section.

4.5.2 Explanations for Weakness of Coronal Signatures

A popular model for the formation of the core-halo-strahl feature is that the halo is formed by pitch angle scattering of strahl electrons by whistler waves, which is counteracted, at least partially, by magnetic focusing to maintain the field-aligned strahl (Owens et al., 2008). The scattering and refocusing processes can occur continuously during propagation, and so electrons which arrive at 1 au as either part of the strahl or halo populations could have been subject to scattering events several times during the course of their propagation. Alternatively, Seough et al. (2015) suggest the strahl population may be expected to have been subject to far less scat-

tering than the halo by the time it reaches 1 au. In both cases, the halo and strahl electrons are predicted to originate from the same population. This appears to be the case within the limits of our measurements, to the extent that the two appear to both be very weakly correlated with O^{7+}/O^{6+} by the time they reach 1 au. We explore the $T_{h\perp}$ and E_s relationships with O^{7+}/O^{6+}, attempting to find evidence as to whether their state at 1 au is a result of an initially weak relationship, counter to Che and Goldstein (2014), or an initially strong relationship weakened by *in situ* processing.

The time period from which Fig. 4.7 (a) is drawn, 2006–2010, includes the declining phase of solar cycle 23. This period has previously been found to feature highly persistent, low-latitude, coronal holes (Gibson et al., 2009; Mursula et al., 2017). The solar wind from such coronal holes is likely to contain the very low O^{7+}/O^{6+} values which are evident in Fig. 4.7 (a). These measurements form a cluster which is in contrast with the main population at higher O^{7+}/O^{6+}. Without these exceptionally low $T_{h\perp}$ and O^{7+}/O^{6+} measurements, the upwards trend which is present in Fig. 4.7 (a) would be unlikely to exist. This is also the case for the upwards trend in (b). Further, this lower population exhibits its own self-contained gradual increase in $T_{h\perp}$ with O^{7+}/O^{6+} which is not seen for the higher values, in which there is a gradual decrease. Perhaps only wind from the coronal hole-proper, and not from transitional regions which produce this solar wind with higher O^{7+}/O^{6+}, preserves an initial coronal temperature signature in $T_{h\perp}$. This could be due to differences in the freezing-in process in these transitional regions, or due to differences in processing which occur in the solar wind as these regions develop stream interactions.

Interestingly, the cut-off between the two distinct regions in Fig. 4.7 (a) seems to be at about $O^{7+}/O^{6+} \sim 0.02$; a far smaller value than those previously found to distinguish coronal hole from non-coronal hole solar wind streams (Zurbuchen, 2002; Zhao and Fisk, 2011). By that measure, this population falls within the extremes of

coronal hole wind charge state, and so likely does not include many samples from the trailing edges of coronal hole wind streams, across which O^{7+}/O^{6+} gradually increases from typical fast to typical slow solar wind values.

Charge state data are available in the ACE-SWICS dataset for elements other than oxygen. These include carbon charge state ratios C^{6+}/C^{5+} and C^{6+}/C^{4+}. Each of these can provide an estimate of coronal temperature at a different freeze-in height from oxygen. Landi and Lepri (2015) modeled coronal charge state evolution including ionisation both by collisional and photoionisation processes. They found that the resulting solar wind value of O^{7+}/O^{6+} is likely more susceptible to photoionisation than either of the above carbon charge states. While initial comparisons with the results which have been covered in Section 4.4 appeared very similar for C^{6+}/C^{5+} and C^{6+}/C^{4+} to O^{7+}/O^{6+}, these have not been studied further at present. Interesting future work would compare the similarities and differences in the relationships for these ions with those discussed in this study for oxygen.

We can compare the increase in the mean $T_{\mathrm{h}\perp}$ value in the low-O^{7+}/O^{6+} regions of Figs. 4.7 (a) and (b) to a best-guess expected increase. Using the results of the freeze-in temperature calculations shown in Fig. 4.1, given the increase in O^{7+}/O^{6+} from around 0.002–0.02, we can predict an increase of around 25% in T_{O} in the corona. The expected core-halo relationship from Che and Goldstein (2014) shown in Equation 2.1 then suggests an increase of 25% should also appear in $T_{\mathrm{h}\perp}$, should it be preserved out to 1 au. The increases in the mean $T_{\mathrm{h}\perp}$ in these regions in (a) and (b) appear to be around 20%, showing reasonable agreement with the prediction. This implies that there may be an underlying relationship between $T_{\mathrm{h}\perp}$ and O^{7+}/O^{6+} which for low-O^{7+}/O^{6+} wind has been smeared-out in a mostly random fashion, either in the corona itself or, by processing in the solar wind.

In the high-O^{7+}/O^{6+} regions of Figs. 4.7 (a) and (b) we observe a downwards trend of $T_{\mathrm{h}\perp}$ with O^{7+}/O^{6+}. This is counter to the expected relationship, and cannot be

explained as a simple spreading out of $T_{\mathrm{h}\perp}$ values. We note that high-$\mathrm{O}^{7+}/\mathrm{O}^{6+}$ values should generally correspond to the sources of the slow solar wind which is typically more prone to fluctuations which can alter electron distributions. The lowering in $T_{\mathrm{h}\perp}$, when compared visually to corresponding $f_\perp$ electron distributions, can be understood as the halo temperature approaching the core temperature. The downward trend in $\mathrm{O}^{7+}/\mathrm{O}^{6+}$ could then show that in the most high-$\mathrm{O}^{7+}/\mathrm{O}^{6+}$ slow solar wind, the halo is more prone to thermalising with the core (if the two were fully thermalised, then they would have identical temperatures) at some point between its initial formation in the corona and its propagation to 1 au. Thermalisation would fully erase any presumed positive relationship between $T_{\mathrm{h}\perp}$ and $\mathrm{O}^{7+}/\mathrm{O}^{6+}$ when measured *in situ* at 1 au.

In Fig. 4.7 (g–i) E_s increases with respect to $\mathrm{O}^{7+}/\mathrm{O}^{6+}$ differently to $T_{\mathrm{h}\perp}$, in that it does so continuously, while $T_{\mathrm{h}\perp}$ appears to form clusters. To a small extent we see the rise in mean E_s increase in rate with increasing $\mathrm{O}^{7+}/\mathrm{O}^{6+}$. Under the presumption of an initial positive relationship between suprathermal temperature and $\mathrm{O}^{7+}/\mathrm{O}^{6+}$ set in the corona, for all values of $\mathrm{O}^{7+}/\mathrm{O}^{6+}$, this can be viewed as $T_{\mathrm{h}\perp}$ entirely losing this relationship in high-$\mathrm{O}^{7+}/\mathrm{O}^{6+}$ solar wind en route to L1, while E_s preserves it. This is because the difference in relationship with $\mathrm{O}^{7+}/\mathrm{O}^{6+}$ for the halo would have to develop during transit of the solar wind to 1 au, if we assume the strahl and halo are of common origin, as described in Section 4.1. Such an occurrence is possible given the strahl's potential to reach 1 au far more rapidly than the halo, which propagates out with the bulk solar wind. Alternatively, the partitioning in $T_{\mathrm{h}\perp}$ could be caused by a change in freeze-in height at the corona for different source regions; changing the initial relationship with suprathermal electrons and ionisation and leading to a discontinuity in the relationship between source regions. However, this interpretation does not explain the lack of break in E_s, and so we favour the former. The fact that the halo temperature seems to best correlate in

low O^{7+}/O^{6+} regions, associated with the leading edge and centres of coronal hole streams, while the strahl relationship is positive in all regions, could be explained as the halo being subject to such processing outside of these relatively unperturbed regions of fast solar wind which the strahl is not.

In Fig. 4.8 we examine correlation coefficients r and $r \cdot |r|$ for relationships between $T_{\text{h-s}}$, E_s and O^{7+}/O^{6+} separated by Carrington rotation. We find that $T_{\text{h}\perp}$ shows most positive correlation with O^{7+}/O^{6+} during the declining phase and subsequent minimum of solar cycle 23. The declining phase of cycle 23 is notable for the presence of extended low-latitude coronal holes; the solar wind from which is compositionally cool (low O^{7+}/O^{6+}). This leads to a period of extended stability in the solar wind streams during this phase. As noted in Fig. 4.7 (a) and (b), this low-O^{7+}/O^{6+} wind features a positive trend with $T_{\text{h}\perp}$, and so these periods may produce more positive values of r because they include more wind of this type. As shown in Fig. 4.9, the strongest positive correlations do not necessarily correspond to the broadest spread in velocity. This may be because the trend appears to invert as we move from compositionally cool to hot wind, as shown in Fig. 4.7 (a) and (b). Calculating a correlation coefficient over the entire spread of O^{7+}/O^{6+} may thus result in lower correlations because of this.

As we see evident in Fig. 4.7 a tendency for distinct trends to exist in compositionally cool (fast) and hot (slow) solar wind, it would be of interest to measure the correlation coefficients for solar wind data collected within isolated fast or slow streams. In this case we refer specifically to data from individual streams; as opposed to combining data from multiple fast or slow streams. Doing so would help to ensure that correlations are being calculated for ions which were frozen-into their charge states at comparable heights in the corona, as they are more likely to have originated from the same region on the Sun, which would not necessarily be the case if we were to combine data from multiple streams of wind. Based on the low

and high-O^{7+}/O^{6+} clusters in Figs. 4.7 (a–c), we may expect that fast streams will produce a mildly positive correlation coefficient between O^{7+}/O^{6+} and $T_{h\perp}$, while slow streams would likely be closer to zero or negative. This would be an interesting topic for future study.

4.5.3 ICME Effects on Suprathermal Electrons

We can also contextualise periods of positive correlation with the ICME histogram data. We note that the strongest period of $T_{h\perp}$ correlation occurs between 2007 and 2008, when there is a clear lack of ICMEs detected, towards the end of the declining phase of cycle 23. This complements the above point that we observe most positive correlation when we are able to sample stable solar wind streams which are relatively uninterrupted by transients.

Alternatively, we can consider the possibility of ICMEs directly affecting suprathermal electron distributions upstream of the observer before reaching L1. Although we have taken steps to remove the *in situ* ICME data from our dataset, suprathermal electrons propagate along the magnetic field line to 1 au more rapidly than the bulk solar wind, or the majority of ICMEs. As such, strahl (and indeed halo, if this population results from *in situ* scattering of strahl) electrons which precede an ICME at 1 au could have been affected upstream of the observer by the ICME through, for example, acceleration by the shock front. CME eruptions would also likely alter the initialisation of the relationship between ionisation states and suprathermal electrons predicted for the corona in Section 4.1. If suprathermal electrons are accelerated by ICME shocks in the corona in a similar manner to suprathermal ions (e.g., Kahler and Vourlidas, 2014; Ding et al., 2015), then this would represent a severe deviation from the scenario described in Section 4.1. In such a case we could not expect a relationship between these electrons and ion charge state to be preserved. It is thus possible that ICMEs would have an adverse effect on the prob-

ability of observing a positive relationship at 1 au both through effects in the corona itself and in the solar wind. This is difficult to separate from the above explanation based on the spread of solar wind parameters, as there are no other large gaps in ICMEs at L1 in the time period of data included here with which we can compare.

There is some evidence that the influence of ICMEs on suprathermal electrons is more pronounced for halo electrons than strahl. In Fig. 4.8, E_s tends to have smaller $|r|$ values than $T_{\mathrm{h}\perp}$, except for one period during the years 2004 and 2005. This is despite the detection of many ICMEs around this period, which we have hypothesised may be limiting the correlation levels for $T_{\mathrm{h}\perp}$. This disagrees with the description of direct ICME influence on the suprathermal electrons, which predicts that ICMEs should have more influence over the beamed strahl electrons than the convecting halo, as the direct ICME times are removed from the convecting solar wind observations. Again, the disruption from standard fast and slow streams caused by ICMEs could be the cause of the difference in correlation. As we have already noted above, a positive $T_{\mathrm{h}\perp}$ relationship with O^{7+}/O^{6+} relies upon samples of low-O^{7+}/O^{6+} fast solar wind streams.

4.6 Conclusions

We have shown that suprathermal temperature proxies, $T_{\mathrm{h}\perp}$ and $T_{\text{h-s1}}$, generally exhibit only very weak correlation with O^{7+}/O^{6+}. From our analysis in the previous section we conclude that, outside of relationships between the large-scale streams in the solar wind structure, the temperature of suprathermal electrons has very little to no residual signatures from the coronal electron temperature of its source by the time it propagates to 1 au. This contrasts with the conclusions drawn by Hefti et al. (1999), who reported that the two were related. We do not fully contradict their conclusions however, as we too find numerous subsets of data with statistically significant correlation between the suprathermal electrons and O^{7+}/O^{6+}. Likewise

E_s, an estimate of mean strahl energy, also shows very little overall dependence on O^{7+}/O^{6+}. Both the halo, which propagates with the bulk solar wind, and the strahl, which travels rapidly down the heliospheric magnetic field, show no consistent evidence of containing a remnant signature of the electron temperature at their coronal source. We find that in periods where there is low solar activity, fewer ICMEs and consistent fast streams, there is a greater positive correlation with O^{7+}/O^{6+} for both E_s and $T_{h\perp}$. A possible explanation is that in these simple configurations of the corona and solar wind, a coronal relationship is set up, as predicted by Che and Goldstein (2014), and partially preserved between the suprathermal electrons and ionisation states. In the more complex states, some combination of coronal conditions (variability of freeze-in heights, ionisation processes, temporal variation of the source) and solar wind processing (increased wave activity due to CIRs, wind streams with more fluctuations, ICME influence on halo and strahl electrons) is acting to destroy this correlation before it can be observed. Alternatively, the explanation for the weak relationships could simply be that the halo formation model of Che and Goldstein (2014), and the prediction of an initial core-halo temperature correlation which follows from it, are incorrect. Overall, we conclude that the Che and Goldstein (2014) model and its resultant predictions are possibly accurate; particularly under the above favourable coronal conditions.

We have noted many features of these relationships in Section 4.5 while attempting to understand whether *in situ* processing or coronal conditions are responsible for their weakness and variability. We find that the large spread in E_s and $T_{h\perp}$; apparent clustering into fast and slow wind; and the lack of positive correlation during periods of increased perturbation in the corona and solar wind, could each be explained by solar wind processing effects or by coronal conditions which are source-dependent. The one observation which appears to clearly favour the explanation of *in situ* processing destroying an initially strong relationship is found when comparing the halo

relationship in Fig. 4.7 (b) to the strahl relationship in Fig. 4.7 (e). The continued upwards trend of E_s in high-O^{7+}/O^{6+} solar wind which is not seen for $T_{\mathrm{h}\perp}$ can be most simply explained through solar wind processing effects being more effective on the halo population than the strahl. We do not find any observations which exclusively favour coronal effects as the cause for the weak correlations. However, it is important to note that this may still be the case because we have not performed analysis of any direct solar observations which would potentially reveal such effects.

Chapter 5

Matching Coronal and Heliospheric Boundaries with Simple Mapping Techniques

5.1 Introduction

In the previous chapter, we tested for a possible link between suprathermal solar wind electrons and their source electron temperature, through the use of an *in situ* proxy; the oxygen charge state ratio. In this chapter we aim to understand the origins of charge states which are not trivially related to the electron temperature at their source; those which fall in the rarefaction regions between fast and slow streams. Such charge states are intermediate in their values; lying between the characteristically low values of the fast, and the higher values of the slow stream (see Chapter 2). It is not immediately obvious whether such intermediate charge states (ICSs) truly result from the electron temperature and other freeze-in properties at their source region, or whether some mixing has been permitted to occur across the fast-slow boundary in the solar wind. Here we map this intermediate solar wind

back to the Sun to identify its source, and explain the mechanism by which the observed ICS arises.

5.1.1 Sources of the Solar Wind

As discussed in Chapter 2, identifying source locations and the mechanisms of production of the various solar wind flows is a key goal of Solar Orbiter, and has been an area of active research since the solar wind's discovery. Observational strategies to constrain and characterise the source of the solar wind range from remote sensing observations of flows in the low and high corona (e.g., Harra et al., 2008; van Driel-Gesztelyi et al., 2012; DeForest et al., 2016), to entirely *in situ* approaches (Kepko et al., 2016), to mapping these *in situ* solar wind measurements back to the Sun; linking these two observational regimes (Krieger et al., 1973; Karachik and Pevtsov, 2011; Culhane et al., 2014; Fazakerley et al., 2016).

While the principal source of the fast solar wind has long been established as coronal holes (Krieger et al., 1973; Zirker, 1977), identifying the source regions and production mechanisms of the slow wind is still an area of active research. A key facet of this problem is that compositional and ionisation signatures (Geiss and Bochsler, 1985; Schwadron et al., 1999; Zhao and Fisk, 2011) suggest the slow wind may be associated with closed magnetic field regions on the Sun. Two of the prominent types of model for slow solar wind formation rely on the process of reconnection to open closed magnetic fields and allow the escape of confined plasma. The first type, "interchange" slow wind models, allow open magnetic flux to diffuse into closed-field regions via interchange reconnection (Fisk et al., 1998; Schwadron et al., 1999). This leads to the escape of the closed field plasma. The second type, S-web models, involve the opening of closed field through continuously-occurring reconnection at a complex open-closed boundary (Antiochos et al., 2011). A subset of models exist which instead argue that apparent closed-field signatures could

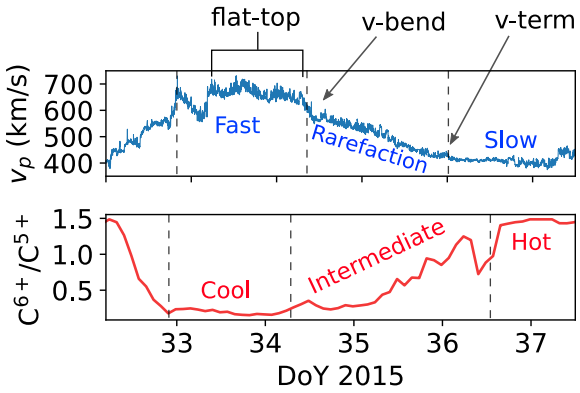

Figure 5.1: Example trailing stream interface as measured by ACE at 1 au, with different sections of the stream, and features labelled as described by Borovsky and Denton (2016). Between the fast and slow streams there is a smoothly-varying region of intermediate velocity; the rarefaction. The carbon charge state ratio C^{6+}/C^{5+} varies less smoothly, but still exhibits intermediate values which clearly lie between those of the compositionally coolest (fastest) and hottest (slowest) parts of the stream.

be a result of wind originating from the edge of coronal holes (Withbroe, 1988; Wang and Sheeley Jr, 1990) which have a larger expansion factor. For more detail on these three models, see Chapter 2. We noted in that Chapter that the expansion factor mechanism could also be employed to explain the intermediate values of velocity and charge state observed in rarefactions.

5.1.2 Sources of 'Intermediate' Solar Wind

As established in Chapter 2, rarefactions which follow fast coronal hole (CH) streams in the solar wind can be characterised by velocity, abundance, and charge state values which transition between those of the fast and slow streams (e.g., Wang et al., 2009). We shall therefore in this thesis describe the velocity and heavy ion properties of this part of the solar wind as "intermediate". An example of velocity and carbon charge state is shown for such a stream measured at L1 in Figure 5.1.

The features of solar wind velocity shown here (flat-top, velocity-bend, velocity termination) are all potentially producible from dynamic effects occurring as the solar wind expands, as argued by Borovsky (2016); Borovsky and Denton (2016). These features are consistent with the simple setup of two distinct sources, between

which there is no magnetic connection which might allow the mixing of plasma. We cannot necessarily understand the concurrently observed values of C^{6+}/C^{5+} in Figure 5.1 using the same basic picture. In this case the expected evolution of C^{6+}/C^{5+} would be a discontinuous jump, embedded at the original stream boundary in the rarefaction, rather than a smooth transition. It appears that either: 1) the intermediate charge states and other properties are intrinsic to the source or 2) there is a change in the connectivity of the magnetic field, such that heavy ions from one source region are able to flow into a stream from another source region and mix. These concepts were explored more thoroughly in Chapter 2.

In Chapter 2, we introduced the study by Schwadron et al. (2005), in which the authors allow mixing of distinct heavy ion populations, through footpoint motion across the coronal hole boundary at the photosphere, resulting in a magnetic connection across stream boundaries, and a change of source region connectivity for some regions of the solar wind. Due to differential streaming and the change in connectivity, heavy ions are able to cross over the region which would otherwise contain a discontinuity in charge state/composition. This potentially creates an extended region with a more continuous transition from low to high charge state; explaining the intermediate values. Using this process, and an intrinsically-intermediate CHBL, the authors reproduce velocity and charge state ratios of solar wind properties in a superposed epoch analysis of Ulysses data at 5 au (Geiss et al., 1995a) to a good agreement.

To our knowledge, the work of Schwadron et al. (2005) is the only test of the effects of footpoint motion and differential streaming to explain intermediate solar wind heavy ion observations which has been carried out so far. Many open questions still remain. The primary question for this chapter is whether these two factors (CHBL and mixing) can explain ICSs in rarefactions as measured at L1 (far closer to the Sun, and at lower latitudes than the case modelled by Schwadron et al.,

2005). Other unknown details include: Can the many other properties of rarefaction regions observed *in situ* such as the total size, magnetic field geometry, charge state/composition profiles (e.g., smooth gradients or a plateau etc.), or absolute values of velocity/charge state/composition be explained by these two factors (CHBL and mixing) alone? Do source region properties such as size, location (particularly latitude which should strongly influence the rate of footpoint motion) and morphology of the coronal hole, as well as properties of the surrounding closed-field regions, influence the properties of the rarefaction? Does plasma attributed to the CHBL originate from that location in reality?

From a Sun-heliosphere connection standpoint, if we are to use solar wind ionisation and composition to trace source properties, then it is crucial to understand as best we can how these properties arise. If the ICS values are in fact a result of interplanetary mixing, and not characteristic of any one source, then we would need to account for this when using these measurements in studies such as Chapter 4. A key motivator for the work in this chapter then is to not only locate and understand the source of a particular region in the solar wind, but also to identify what charge state and composition measurements can truly tell us about source region properties.

In this chapter we search for observational evidence which backs or opposes either coronal conditions (CHBL or another source) or footpoint motion processes as the explanation for ICSs observed in solar wind rarefactions at L1. We seek this evidence both in the heliosphere and at the Sun, by linking *in situ* solar wind to remote sensing coronal observations.

The Two-Step Backmapping Procedure

To briefly recap Section 3.6 in Chapter 3, two-step backmapping is a straightforward method for mapping *in situ* solar wind measurements to a source location at the Sun. Figure 3.3 displays a schematic for the solar wind propagation assumed

in the technique. The steps are first to ballistically propagate solar wind back to coordinates θ_{ss} and ϕ_{ss} source surface of a PFSS magnetic field model, and then to follow the path of the open flux at these coordinates down to the photosphere, producing final coordinates for the source; θ_{ph} and ϕ_{ph}.

In this chapter, we use the two-step backmapping technique to combine *in situ* solar wind and remote sensing coronal observations for a collection of fast CH streams, their associated rarefactions, and the sources of both. We do so to further investigate the origins of ICSs observed at 1 au. We also evaluate the effectiveness of the backmapping procedure for linking *in situ* and remote EUV coronal observations such as these. This chapter thus presents a study on both identifying the role of different processes in the origins of this particular intermediate type of solar wind, and the principles of linking the Sun and the heliosphere observationally. The former deals in the fundamental understanding of the production and evolution of the solar wind, as well as the interpretation of measurements of established tracers of source properties; heavy ion charge state and composition. The latter meanwhile is of critical importance in achieving the science goals of the upcoming Solar Orbiter mission.

The chapter is structured as follows. First, in Section 5.2 we describe the *in situ* and remote sensing data used in the study. In Section 5.3 we describe how we apply a simple solar wind model, detailed in Appendix B, to produce estimates of the durations of intermediate composition streams arising from minor ion differential streaming and footpoint motions, for the purposes of this study. We then describe our implementation of the two-step backmapping technique, and our selection of events which we hope to provide the most reliable *in situ*-source region link for the study. In Section 5.4 we present the results for the durations of intermediate composition streams predicted by our solar wind model. We then present results comparing backmapped solar wind data to remote sensing coronal hole imagery

to evaluate the success of the backmapping technique. Following this, we apply the most successful mapping for each event to identify the origins of intermediate composition in those events. In Section 5.5 we discuss the implications of our results regarding the backmapping technique. Further, we discuss the origins of the ICSs implied by both the observational results and those of the simple solar wind model. Finally, in Section 5.6 we draw conclusions on both the principles of backmapping solar wind, and the origins of distinct compositional signatures in rarefactions. We discuss some implications of these conclusions for the Solar Orbiter mission.

5.2 Data

5.2.1 *In Situ* Data

In situ solar wind data for the time period 2012–2016 are obtained from ACE and WIND spacecraft measurements from L1. Minor ion charge state, relative abundance, and differential streaming data are obtained from ACE-SWICS (Gloeckler et al., 1998). Interplanetary magnetic field measurements are from ACE-MFI (Smith et al., 1998); solar wind proton bulk speed and other proton parameters are from ACE-SWEPAM (McComas et al., 1998). Suprathermal electron pitch angle distributions are from WIND-3DP Lin et al. (1995). Details of these spacecraft, instruments and data products can be found in Chapter 3. A key limitation of the dataset is that the publicly available SWICS charge state ratio and composition data for this time period is at a reduced time-resolution of 2 hours. This limitation is accepted as we wish to use remote sensing data from SDO, which is only available from 2011 onward.

We choose to use the charge state ratio C^{6+}/C^{5+} as our tracer of coronal electron temperature, and heavy ion composition in general, for the purposes of the work in

this chapter. This choice is made due to the drawbacks of applying oxygen charge states described in Chapter 2. Further, relative abundance measurements such as Fe/O from SWICS tend to be quite variable, making them more difficult to use to consistently distinguish solar wind streams from different sources. We thus limit this study to only charge state at this time.

5.2.2 Remote Sensing Data

We use full-disk EUV observations from SDO-AIA (see Chapter 3) to identify and characterise coronal structures as candidate source regions for backmapped solar wind streams. We use the AIA channel centred around 193 Å, as coronal hole targets appear very clearly as dark regions at this wavelength. This channel is also recommended for use in imaging the corona, both quiet and active, which provides a synoptic picture of both of these aspects of the corona with a single band (Lemen et al., 2011). Magnetogram data from SDO-HMI comprise input data for the full-photospheric flux maps which are used by the PFSS software (details in Section 3.6.2).

5.3 Methodology

5.3.1 Implementation of the Simple Solar Wind Model

In Appendix B we describe a simple solar wind model, designed to predict the sizes of mixed composition regions in the solar wind (which we expect to manifest as intermediate charge state regions when measured *in situ*) resulting from the combination of footpoint motion across a CH boundary in the corona, and differential streaming of minor ions in the solar wind. In order to better interpret the observed *in situ* properties of solar wind regions of intermediate composition, we apply this model here. We will now describe the specific implementation of the model to the

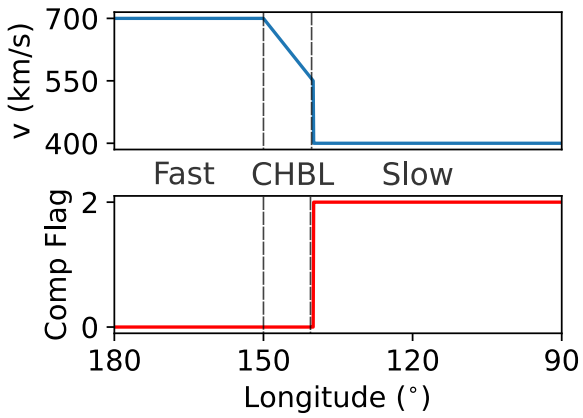

Figure 5.2: Example input configuration for model. The top panel shows, as a function of source longitude, the initial model velocities. Left to right: fast, CHBL transition, slow. The bottom panels shows the associated composition flag, which is 0 in the fast stream and CHBL, and 2 in the slow.

current study.

We adapt the model parameters described in Schwadron et al. (2005). We follow their inner boundary conditions; a fast stream separated from a following slow stream by a coronal hole boundary layer (CHBL) with linearly varying velocity. The CHBL in their model falls from the fast solar wind speed (v_{fast}) of around 750 km s^{-1} to a speed of 600 km s^{-1} over 10° at 30 R$_{\odot}$. There is then a discontinuity in speed from the CHBL to the slow solar wind speed (v_{slow}) of around 400 km s^{-1}. We model different fast and slow speed combinations, and follow a similar profile; a 10° CHBL with a linear velocity decrease of $0.5(v_{\mathrm{fast}} - v_{\mathrm{slow}})$. The composition in the fast stream and CHBL is considered to be characteristically cool (lower charge states), while that of the slow stream is characteristically hot (higher charge states, as is shown in e.g., Figure 5.1).

The top panel of Figure 5.2 shows an example of initial outflow speed parameters at the inner boundary. We do not model the compression which would form at a slow-to-fast transition, as the region in which we are interested for the rest of this chapter is fast-to-slow. The bottom panel shows the corresponding composition flag for the three source regions. We do not model heavy ion densities directly, as we are only interested in determining the size of the regions for which they are mixed. Instead we label compositionally cool ion regions with a 0, and hot with a 2. Any intermediate regions which form during a model run will be labelled with

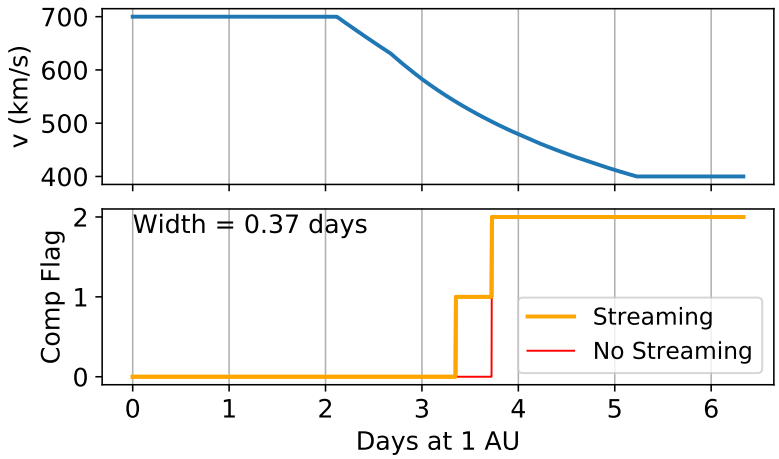

Figure 5.3: Example synthetic time series for solar wind at 1 au given the input parameters shown in Figure 5.2 and described in the text. Top panel: bulk velocity, bottom panel: composition flag, both with and without differential streaming considered. An intermediate region is apparent in the case with differential streaming, which persists for (has a width of) 0.37 days.

a 1. In contrast with Schwadron et al. (2005) we do not assign the CHBL plasma an intermediate flag, because we wish to isolate the size of an intermediate region arising solely from streaming effects. From such starting parameters, we produce the initial super-particles at the inner boundary and iterate the model as described in Appendix B.

To simulate observations by an *in situ* spacecraft of the modelled solar wind, we take a measurement of the modelled parameters at a chosen observer location along R (usually 1 au) at each time step. Figure 5.3 shows an example time series taken at 1 au of v and Comp Flag for the initial parameters shown in Figure 5.2, for a footpoint latitude of 75°. For composition, we plot the result for model runs both with and without differential streaming enabled. In this model an intermediate region exists only in the case with differential streaming; without it there is a discontinuous jump from compositionally cool to hot solar wind.

5.3.2 Backmapping

We apply the two-step backmapping procedure as described in Chapter 3, Section 3.6, to link measurements from the *in situ* and remote sensing datasets described above. We calculate Δt_c using 64-second solar wind bulk velocity measurements from ACE-SWEPAM. For each data point we map the *in situ* measurement to a source surface latitude and longitude; $\theta_{\rm ss}$ and $\phi_{\rm ss}$ respectively. For the ACE-SWICS data which is at 2-hour resolution, we average the solar wind velocity over time to match it, and then calculate $\theta_{\rm ss}$ and $\phi_{\rm ss}$ for each of these measurements also. We then apply magnetic field tracing for the appropriate PFSS models, to link each source surface coordinate to a set of coordinates at the photosphere; $\theta_{\rm ph}$ and $\phi_{\rm ph}$.

The results of Neugebauer et al. (1998) indicated that the constant velocity backmapping assumption may systematically shift $\phi_{\rm ss}$ coordinates to the west (details in Section 3.6.3). This shift was thought to arise as a consequence of the failure of the assumption of cancellation of errors arising from two of the key assumptions made by the model: that of constant radial solar wind velocity, and that of rapid corotation drop-off. To study this further, we wish to test whether increasing the ballistic propagation time Δt (which would result in the aforementioned westward shift in $\phi_{\rm ss}$) improves the accuracy of the mapping. To this end, for each solar wind period studied here, we perform backmapping using both Δt_c; the time-shift for constant velocity solar wind, and Δt_a; the time-shift for solar wind which accelerates during its propagation according to Equation 3.7 (Chapter 3). Equation 3.8 relates these two times as simply $\Delta t_a = (4/3)\Delta t_c$. The accuracy of the mapping which results from each Δt is compared in Section 5.4.3, and subsequent sections use the Δt which is found to produce the most accurate mapping for each period individually.

5.3.3 Event Selection

We select fast solar wind streams paired with their inferred coronal hole sources for study based on a set of selection standards. This is to ensure the highest likelihood that solar wind source regions are being correctly identified, and that the *in situ* and remote sensing observations are suitable for both testing the quality of the mapping, and observing coronal hole trailing boundaries in the solar wind and corona.

Considering data between the years 2012–2016, events were selected based on the principles described in this section. We note here however that this process of selection was not exhaustive; not all solar wind streams from this time range were evaluated, and so some may be left out which meet the same standards as others which were included. Instead events were selected until a reasonable number (a requirement of at least 10 was initially targeted) for study were found. We therefore acknowledge that we perhaps should not draw generalised conclusions based on any results which arise from these events only. Having carried out this process however, we believe that our selection is probably a representative sample of events. Producing a rigid set of selection criteria such that the selection process is exhaustive is left to future work.

We select time periods based on the ACE *in situ* solar wind measurements and the AIA full-disk data. We select only solar wind streams with bulk speeds measured by SWEPAM of $> 500\,\mathrm{km\,s^{-1}}$, which last for greater than 1 day *in situ*. For each of these streams, we examine AIA 193 data from 2–6 days prior to the onset of each fast stream. We choose only events which feature, during this time, a coronal hole which at least partly inhabits the region $\pm 45°$ latitude from disk centre and meets a minimum size criterion; an on-disk cross-section on the order of at least $200''$ at its widest point. This is an attempt to remove streams which can not realistically originate from coronal holes, or which do originate from coronal holes whose size

or location on the disk will limit our later analysis. A set of 61 time periods were found in this way, some of which contain multiple fast streams within them, to which we apply the backmapping procedure.

For the 61 time periods, we select PFSS models corresponding to the time when the expected source coronal hole was near disk centre. From these we produce maps of open flux footpoints at $1\,R_\odot$ on a 1° resolution grid. We plot white points denoting these open field lines over the corresponding EUV image, three examples of which are shown in Figure 5.4. As is clear from the top and bottom images, regions of open flux produced by these PFSS models do not necessarily correspond well to dark coronal hole regions in EUV data. This has been explored in detail by e.g., Cranmer (2009); Linker et al. (2017), and is a result of both the limitations of the PFSS approach (reliance on synoptic magnetograms and flux-transport models, sensitivity to source surface height) and the physical response of coronal plasma and emission to open and closed flux (e.g., plasma which exists on newly-opened magnetic field lines will escape into the solar wind, but on a finite timescale; presumably leading to gradual, rather than instantaneous dimming). In short, this may arise because the model incorrectly describes the true coronal open flux, or because low-corona EUV emission does not perfectly correspond to open flux. Regardless, we do not consider such events further in the study, as we cannot distinguish the first case from the second. Thus, we remove 22 events where the morphology of the CH implied by the open flux locations does not match the morphology of the EUV coronal hole, such as in the top and bottom images of Figure 5.4. We contrast these with the central image, for which the agreement is generally good. The exclusion of events based on coronal hole morphology here is carried out by inspection only. For future work in which events are selected through a more exhaustive process, we hope to also apply a quantitative approach to consistently remove events where open flux does not match with EUV coronal holes based on a rigorous criteria.

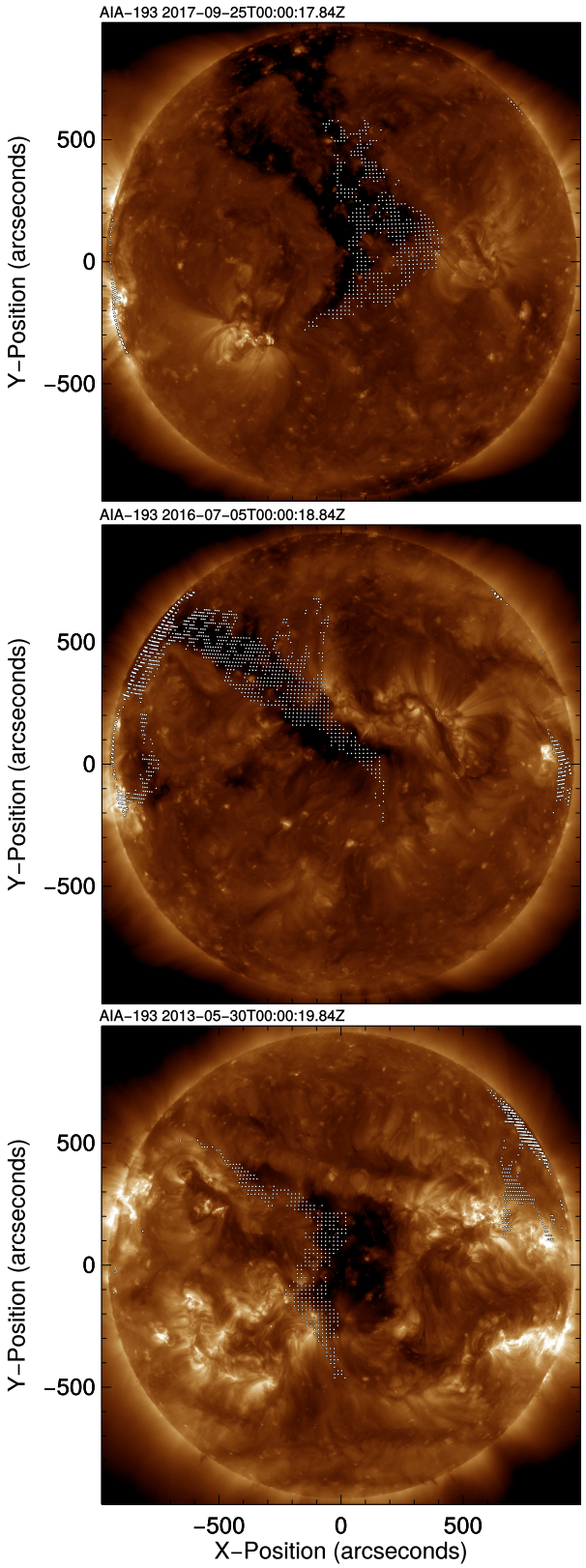

Figure 5.4: Three 193 Å images of the solar corona, overlaid with points marking footpoints of open flux calculated by a PFSS model at 1 $R_{\odot}$. The top and bottom images illustrate poor agreement between the dark coronal hole regions in the image and the open flux footpoints. The central image illustrates acceptable agreement between the two.

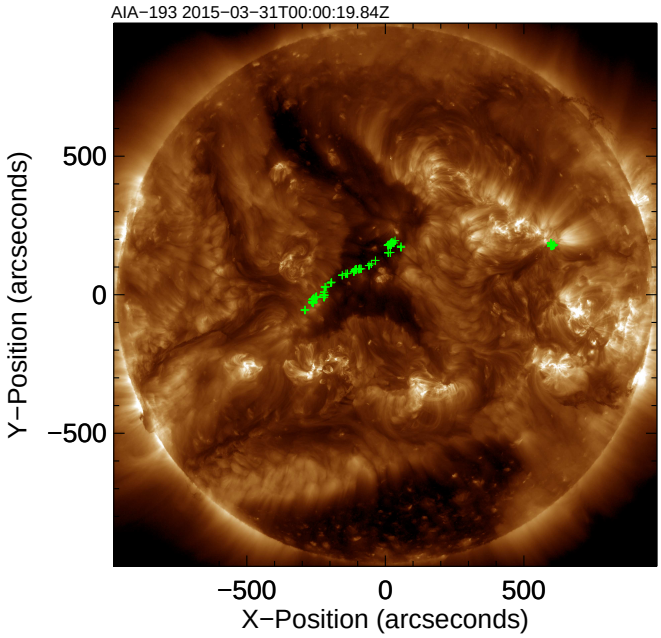

Figure 5.5: Example of an AIA-193 Å image of a coronal hole, overlaid with locations of solar wind sourcepoints resulting from the backmapping procedure in green. In this example, points trace smoothly across the coronal hole, suggesting solar wind escapes from the centre of the coronal hole, and both eastward and westward boundaries.

We also compare the time periods under study with the ICME list published by Richardson and Cane (2010), and remove any for which the fast stream is potentially associated with an ICME period. We do so as ICMEs fall outside of the expected configuration we hope to observe; a persistent fast and slow stream and the boundary between the two. We keep periods where there are ICME signatures indicated during small portions of the fast stream and rarefaction, but highlight these such that they are considered separately during further analysis.

We perform constant-velocity backmapping as detailed in Section 3.6 for the set of 61 preliminary events. Figure 5.5 shows an example of the mapped sourcepoints of a solar wind stream detected *in situ* at 1 au to a disk-centre coronal hole imaged in 193 Å by AIA. Each sourcepoint corresponds to a single ACE-SWICS data point measured *in situ*. As the Sun rotates east to west (left of the image to right of the image) earth-directed solar wind is released from more easterly locations with time. The connectivity of the spacecraft to the Sun thus changes from westward

to eastward sourcepoints as seen in the figure. For simplicity we describe this as the "trajectory" or "path" of the spacecraft sourcepoint from west to east in time. This motion is slightly complicated by dwells, which will invert the sourcepoint trajectory. We stress that the sourcepoint path is not equivalent to the concept of footpoint motion, described in Section 5.1.2 and Schwadron et al. (2005), which refers to the physical motion of magnetic footpoints resulting from differential rotation. We remove any events for which the *in situ* data does not map to within the vicinity of a coronal hole meeting the dimensional and positional criteria described above, again as these will not be ideal candidates for study due to their location on the disk. We also discard periods where the source coronal hole is particularly complex, or where there appears to be more than one feasible source coronal hole. Removing these periods makes later evaluation of the mapping less ambiguous.

Following other authors (Neugebauer et al., 1998; Fazakerley et al., 2016; Heidrich-Meisner et al., 2016) we check for each preliminary event that solar wind with inward (outward) directed *in situ* magnetic field maps to a source surface location with inward (outward) from the PFSS model. We define the inward/outward polarity of the *in situ* fields following the method detailed in Heidrich-Meisner et al. (2016). Our criteria for study is that the *in situ* magnetic field direction agrees with the PFSS field direction for $> 50\%$ of the time, with deviations which last at most 8 hours. We further examine the periods which do not meet this criteria; we wish to allow for brief deviations in sign, which can be attributed to short-lived "kinks" in the IMF (Crooker et al., 2004; Heidrich-Meisner et al., 2016). We check suprathermal electron pitch angle data from WIND-3DP to verify if the strahl is flowing sunward or anti-sunward at these times. In the case of a kink we expect the alignment of otherwise anti-sunward strahl to be consistent with a sunward beam (anti-parallel strahl in the case of anti-sunward IMF, and parallel strahl in the case of sunward IMF). If the presence of sunward strahl does not indicate that a > 8 hour deviation

in field polarity during a period is a result of kinked IMF, then we do not consider the time period in this study.

Following the above selection process, 14 time periods are identified for study which meet all of the above criteria. A further 4 periods are selected which have some apparent ICME activity for a fraction of the time, which we also study. The following sections discuss only these 18 periods.

5.4 Results

In this section, we present the results from our simple solar wind model, and for the observations of the 18 events which are studied in this chapter. First, we examine the sizes of intermediate composition streams arising solely from changing connectivity at the Sun and differential streaming of heavy ions, as predicted by the model. Next, we outline some basic relevant *in situ* properties for the streams which correspond to the events selected in the previous section. Following this, we evaluate the accuracy of the two-step backmapping technique for each event's fast stream, by comparing *in situ* stream features with remote sensing features in the EUV. In particular we compare the accuracy of the mapping using both Δt_c and Δt_a for the ballistic step. Finally, we identify the source regions and source region properties of the ICS solar wind for each event, and compare this to different *in situ* properties of the corresponding streams. Discussions of these results are presented in subsequent sections.

5.4.1 Simple Solar Wind Model Results

We now present the relevant results of mixed composition region durations, resulting from minor ion differential streaming and footpoint motions, as produced by our simple solar wind model. First, we verify the model against the more complex model of Schwadron et al. (2005). We then find the sizes of intermediate regions

which are produced as a result of steady footpoint motion resulting from differential rotation across a range of footpoint latitudes. We also investigate the effects of footpoint motion through interchange reconnection between a coronal hole and a neighbouring active region.

Comparison of Modelled Composition with Previous Results

By selecting the appropriate model inputs, and generating a synthetic time series at 5 au, we compare the duration of an intermediate composition region, produced from differential streaming in the model, to that found in Schwadron et al. (2005). The relevant initial conditions are $v_{\mathrm{slow}} = 400\,\mathrm{km\,s^{-1}}$, $v_{\mathrm{fast}} = 750\,\mathrm{km\,s^{-1}}$, and latitude $b = 75°$. Schwadron et al. (2005) find the duration of the intermediate region resulting from these conditions to be ~ 1.8 days, while we find it to be ~ 2.0 days. Our simple model is thus able to produce a comparable result to the far more complex MHD model of Schwadron et al. (2005), and so we proceed with some confidence that it can produce sensible values for other heliospheric distances and latitudes for the rest of the study.

Low-Latitude Intermediate Regions at 1 au from Footpoint Motion

To give useful predictions for the effects of differential streaming observed at 1 au, we now attempt to apply our model using differential rotation rates more often found at lower latitudes. As differential rotation is greatly reduced at the equator, this results in considerably lower footpoint motion rates from Equations B.2 and B.3. Solar wind observations in the ecliptic usually originate from solar wind sources within a photospheric latitude band of around $\pm 30°$ about the rotational equator, so latitudes within this range are of key significance for our observations made in this chapter.

Figure 5.6 shows model outputs at combinations of initial v_{fast} and v_{slow} with each

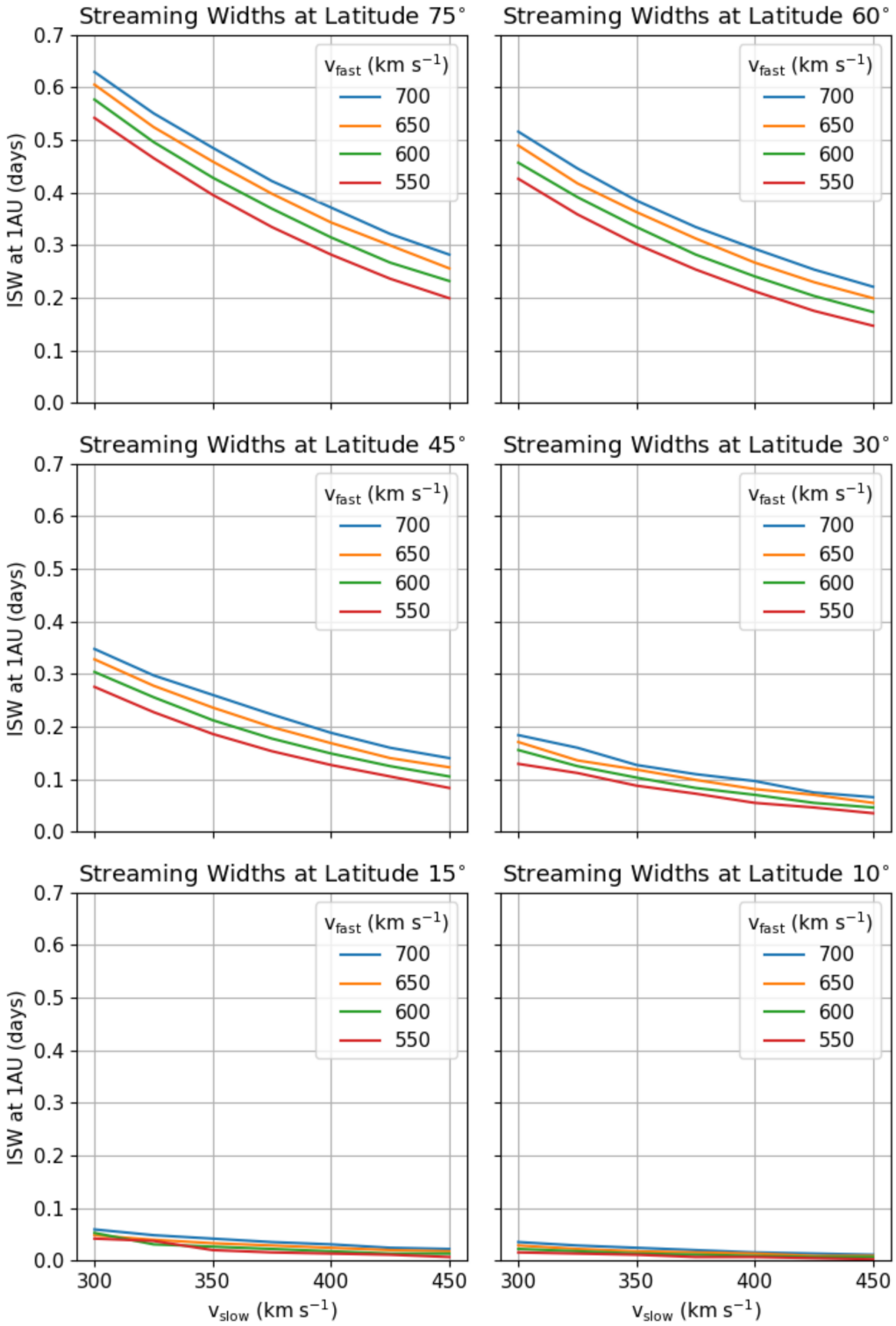

Figure 5.6: Outputs of intermediate region *in situ* width (ISW) in days, derived from the simple solar wind model. Each panel corresponds to a different footpoint source latitude, and plots lines of output ISW against input v_{slow}, where each line corresponds to a different value of v_{fast}. ISW approaches zero with decreasing latitude due to the reduced footpoint motion. Greater differences between v_{fast} and v_{slow} produce larger values of ISW.

panel corresponding to a different latitude. We plot curves of the *in situ* width (ISW) of the resulting intermediate composition region against v_{slow}, with the different lines corresponding to different values of v_{fast}. At all latitudes, slower v_{slow} and faster v_{fast} streams result in wider intermediate regions. This is because a greater difference in speeds leads to an expanded rarefaction region, where the intermediate composition is found.

With decreasing latitude, we observe a decrease in all streaming region widths for each pair of v_{fast} and v_{slow}. This is due to the decrease in the magnetic footpoint angular velocity, $\omega_{\text{fp}} = -(\Omega_{\odot} - \omega)$ (see Equation B.3), which accompanies decreasing latitude.ω is the photospheric differential rotation rate, which follows an exponential sinusoid relationship with latitude (from Equation B.2). As a result of this relationship, a far smaller value of ω_{fp} is produced at low latitudes. At latitudes below 10° (the lowest shown in Figure 5.6) the footpoint motion is not sufficient to produce an intermediate composition region. It is then likely true in reality that footpoint motion is too minor at such latitudes to produce any significant mixing by the time ions reach 1 au. In the ranges of latitudes from which we expect to encounter solar wind in the ecliptic plane (0–30°) ISW ranges from values of $\sim$ 0–0.2 days.

Emerging Active Region Interchange Reconnection

Interchange reconnection presents another mechanism by which the magnetic footpoints of solar wind plasma can change connectivity to a different source region, potentially leading to the mixing of distinct composition signatures along the field line. Importantly, not all forms of reconnection rely explicitly on differential rotation as their driver and so these processes might produce significant mixing, even at low latitudes where footpoint motions might be less significant. We can model gradual reconnection similarly to the footpoint motion case, with a modified rate of footpoint motion to describe the steady reconnection of flux. Such reconnection has

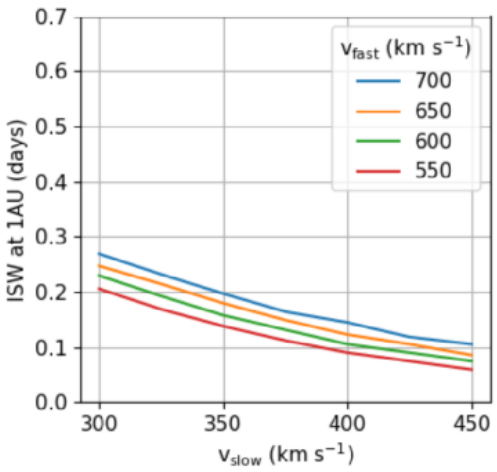

Figure 5.7: Outputs of intermediate region *in situ* width (ISW) in days, derived from the simple solar wind model, for the change in footpoint connectivity resulting from an example of interchange reconnection between an emerging active region and a coronal hole. The format is identical to that for a single panel of Figure 5.6. The rate of footpoint motion from the CH to the active region is thought to be equivalent to that of footpoint motion for a coronal hole at $\sim 38°$ (details in text). The behaviour is similar to that shown for latitudes of 30° and 45° in Figure 5.6.

been observed in the form of interchange between an emerging active region and an adjacent coronal hole by Baker et al. (2007), and so we apply our model to a similar case.

In Baker et al. (2007), the authors observed the retreat of the eastward boundary of a coronal hole, as the open flux there was closed by interchange reconnection with an emerging bipolar active region (see Chapter 2 for details). The open heliospheric flux originally connected to this coronal hole was then presumably rooted in the neighbouring active region - a source of higher charge state plasma and characteristically closed-field composition. The coronal hole boundary was observed to retreat by $30''$ west of the active region, and $60''$ to the south-west, over the course of around 2.4 days. Given the position of the boundary on the disk, we estimate that this corresponds to a heliographic distance of $\sim 2.44°$, or a rate of around 1 °day^{-1} in the low corona. From inverting Equation B.2 we see that this is equivalent to the footpoint motion rate we would expect at a latitude of 38°.

Figure 5.7 shows the result of applying the interchange reconnection rate measured by Baker et al. (2007) in the solar wind model. We plot intermediate widths at 1 au for different pairs of fast and slow streams, as again the widths depend strongly on the size of the rarefaction which forms between streams. As expected, the results

lie between those produced using footpoint motions between latitudes of 30° and 45° as shown in Figure 5.6. The range of ISW values predicted here range from ~ 0.05–0.3 days.

To summarise, we have developed a simple solar wind model which predicts the sizes of intermediate charge state regions, which exist near the ecliptic plane, at 1 au. These regions result purely from mixing of ions, enabled by minor ion differential streaming, as opposed to originating from intrinsically intermediate composition sources. For footpoint motions resulting from photospheric differential rotation, we expect the durations of the resulting intermediate regions to be on the order of $\sim$ 0–0.2 days). From a case study of the event from Baker et al. (2007), when the connectivity changes as a result of interchange reconnection, we expect a region of duration of $\sim$0.05–0.3 days. We shall discuss these results in Section 5.5.3.

5.4.2 Events and Stream Properties

Here we shall describe the observations which cover the 18 events of this study, and summarise some of the important charge state properties for each. The main results for this section are contained in Table 5.1. Columns 1–8 contain basic observational properties of each event from the *in situ* and remote sensing data. "#" labels each period with a number, and "*" distinguishes those which contain ICME signatures, as described in Section 5.3.3. The date of the AIA-193 Å image which is used for each event is listed under the column header t_{IMG}. Unless stated otherwise, the image used simply corresponds to the image taken nearest to 00:00 (UTC) on the date given by t_{IMG}. Column CR lists the Carrington rotation number which applies to each period. In the case that the period extends over two Carrington rotations, CR refers to the rotation which applies to the majority of the period. Column t_{fast} is the time of the start of fast solar wind as measured by ACE ($> 500\,\mathrm{km\,s^{-1}}$) in each period studied. If there are multiple sub-periods of fast wind ($> 500\,\mathrm{km\,s^{-1}}$), then

Table 5.1: Data for the 18 periods studied in this chapter. The entries are explained in the key below.

#	t_{IMG}	CR	t_{fast}	FT	$\mathrm{C_{low}}$	$\mathrm{C_{high}}$	Δt_i	S_c	a	CHB	C+B	AR	θ_B
1	2016-09-26	2182	271.3	✓	0.23	0.79	1.02	×	×	✓	✓	×	21.61
2	2016-07-05	2179	190.0	✓	0.40	0.92	0.43	×	✓	×	✓	×	18.86
3	2016-06-09	2178	163.8	✓	0.36	1.11	0.50	×	×	✓	×	×	15.38
4	2016-04-20	2176	114.0	✓	0.43	0.74	×	–	✓	✓	✓	✓	-9.74
5	2016-03-24	2175	89.1	✓	0.36	1.40	1.54	✓	✓	✓	✓	×	-9.52
6	2016-01-03	2172	6.3	✓	0.31	0.61	1.23	×	✓	✓	✓	×	-10.66
7	2015-12-07	2171	340.8	✓	0.21	1.16	1.43	✓	✓	✓	✓	×	-9.28
8*	2015-10-31	2170	308.4	✓	0.30	0.89	2.08	×	✓	×	×	×	-2.76
9	2015-10-05	2169	281.5	✓	0.29	0.93	1.47	✓	✓	✓	✓	✓	-4.86
10*	2015-09-09	2168	255.0	×	0.17	0.96	1.23	✓	✓	×	✓	✓	10.11
11	2015-08-12	2167	228.8	✓	0.41	1.34	0.57	×	✓	✓	×	×	7.89
12	2015-03-31	2162	94.0	✓	0.44	1.40	0.93	×	✓	✓	✓	×	-7.39
13	2013-12-30	2145	3.8	✓	0.33	0.88	1.11	×	×	✓	×	✓	-7.23
14	2013-10-11	2142	289.3	✓	0.34	1.27	1.42	✓	✓	✓	✓	✓	-7.47
15	2013-09-14	2141	262.9	✓	0.28	1.32	0.95	×	✓	×	×	×	-1.67
16	2012-08-22	2127	238.6	×	0.23	1.29	0.77	×	✓	✓	×	✓	13.30
17*	2012-06-30	2125	182.9	✓	0.30	1.47	2.00	✓	✓	✓	✓	✓	14.79
18*	2016-06-03	2124	157.0	✓	0.23	1.28	2.16	✓	✓	✓	✓	✓	12.03

= event number (* indicates period with ICME) | t_{IMG} = date associated AIA image was taken (UTC) | CR = Carrington rotation number for t_{IMG} | t_{fast} = onset time of studied fast stream (DoY) | FT = Flat-top present in stream | $\mathrm{C_{low}}$ = mean $\mathrm{C^{6+}/C^{5+}}$of fast stream | $\mathrm{C_{high}}$ = mean $\mathrm{C^{6+}/C^{5+}}$of slow stream | Δt_i = size of intermediate region following fast stream (days) | S_c = ICS region has some splitting *in situ* | a = acceleration scheme improves mapping as in Section 5.4.3 | CHB = ICSs map to eastward coronal hole boundary partially or fully | C+B = sourcepoints map to both the coronal hole centre and coronal hole boundary | AR = active region eastward, and within 20° of CH | θ_B = latitude of sourcepoint boundary crossing (°)

t_{fast} refers to the first. We identify each period in which there is a flat-top present in the solar wind speed, and record this under column FT in Table 5.1. Following similar observational criteria to Borovsky (2016), we identify periods of > 1 day as a flat-top when: 1. Solar wind speed $v_p > 500\,\mathrm{km\,s^{-1}}$. 2. There is long-timescale variation of $< 100\,\mathrm{km\,s^{-1}}$. 3. These velocity signatures end in a systematic decrease to $v_p < 500\,\mathrm{km\,s^{-1}}$. The flat-top spans the times between the initial velocity increase to $> 500\,\mathrm{km\,s^{-1}}$, and the beginning of the systematic decrease which will bring it to below $500\,\mathrm{km\,s^{-1}}$. Defining this flat-top is important as we shall use it later as a metric for the success of the backmapping technique.

While work has been done which splits solar wind by origin into different charge state categories (Zurbuchen, 2002; Zhao et al., 2009; Heidrich-Meisner et al., 2016),

we do not apply a global cutoff to define our low and high charge state regions in this study. We instead identify these regions independently for each period, as we observe a large spread across events in the values of charge state which map to inside and outside of coronal holes, and are observed inside and outside of fast solar wind streams. We define C_{low} (C_{high}) as the mean value of C^{6+}/C^{5+} in the low-C^{6+}/C^{5+} (high-C^{6+}/C^{5+}) region of the stream of interest in each period, and record them in Table 5.1. Similarly, we define σ_{low} and σ_{high} as the corresponding standard deviations of C^{6+}/C^{5+} in these streams (these values are not recorded in the table).

The extent to which we observe ICS, and intermediate composition in general, must be controlled by a combination of source region properties, and any processes which could result in the mixing of distinct regions of composition during transit. For each period we thus quantify the duration, Δt_i, of the transitional ICS region which lies to the trailing edge of the fast solar wind stream. We identify first the region between C_{low} and C_{high}, for which the criteria $C^{6+}/C^{5+} > C_{low} + \sigma_{low}$ and $C^{6+}/C^{5+} < C_{high} - \sigma_{high}$ is true, as the initial guess at the transitional region. We then inspect this region, and accept this guess if it presents one continuous time period between the two clear streams. Often between the C_{low} and C_{high} regions, however, C^{6+}/C^{5+} dips in and out of the criteria band as a result of the variability of the data. In such cases we manually define the transitional region as starting at the first instance where this criteria is met towards the end of the C_{low} period, and ending at the last, towards the start of the C_{high} period. Some of the resulting transitional regions will thus contain data points which we would otherwise define as typically low or high in C^{6+}/C^{5+}.

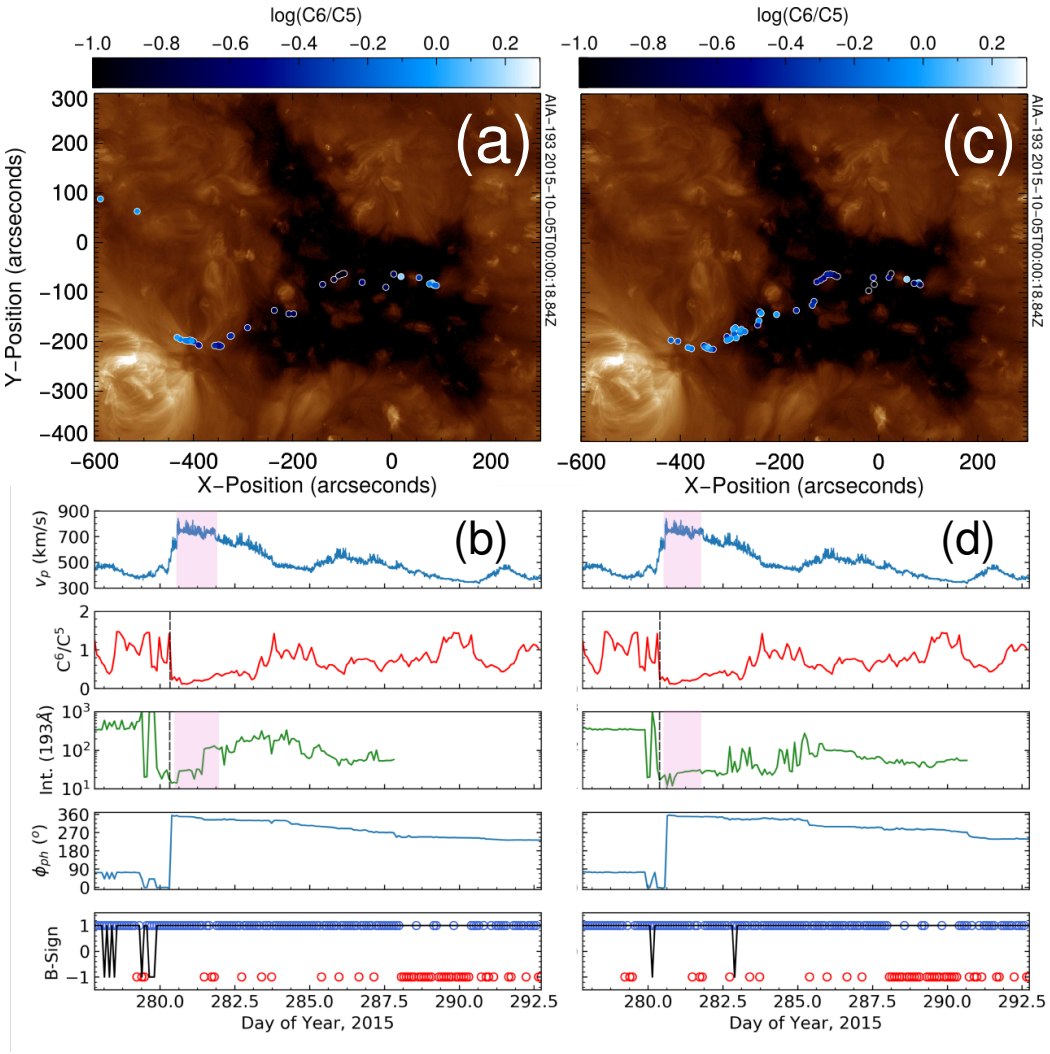

Figure 5.8: Combined time series and image plots of Event 9. Plots (a) and (c) show a sub-field of the AIA-193 Å image of the coronal hole source region for this period. The time of the image is as indicated by t_{IMG} in Table 5.1. Overplotted on Panel (a) are sourcepoints calculated from the two-step backmapping procedure, using solar wind travel time Δt_c. Panel (c) shows these sourcepoints as calculated instead using Δt_a. The sourcepoints are coloured according to the value of $\log \mathrm{C}^{6+}/\mathrm{C}^{5+}$ associated with the corresponding *in situ* measurement. Panel (b) displays *in situ* data associated with Event 9, in addition to remote sensing and modelled data associated with it based on the mapping using Δt_c. The top panel plots the solar wind bulk velocity v_p, while the next panel shows $\mathrm{C}^{6+}/\mathrm{C}^{5+}$. For each data point in the $\mathrm{C}^{6+}/\mathrm{C}^{5+}$ dataset, the third panel plots the intensity of the AIA-193 Å image in (a) which corresponds to that sourcepoint. This shows which data points map to inside or outside the the coronal hole. The fourth panel shows the longitude at the photosphere, ϕ_{ph} of the sourcepoint associated with each $\mathrm{C}^{6+}/\mathrm{C}^{5+}$ data point. This shows where significant changes in mapping location occur. The fifth panel shows the *in situ* polarity of the IMF, where 1 is anti-sunward (blue points), and -1 is sunward (red points). The solid black line plots the polarity of the mapped PFSS magnetic field which is associated with each *in situ* data point. Panel (d) shows the same information as (b), but with the associated mapped data based instead on backmapping with a time shift of Δt_a.

5.4.3 Mapping Adjustment

This section presents backmapping results from a critical standpoint. In particular, we shall evaluate the success of mapping fast solar wind streams back to their expected coronal hole sources, and whether the accuracy of the mapping is best when the solar wind propagation time is taken to be Δt_c or Δt_a. Figure 5.8 presents an example of combined remote sensing and *in situ* observations, for the time period labelled as Event 9 in Table 5.1. Panel (a) shows a subsection of the AIA-193 Å image, cropped to the source coronal hole, and part of the neighbouring eastward active region. Sourcepoints resulting from a two-step mapping using the constant-velocity timelag Δt_c from Equation 3.6 are plotted over the image, coloured based on the value of $\log \mathrm{C}^{6+}/\mathrm{C}^{5+}$ from the ACE-SWICS *in situ* data.

Panel (b) plots corresponding *in situ* data, as well as corresponding values extracted from the PFSS model and AIA-193 Å image, as a time series at L1. The top two panels plot v_p and $\mathrm{C}^{6+}/\mathrm{C}^{5+}$ as measured at ACE. The flat-top region of v_p is highlighted in pink, while the leading boundary in $\mathrm{C}^{6+}/\mathrm{C}^{5+}$ is marked by the dashed line. The next panel shows the intensity of the AIA-193 Å image, in arbitrary units, which corresponds to each mapped $\mathrm{C}^{6+}/\mathrm{C}^{5+}$ data point as it is shown in (a). The coronal hole which is visible in the image is identifiable in the time series as the region which has intensity of < 50. (We note that as these are arbitrary units not all coronal holes in this study are characterised by this threshold.) The fourth panel plots the Carrington longitude of the mapped sourcepoints of the ACE-SWICS data at $1\,\mathrm{R}_\odot$, ϕ_{ph}. This allows tracking of the rough location of the sourcepoints across the solar surface, and clearly shows when the solar wind connectivity moves rapidly from one location to another. The fifth panel plots the *in situ* IMF polarity in terms of anti-sunward (1) or sunward (-1) flux, as described in Section 5.3.3, as blue and red circles. The PFSS polarity at the backmapped location is also plotted, as a solid

line. As discussed in Section 5.3.3, we expect the two to agree if the mapping is broadly correct. Panels (c) and (d) of Figure 5.8 show the same information as panels (a) and (b) respectively, but applying the timelag of Δt_a from Equation 3.8 to the mapping.

Figure 5.8 displays our time series using the time at which the *in situ* measurements were taken at L1, as opposed to the times at the source surface produced from the mapping. This shows the *in situ* data clearly, as it is absent of dwells and other backmapping artefacts (Figure 3.4). However, the data taken from remote observations appear distorted when viewed this way, as they are extracted based on the source surface coordinates following backmapping. The alternative, plotting the data instead as a function of time at the source surface, or as a function of source surface longitude, will make the data derived from backmapping clearer, but then the data taken at L1 will themselves be distorted.

We address first the constant-velocity mapping shown in Figure 5.8(a, b); panel (a) shows that the sourcepoints for the fast stream in this period map to within the vicinity of the coronal hole as expected. This shows a success of the mapping to the first-order. Further, the low-charge state portion of the stream also maps to near the coronal hole. Panel (a) shows the coolest C^{6+}/C^{5+} solar wind mapping to approximately the centre of the sourcepoint path across the coronal hole. C^{6+}/C^{5+} appears to transition from cool to hot values beginning at the point where the sourcepoints cross the coronal hole boundary; reaching hot values as the sourcepoints map to the north-west of the neighbouring active region. Panel (b) gives further details on these results. From the time series of v_p, it is clear that while the fast stream maps close to the coronal hole, the flat-top in particular only appears to partially map to the coronal hole proper; the remainder appears to map to the coronal hole boundary approaching the active region. The rapid drop of C^{6+}/C^{5+} which we expect to correspond to the transition from a NCH to CH source also appears to occur at

a sourcepoint already well-within the coronal hole. These two features point to a possible deficiency in the mapping; in both cases a shift in the backmapping time lag Δt to a longer propagation time would better align these solar wind and coronal features.

Panels (c) and (d) of Figure 5.8 show the results using the propagation time Δt_a, to contrast with results in panels (a) and (b). Panel (c) shows the same image as panel (a), with different sourcepoint locations across the coronal hole as a result of the altered mapping. We note that the mapped location of the lowest C^{6+}/C^{5+} values, which *in situ* occur towards the beginning of the flat-top region, are now located more towards to the leading (westward) edge of the CH.

In panel (d), v_p, C^{6+}/C^{5+}, and the *in situ* magnetic field sign are identical to those in panel (b), as we are plotting against the time of the *in situ* measurements at ACE. However the mapping positions for the sourcepoints of the *in situ* data change, so the time history of mapped pixel intensities, ϕ_{ph}, and the PFSS field direction are altered. The coronal hole now apparently corresponds to a greater period of time, meaning that more of the solar wind data points are mapped to within it. The location of its leading boundary is also apparently shifted backwards in time, indicating that the longer propagation time Δt leads to earlier-observed plasma mapping to this edge. The flat-top region of v_p now fully maps to within the coronal hole proper, as highlighted in pink. If we accept that the flat-top portion of the stream represents the unperturbed coronal hole wind (as in Borovsky, 2016), then we should expect it to map to the coronal hole proper in the case of an ideal mapping. The consistent high velocity of the flat-top indicates that it is likely from the central regions of the coronal hole, and not the boundaries across which the smooth expansion of field lines in the corona should lead to a smoothly varying velocity. We can thus judge a successful coronal hole mapping by the degree to which the flat-top maps to within the centre of the coronal hole. Further, we note that in this mapping, the rapid drop

Table 5.2: Comparison of performance of mapping under a constant velocity assumption c with that under an accelerating assumption a. For each time period 1–18 the mapping which produces better agreement of different features (detailed in the key and elaborated in the text) is marked by a for acceleration, c for constant speed, $\sim$ when the two are comparable, and $-$ when the feature is absent. Events with ICME periods within them are denoted *.

	1	2	3	4	5	6	7	8*	9	10*	11	12	13	14	15	16	17*	18*
FT	c	$\sim$	c	a	a	a	a	a	a	$-$	a	a	c	a	a	$-$	$\sim$	a
C^{6+}/C^{5+}	c	a	a	a	c	$\sim$	a	a	a	a	a	a	c	c	a	a	a	a
$B_{CH(B)}$	$\sim$	$\sim$	$\sim$	$\sim$	$\sim$	$\sim$	$\sim$	$\sim$	$\sim$	$\sim$	$\sim$	$\sim$	c	$\sim$	$\sim$	$\sim$	$\sim$	$\sim$
B_{NCH}	c	c	c	$\sim$	c	$\sim$	c	c	$\sim$	c	$\sim$	c	$\sim$	$\sim$	$\sim$	$\sim$	a	$\sim$

FT = flat-top alignment | C^{6+}/C^{5+}= charge state-drop alignment
$B_{CH(B)}$ = PFSS-IMF polarity agreement in the CH/CH boundary of interest
B_{NCH} = PFSS-IMF polarity agreement outside of the CH/CH boundary of interest

in C^{6+}/C^{5+} at the leading edge of the fast stream now also aligns closer to the leading edge of the boundary. By these metrics, which only indicate the quality of the mapping for the fast stream, it appears that the travel time Δt_c for the mapping is inferior to Δt_a for Event 9.

Other authors (Neugebauer et al., 1998; Fazakerley et al., 2016) have relied upon the polarity-agreement between *in situ* and PFSS magnetic field to support their backmapping. This primarily indicates an agreement on the location of the HCS. Crossings of the HCS are typically embedded in slow solar wind (Zhao et al., 2009), and so we argue this test of the mapping is generally less useful for fast wind and coronal holes (beyond cases where the results are catastrophically incorrect; leading to completely different regions on the Sun). Testing the mapping by instead using the alignment of EUV coronal hole features with *in situ* velocity and composition data provides support for successful mapping for fast solar wind streams. To our knowledge this is the first time this alignment has been used to test the effectiveness of a backmapping technique, and we now apply it to judge the successful mapping of all 18 events in the study.

Table 5.2 compares the agreement of different *in situ* features with features in the

EUV image and PFSS magnetic field after mapping using both propagation time assumptions (Δt_c and Δt_a, as described above) for periods 1–18. Cases where agreement is better (the ways in which the 'better' agreement is chosen are defined below for each metric) using Δt_c are denoted 'c', while those where it is better using Δt_a are denoted 'a'. When neither assumption is clearly better (e.g., when the flat-top maps fully to within the coronal hole using both Δt_c and Δt_a), the case is marked with '$\sim$', and when the feature is not present in the event in question, it is marked with a '$-$'. We include ICME events (denoted by '*') but do not consider the agreement of any features which occur during ICME times within these events.

For entries under the 'FT' column of Table 5.2, we choose the scheme which maps a larger portion of the flat-top as measured at L1 (i.e., the most data points), into the coronal hole as identified by the low-intensity region of the AIA-193 Å time series. Events 10 and 16 are marked '$-$' as they do not possess a flat-top by our selection criteria, and so are not eligible for this test. In 11 out of 16 remaining eligible events, the Δt_a scheme maps a greater portion of the flat-top into the coronal hole, compared to the 3 out of 16 which are mapped better with Δt_c. Excluding ICME events, 9 of 12 eligible events align better with Δt_a, compared to 3 with Δt_c. Based on the mapped location of the flat-top then, the accelerating velocity profile appears to be most suitable. Examining the time series directly, the periods 1 and 13, the timeshift of Δt_a appears to shift the flat-top partially across the westward edge of the coronal hole; overshooting it.

The mapping schemes which place the sharp drop in C^{6+}/C^{5+} closest to the sharp drop in intensity at the edge of the coronal hole are judged to be the 'best', and are shown for each event in the row labelled 'C^{6+}/C^{5+}' in Table 5.2. In 11 out of 18 cases the Δt_a maps these boundaries closer together, compared to 4 cases for Δt_c. Again excluding ICME events, 9 out of 14 cases are closer with Δt_a, while 4 cases are closer with Δt_c. Again, the accelerating velocity profile appears to perform

marginally better. The cases 1 and 13, marked *c* for 'FT', are again marked as *c* in 'C^{6+}/C^{5+}', with two additional periods now marked *c*. In both of these latter cases the sharp drop of C^{6+}/C^{5+} occurs earlier than the beginning of the flat-top, and overshoots the edge of the coronal hole when using Δt_a.

In the final two rows, $B_{CH(B)}$ and B_{NCH}, the 'best' mapping is that for which the most data points (in the the coronal hole/coronal hole boundary regions for $B_{CH(B)}$, and other regions of the *in situ* data for B_{NCH}) have an *in situ* polarity which agrees with the corresponding PFSS polarity. The former are regions of interest, and in all cases but one the agreement is identical between Δt_a and Δt_c schemes. This event has better agreement using Δt_c, and is also better mapped in FT and C^{6+}/C^{5+} using Δt_c. We cannot distinguish a most suitable mapping for the rest of the events based on $B_{CH(B)}$, as the CH(B) periods for the other events are unipolar. This illustrates that testing the mapping based on polarity of the field is not sufficient for coronal holes, and other regions unlikely to contain current sheets.

B_{NCH} is included for completeness, and shows that in 6 out of 14 non-ICME cases, Δt_c mapping performs better for mapping non-fast solar wind streams than Δt_a mapping, which is better in only one case.

We combine the results above to determine the most accurate backmapping scheme for each time period. For each period we use the entries in Table 5.2 to decide whether the most accurate mapping is produced by using Δt_c or Δt_a. We give preference first to the entry in the 'FT' row; periods marked with '*c*' are considered to be best mapped overall by Δt_c, and those with entry '*a*' with Δt_a. For the periods for which 'FT' does not indicate '*c*' or '*a*', we then defer to the entry in the 'C^{6+}/C^{5+}' row. We do this as the flat-top criteria for the mapping is based on the agreement over a range of times, while the C^{6+}/C^{5+} criteria is based only on one time; the sharp drop. With this order of priority it is unnecessary to include B_{NCH} as it does not apply to fast solar wind streams and coronal holes. From this process, a total

of 15 out of 18 (11 out of 14 non-ICME) periods are judged to map better under the time shift of Δt_a, while 3 out of 18 (3 out of 14 non-ICME) periods map better under Δt_c. Periods where Δt_a is the preferred mapping scheme are recorded with a tick in the column labelled '*a*' in Table 5.1. Overall, the mapping for the majority of solar wind streams of interest in this study is improved when backmapping using a velocity profile of $v = Kr^{1/4}$, resulting in a backmapping time of $\Delta t_a = \frac{4}{3}\Delta t_c$.

5.4.4 Solar Wind Boundaries

The results presented in this section are predicated on a backmapping technique with drawbacks discussed in Chapter 3, Section 3.6. We note that the technique likely has inaccuracies such that direct "point-to-point" comparisons of the solar wind properties at a given time to some feature (a structure in the corona or emission at some point) at the precise location which it maps to under the two-step procedure cannot be absolute. While we do draw on these comparisons in this section, we avoid forming conclusions based on any single point-to-point comparison. Instead, we compare locations of collections of sourcepoints, associated with particular solar wind streams or substreams, to broader regions on the Sun, such as the centre, boundary, or outside of a coronal hole. To supplement results achieved in this way, we also perform "feature-to-feature" comparisons, either to the properties of many solar wind data points related to a given broader location at the Sun, or of some feature in the solar wind data (values of different parameters, sizes of different regions) to variations along the 'path' of the mapped sourcepoints across the Sun. Comparing the 'path' of the sourcepoints is likely more trustworthy than point-to-point comparisons, as the path taken does not rely on the distribution of points in longitude along the model source surface (which is subject to the many uncertainties of the ballistic portion of the mapping). These comparisons are likely to be more robust in the face of possibly large unquantified uncertainty in the mapping

technique.

Boundary Erosion from Differential Streaming

As previously discussed, solar wind footpoint motions across coronal hole boundaries, resulting in compositional mixing through heavy ion differential streaming, may be partially responsible for the size and structure of ICS regions observed during this study. First considering the durations of the ICS regions for the 18 events observed, Δt_i, we find a mean value of around 1 day. Values typically span from $\sim$ 0.5–2 days. These durations appear to be too long to be explained through mixing resulting from footpoint motions and differential streaming alone, based on the theoretical ICS durations calculated in Section 5.4.4. An additional cause of ICS solar wind seems to be required.

The extent of ICS regions resulting from footpoint motions and differential streaming for each event can be inferred from the source region latitude, since this controls the footpoint motion rate at the Sun through Equations B.2 and B.3. This is illustrated between the different panels of Figure 5.6. We determine the Carrington heliographic latitudes at which the sourcepoints of the mapped solar wind appear to cross the coronal hole boundary for each event, and record these in the column θ_B of Table 5.1. The absolute values of θ_B span from a few degrees to around 20°, and average at around 10°. Footpoint motion resulting from differential rotation at these latitudes is expected to be relatively weak.

Charge States at Coronal Hole Boundaries

We now examine the mapped source regions of the ICS solar wind for the 18 periods in question. Figures 5.9 and 5.10 show the full-disk image associated with each event, with the inferred source coronal hole at approximately central meridian. For each period, the sourcepoints of ICS solar wind data points are plotted over the

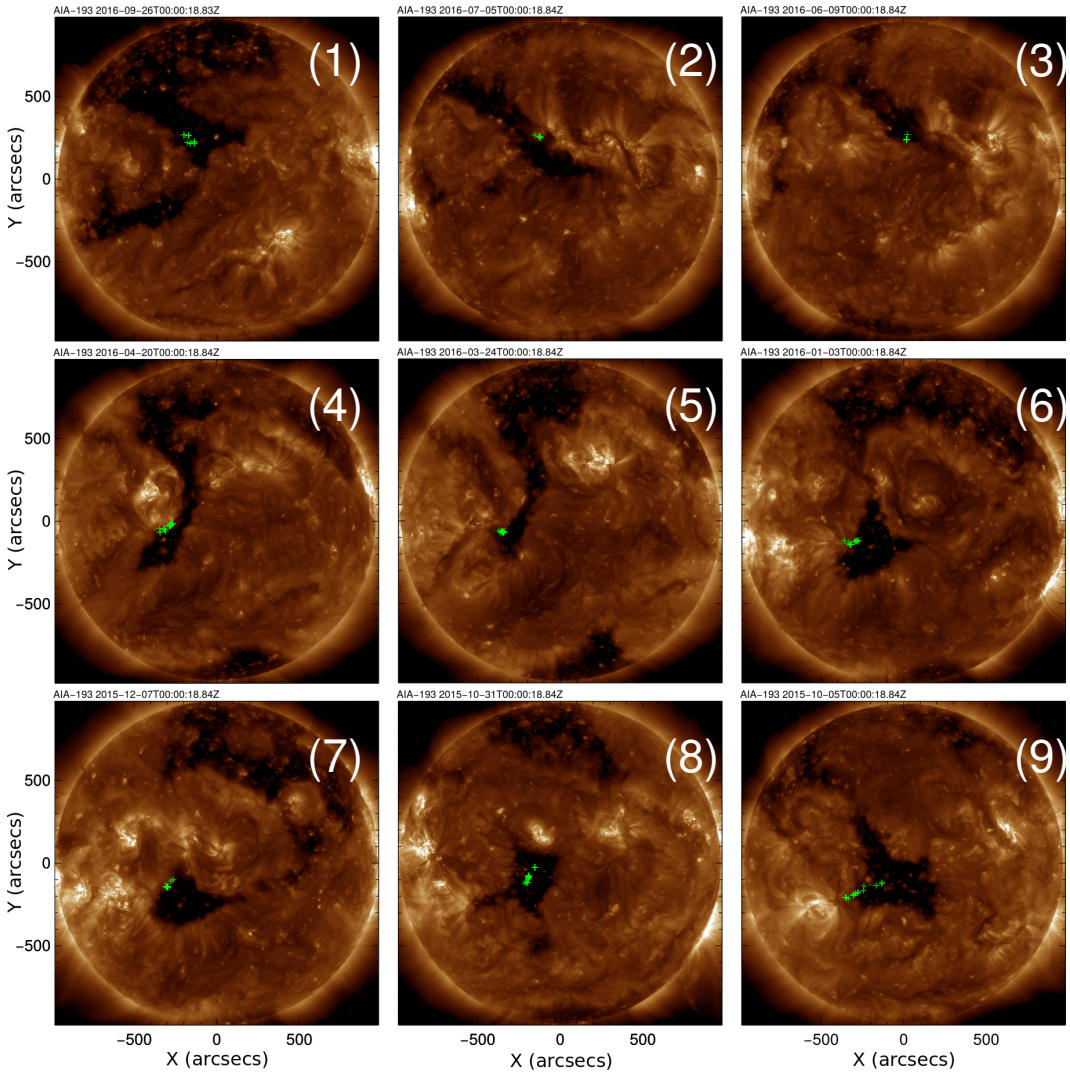

Figure 5.9: AIA-193 Å images of backmapped source coronal holes for events 1–9 as labelled in Table 5.1. Sourcepoints of solar wind measurements which display intermediate values of C^{6+}/C^{5+} are plotted in green.

corresponding image. These sourcepoints are produced by mapping using either Δt_c or Δt_a based on the preferred backmapping scheme indicated by the column labelled '*a*' in Table 5.1. The ICS regions are selected as described in Section 5.4.2. From these figures, 14 of 18 events contain at least one intermediate-wind sourcepoint which maps to the vicinity of the trailing coronal hole boundary, while 4 do not. Of these 4, 3 show the ICSs mapping inside the coronal hole but not at the trailing edge, while one shows the ICSs mapping entirely outside of the (comparatively small) coronal hole. Excluding ICME-associated periods, 12 of 14 events map ICSs to

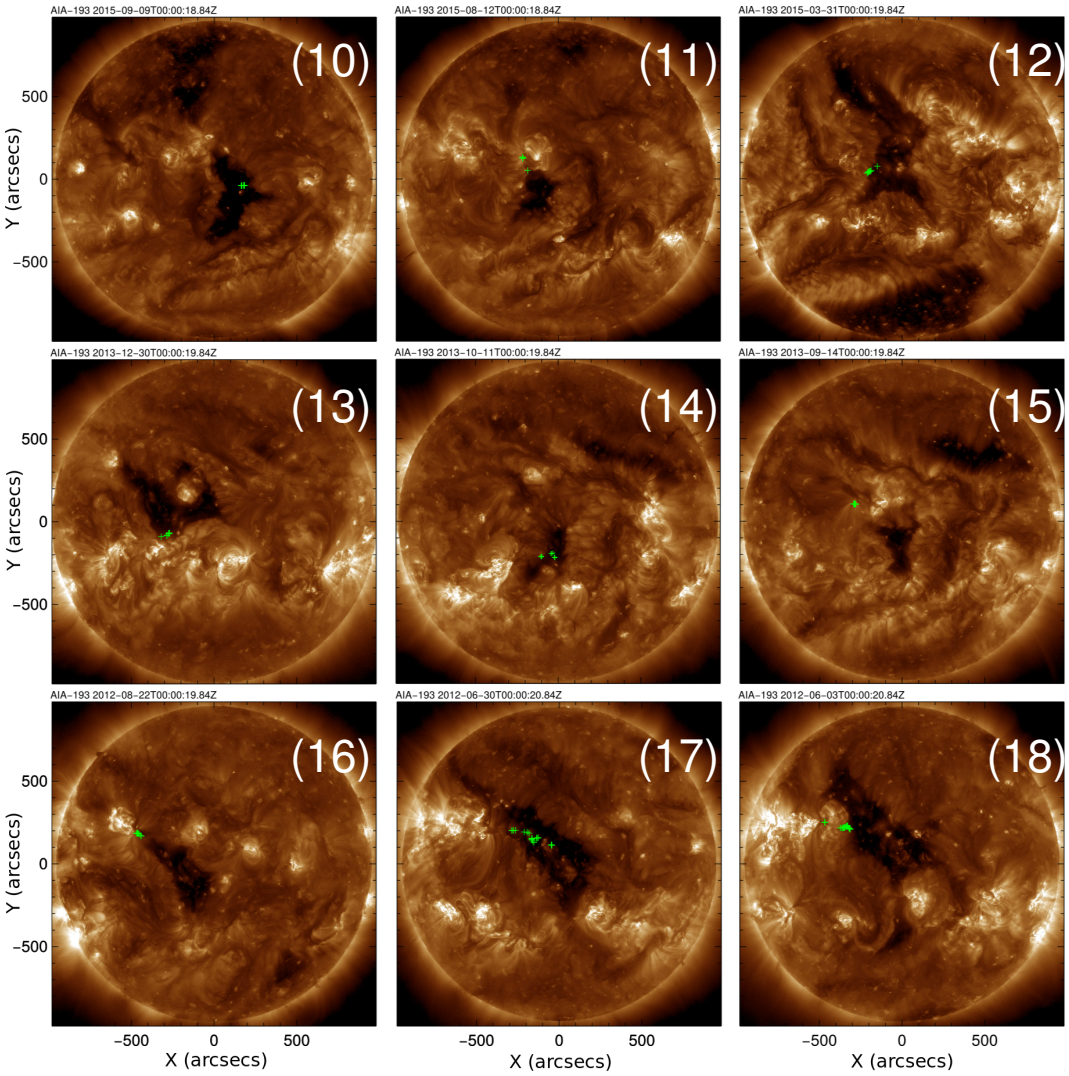

Figure 5.10: Images and sourcepoints for events 10–18 in the same format as Figure 5.9.

near the coronal hole boundary, while 2 of 14 do not. These results are recorded for each event in the column CHB of Table 5.1.

Finding that intermediate composition is most often associated with the coronal hole boundary is consistent with the different hypotheses for its origins laid out in Section 5.1.2. We must note however that in several periods (events 11, 13, 16) within our database, all of the sourcepoints from the fast stream and trailing region map to the boundary of the coronal hole, regardless of charge state. Discounting also these cases we are left with 9 of 11 eligible, non-ICME, periods where ICS solar wind appears to be, at least partially, associated with the boundaries of EUV

coronal holes. Of these cases, only Events 9 and 11 do not have the majority of ICS sourcepoints located at the boundary; many are instead located towards the centre (Event 9) or outside (Event 11) of the coronal hole. Overall, these results suggest that these boundaries are indeed a source of solar wind which either has intermediate levels of ionisation at its source or becomes intermediate through some later process. Examining the 4 cases where no intermediate composition appears to originate from the eastward coronal hole boundary, it is not clear that Δt_i is significantly different to the other periods.

Indirect Mapping Results

In this subsection we perform feature-to-feature comparisons. First, disregarding the charge states assigned to each sourcepoint, we record for each event whether there are sourcepoints located both in the coronal hole proper, and at the coronal hole boundary, or in only one of the two. This is recorded under the C+B header in Table 5.1. While we have noted above that not all events map to the coronal hole boundary, all of the events are found to exhibit a transition in charge state, including intermediate values. Here we wish to differentiate those cases where the mapping suggests only one of these two sources (coronal hole or coronal hole boundary) are contributing solar wind, with those where Earth-directed solar wind appears to be released first from the coronal hole, and then the coronal hole boundary.

First comparing, in Table 5.1, data in the column labelled C+B to that labelled Δt_i, we do not find a clear relationship between the two. Next, C+B is compared to the structure of the ICS region observed *in situ*. We occasionally observe cases where there are apparently multiple distinct sub-regions within the intermediate region. These were also observed by Borovsky and Denton (2016), on either side of what they labelled the "charge state jump". An example of this phenomenon can be seen in the charge state profile in Figure 5.8. There appear to be two regions of ICS,

one which gradually increases from DoY ∼281.5–283, and one which then rapidly rises until 283.75. There are also cases where the ICS appears at a constant level, as opposed to a steady climb, with sharper gradients on either side. We classify both of these features as "split" intermediate regions. This splitting could be due to distinct sources or separate processes contributing ICSs, which are then observable as distinct sub-regions within the overall intermediate region. We record cases of split C^{6+}/C^{5+} charge state under the header S_c in Table 5.1. Comparing these periods to the C+B periods, we find that in events where the sourcepoints only fall into one source (coronal hole boundary or coronal hole centre) there is never a clear split in the intermediate charge state values. Of the events where the footpoints connect to both the coronal hole and coronal hole boundary, excluding ICME periods, 4 of the remaining 9 periods exhibit split intermediate regions. (Including ICME periods this increases to 7 out of 12. However, many exhibit ICME signatures around the intermediate regions which could lead to the apparent splitting.)

Intermediate Composition and Active Regions

Several of the events feature an active region adjacent to the inferred source coronal hole. As well as allowing mixing through the interchange reconnection process modelled in Section 5.4.1, active regions may also contribute plasma to the solar wind in their own right. We expect that rarefactions associated with coronal holes with active regions to their east are the most likely to be affected. In the column labelled 'AR' in Table 5.1, we record whether there is an active region adjacent (within 20°) of the eastward coronal hole boundary for each event. A total of 8 events meet this criterion, of which 3 exhibit ICME signatures, and one has no valid measure of Δt_i. The remaining 4 events do not exhibit a tendency towards an ICS size which is larger or smaller than those corresponding to non-AR events. Including the ICME-related events, the mean value of Δt_i is ~ 0.5 days greater when an active region is present than not, which would appear to be a result of the ICME

periods themselves, which occur near the trailing edge of the fast solar wind stream.

5.5 Discussion

This section consists of three parts. First, the results of testing the two-step backmapping technique for the events in this study will be discussed. The potential impact of the sources of uncertainty will be described qualitatively, and we will comment on their possible effects on the results presented in Sections 5.4.3 and 5.4.4. We offer explanations for, and discuss the implications of, the findings regarding the preference for an accelerated rather than constant velocity solar wind propagation time in the mapping technique. Second, we evaluate the results of intermediate composition region sizes from the simple solar wind model. Third, we will discuss the results pertaining to the source of the ICS solar wind. We shall explore the conclusions which may be drawn comfortably from the results, given the limitations of the method. The implications of these results for knowledge of the source of the solar wind, use of composition as a tracer of coronal properties, and observations which can be made by future heliospheric missions will also be discussed.

5.5.1 Backmapping Technique

Uncertainties and Limitations

As described in Section 5.1.2, the backmapping technique used in this study, though widely applied (by e.g., Neugebauer et al., 1998; Zhao et al., 2009; Ko et al., 2014; Culhane et al., 2014; Fu et al., 2015; Fazakerley et al., 2016; Heidrich-Meisner et al., 2016), has potentially severe limitations as a result of some of its simplifying assumptions. We qualitatively discuss which limitations of both the ballistic and PFSS steps of the mapping are likely to have a sizeable effect on results.

In Section 3.6, Chapter 3, we described the argument made by Nolte and Roelof (1973) which is the basis for the error estimate in ϕ_{ss} of $\pm 10°$. Briefly, this argument relies on the approximate cancellation of two sources of error: 1. The assumption of constant velocity (when the solar wind likely accelerates); 2. The assumption of no corotation (when corotation likely persists some way out into the heliosphere). The observation in Section 5.4.3, that the accelerating solar wind profile (Δt_a) tends to improve mapping for coronal holes, suggests that this cancellation may not occur as previously expected by Nolte and Roelof (1973). For this reason we do not apply this $\pm 10°$ error estimate to the results in this study.

In this study, dwells frequently coincide with the ICS regions following the mapping. We find that dwells (see Section 5.1.2) within the events in this study typically span 5–10° longitude at the source surface. Within the dwell, individual sourcepoints must be displaced relative to their "true" longitude. It is not possible to predict exactly how large this displacement should be without modelling the expansion of the solar wind and including stream interactions. The least that can be said is that the size, in longitude, of this displacement is likely on the same order as the size, in longitude, of the dwell, and so we expect that each mapped point in a dwell should have an uncertainty of $\sim 10°$ at the source surface; this is comparable to the uncertainty in the mapping predicted for all types of solar wind by Nolte and Roelof (1973).

In Section 3.6.2 of Chapter 3 we outlined the primary sources of uncertainty that are introduced into the backmapping procedure while tracing down magnetic field lines produced by PFSS modelling. We highlighted that the expansion of coronal magnetic field between the photosphere and source surface can potentially lead to large uncertainties in sourcepoint coordinates at $1\,R_\odot$. A result of this expansion is observed in the 'jumps" which sourcepoints make between widely separated regions, as exemplified in Figure 5.5, where mapping jumps from west (right) to east (left),

from a bright region to the leading coronal hole boundary. However, the longitudes at the source surface in this case are more-or-less continuous. The uncertainties are thus strongly dependent on the magnetic topology in the vicinity of each source-point. A simple way to quantify this uncertainty, or to make a best-estimate of the true source region, is to place a random array of points on the source surface around each location predicted by the ballistic model, and generate sourcepoints for each of these. Closely grouped sourcepoints would suggest a more robust mapping. This analysis should be investigated in the future.

The inability of the PFSS approach to describe non-potential, energy-storing mechanisms (see Chapter 3, Section 3.5) is in general a major limitation of this class of model. In this study however, the impacts of these effects are minimised, as we are primarily concerned with the large-scale open magnetic flux from coronal holes, which PFSS models adequately describe. An effect of the PFSS model on our mapping, which has not been explored in this thesis, is the choice of source surface distance, $R_{ss} = 2.5\,R_{\odot}$. Varying R_{ss} may improve the agreement between open flux and EUV coronal hole area (Linker et al., 2017), which was a factor in the selection process in Section 5.3.3. Applying a different R_{ss} may also affect the mapping quite drastically. Choosing the widely-applied $R_{ss} = 2.5\,R_{\odot}$ is likely justified for this study, as there is no consensus on the ideal value of R_{ss}, since the existence of a source surface is in itself an approximation. The height at which the solar wind plasma transitions from low to high β (the transition which is represented by the source surface) is also likely variable for different solar wind streams and sources. Applying a variable source surface height to the backmapping process would thus require a far more careful treatment.

We expect that the limitations to the mapping, described in the above sections for both ballistic and PFSS steps, should primarily result in offsets to individual sourcepoint longitudes. Therefore, results drawn from collections of sourcepoints, and

sourcepoint 'paths', should be more robust than those drawn from only point-to-point comparisons (Section 5.4.4). While none of these approaches are fully robust, by combining results for multiple events the impacts of non-systematic errors on our ultimate conclusions should also be reduced.

Mapping Time Lag

Based on the alignment of *in situ* velocity and charge state features with coronal features imaged at 193 Å, we find in Section 5.4.3 that the ballistic mapping of fast coronal hole solar wind is improved when a longer time shift, Δt_a, consistent with a wind which accelerates with r, is used instead of the typical time shift for constant velocity wind Δt_c. Specifically we use $\Delta t_a = 4\Delta t_c/3$, the delay for a radial acceleration of $v = Kr^{1/4}$; a fit to the Parker (1958) model from Burlaga (1967). Conversely, we also find that the use of Δt_a worsens the agreement between many PFSS-predicted and *in situ* observed current sheet crossings. We now explore the implications of these findings.

The result that mapping with Δt_a outperforms mapping with Δt_c suggests that the balance between interplanetary acceleration and corotation effects on the mapped longitude, ϕ_{ss}, is not as predicted by **?** for the periods in this study. As detailed in Section 3.6, these authors predict approximate cancellation of the effects of acceleration, $v = Kr^{1/4}$, and corotation below a radius of 0.1–0.25au, which they consider to be the "true" release radius r_0. Our results suggest either: solar wind acceleration is more gradual than $v = Kr^{1/4}$, corotation drops off rapidly below 0.1–0.25au, or some combination of the two.

In Section 3.6 we noted that Neugebauer et al. (1998) find results which are more consistent with the dropoff of corotation occurring within 2.5–3.25 $R_\odot$; significantly closer to the Sun than the 0.1–0.25 au suggested by Nolte and Roelof (1973). This suggests that we should assume $r_0 \sim 2.5$–$3.25\,R_\odot$ (~ 0.01 au). The solar wind (non-

corotational) travel time is very sensitive to a reduction in r_0 (see Chapter 3, Section 3.6.1), as the majority of the acceleration (assuming $v = Kr^{1/4}$) occurs below 0.1–0.25 au: $v(0.25\,\mathrm{au})/v(1\,\mathrm{au}) = 0.7$, while $v(0.01\,\mathrm{au})/v(1\,\mathrm{au}) = 0.3$. We can estimate the change in timeshift required to map to the source region given these lower values of r_0, by calculating the time for the solar wind to travel from 2.5 $\mathrm{R}_\odot$ to 0.1–0.25 au. Solar wind of velocity 600 $\mathrm{km\,s^{-1}}$ at 1 au is expected to have a velocity of 330–420 $\mathrm{km\,s^{-1}}$ at 0.1–0.25 au given the acceleration represented by Equation 3.7. The additional travel time should then be of the order of $\Delta t_+ = 0.5$–1.3 days, if we assume the same $Kr^{1/4}$ acceleration profile. For $v = 600\,\mathrm{km\,s^{-1}}$, $\Delta t_c/3 \sim 0.9$ days. Thus, the additional travel time of $\Delta t_c/3$ applied in this study is in the middle of the estimated delay time range Δt_+. We agree with Neugebauer et al. (1998), that the breakdown of the Nolte and Roelof (1973) argument for corotation effects cancelling with acceleration is a result of their overestimate of the "true" height of r_0.

Results testing mapping through the alignment of current sheet crossings (in the form of PFSS and mapped *in situ* field polarity; the column labelled B_{NCH} in Table 5.2) do not show Δt_a outperforming Δt_c. In only one instance do we find this to be the case. This may be a result of the HCS being typically embedded in slow solar wind (Zhao et al., 2009). It appears that while the mapping of fast streams to coronal holes is usually improved by assuming an accelerating solar wind, the quality of mapping for other classes of wind may be diminished. We thus conclude that, for the slow solar wind, either corotation persists up to greater heliocentric distances, or more significant interplanetary acceleration occurs close to the Sun; within the distances that corotation is significant.

The longitude shifts derived by Neugebauer et al. (1998) were obtained by testing magnetic field alignment, and suggest that a shift in longitude, equivalent to a longer propagation time, should be applied to produce the best alignment. This is the opposite result to that which we arrive at by testing magnetic field alignments

(i.e., B_{NCH} above). This discrepancy suggests a different acceleration or corotation profile for the slow solar wind in this study, than that prevailing in the Neugebauer et al. (1998) events. This may be an effect of the periods selected for each study. It could also be related to the timing of the two studies in their respective solar cycles; this work samples streams across the maximum and declining phase of cycle 24, while the Carrington rotations studied by Neugebauer et al. (1998) occur around minimum between cycle 22 and 23.

The offset to the ballistic mapping technique applied here is pivotal to the accuracy of results found in Section 5.4.4. We also expect it to be potentially important for other backmapping studies. The additional $\Delta t_c/3$ backmapping time results in longitude changes on the order of $\sim$10–25°, which are large enough to change sourcepoint locations to different regions of a coronal hole, or to different sources entirely. Additionally, the associated time shift of 1–2 days may also be important for studies which attempt to relate temporal variation at the Sun to *in situ* solar wind. Therefore, the appropriate offset should be at least considered whenever applying this ballistic mapping technique, particularly to coronal holes.

5.5.2 Simple Solar Wind Model

Differential Streaming from Footpoint Motion

In Section 5.4.4, we presented results regarding the sizes of mixed composition regions, resulting from heavy ion differential streaming and steady footpoint motion across a coronal hole boundary. Physically, we expect that low latitude solar wind measured at 1 au should exhibit a smaller mixed region than high latitude solar wind measured at 5 au. This expectation is due to the reduced differential rotation at lower latitudes, and reduced solar wind travel time at smaller heliospheric distances. Our expectations are confirmed by the model results shown in Figure 5.6, which shows that these regions should only last $\sim$ 0–0.2 days. The size of the regions also

depends on the different fast and slow stream bulk speeds, although this is a less critical factor than the footpoint latitude.

Differential Streaming from Active Region Footpoints

We now turn to the change in footpoint location due to interchange reconnection between a coronal hole and active region. We conclude from Figure 5.7 that it is reasonable in such an event to expect minor ions from active regions to mix with those from coronal hole streams in the solar wind, producing mixed composition regions with widths of $\sim$0.05–0.3 days. As we have obtained these illustrative results based on the lone case study of Baker et al. (2007), there may be a great deal of variability possible in the rate at which the coronal hole boundary recedes. We therefore present this prediction as a rough indicator that these processes are likely to have an effect on *in situ* solar wind composition, even at low latitudes, and that this effect is likely greater than that expected from footpoint motion by differential rotation alone.

5.5.3 Intermediate Charge States

Section 5.4.4 presents results on the origins of charge states observed in solar wind rarefaction regions. When considered together, these results suggest that the CHBL is the primary source of ICS (and likely also intermediate composition in general) in the rarefaction regions of fast solar wind streams as observed in the ecliptic near 1 au. The transition in charge state is still observed to be steeper than the transition in velocity, because the acceleration and deceleration which occurs on either side of the rarefaction tends to flatten the velocity profile across it. This suggests that ICSs are a result of intrinsic properties of the CHBL, and that in this region charge states are good tracers of source region properties. We come to this conclusion through a combination of results:

First, we have found that ICSs identified in the rarefaction regions of studied solar wind streams most commonly map to near the eastward coronal hole boundary as determined from images of wavelength 193 Å. Table 5.1 records events in which any of the ICS sourcepoints map to the boundary. This is a soft condition that is justified given that not all ICS plasma will map to the exact same location. We find that most events which meet this criteria anyway exhibit the majority of ICS sourcepoints in the boundary region. It seems clear that in these events, for the majority of periods in which ACE observes ICSs, the solar wind has originated from the eastward boundary of the source coronal hole. This is in fact expected for ICS resulting both from intrinsically intermediate CHBL composition, and interplanetary mixing resulting from footpoint motions. This observation in itself thus does not exclude either process.

Second, we have found that differential streaming, resulting from either smooth footpoint motion across source region boundaries, or perhaps interchange reconnection with an active region, can only account for ICS regions of duration 0–0.3 days for solar wind data measured at L1. This is far smaller than the observed durations of ICS regions, Δt_i, of $\sim$ 0.5–2 days, measured for the events in Table 5.1. The contribution from differential streaming is thus insufficient to explain the size of the observed ICS regions in this study. Further, we find no dependence of Δt_i on the latitude of the source region or mapped sourcepoints. This is despite the predictions of the simple solar wind model (Figure 5.6), which indicate that larger intermediate widths should be produced for solar wind with footpoints located at higher photospheric latitudes. Since a relationship between latitude and Δt_i is not observed, we conclude that either this process is not occurring as expected, or the contribution of differential streaming to the overall Δt_i is so small that its effect is negligible.

Finally, we consider the implication of mapping results to CHB vs. CH proper. In the cases where the solar wind sourcepoints suggest two distinct sources; the CH or

the CHB, we might expect to observe a split in the *in situ* ICS region, corresponding to the distinct contribution of the two sources. Indeed, we find that the observed splitting of the ICS region (S_c) only occurs when the mapping places sourcepoints in both the CH and CHB. We are cautious to draw firm conclusions from this particular observation due to the low number of total events in this study, and the fact that of the events which do meet the CH + CHB criteria, only around half exhibit this splitting. Explanation of this splitting likely requires further study, with enough events to produce statistically significant results.

Overall, we find that ICSs frequently map to the trailing coronal hole boundary, and the contribution of compositional mixing through differential streaming to the ICS region is minor. As a result, we can conclude that the ICSs that we observe *in situ* result from intermediately ionised plasma being contributed to the solar wind from the coronal hole boundary layer. This points to the specific charge state freeze-in properties of the CHBL being themselves in some way intermediate. Finding that it is a coronal property which controls the charge states in the ICS regions, and not interplanetary mixing, is a positive result for the validity of applying charge states to trace coronal origins. Were charge states and other compositional signatures being mixed in the interplanetary medium, this would add an additional layer of complexity to the link between these signatures and source region properties. These results then reaffirm the robust nature of minor ion charge state and composition for Sun-heliosphere connectivity studies.

We do not fully discount ion differential streaming as a possible factor in shaping the appearance of composition and charge state of solar wind at L1. We note that our selection of events purposefully excluded source coronal holes above latitudes of 45°. From Equation B.2, differential rotation is significantly increased at such latitudes, and so solar wind originating from coronal hole boundaries there may experience greater mixing. Further, the change in footpoint connectivity through

active region-coronal hole interchange reconnection has the potential to lead to more significant mixing, if the rate of reconnection were larger than the case observed by Baker et al. (2007).

Some other observations however do not clearly support the conclusion that intrinsic composition of the CHBL is the dominant source of ICSs in this study. In events where all of the *in situ* data maps to only the CH boundary, we nevertheless see a range of cool, hot, and intermediate charge states in the *in situ* data. This result appears to contradict the notion that the solar wind from the CHBL only should possess intermediate composition, and that typical cool and hot composition plasma should originate from elsewhere. Further, cases where the ICSs do not map to the coronal hole boundary at all do not appear to exhibit systematically different *in situ* properties in Table 5.1 either. Both of these results might suggest that ICSs are being produced from some other process such as footpoint motions or reconnection. What seems more likely however is that these are a result of some mapping error shifting the sourcepoint of intermediate values away from or towards the boundary.

5.6 Conclusions

In this study, we have linked *in situ* observations of intermediate charge state solar wind streams with remote sensing observations of their likely source regions in the corona. Due to its falling between typically low and high charge state streams, the origins of this type of solar wind are not obvious. We have gained insight into both the location of its source, and the processes by which the intermediate composition it possesses is likely produced. As an additional result, we have also challenged the performance of the widely-applied two-step backmapping procedure in a new way which combines *in situ* and remote sensing observations of coronal hole boundaries. Through this we have found that a simple correction to the constant-velocity approximation improves the fast wind mapping quality notably, with no additional

complexity introduced to the method.

For mapping fast solar wind streams to low-latitude coronal holes, our results show that considerable improvements can be made by applying a larger time shift than that calculated assuming a constant velocity solar wind. Specifically, we have shown this holds for a defined time Δt_a, although the ideal backmapping time is likely to be different from stream to stream. Our analysis is distinct to Neugebauer et al. (1998), who found a similar result by mapping *in situ* and PFSS HCS crossings, which occur in other types of solar wind. This highlights that both tests are likely important to consider when testing mapping quality. We recommend that whenever possible and appropriate, authors applying the two-step backmapping procedure check these alignments, as well as agreements between PFSS open flux and coronal hole area.

Following Neugebauer et al. (1998), we have argued that the reason for this timeshift is likely to be the relaxation of the effects of corotation closer to the Sun than previously assumed. This is instead of a significant acceleration, unaccounted for in the original treatment by Nolte and Roelof (1973). Aligning coronal with *in situ* features has the potential to give insights into the true corotation and acceleration profile of the solar wind, through combining these as parameters in more sophisticated models to maximise alignment. This would then feed back into improvements of both outward and backmapped solar wind propagation models.

From combining observations with a simple solar wind model, we have found that the intermediate charge states in fast-slow solar wind transitions at ACE are primarily a result of the charge state freeze-in properties in the coronal hole boundary layer. From the model outputs we conclude that the contribution from differential streaming resulting from footpoint motion is likely to be far less significant. Even ICS regions mapping back to the highest latitudes in this study do not appear noticeably enhanced by mixing through differential streaming. This may be a result of the

weakness of this process in general, or perhaps simply an artefact of the low number of events in this study; particularly those at high latitudes since we select against them. This also likely contributes to the lack of identifiable link between other *in situ* parameters (e.g., sourcepoint placement/absence in the CH/CHBL vs. Δt_i).

The result that interplanetary mixing of distinct compositional regions is weak is encouraging for current and future missions which use compositional signatures to link solar wind observations to the Sun. Solar Orbiter in particular will rely heavily on minor ion properties to establish this link. This study implies that for the in-ecliptic phase of the mission, mixing will not be a critical issue for Solar Orbiter. The later high-latitude phase may need more careful consideration. It also offers some useful insight into reconstructing the boundary between fast and, still mysterious, slow solar wind regions. We expect that for the cases studied here the intermediate composition solar wind originates from the CHBL, and "true" slow solar wind begins later in the stream.

Chapter 6

Active Region Modulation on Coronal Hole Solar Wind

The work in this chapter was carried out with collaborators at MSSL. In particular, Hinode-EIS quick-look data and maps were produced by Dr Deborah Baker. SDO-AIA lightcurves were produced by Dr David Long. GOES flare times were provided by Prof. Louise Harra. All other figures and data analysis were produced by the author.

6.1 Introduction

Following the previous chapter's multi-event study on intermediate composition in solar wind originating to the east of a coronal hole, this chapter presents a particular case study of two solar wind periods, associated with the same low-latitude coronal hole but one solar rotation apart. Between observations made in Carrington rotations 2175 and 2176, an active region (NOAA 12532) emerges towards the eastward boundary of a persistent coronal hole. As discussed in Chapter 5, the contributions of active regions to solar wind production are yet to be fully understood. In that chapter we focussed on the origins of intermediate charge states at the solar

wind boundaries. However, active regions are thought to make significant contributions to the ambient solar wind through a range of potential mechanisms, which we outlined in Chapter 2, Section 2.5. The emergence of AR-12532 appears to bring significant change in the associated *in situ* data, yet the two-step backmapping technique as applied in Chapter 5 reveals very similar solar wind sourcepoint locations for both times. The emergence of the active region is thus the only new factor which appears to be affecting the solar wind observed *in situ*. This then presents a unique opportunity to contrast the differences in solar wind associated with a trailing coronal hole-quiet Sun (CH-QS) boundary and a trailing coronal hole-active region (CH-AR) boundary.

As discussed in Chapter 2, one potential source of the slow solar wind are coronal hole boundaries. In the previous chapter, we linked the coronal hole boundary layer (CHBL) to intermediate solar wind charge state signatures. The relatively smooth transition from fast to slow speed and other properties across a coronal hole boundary may be a result of the changing expansion factor of the field lines (Wang and Sheeley Jr, 1990), or alternatively due to changing properties of the small loops in CHs (e.g., Borovsky and Denton, 2016) which open via interchange reconnection with the CH open flux.

Similarly, active regions may also play a key role in the origins of the solar wind; particularly the slow wind. Mapping efforts, including those described in the previous chapter, have linked primarily slow and intermediate solar wind to active region sources (Kojima et al., 1999; Neugebauer et al., 2002; Culhane et al., 2014; Fazakerley et al., 2016; Fu et al., 2017). The composition of certain slow wind streams has also been matched to spectroscopically observed abundances in ARs (e.g., Brooks and Warren, 2011; Culhane et al., 2014).

The suggested mechanisms by which solar wind might emerge from active regions are numerous, as described in detail in Chapter 2. To summarise, these include:

1. Loop expansion: AR loops gradually expand into the heliosphere, entering the solar wind (Uchida et al., 1992; Morgan et al., 2013). 2. Interchange reconnection: AR loops reconnect with neighbouring open magnetic fields, opening them to the heliosphere (Sakao et al., 2007; Harra et al., 2008). 3. Multi-step reconnection: Complex reconnection at QSLs and nulls allows AR plasma to escape from otherwise apparently closed regions (Culhane et al., 2014; Mandrini et al., 2014).

Evidence of the above release processes should appear in *in situ* observations. For example, the solar wind from AR loops can be expected to have compositional abundance signatures which result from the locations where the loop footpoints are rooted in the corona (barring any reconnection processes) and charge state signatures for these same regions over the range of heights where freeze-in occurs. If both footpoints of the loop are connected to the Sun, then the electron strahl is expected to be either bidirectional, or highly scattered, depending on the size of the loop. Opened loops will usually show either sunward or antisunward strahl, depending on which side disconnects from the Sun. *In situ* signatures of closed and opened loops are summarised in Figure 2.3 of this thesis, from Owens et al. (2013).

It is clear that the ways in which an AR may contribute solar wind to the heliosphere are varied and often complex. Case studies of AR solar wind such as those reviewed in Chapter 2 are thus crucial in exploring these. Once the key processes (be those reconnection, loop expansion, or otherwise) are revealed through studies such as these, then wider statistical studies comparing linked solar wind and active region properties will be the next step towards identifying the relative significance of each process in creating the solar wind.

The case study contained in this chapter aims to locate and explain the source regions and mechanisms of the solar wind from a CH-AR boundary, specifically in contrast with the wind from a CH-QS boundary. In this way we aim to isolate the effects of an AR on the solar wind escaping a CH, and thus be able to draw robust

conclusions on the processes responsible for solar wind contribution from active regions.

Key questions which we address with this study include: 1. How does a nearby AR influence solar wind from a CH boundary? 2. Does the complexity of AR solar wind make backmapping perform more poorly? 3. Which of the 3 AR solar wind generation processes best match the data? 4. If reconnection is a part of the process, what is the precise configuration? 5. What opportunities exist for Solar Orbiter and Parker Solar Probe to improve these results? What issues need to be addressed to do so?

The structure of this chapter is as follows. In Section 6.2 we describe the remote and *in situ* data used in the study, and how observations were selected. Next, Section 6.3 describes the relevant results of these observations. It presents an overview of the observational periods, the results of the backmapping procedure, and then detailed results from remote and *in situ* observations. In Section 6.4 we discuss the observations both before and after AR-12532 emerges at the Sun, and identify and explain the changes to the solar wind which arise as a result of its presence. Finally, in Section 6.5 we draw conclusions regarding the nature of solar wind from ARs.

6.2 Data and Methodology

6.2.1 *In Situ* Solar Wind Data

Solar wind data for this chapter are obtained from ACE and Wind, both of which are located at L1 (details in Chapter 3). Solar wind bulk speed data (v_{sw}) are obtained at 1-minute resolution from ACE-SWEPAM (McComas et al., 1998). Carbon charge state ratio, C^{6+}/C^{5+}, and iron abundance measured relative to oxygen, Fe/O, data are obtained from ACE-SWICS (Gloeckler et al., 1992).

Vector magnetic field data, **B**, are obtained from the ACE Magnetic Fields Experiment (Smith et al., 1998) at 4-minute resolution. To compare more easily with composition data, we smooth the magnetic field components in time to a 2-hour resolution. We convert magnetic field vectors from Cartesian to a spherical coordinate system to define whether field is inward or outward polarity. The IMF may be labelled inward or outward based on different criteria. Kahler et al. (1998); Heidrich-Meisner et al. (2016) define the field polarity relative to the nominal Parker spiral angle for outward-directed IMF; field orientations within $\pm 90°$ of the expected outward Parker azimuth angle are positive, while all others are negative. Following Heidrich-Meisner et al. (2016), we define the azimuthal Parker spiral angle for outward-directed IMF:

$$\phi_P = \cos^{-1}\left(\sqrt{\frac{1}{1+(\Omega_\odot r \sin\theta)/v_{\rm sw}}}\right) \tag{6.1}$$

where $\Omega_\odot$ is the solar angular rotation rate, r is the heliocentric distance of ACE, and θ is the ecliptic latitude. The polarity of the magnetic field is 1 (-1) if the observed field azimuth is less (greater) than $\pm 90°$ from ϕ_P. We note that other authors, such as Owens et al. (2013), define the polarity relative to the radial direction; field which is within $\pm 90°$ of the radial outward direction is positive, while others are negative. For this study we shall define the field polarity based on the Parker angle criteria.

Finally, suprathermal electron flux data at L1 are obtained from WIND-3DP (Lin et al., 1995). We are mostly interested in the direction of the strahl, and so we consider only one energy bin, which is ~ 427 eV. We find that data in this energy bin most often clearly shows the strahl imposed over the quasi-isotropic halo.

6.2.2 Remote Sensing Data

Candidate solar wind source regions are studied here using remote sensing observations from SDO and Hinode spacecraft; described Chapter 3. Full-disk coronal im-

ages are obtained in the 193 Å band from SDO-AIA (Lemen et al., 2011). LOS photospheric magnetogram observations are obtained from SDO-HMI (Scherrer et al., 2012).

Intensity and physical parameters derived from the Fe XII, 195 Å, S X, 258.3 Å, and Si X, 264.3 Å, lines are obtained from Hinode-EIS. These observations are rastered spectral images (see Section 3.3.1). The Fe XII spectra are used to derive intensity, LOS Doppler velocity and non-thermal velocities ($v_{\rm nt}$). To make these measurements, the Fe XII emission line at each pixel is fitted with a Gaussian profile.

Doppler shift is used to find LOS velocity, while $v_{\rm nt}$ is derived from the excess line width (see Chapter 3 for details). S X and Si X spectral images are used to derive relative abundance ratios between these two elements. These images are derived through a weighted intensity ratio of the lines, as detailed in Feldman et al. (2009). From these data the degree of fractionation (FIP bias) is estimated by comparison to theoretical photospheric values. Further details on this can be found in Chapter 3.

6.2.3 Event Description

In this chapter, the first rotation of interest (which is during CR-2175) shall be referred to as "R1". It features a source CH with a simple CH-QS trailing boundary. The second rotation, occurring during CR-2176, features a source CH with a CH-AR boundary and shall be referred to as "R2". Data are selected from the datasets described in the previous section to best represent the solar wind source regions and streams for both R1 and R2.

For both R1 and R2 the "regions of interest" for all remote sensing observations are the CH and surrounding structures. The EIS instrument has a small field of view, and hence changes its pointing depending on the science priorities on the day. Times when the EIS instrument made observations of the coronal hole and active

region are thus constrained. In studying each region, we choose the observation time which corresponds most closely to the time at which that region is expected to have produced Earth-directed solar wind. This time is predicted by the ballistic backmapping technique (Chapter 3). Choosing this time minimises error caused by the natural evolution of the source region. Conveniently, this time also typically corresponds to times when the source region is near disk centre. The selected measurement times for AIA images are chosen either to best place the region of interest at the centre of the image, or to align in time with a particular EIS observation.

The time ranges we choose for *in situ* periods of interest are those which definitively map to the source regions of interest. We also include surrounding regions lasting 2–6 days to give context, and to ensure we do not unintentionally exclude streams which may in fact originate from source regions of interest. For both R1 and R2 we find fast solar wind streams directly preceding those which map to the CH. These may also be associated with the CH, and so we extend the observational to earlier times to include these regions. The chosen *in situ* period for R1 is: 2016-03-22 12:00 (UTC) to 2016-04-04 12:00 (UTC), and for R2: 2016-04-20 12:00 (UTC) to 2016-05-02 12:00 (UTC). For convenience of presentation, we plot time in day of year (DoY) format. The time ranges are then DoY 81.5–94.5, 2016 for R1 and 110.5–122.5, 2016 for R2.

In situ and remote sensing observations are linked using the same ballistic backmapping approach as described in Section 3.6 of Chapter 3. Analysis in Chapter 5 showed that the two periods under study here were best-mapped using Δt_a; a time lag calculated for an accelerating solar wind. We thus apply this backmapping time shift to the data in this chapter.

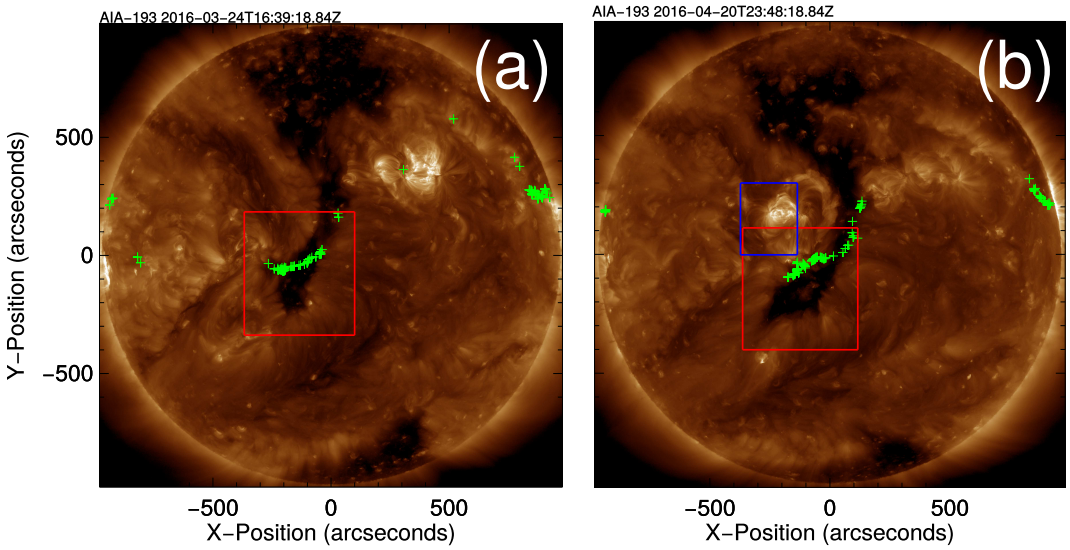

Figure 6.1: AIA-193 Å images of the Sun during (a) R1 and (b) R2. The coronal hole is positioned at approximately disk centre in both cases. Mapped solar wind sourcepoints (in green) show that wind measured at ACE maps to this coronal hole and its trailing boundary for R1 and R2. In R1, the CH is surrounded by quiet Sun (other than the AR to the north-west of the CH). In R2, an active region has emerged at the eastward edge of the CH, and the AR to the north-west has decayed. The morphology of the coronal hole, and sourcepoint locations, are surprisingly similar between R1 and R2 despite the emergence of the AR. The red and blue boxes show the FOV of EIS observations described later in this chapter.

6.3 Results

6.3.1 Overview of Observation Periods

As an overview of the consecutive periods under study in this chapter, Figure 6.1 shows full-disk images of the source coronal hole as imaged in 193 Å with AIA, at times where the CH is approximately at disk centre during each rotation. Figure 6.1a shows the source coronal hole during R1, with mapped L1 solar wind sourcepoints plotted in green, and the field of view of EIS observations of the same CH in red. The trailing eastward (left) boundary of the coronal hole, at the location where the solar wind mapped sourcepoints cross it, borders a quiet Sun region. There is an AR to the north-west of the coronal hole. PFSS modelling predicts this AR to be a source of some open flux, although ballistic mapping results in only a single sourcepoint for L1 solar wind plasma within it. Groups of sourcepoints are also

present on either limb of the Sun. These correspond to streams which lie either side of the stream of interest, and map back to these locations on the Sun (but must have in fact been released when those locations were approximately earth-facing).

Figure 6.1b shows the same coronal hole one Carrington rotation later. Again, mapped solar wind sourcepoints are plotted in green. Red and blue boxes now show the approximate locations of EIS observations of the CH and AR respectively. Around the coronal hole, the AR to the north-west has decayed substantially, with only relatively dim loops remaining at this wavelength. However, on the eastern (left) side of the coronal hole a new AR, AR-12532, has emerged since the previous rotation. Its location is such that it lies to the north of the mapped solar wind sourcepoints at the trailing CH boundary, to which it is connected by dim loops.

Baker et al. (2007) observed that AR emergence can result in the CH boundary receding from the AR, as open CH flux transfers to the AR through interchange reconnection (Chapter 2). However, comparing the CH structure between R1 and R2, we note that its morphology is qualitatively unchanged: the CH boundaries each shift westward by just a few degrees in longitude between rotations. The mapping of sourcepoint locations is also qualitatively very similar between R1 and R2; the path tracks from north to south across the CH. Sourcepoints in R2 do however appear more to the north than R1; towards the AR boundary. It seems apparent that, despite the emergence of AR-12532, the morphology of the CH, and location of solar wind sourcepoints, are very similar between R1 and R2. This uncommon occurrence represents a situation where the dominant factor driving differences in the CH solar wind between R1 and R2 should be the emergence of AR-12532.

To better understand the magnetic configuration of the source regions during R1 and R2, in Figure 6.2 we show magnetic flux data from HMI line-of-sight (LOS) magnetograms overlaid on the AIA imagery. The images are sub-fields of those in Figure 6.1, centred around the source coronal holes. Figure 6.2 reveals how the

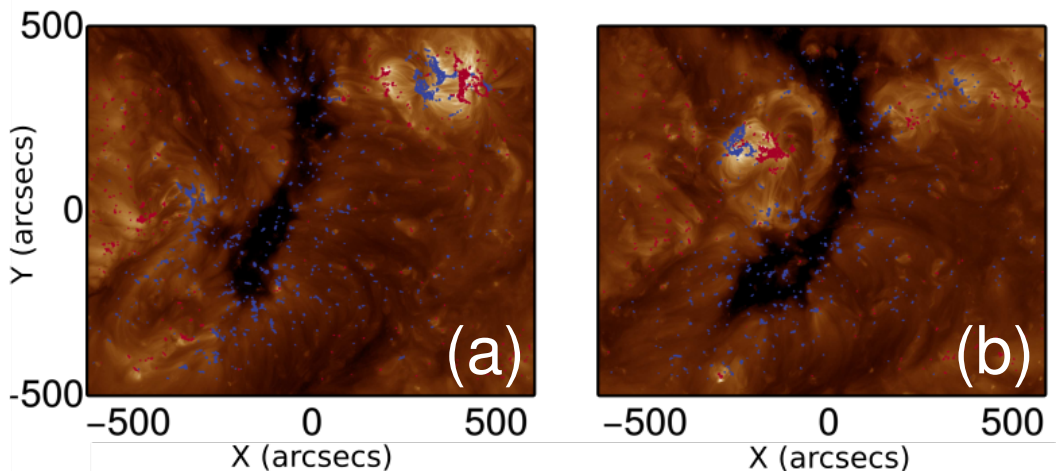

Figure 6.2: Cut-out AIA images of the Sun at the same time and channel as Figure 6.1, with HMI line-of-sight magnetogram contours overlaid on top. The contour value is ±300 Gauss. Blue contours indicate a positive (anti-Sunward) LOS-component of flux, while red is negative. The active region to the east of the CH in R2 is revealed to be dipolar in this image. In R2 the coronal hole, and trailing boundary region which we see solar wind sourcepoints mapped to in Figure 6.1 are both broadly unipolar and positive. The negative polarity footpoint of the AR is found to be the footpoint closest to the positive CH.

magnetic polarity changes between R1 and R2.

Figure 6.2a shows the HMI magnetogram contours and AIA-193 Å image for R1. The source CH is dominantly unipolar, in this case with positive (i.e., outward) field. The regions to the west of the CH are also positive. To the east of the CH, the field is again predominantly positive. To the south-east of the coronal hole, more negative flux is apparent. A concentration of negative flux is associated with one side of some faint loops in the EUV imagery. The active region to the west of the CH has a tripolar configuration, oriented such that there are negative footpoints near the positive CH. A small set of loops in a dipolar configuration is located on the western CHB itself.

Figure 6.2b shows the same information as 6.2a, now plotted for R2. The unipolarity of the coronal hole is preserved, as is the dominantly positive polarity of the surrounding QS regions. Looking to the east of the CH, QS regions change polarity not far from the CH edge. The remnants of the decayed westward active region

persist with some weak concentrations of negative and positive flux. Our main target of interest however is the newly-emerged active region AR-12532 to the east of the CH. At the footpoints of the bright loops of the AR, we find a dipolar configuration. This is oriented such that the negative polarity is adjacent to the coronal hole. This configuration is similar to that found by Baker et al. (2007) which lead to the shifting of the CH boundary through interchange reconnection. Dimmer loops extend from the CH boundary, also joining to the negative polarity footpoint of the AR. In particular, some of these loops are rooted in the CHB region at which solar wind sourcepoints are located in Figure 6.1. We shall refer to this region as the "AR-connected" CH boundary.

6.3.2 Linked Observations

We now consider the mapped *in situ* properties of the solar wind for R1 and R2, in a similar manner to the analysis in Section 5.4.3 of the previous chapter. Figure 6.3 shows combined ACE *in situ* and AIA-193 Å remote sensing observations for R1 (a, b) and R2 (c, d), in the same format as Figure 5.8 in Chapter 5. Figures 6.3a and 6.3c show the CH and other features during R1 and R2 in more detail, with mapped sourcepoints coloured by the corresponding C^{6+}/C^{5+} value measured *in situ*. The images shown are AIA sub-fields at the same helioprojective coordinates, with the Earth located at the same Carrington longitude, separated by one solar rotation. We observe that in both cases the lowest C^{6+}/C^{5+} values map to near the centre of the CH. Increasing C^{6+}/C^{5+} is found towards the respective trailing boundaries. There are some differences in the evolution of the mapped sourcepoints, which we again refer to as the sourcepoint "path". First, in R1 the sourcepoint path crosses the centre of the CH, reaching the eastward boundary, and then jumping to a source region which is off-disk. In R2, however, the points appear to cluster to the north, towards the CH-AR boundary, instead of the CH centre. The solar wind

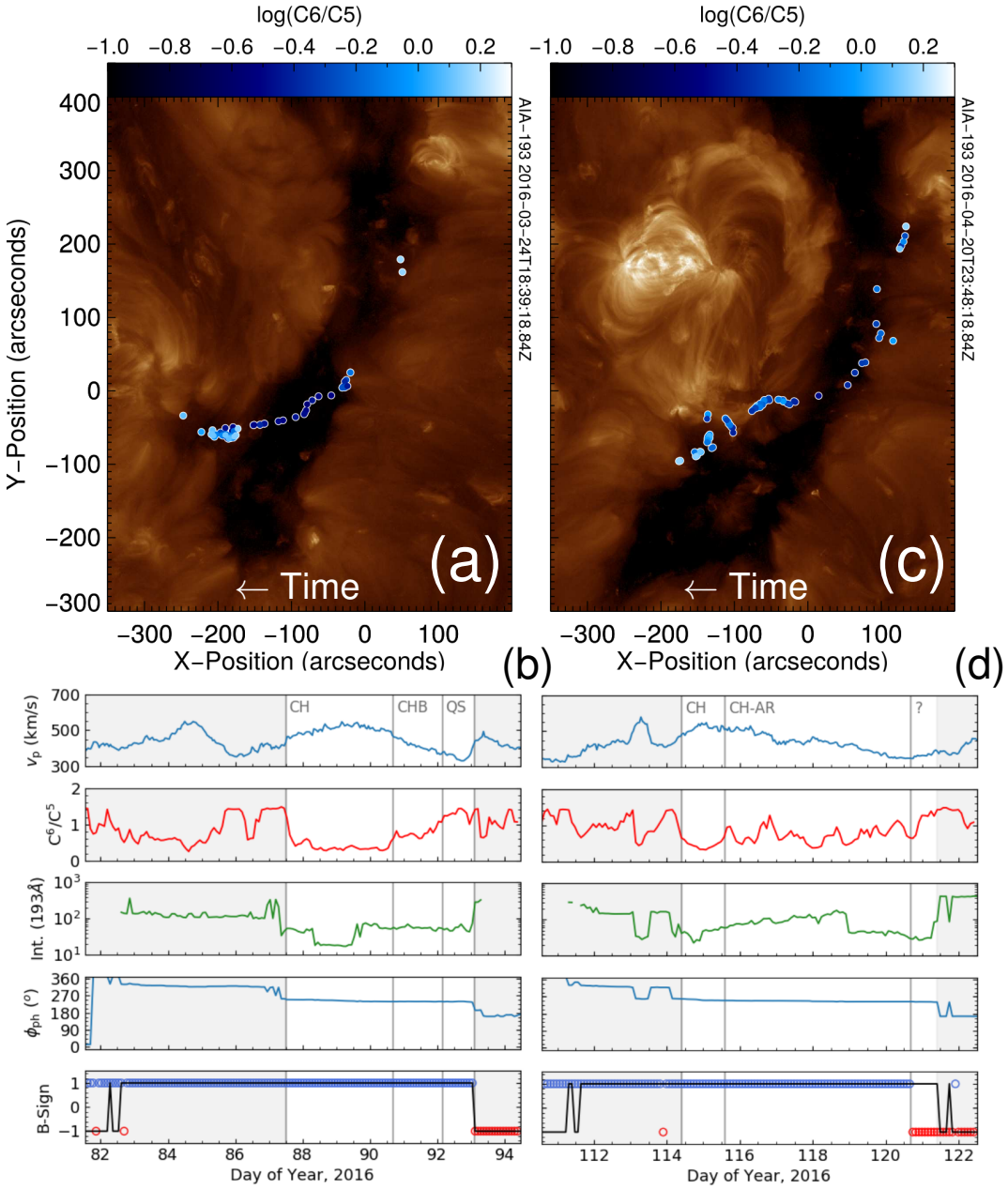

Figure 6.3: Combined *in situ* solar wind and 193 Å image plots of the CH-QS and CH-AR boundaries for R1 and R2. Panel (a) shows a sub-field of Figure 6.1a, centred on the source CH. Solar wind sourcepoints are again plotted over the image, now coloured by the *in situ* charge state ratio from SWICS. The lowest charge state solar wind appears to originate primarily in the centre of the coronal hole. Panel (c) shows the same type of plot, but for R2. An arrow in each panel indicates that solar wind from later times originates from sourcepoints further to the east (left) of the image. Panel (b) shows selected variables extracted from the *in situ* data, the AIA-193 Å data at sourcepoint locations, and the PFSS model outputs for R1. This is the same format as the panels (b) and (d) of Figure 5.8 in Chapter 5. Based on the *in situ* velocity, charge state and IMF polarity data, and mapping location (detailed in the text) solar wind which does not originate from the CH or associated boundary is greyed-out. Panel (c) shows the same data for R2; now greying-out data which we conclude do not originate from the CH, CH-QS boundary, CH-AR boundary or AR.

at L1 then originates from sourcepoints which lie along the boundary to the eastern edge of the CH, before again connecting to an off-disk source. This difference in sourcepoint location for the boundary crossing indicates that we might expect different properties of solar wind to be observed for the boundary in R2 compared to R1. However, these differences are also subject to changes in the source properties resulting from the emergence of the AR. We now discuss the degree to which this mapping can be trusted.

Given the complexity of reconnection phenomena often seen in AR solar wind production detailed in Section 6.1, we do not necessarily expect the magnetic structure predicted by the PFSS model to fully represent the magnetic field configurations which might allow solar wind outflow from the AR. This is because of the assumptions intrinsic to the PFSS approach, discussed in Chapter 3. In such complex cases, we can only use the mapping to guide us to the general region most likely to produce the observed solar wind. For R2, this is then the CH and CH-AR boundary, which is connected by loops to the inward polarity side of the AR dipole. We shall thus consider the entirety of this boundary region in our study, as opposed to only specifically-predicted sourcepoint locations. Since the PFSS is also unlikely to capture magnetic field configurations resulting from reconnection processes, such as could occur between the open CH flux and other parts of the AR, we also do not discount the possibility that contributions to the solar wind may originate from other locations near the AR. We shall consider evidence from comparisons between detailed remote sensing and *in situ* observations which may indicate that the wind originates from these other parts of the AR. In the absence of strong evidence to the contrary, we shall default to the mapped locations.

Figures 6.3b and 6.3d plot the associated *in situ* data for the observations shown in 6.3a and 6.3c respectively. The data are plotted against measurement time at L1, rather than estimated release time from the Sun, which could be derived from

the mapping. In terms of the release times, the solar wind associated with the CH and CH boundary through the mapping for R1 (corresponding to the mapped sourcepoints on Figure 6.3a) is estimated to be released over DoY $\sim$ 81–86 (21–26 March) 2016. The CH and AR-associated wind for R2 is estimated to be released over DoY $\sim$ 110–114 (19–23 April) 2016.

The top two panels of Figures 6.3b and 6.3d show ACE bulk solar wind, v_{p}, and C^{6+}/C^{5+} observations, for time ranges laid out in Section 6.2.3. The third panels show the intensity of emission at 193 Å in the corona at the mapped solar wind sourcepoints, for the corresponding AIA image. R1 and R2 both clearly show the location of the same source CH, as an order-of-magnitude drop in intensity. The photospheric Carrington longitude ϕ_{phot} at the mapped locations in the fourth panel shows when sourcepoints change location gradually or rapidly. Based on the EUV intensity, the grey line marked "CH" shows the beginning of fast speed/low-C^{6+}/C^{5+} values for the streams associated with the CH for both R1 and R2.

In R1 (Figure 6.3b) the C^{6+}/C^{5+} evolution is relatively simple. Following the start of the CH stream, it remains relatively constant at $\sim$ 0.4 before rapidly climbing to $\sim$ 0.7, and plateauing there for $\sim$1.5 days, before increasing further. These signatures are consistent with those of the intermediate regions identified as arising from CH boundaries in the previous chapter. We thus identify this region as the CH-QS boundary, and mark it as coronal hole boundary (CHB) in Figure 6.3b. The part of the stream following the CHB has a higher charge state, and lower velocity. Thus, we consider it to originate further into the quiet-Sun region, and label it QS. We note that the mapping still places this region at the coronal hole boundary, despite our labelling it QS. It is possible that this solar wind is in fact also from the CHB; perhaps simply more towards the east of the CH, and so slower and compositionally hotter as result of the expansion factor (Chapter 2, and Wang and Sheeley Jr, 1990). Alternatively, it could truly originate from the QS, through one of the other candi-

date slow wind mechanisms outlined in Chapter 2. The mapping procedure cannot distinguish the difference between these two cases, and so we label this period as 'QS' simply to distinguish it from the preceding intermediate region.

In R2 (Figure 6.3d) we note the *in situ* data are slightly complicated by the ∼half-day long fast stream which precedes the apparent CH stream by around a day. This stream likely originates in a coronal hole, based on the associated low-C^{6+}/C^{5+} values. In panels 3 and 4 we see that this stream is mapped to the same source CH, but the solar wind which follows it maps outside of the coronal hole, at a more westward location. It is clear that in this case the rapid change in $v_{\rm p}$ leads to a large 'dwell' in the mapping process which produces these longitudes. The mapped location of this small stream therefore must be considered with caution. Comparing this feature of R2 to the *in situ* data for R1, we note that in R1 there is a weak increase in velocity, accompanied by a larger dip in C^{6+}/C^{5+}, around a day before the onset of the CH stream. It may be the case that the small fast stream in R2 corresponds to this increase in velocity in R1, evolved by one solar rotation and observed at a slightly different latitude *in situ*. If this is true, then we can be more confident that this stream should not be considered a part of the CH under study in this chapter. In any case, it falls on the opposite side of the CH from the CH-AR boundary which is of primary interest here.

In R2, the CH stream which we identify *in situ* from the low-C^{6+}/C^{5+} values is far shorter than that for R1; lasting just over one day. Following this, C^{6+}/C^{5+} proceeds to fluctuate for around 5 days, between the values found in the CH, QS and CHB in R1. $v_{\rm p}$ at this time decreases, but not in a steady fashion as in the rarefaction in R1. Beyond the initial CH region, it is not clear where other parts of the stream may originate from based on their C^{6+}/C^{5+} and $v_{\rm p}$ values alone. We mark this entire region as 'CH-AR' as it is possible that different streams within this region may originate from the coronal hole, active region, or from the AR-connected boundary,

as described above. We are confident, as a result of the comparative simplicity of the trailing boundary for R1, that the CH-AR region arises primarily as a result of the emergence of AR-12532.

The degree of agreement between the PFSS and *in situ* observed magnetic field direction, shown in the lower panels of Figures 6.3b and 6.3d are useful indicators of what sections of the mapped data are trustworthy. In R1 the full region of interest; CH, CHB and QS, shows agreement. Following the QS boundary we see that the polarity of the field flips, and connectivity of the mapping moves to a location far eastward on the Sun. This polarity inversion is most likely a consequence of a HCS crossing. As the CH and surrounding regions are found to be unipolar (Section 6.3.1), we have confidence that the stream is correctly mapped, and that the regions we are interested in are limited to the times DoY $\sim$ 87.5–93, 2016. For this reason we place the line marking the end of the QS region at the location of the HCS.

R2 on the other hand, does not have such good polarity agreement. The *in situ* magnetic field polarity switches from 1 to -1 around a day before the mapped PFSS model polarity does. From Figure 6.2, we expect that any solar wind which falls between the CH and the HCS (i.e., has a polarity of $+1$) must originate from the CH-AR region. However, wind with polarity of -1 might originate either in the QS, or perhaps the negative AR footpoint. The final $\sim$ 1 day of data (DoY $\sim$ 120.5–121.5) which maps to the CH-AR boundary, identified by the low intensity shown in the 3rd panel of Figure 6.3(d), thus may or may not be a part of the CH-AR region which we are interested in for this study. For now we place the cut-off of the CH-AR period at the location where the polarity inverts, marking the period we are confident is from the CH-AR source region, and describe this last day as ambiguous. This ambiguous period will be investigated further in Section 6.4.4.

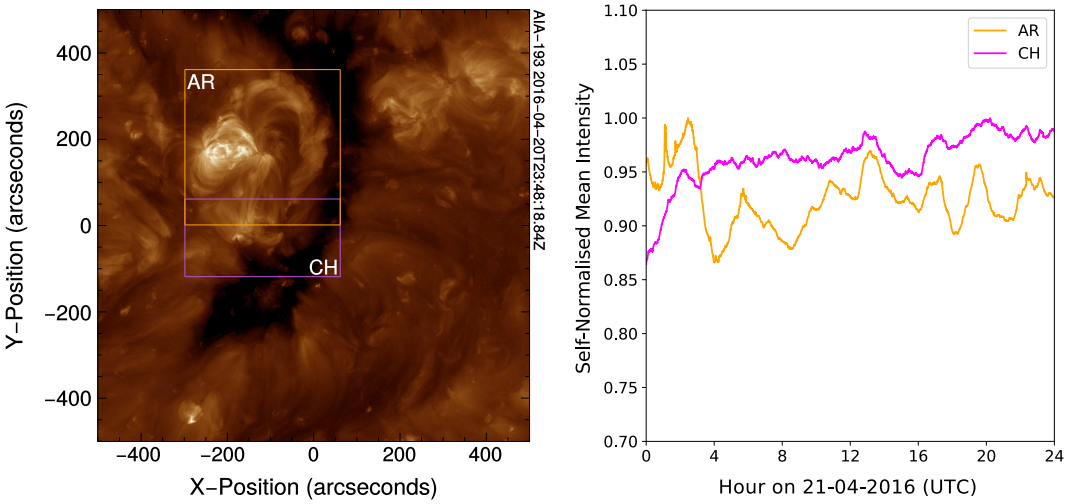

Figure 6.4: Left: AIA-193 Å image of the source CH and AR-12532 for the R2 period, taken 12 minutes before the beginning of the day-long period over which the lightcurve shown in the right panel is produced. Two boxes show the two areas which make up the two lightcurves. The orange box contains primarily AR-12532, and a portion of the CH boundary and CH. The pink box contains part of the CH and CH boundary, at the location where mapped solar wind sourcepoints are found. The positions of the boxes in helioprojective coordinates are shifted in time to account for solar rotation. Right: Time series of mean intensity or "lightcurves" for the two regions highlighted in the left panel over one day, using the same colour coding. Each lightcurve is normalised such that its maximum is 1.

6.3.3 Activity in the Source Regions

We wish to classify the *in situ* observations, as to whether they are characteristic of emission from a dynamic active region, or one which is relatively steady. We examine the GOES X-ray flare list (Section 3.4.3) during the period when AR-12532 is expected to produce ACE-directed solar wind. Only one flare is listed, which is of B-class (see Section 3); representing very weak releases of energy and minor reconfiguration of the AR magnetic field.

We also examine the evolution in time of AR-12532, the source coronal hole, and the boundary between the two. The right panel in Figure 6.4 shows a plot of mean, normalised, intensity in the 193 Å channel across two regions of the Sun during R2, over one day of consecutive images. These "lightcurves" measure intensity within

the overlapping boxes shown at the left of the figure, which are moved in time to account for solar rotation. The orange (upper) box is chosen to capture the AR, and part of the CH-AR boundary, while the purple (lower) box captures the CH itself, as well as part of the CH-AR boundary. Each curve is normalised so that its maximum value is 1.

The lightcurves are produced on 5-minute cadence over the full day of 2016-04-21; the centre of the expected release time range of the CH-AR solar wind. We note that both the CH and AR lightcurves show little variability over the day. The standard deviations of both curves are around 3 % of their respective means. The larger changes in CH brightness relate to brightening of the AR-connected loops. The gradual increase in brightness with time is likely due to projection effects causing the loops to obscure the darker CH. Changes in the AR brightness relate to changes in the loops at its core. The small changes in brightness represent only weak flaring, as is consistent with the GOES observations. The AR source here thus appears to be very steady, without strong flares, which are associated with reconfigurations of the magnetic field, or heating of the plasma.

6.3.4 Physical Properties of Source Regions

EIS Observations for R1: Coronal Hole

We now extend the analysis of the AR and CH sources under study to infer physical properties at these locations. These are derived from ultraviolet spectral images from Hinode-EIS. We show parameters derived from three periods of observation. First, in Figure 6.5, we show observations at 10:06 UTC on 2016-03-25, centred on the source CH during R1. Panel (a) shows the Fe XII intensity map, which shows similar emission to the 193 Å imagery shown in Figure 6.1. This image confirms that the CH morphology imaged over the rastered EIS observations is comparable to that established from the AIA observations. The Fe XII-derived Doppler veloc-

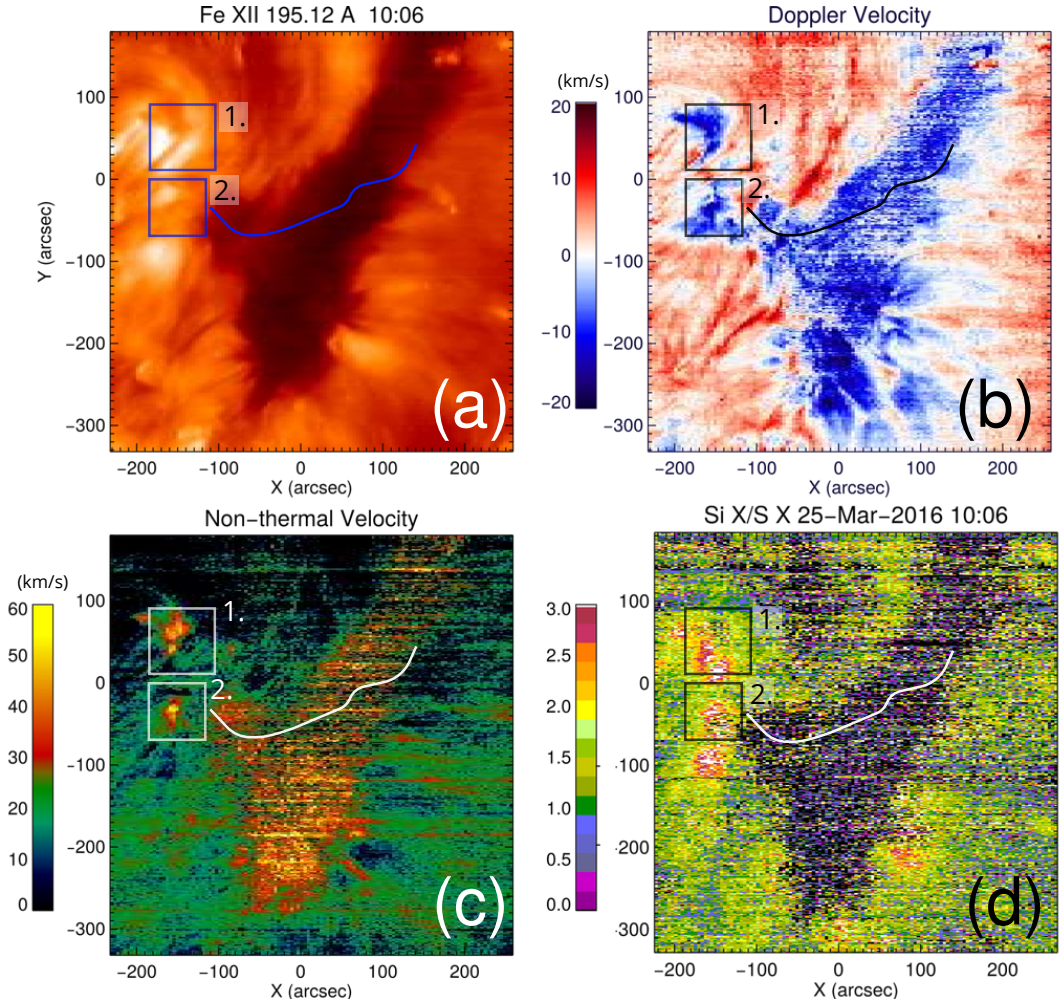

Figure 6.5: EIS observations of the southern portion of the source CH for R1 starting at 2016-03-25-10:06 UTC. Panel a: map of Fe XII intensity. Panel b: LOS Doppler velocity map derived from Fe XII line. Positive (red): downflows, negative (blue): upflows. Panel c: non-thermal velocity map derived from Fe XII line, again overlaid with HMI contours. Panel d: FIP bias map from intensity-derived abundance ratios of Si X/S X. On each panel a line (blue in a, black in b, white in c and d) serves to guide the eye to the sourcepoint path calculated from the mapping shown in Figure 6.3a for R1. Numbered boxes highlight areas of interest which are referred to in the text.

ity map in Panel (b) shows the body of the CH contains predominantly upflowing plasma, on the order of around $20\,\mathrm{km\,s^{-1}}$. At the eastward CH boundary where sourcepoints approach QS, there is a mixture of strong and weak upflow regions. Upflows are found quite far east through the boundary into QS regions, e.g., at Box 1 ($x = -150''$, $y = 60''$), and Box 2 ($x = -150''$, $y = -50''$).

Panel (c) maps non-thermal velocity, v_{nt}, derived from the width of the Fe XII line. Non-thermal velocities of 40–$60\,\mathrm{km\,s^{-1}}$ are found in the CH, although the data are quite noisy due to low counts. In the QS regions to the west, east, and south of the CH, non-thermal velocities are around 20–$30\,\mathrm{km\,s^{-1}}$. In the quiet Sun directly east and north-east of the CH boundary where the sourcepoints are located, two regions of particularly strong v_{nt} are found, also within Boxes 1 and 2. These two regions are to the north and south of the bright region seen in Fe XII in Panel (a). They are also spatially coincident with upflow regions evident in Panel (b).

Panel (d) maps FIP bias derived from weighted intensity ratios Si X/S X. The expected FIP bias values are ≥ 1, as 1 corresponds to photospheric abundances. Pixels of bias < 1 are present in the coronal hole, which is noisy as a result of low counts of Si X and/or S X. As coronal holes are expected to exhibit photospheric composition (Bochsler, 2007) we assume that all of the < 1 values in the coronal hole should in fact be ~ 1. This map is really then only useful in the regions outside of the CH-proper, with bias ≥ 1. The QS/CH boundary to the east of the sourcepoint locations exhibits variable FIP biasing. The typical values of bias appear to be in the range of 1–2, with regions ≥ 3 being more localised. There are 3 localised regions of this level of bias, all of which are at $x \sim -150''$, and are at $y \sim -100''$, $-50''$ and $30''$. While the lower region coincides with weak downflows in Panel (b), the other two lie in Boxes 1 and 2; the aforementioned strong upflow regions. The regions are also both partially coincident with enhancements in v_{nt}; in both cases the enhanced v_{nt} regions appear smaller, and are offset from the centre.

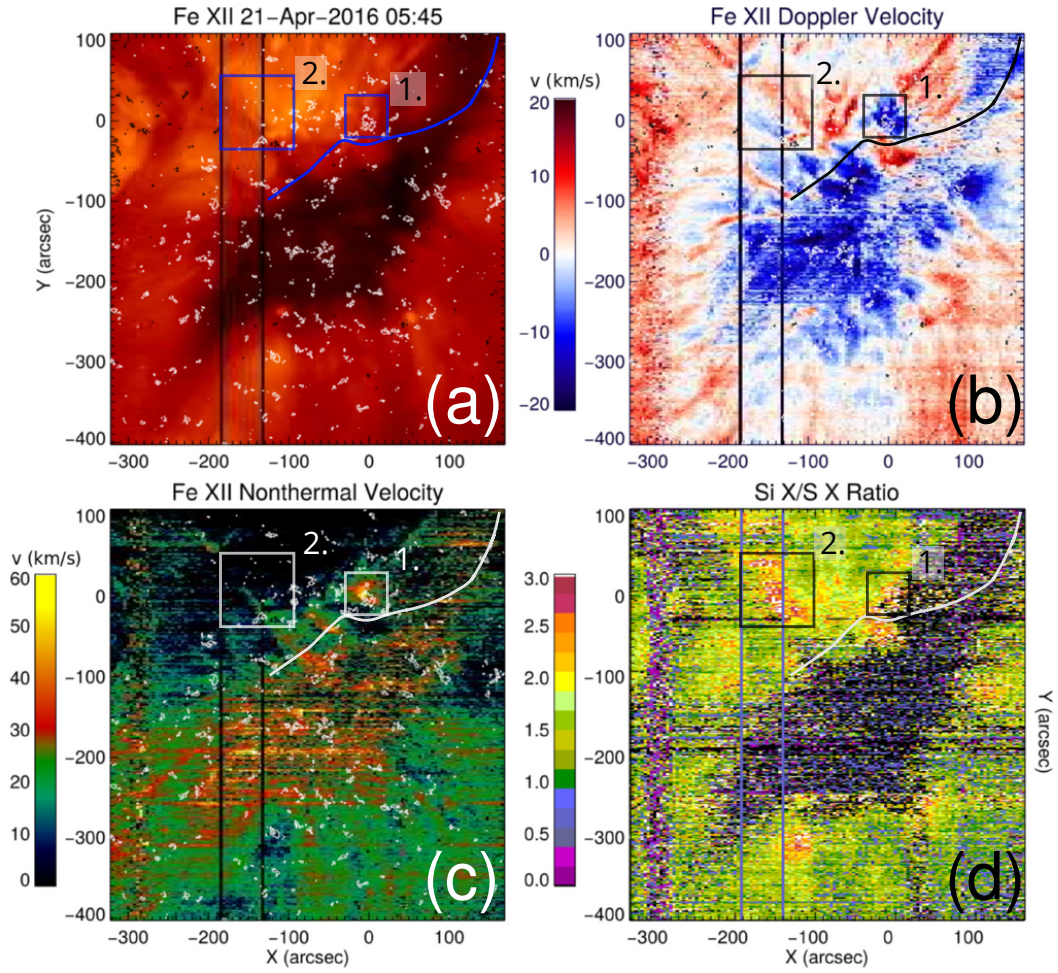

Figure 6.6: EIS observations of the southern portion of the source CH for R2 starting at 2016-04-21-05:45. The format is identical to that for Figure 6.6, with overplotted lines now instead showing mapping for R2. Additionally panels a–c are overlaid with contours from HMI LOS-magnetogram data. White is positive field, black is negative.

EIS Observations for R2: Coronal Hole

EIS observations of the source CH during R2 are shown in Figure 6.6. The format is the same as that of Figure 6.5. Panel (a) shows the Fe XII intensity, and confirms for R2 that the CH morphology for the EIS observations is again comparable to that established from the AIA observations. The Doppler velocity map in Panel (b) shows that the CH still contains upflowing plasma, on the same order as seen during R1. At the boundary where SW sourcepoints are found, towards the top of the image, there are both upflows (e.g., at $[x = 0, y = 0]$; Box 1) and downflows

(e.g., at [$x = 0$, $y = -40$]; directly south of Box 1). Moving further north of this boundary, towards the AR, the LOS flows are weaker.

Panel (c) plots non-thermal velocity for the source CH during R2. $v_{\rm nt}$ observations appear noisy in the CH and inner portion of the boundary, however this does appear to be where most enhanced $v_{\rm nt}$ is found. Further to the north in the region showing weak Doppler velocity, very low $v_{\rm nt}$ values are observed. There is large spatial variability of $v_{\rm nt}$ in the boundary region where mapped sourcepoints are found. The upflow region located in Box 1 appears spatially coincident with strongly enhanced $v_{\rm nt}$. The downflow region directly south of it matches to very low $v_{\rm nt}$.

In Panel (d) we again assume that all of the < 1 FIP bias values in the coronal hole are in fact ~ 1. The northern CH boundary on the AR side, where sourcepoints are located, exhibits FIP biasing of 1 to > 3. Again values are typically in the range of 1–2, with localised regions of ~ 3. The strong upflow region in Box 1 exhibits values of ≥ 3, as does the downflow region which lies to the south of the box. Another region of bias ≥ 3 appears within Box 2; at the location of weaker LOS flows and lower $v_{\rm nt}$. Comparisons with the AIA image in Figure 6.3 imply that these enhanced-bias regions coincide with the footpoints of the loops which connect the CH boundary to the AR. Elsewhere in the CH boundary, such as on the southern edge, the typical FIP bias values of 1–2 appear to persist. Regions of bias ~ 3 also occur, but are smaller and more spread out.

We find from these observations that the CH-AR boundary is a location of enhanced, although variable, FIP biasing relative to the CH. If this source region is able to contribute to the solar wind, then we expect to see enhancements of the *in situ* FIP bias, relative to solar wind from the CH. Comparing the FIP biasing of this CH boundary to that during R1 in Figure 6.5, we note that there are regions of high FIP bias in both cases. This CH-AR boundary in R2 does not feature FIP biases larger than the CH-QS boundary of the previous rotation, and in fact the CH-QS boundary

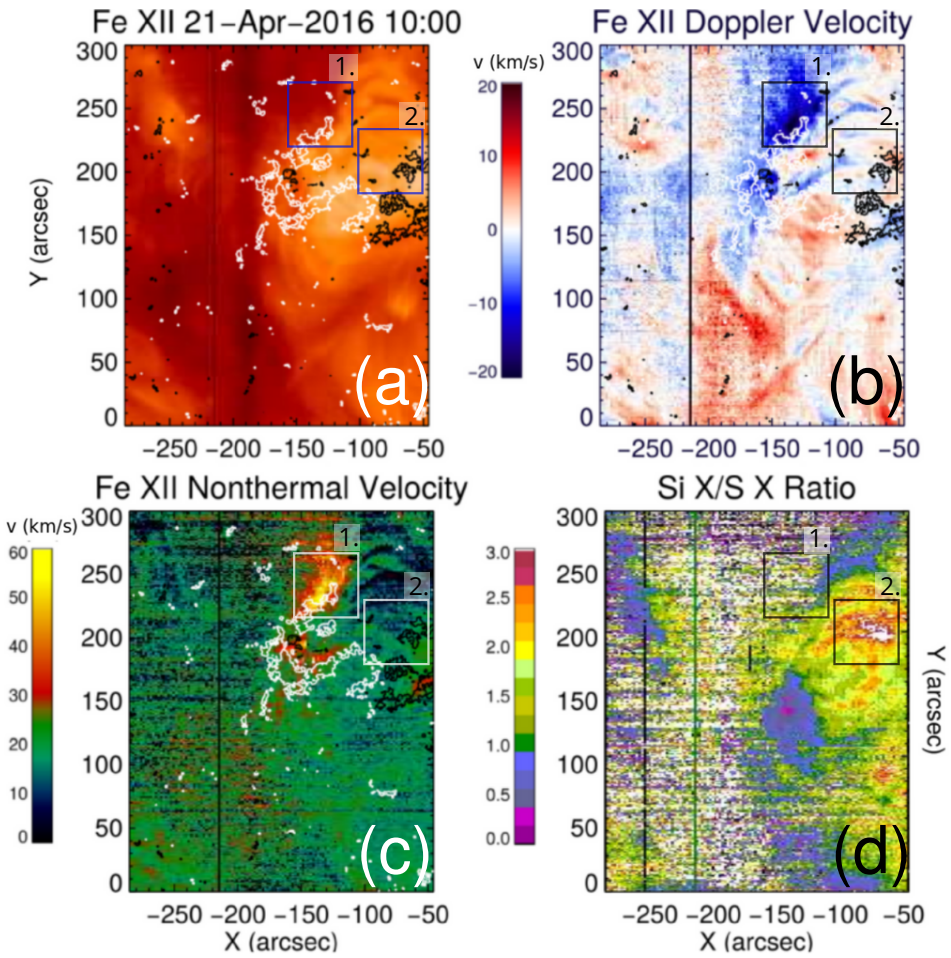

Figure 6.7: EIS observations of the southern portion of AR-12532 starting at 2016-04-21-10:00. The format is identical to that for Figure 6.6.

in R1 has larger regions which are saturated in FIP bias and therefore likely > 3.

EIS Observations for R2: Active Region

Figure 6.7 shows the same observations for AR-12532 as are shown for the CH in Figure 6.6. The FOV of these observations is indicated by the blue box in Figure 6.1(b). The measurements are made shortly after those for the CH, at 10:00 UTC on 2016-04-21. In these maps the polarity of the field is important, as the AR is dipolar. If a given part of the AR is thought to be contributing to the SW, the polarity of the associated magnetic field is crucial when linking it to the *in situ* observations shown in Figures 6.3 and discussed in more detail below. In the Fe XII intensity maps, the

core of the AR is visible in the right half of the image. The HMI contours show the polarity of the AR, although the negative polarity region of the core is cutoff at the edge of the map. In Panel b the Doppler velocity shows a region with upflows of $\sim 20\,\mathrm{km\,s^{-1}}$ to the east, and particularly north-east of the AR core, marked at Box 1. This region appears to be quite dim in Fe XII, and indeed in 193 Å also, and lies to the positive polarity side of the AR. Other dimmer regions within the AR loops also show upflows. AR dimming is consistent with outflows, as plasma leaves the region and so emission drops. Upflows seem apparent also in the strongly negative polarity region of the AR, but again this is cut off at the edge of the map.

Panel c shows v_{nt} is uniform for most of the FOV, at around 10–20 $\mathrm{km\,s^{-1}}$. One exception is within the loops at the core of the AR, where v_{nt} approaches zero. Another notable exception is in the strong upflow region in Box 1. Here v_{nt} approaches the saturation value of $60\,\mathrm{km\,s^{-1}}$.

In Panel d, FIP bias measurements of the AR and surrounding regions indicate that most enhancement is found in loops near the core of the AR, where the values exceed 3. We highlight this region in Box 2, and note that it is in the negative polarity region of the AR. To the north and south of Box 1 the FIP bias falls to 1.5–2.5. Unfortunately the noise in the enhanced upflow and v_{nt} region in Box 1 makes it impossible to reliably estimate the associated FIP bias. Other regions in the map are either also noisy, or show values < 1. To the eastern side of the map, FIP bias values of 1.5–2.5 can also be found, but these are again quite noisy.

Open Flux Near Source Regions

An idea of the locations where solar wind may be able to escape from the Sun can be obtained using magnetic field models of the corona. We apply the same PFSS model as is used in the backmapping process to show locations of open flux footpoints at $1\,\mathrm{R_\odot}$ for both R1 (left) and R2 (right) in Figure 6.8. The left panel of the

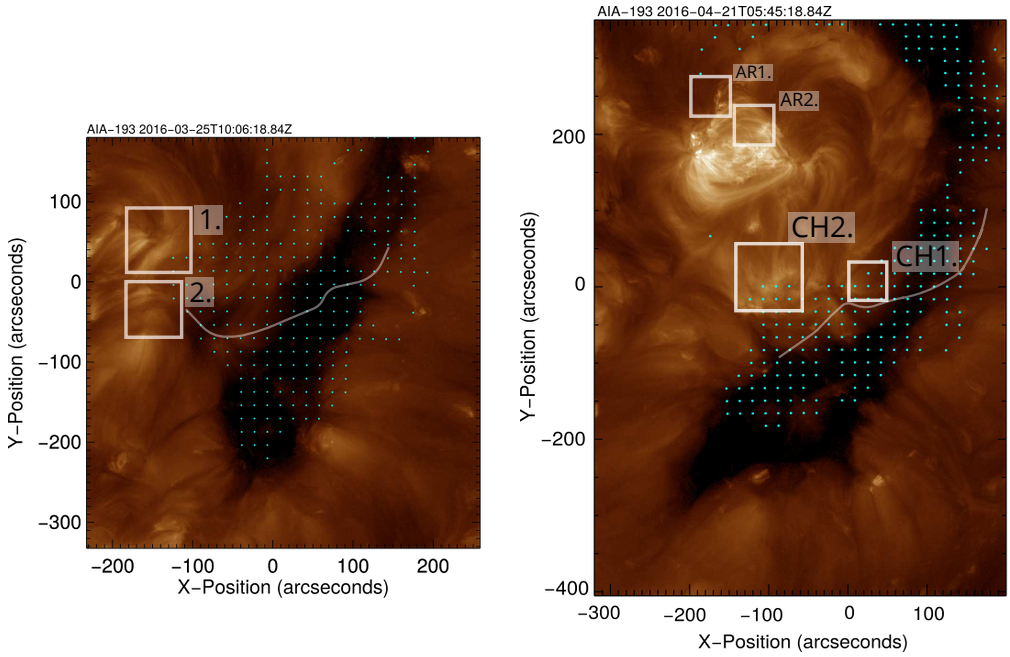

Figure 6.8: Left: Sub-region of full disk AIA-193 Å images at time corresponding to EIS observation of the CH during R1 in Figure 6.5. The field of view size is approximately the same as in 6.5a. Footpoints of open magnetic flux derived from the PFSS model are plotted in light blue based on a 1°-resolution grid at 1 $R_\odot$. Open flux is found in the CH, and part of the eastern CH boundary. The line and boxes are the same as in Figure 6.5. Right: same format as the left panel, but for the two EIS observations during R2 shown in Figures 6.6 and 6.7. The image is taken at the time corresponding to the CH observations in Figure 6.6. The line and boxes are the same as in Figures 6.6 (boxes now labelled CH) and 6.7 (boxes now labelled AR). The field of view encloses both the AR and CH observations. Open flux is found in the CH, the CH boundary, and to the north of the AR core.

figure shows open flux derived from the PFSS model at 1° resolution (heliographic coordinates) overlaid on an AIA 193 Å sub-field image at the same time and coordinates as Figure 6.5. The right panel shows corresponding open flux footpoints for the CH and AR for R2, overlaid on a sub-field of an AIA-193 Å image which contains both of these regions. The coordinates on the image match as close as possible, given that the two are from different instruments, those in Figure 6.6 as the image time corresponds to the start time of the EIS rastering for this region.

For R1 (left panel), we note that flux rooted in the CH is predominantly open, while the QS region surrounding it is closed. Open flux extends into the CH boundary; particularly to the east. We find that the two locations of strong upflow, $v_{\rm nt}$, and FIP

bias from Figure 6.5 (Boxes 1 and 2) lie on closed field regions, but both are within $30''$ of open flux rooted in the CH boundary.

For R2, we show the open flux predicted for the CH and AR in the right panel of Figure 6.8. Considering the CH boundary, open flux is found directly adjacent to the strong upflow/$v_{\rm nt}$/fractionation region of Box CH1. Open flux is also found adjacent to the AR-connected boundary in general. This may lead to a QSL between the closed loops and the open CH field lines; the loops extend northward towards the negative AR footpoint, while the CH field is expected to open to the heliosphere. This cannot be proven without use of a more detailed magnetic field model however.

While the mapping predicts that only the CH-AR boundary region should produce solar wind observable at ecliptic latitudes (as this is the region where the mapped sourcepoints are located) Figure 6.8 shows open flux rooted also close to the upflowing region (Figure 6.7) in Box AR1. This region is thus another possible QSL location. No such open flux is predicted to be rooted in the high-FIP AR core, although plasma could still escape from these locations.

To summarise these results, we find that beyond structural differences, and the presence of AR-12532 itself, the properties of the mapped source regions for R1 are similar to those for R2. Around the coronal hole and its respective boundary there are signatures of upflows, enhancement of $v_{\rm nt}$, and enhanced FIP bias (> 3). This is the case for both periods. Regions which display these signatures are located more on the eastern boundary of the CH in R1, and to the north-eastern boundary of the CH in R2. Both periods feature regions where all three of these are coincident, and are adjacent to open flux footpoints predicted by the PFSS model. QSLs between open and closed regions may exist in both regions. The main structural difference in the coronal hole boundary between R1 and R2 is that the former is adjacent to QS, while the latter is adjacent to brighter loops which are connected to the AR to the north. Around the AR in R2 there are again upflows, enhanced $v_{\rm nt}$, and enhanced

FIP bias, although these are not all coincident. Open flux footpoints are predicted to lie near an upflow region at the AR, but the FIP bias measurements in this region are unknown.

6.3.5 Detailed *In Situ* Observations

We perform a more detailed analysis of *in situ* data for both R1 and R2 to assess whether the influence of AR-12532 on the CH boundary changes the *in situ* properties between the two. Figure 6.9 plots all of the *in situ* data considered for both R1 (6.9a) and R2 (6.9b).

The first two panels of 6.9a and 6.9b show fluxes of suprathermal electrons measured by WIND-3DP. The first panel plots electron flux (as colour) in the 427 eV energy bin, binned in vertical (y) by the 8 3DP pitch angle (PA) bins, and in horizontal (x) by time. Flux units are $\mathrm{cm^{-2}\,sr^{-1}\,eV^{-1}\,s^{-1}}$, which we denote as FlU on the figures. The PA bins for 3DP are described in Chapter 3. They approximately span from 0–180° and are gapless. Bin 1 is the bin looking nearest 0° and 8 is nearest 180°. The PA bins are constructed from 88 discrete look-direction bins, based on the current local IMF direction. As a result, the central PA of each bin changes slightly with time (Wilson, 2015). It is for this reason that we plot as a function of bin number, as opposed to PA. These plots show periods of enhanced suprathermal flux clearly, such as in Figure 6.9a at DoY $\sim$ 87–89. In the second panels we plot the same electron data, now with the flux in each bin column-normalised by the total flux for each timestep. This largely removes the effects of isotropic flux enhancements, as the flux contained in each PA bin is now shown relative to the flux in the other PA bins. A narrower strahl manifests as an enhancement of this normalised flux, whereas in Panel 1 it is difficult to distinguish if the total isotropic flux is also varying. Likewise, periods where the strahl direction changes, or where bidirectional strahl is present are also clearer. We calculate a mean PA of the suprathermal

electrons, μ_{PA}, by weighting each bin PA value by the flux in that bin. μ_{PA} is plotted in white over Panel 2. The 3rd panels of these figures show the same information as the 5th panel in Figure 6.3b and 6.3d, without the PFSS polarity line, and instead with the strahl alignment derived from μ_{PA}.

The fourth panels plot $\Delta\phi_P$; the difference between the azimuthal angle of $\mathbf{B}$ (ϕ) and the Parker spiral angle calculated by Equation 6.1. The Parker angle is always positive, so following the method detailed in Section 6.2 a positive (anti-Sunward) IMF field should have azimuthal angle within $\pm 90°$ of it, while negative IMF will be outside of these bounds. We show the lines separating positive and negative field defined this way in grey on the figure. We also show lines separating positive and negative flux defined relative to the radial direction (as in Owens et al., 2013) in purple. We show the elevation angle, θ_{el}, of the IMF in Panel 5; 0° field is aligned with the ecliptic plane, while $> 0°$ field has a northward component and $< 0°$ a southward.

Panels 6 and 7 of Figure 6.9 plot $|\mathbf{B}|$ and v_{sw}. In Panel 8 we plot the carbon charge state ratio C^{6+}/C^{5+}, as in Figures 6.3b and 6.3d. We also show error bars as provided with the ACE-SWICS dataset. Panel 9 plots the Fe/O *in situ* measurements. Error bars are placed on these values in the same manner as for C^{6+}/C^{5+}. The associated FIP biases for these Fe/O values are calculated by dividing them by the photospheric Fe/O ratio; $\mathrm{Fe/O_{phot}} = 0.064$ from Asplund et al. (2009).

IMF Kinks and Deflections

From Panel 3 of Figure 6.9, for both R1 and R2 the observed solar wind is primarily unipolar. This is apart from the unidentified inward polarity region for R2. The strahl alignment switches from parallel to anti-parallel, primarily at the large inversion of IMF polarity in both cases. This indicates that the strahl is travelling mostly anti-Sunward. Exceptions to this are the brief periods of R1 and R2 where a single

data point in IMF polarity flips, but the strahl alignment remains the same. These short periods of inverted field therefore exhibit Sunward strahl; indicating that the field has been "kinked" or folded-in on itself. Other exceptions are short-lived anti-parallel strahl measurements in the positive field region of R1. These are changes in the strahl alignment which do not coincide with magnetic field inversions. Only one such point exists in the R1 period of interest, at DoY ~ 91.

Examining $\Delta\phi_P$ we see that both around strahl inversions, and at other times, the field orientation approaches the opposite polarity, relative to the Parker spiral direction, without necessarily passing over. These deviations could thus also be a result of residual kinks in the IMF. Indeed, when considering the field orientation relative to the radial, rather than Parker spiral, direction (as in Owens et al., 2013) many of these deviations can in fact be considered inversions. This can be seen in the Figure, where $\Delta\phi_P$ crosses the purple line.

Considering in particular the regions mapping to the CH, CHB and QS in R1, and CH and CH-AR in R2 (Figure 6.3), we note that there appears to be more fluctuation between extremes of $\Delta\phi_P$ during R2 than R1. However, examining the standard deviation of $\Delta\phi_P$, σ_θ, we find $\sigma_\theta = 31°$ for R1 and $\sigma_\theta = 33°$ for R2. By this measure of variability, there is little difference between R1 and R2. Considering instead deviations of the field away from the Parker spiral direction, we quantify the number of instances where $\Delta\phi_P$ crosses, and subsequently returns from, the threshold of $\pm 45°$. For a typical Parker angle of $\sim 45°$, these thresholds represent deflections to $0°$ and $90°$ relative to the Sun-Earth line. (Thus in the positive direction, on average this threshold indicates the radial inversion of the field, according to Owens et al., 2013). The number of times $\Delta\phi_P$ crosses $\pm 45°$ in R1 and returns is $n_{R1} = 3$, while for R2, $n_{R2} = 9$. This is considerably fewer for wind from the CH boundary during R1 than for R2. Reducing the threshold angle to $\pm 35°$ we find $n_{R1} = 6$, while $n_{R2} = 9$. Increasing it to $\pm 55°$ produces $n_{R1} = 2$ and $n_{R2} = 6$. Beyond these angles

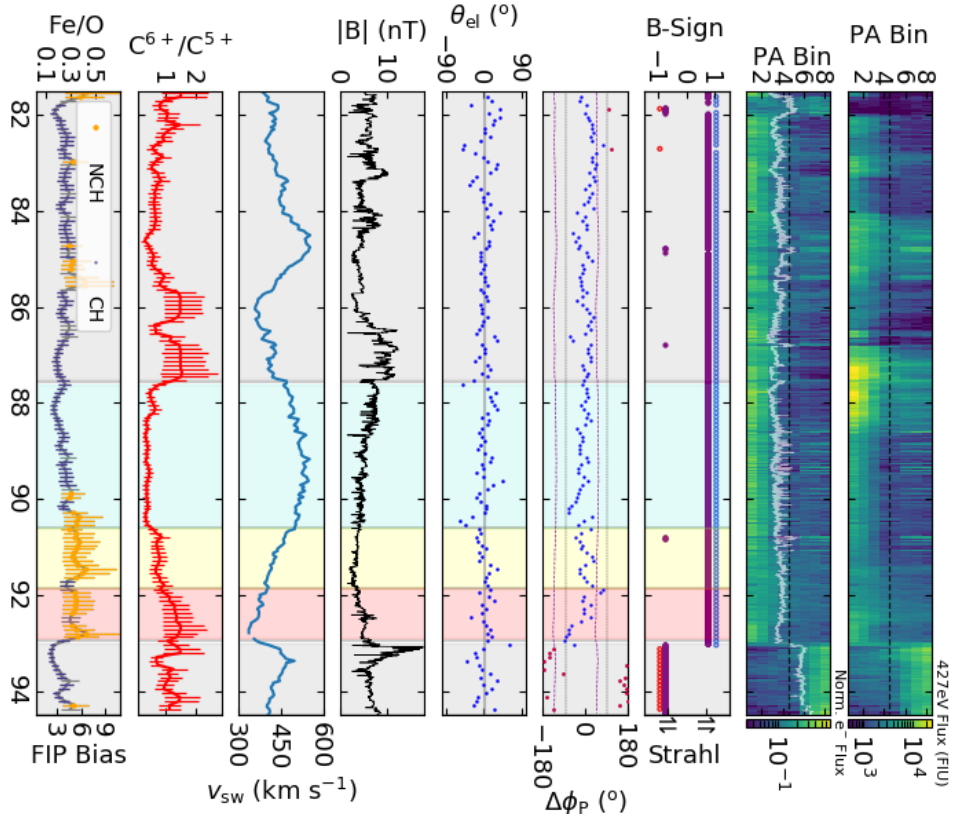

(a) Solar wind data for R1.

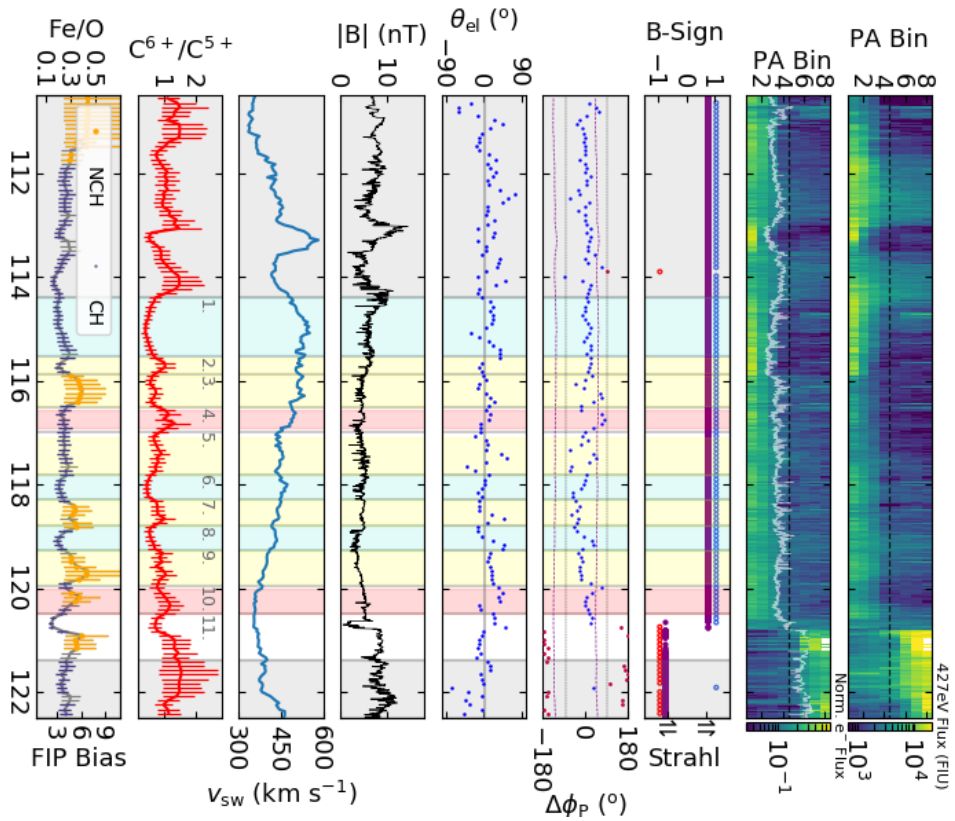

(b) Solar wind data for R2.

Figure 6.9: Opposite page: Solar wind data for the *in situ* periods associated with R1 and R2 from WIND and ACE. The top two panels plot WIND-3DP measurements of suprathermal electrons at $\sim 427\,\mathrm{eV}$, as a function of pitch angle bin. The bins 1–8 span pitch angles 0–180°. The top panel plots the flux in each bin as a function of time, with units FlU ($= \mathrm{cm^{-2}\,sr^{-1}\,eV^{-1}\,s^{-1}}$) The 2nd panel plots the same data, with flux normalised by the integrated flux over all 8 bins for each time step. The white line shows the flux-weighted mean pitch angle; μ_{PA}. The 3rd panel shows in blue and red IMF direction calculated as described in the text (1 is anti-Sunward, -1 is Sunward). Also shown is the alignment of the strahl, derived from μ_{PA} in the 2nd panel. The 4th panel shows the IMF azimuthal angle deviation from the expected Parker spiral direction. The grey lines at $\pm 90°$ show angles within which the field is considered to be anti-Sunward relative to the Parker direction. Sunward field is coloured red while anti-Sunward field is coloured blue. The purple lines show angles within which field is considered anti-Sunward relative to the radial direction. The 5th panel shows the elevation angle, θ_{el}, of the IMF. Positive angles are ecliptic northward and negative angles are southward. The 6th panel shows IMF magnitude $|\mathbf{B}|$ from ACE-MFI. The 7th panel shows solar wind bulk velocity from ACE-SWEPAM. The 8th panel shows C^{6+}/C^{5+} from ACE-SWICS. The final panel shows Fe/O also measured by SWICS, with the right-side of the axis showing the inferred FIP bias: $(\mathrm{Fe/O})_{\mathrm{SWICS}}/(\mathrm{Fe/O})_{\mathrm{phot}}$. Purple points are those which lie within the range of values found in the CH for R1, while orange points are those values which are greater. Sections of the plot are coloured by the C^{6+}/C^{5+} values for R1 seen in the presumed CH (blue), CH boundary (yellow), and NCH (red) sections of the data (details in the text). Regions which definitely do not map to the regions of interest for R1 or R2 are greyed-out. In plot (b) coloured sections are numbered 1–11; and are referred to as S1–11 in the text.

n_{R1} and n_{R2} are more similar. Further, the number of IMF inversions as judged relative to the radial direction (crossings of the purple line) is only 1 for R1, but 4 for R2. More generally then, there are more instances of deviations in the field reaching angles of 35–55°, and also becoming radially inverted, in R2 than in R1.

Kinks in the IMF can occur out of the ecliptic plane, as well as being confined within it. If present, these kinks will manifest themselves in θ_{el} as deviations from the unperturbed elevation angle. For R1 we find a mean θ_{el} of 0.9° with variability shown by the standard deviation of 18.6°. We note that of the three periods of interest (mapping CH, CHB and NCH) the CH shows most deviation from 0°, while the CHB and NCH periods are relatively steady. This contrasts with $\Delta\phi_P$, where the CH stream was relatively calm, and the CHB and NCH periods showed strongest deviations. R2 has a mean θ_{el} of 6.4° with standard deviation 24.1°. Examining

the CH-AR period following the CH stream, we see numerous strong deviations in elevation. Most of these are in the positive direction, accounting for the higher mean value.

Considering the magnetic field magnitude and solar wind bulk velocity, we note that enhancements of $|\mathbf{B}|$ often correspond to time periods preceding an increase in v_{sw}; presumably a result of the compression at the stream interaction region. In R1, at the location where the IMF becomes negative, we do not see a dip in $|\mathbf{B}|$ which is typical of a HCS crossing. This can likely be explained by the fact that a $\sim 500\,\mathrm{km\,s^{-1}}$ stream here directly follows the HCS. The resulting compression likely reduces the size of the HCS, and obscures the dip in field strength. The current sheet crossing for R2 exhibits a more pronounced dip in $|\mathbf{B}|$; likely because here the speeds on either side of the sheet are comparable. We note that a further dip in $|\mathbf{B}|$ occurs around half a day after the first.

Composition Properties

Compositionally, R1 and R2 show many similarities. The ranges of values for Fe/O during the periods of interest are 1.7–4.6 for R1 and 1.8–4.9 for R2. These differences between R1 and R2 are well-within the error bars for both minimum and maximum Fe/O. The ranges for C^{6+}/C^{5+} are 0.19–1.44 for R1 and 0.24–1.22 for R2. The differences in these values between R1 and R2 are outside of the errors for C^{6+}/C^{5+}only for the lowest values.

We note that the values of Fe/O associated with the CH for both rotations, which are around 0.23, appear to be above the typical observed values of CH abundance (Bochsler, 2007; Laming, 2015; Kilpua et al., 2016; Fu et al., 2017). The values of Fe/O found outside of CH streams also are greater than the typical ranges found by Kilpua et al. (2016) and Fu et al. (2017). As as a result, the FIP bias estimates resulting from these measurements are also higher than normal. Figure 6.9a shows

that in the CH stream, as identified by the v_p flattop and C^{6+}/C^{5+} minima, the lowest FIP bias value is 2.3, and that in the highest cases the FIP bias reaches 6.7. Again these are on the upper end of FIP bias values reported *in situ* (Bochsler, 2007) and also considerably larger than the CH, QS, and AR FIP bias values measured by EIS in Figures 6.6 and 6.7.

We use Fe/O measurements to narrow-down the sources of the solar wind in R1 and R2. Searching for typical values in the literature, Kilpua et al. (2016); Fu et al. (2017) carried out statistical studies of compositional properties for AR-linked solar wind (details in Chapter 2). Kilpua et al. (2016) found very little difference in the statistical values of Fe/O between CH, QS and AR source regions. Fu et al. (2017) find that CH streams limited to Fe/O values of 0.12 ± 0.05 ($\pm$ is standard deviation). AR and QS streams exhibited Fe/O values of 0.17 ± 0.09 and 0.146 ± 0.07 respectively. As AR and QS-associated streams appear to have access to these greater Fe/O abundance values (higher FIP bias) we assume a relatively high Fe/O to be indicator of connectivity to outside of the CH - particularly to a region of high FIP bias levels. While it does not seem possible to uniquely identify the type of source region from Fe/O measurements alone, we recall that as this is a compositional signature (similar to C^{6+}/C^{5+}) any notable change in Fe/O must be a result of some change in the source. We shall thus use Fe/O to search for such changes.

We set thresholds in Fe/O by which to differentiate solar wind of different origins. As the values of Fe/O in both R1 and R2 appear particularly high, we define these thresholds based on our data directly, rather than values found by previous authors. Here we are able to leverage the initial *in situ* observations in R1, by defining the high and low values for both R1 and R2, based on R1 observations only. This is useful as it seems apparent that FIP bias measurements from EIS can not be expected to correspond one-to-one with the *in situ* estimates. In R1 there is a clear distinction between the streams mapped to CH, CH-boundary and QS regions which

we use to classify Fe/O. We only, however, split into two groups as the CHB and QS regions in R1, which are clearly distinct in C^{6+}/C^{5+}, display very similar Fe/O values.

We make the classification by Fe/O as follows: The CH stream in R1 is identified as the region of $C^{6+}/C^{5+} < 0.6$, from DoY ∼88–90. We find the mean Fe/O value in this period, $\langle \text{Fe/O} \rangle_{\text{CH}} = 0.23$, and standard deviation $\sigma_{(CH)} = 0.04$. The mean Fe/O value in the combined CHB and QS period is $\langle \text{Fe/O} \rangle_{\text{NCH}} = 0.33$, and standard deviation $\sigma_{\text{NCH}} = 0.04$. On Figure 6.9 we mark data points for which $\text{Fe/O} < \langle \text{Fe/O} \rangle_{\text{CH}} + \sigma_{\text{CH}}$ with a purple point; we consider these characteristic of the coronal hole. We mark data points for which $Fe/O > \langle \text{Fe/O} \rangle_{\text{NCH}} - \sigma_{\text{NCH}}$ with an orange point; we consider these characteristic of the R1 coronal hole boundary or quiet Sun. The classification of CH or NCH for Fe/O does not indicate that this solar wind conclusively came from this region; only that its relative abundances are similar to solar wind which does.

We perform a similar analysis for C^{6+}/C^{5+} as for Fe/O. As noted in Section 6.3.2, C^{6+}/C^{5+} for R1 appears to partition the mapped solar wind into three regions; the CH, CHB, and QS. We shade the time series panels of Figure 6.9 for R1 by these regions; blue for CH (low-C^{6+}/C^{5+}; l_C), yellow for CHB (intermediate-C^{6+}/C^{5+}; i_C) and red for QS (high-C^{6+}/C^{5+}; h_C).

One of our goals is to identify the source for solar wind in the CH-AR region in R2, highlighted in Figure 6.3d. Both C^{6+}/C^{5+} and Fe/O compositional signatures change more rapidly here than in the CHB or QS region of R1; an indication that the source location, source properties, or source mechanisms, of the observed solar wind is changing with time. To test if this is truly the case, and to investigate the possible sources themselves, we distinguish between apparent structures in C^{6+}/C^{5+} on timescales of 0.5–1 days in Figure 6.9b. We colour these structures by the same scheme as 6.9a, by l_C, i_C and h_C values of C^{6+}/C^{5+}. To classify a given structure,

we compare the mean C^{6+}/C^{5+} there to the mean C^{6+}/C^{5+} in the l_C, i_C and h_C regions of R1. The structure is classified into the R1-defined category that its mean C^{6+}/C^{5+} value is nearest to. We do not highlight the ambiguous negative polarity region in R2 (at DoY $\sim$ 121) in order to separate it from solar wind which we are more confident is from the CH and CH-AR boundary.

In total, there are 10 separate solar wind stream structures identified in Figure 6.9b for R2, compared to the 3 in R1 which their identification is based on. We label these structures sequentially in time from S1–S10. We also label the ambiguous negative polarity period as S11. The structures are labelled 1–11 in the figure. It is immediately obvious that the l_C, i_C, then h_C (CH-CHB-QS) ordering in R1 is not preserved in R2. From S1 to S10, C^{6+}/C^{5+} moves back and forth between these three classes of charge state. As noted in Section 6.3.2, S1 appears to originate from the CH, and is the only structure with a clearly identifiable source region. S1 persists for around one day in R2, while the CH stream in R1 (which originates from the same CH) persists for around 3 days.

As above for C^{6+}/C^{5+}, Fe/O appears also to be split into small $\sim$ 0.5–1 day structures in the CH-AR boundary of R2. These smaller structures in Fe/O move between characteristic CH and NCH values based on the criteria described above. To account for the considerable error in Fe/O, particularly at higher values, we consider only those structures which last more than 6 hours (contain more than 3 consecutive data points) to be reliable. The boundaries of these structures roughly correspond to those of S1–10, as can be seen through their alignment with the boundaries in Figure 6.9. The three l_C regions in R2 all correspond to low-Fe/O (marked CH). Of the 5 i_C regions, 2 (S2 and S5) correspond to low-Fe/O values, and 3 (S3, S7 and S9) to high. It is likely that these compositional differences indicate that S2 and S5 are of different origin to S3, S7 and S9. We note particularly that S3 exhibits C^{6+}/C^{5+} values which are very near the range of l_C, and high Fe/O values. This itself may

represent wind of an additional distinct origin. The two h_C regions in R2, S4 and S10, correspond to low and high Fe/O values respectively. Combining the classifications by C^{6+}/C^{5+} and Fe/O, we have found five of a possible six combinations of these classifications in R2.

Finally, we observe that in S11 there is a dip in C^{6+}/C^{5+} and Fe/O followed by an increase in both. Fe/O drops-off coincidentally with the second dip in $|\mathbf{B}|$ noted above, while C^{6+}/C^{5+} remains at similar levels. These signatures do not exclusively associate this region with either AR or QS, although they do confirm that it is not a CH stream as is found following the HCS in R1. In the 427 eV electron flux, we note an enhancement towards anti-parallel pitch angle bins at this time. Unfortunately data from bins 7 and 8 are missing in many measurements, so the true increase in intensity and extent of any increased focusing cannot be observed. While this may be a result of a drastic increase in flux in these bins, we cannot state this conclusively when data are missing.

To summarise, we collect the key comparative results from this section in Table 6.1. We see from the table that absolute values of parameters such as v_{sw}, Fe/O, and C^{6+}/C^{5+} are very similar between R1 and R2. The main differences between the two periods are in fact in the composition (through combinations of Fe/O and C^{6+}/C^{5+}), structure, and the variability of IMF orientation.

6.4 Discussion

In this section we synthesise all the results for R1 and R2 to explain the influence of AR-12532 on the solar wind from a trailing CH boundary. First, we argue that the changes observed in the *in situ* data between R1 and R2 are primarily a result of the emergence of AR-12532. Second, we discuss the possible configurations for reconnection. The results in Sections 6.3.4 and 6.3.5 are consistent with this process taking place. Third, we use *in situ* and remote sensing results for R1 to

Table 6.1: Key results for the periods of interest in Section 6.3.5, split into R1 and R2. The rows from top to bottom are: maximum solar wind bulk velocity; minimum Fe/O value, maximum Fe/O value; minimum C^{6+}/C^{5+} value; maximum C^{6+}/C^{5+} value; number of instances where $|\Delta\phi_P|$ exceeds 45° before returning to $< 45°$; number of instances where the IMF inverts based on $|\Delta\phi_P|$ and strahl alignment; the number of distinct structures identified by composition signatures; and the duration of the stream which originates in the CH.

	R1	R2
Max. v_{sw} ($km\,s^{-1}$)	550	550
Min. Fe/O	1.7	1.8
Max. Fe/O	4.6	4.9
Min. C^{6+}/C^{5+}	0.19	0.24
Max. C^{6+}/C^{5+}	1.44	1.22
Distinct Structures	3	10
Fe/O-C^{6+}/C^{5+} combinations	3	5
Instances of $\|\Delta\phi_p\| > 45°$	3	9
Radial IMF Inversions	1	4
CH Stream Duration (days)	3	1

explain where and how the solar wind from the CH and CH-QS boundary originates on the Sun, and how this could have influenced its *in situ* properties. Fourth, we do the same for R2, and contrast the locations and processes with those of R1 to find which are uniquely a result of the presence of AR-12532. Fifth, we evaluate these results in the context of the selection of AR solar wind release mechanisms outlined in Section 6.1. Wherever possible throughout our discussion of the results for the origins of solar wind during R2, we shall draw comparison with the observations for R1. Finally, we discuss the implications of these results for connecting solar and heliospheric observations; particularly in the context of the Solar Orbiter and Parker Solar Probe missions.

6.4.1 Isolation of AR Effects on Coronal Hole Wind

In Section 6.3.1, we found that the morphology of the source coronal hole is relatively unchanged between R1 and R2, despite the emergence of AR-12532. The preservation of CH morphology, and mapping location, leads us to conclude that any changes in the nature of the solar wind are likely a result primarily of the emergence

of the AR. The most noticeable change in mapping, described in Section 6.3.2, is the deviation of mapped sourcepoints northwards towards the CH-AR boundary in R2. As this region shows connection to the core of the AR (Figure 6.1) this change is also attributed to the emergence of the AR.

In Section 6.3.3 we found that both the AR and the CH/CHB during R2 were relatively quiet; exhibiting no significant flaring or reconfiguration of the magnetic field. From this we conclude that the solar wind observed during R2 is produced under steady conditions, rather than through large sporadic events, and expect the *in situ* observations also to reflect this. This is observationally advantageous, since we can be confident that the *in situ* solar wind observations are representative of the general state, and not some transient. We are also confident that our understanding of the AR and CH sources, which is primarily based on snapshot AIA and HMI imagery (and Hinode-EIS observations rastered over a few hours), is applicable over the entire *in situ* observational period of solar wind from these regions; ~ 5 days.

6.4.2 Signatures of Interchange Reconnection

Results in Sections 6.3.4 and 6.3.5 provide evidence of the role of interchange reconnection in the release of solar wind during R1 and R2. (The former through remote sensing signatures of non-thermal velocity, the latter through *in situ* inversions/deflections of the IMF.) We describe here how reconnection might be occurring at the Sun for R1 and R2, and how signatures of this manifest themselves in the *in situ* and remote sensing data.

Interchange Reconnection in the Low Corona

All three sets of EIS observations presented in Section 6.3.4 showed enhancements in $v_{\rm nt}$; a signature of reconnection-associated plasma motions (Harra et al., 2001). Reconnection at these heights ($< 0.1\,R_\odot$ above the photosphere) occurs before sig-

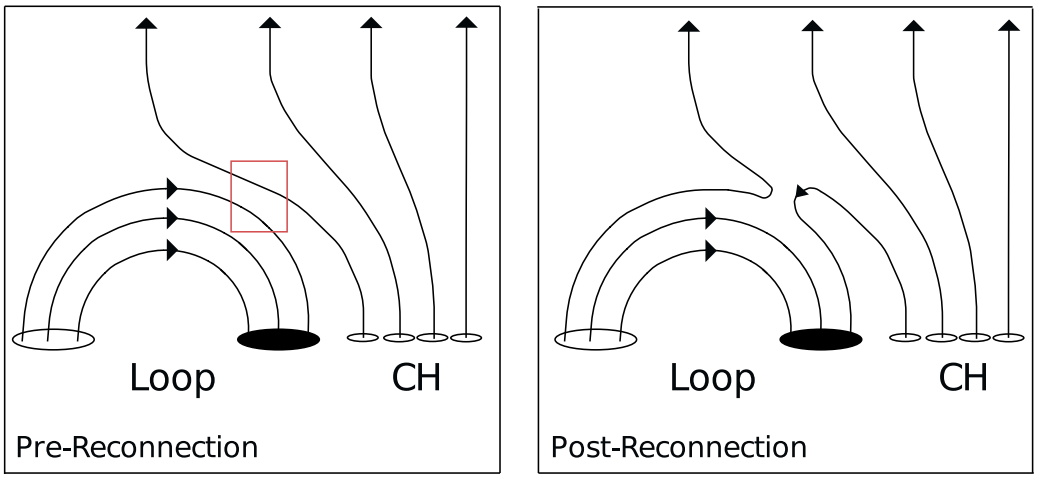

Figure 6.10: A schematic of antiparallel interchange reconnection occurring between oppositely-directed fields; open positive CH field and a closed negative loop near the footpoint. Reconnection occurs somewhere in the red box of the pre-reconnection panel, producing the new topology in the post-reconnection panel. The process opens flux in the positive footpoint of the loop, opposite to the reconnection site, and closes it in the CH.

nificant expansion of the magnetic field has taken place. Thus, we expect the reconnecting regions to be approximately adjacent to each other when mapped to the photosphere. Given this, and our estimates of where open flux is rooted in the photosphere from PFSS modelling, we can infer the relative polarities of the open and closed flux, in the case of interchange reconnection.

Interchange reconnection inferred from the EIS observations could take the form of either antiparallel (x-point) or component reconnection (see Chapter 1, Section 1.1.7). In the cases where only one source of open flux is rooted near the location of the reconnection signature, the type of reconnection taking place can be predicted through the relative polarities of the open and closed regions. If the closed loop and nearby open flux are of opposite polarity, then we infer antiparallel reconnection. If they are of the same polarity, then we infer component reconnection. Schematics of these two processes are shown in Figures 6.10 and 6.11 respectively.

Depending on which type of reconnection takes place, the actual footpoint location of the post-reconnection open flux may vary drastically. In the like-polarity case

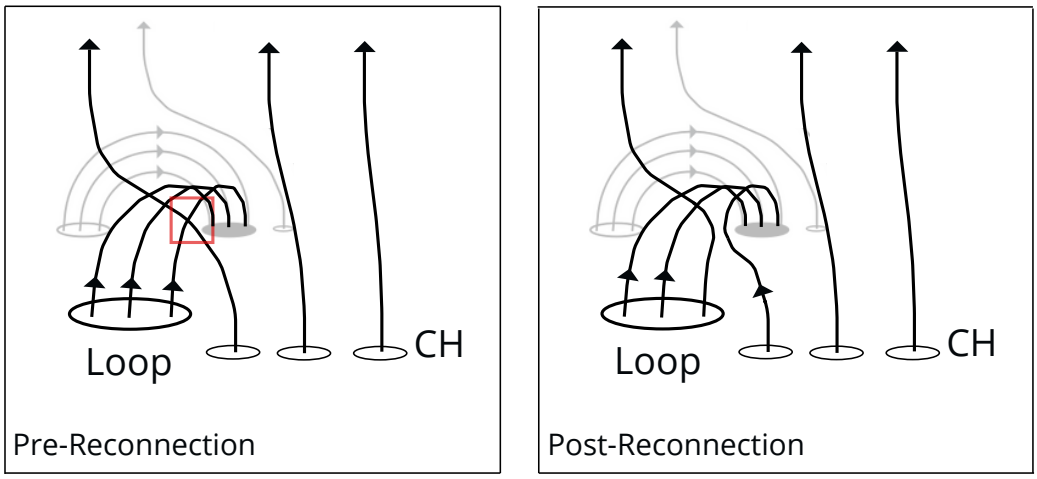

Figure 6.11: A schematic of component interchange reconnection occurring between like-directed fields; open positive CH field and a closed positive loop footpoint. The loop connects to out of the plane of the CH-loop line, in order to allow component reconnection to take place. Reconnection occurs somewhere in the red box of the pre-reconnection panel, producing the new topology in the post-reconnection panel. The process opens flux in the positive footpoint of the loop, near the reconnection site, and closes it in the CH.

of Figure 6.11, open flux will become rooted in the side of the loop at which the reconnection occurs. The compositional properties (such as fractionation) which are found close to the reconnection site are therefore the best guesses at the composition of the plasma on the newly-opened field. In contrast, in the antiparallel case, the open footpoint will be rooted on the other side of the loop. The footpoint of the open flux in the antiparallel case is likely to be transferred further away than in the component reconnection case, and a longer section of previously-closed loop will be opened to the heliosphere. Associated plasma compositional properties in this case might not be the same as those near the reconnecting side of the loop as seen by EIS.

Interchange Reconnection in the High Corona

EIS only observes reconnection which takes place low in the corona ($< 0.1\,R_{\odot}$) relative to the solar wind formation height. Interchange reconnection may thus occur at greater heights in the corona than can be detected by EIS. This could also

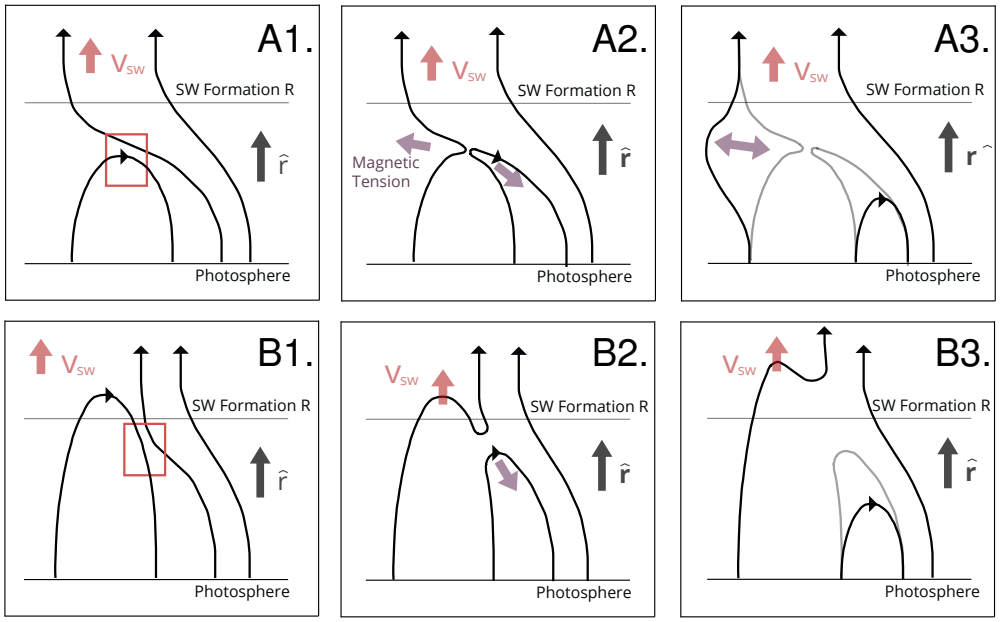

Figure 6.12: Schematic of antiparallel interchange reconnection between an open field line and loops of two different heights in the corona. Solid horizontal lines represent the photosphere and solar wind formation height. Below the solar wind formation height the magnetic energy density is greater than the plasma energy density, while above it the plasma energy density is greater, and so the radial solar wind flow dominates the magnetic field evolution. Panels A1–3 and B1–3 each show the timeline of two different interchange reconnection events for select field lines. In panels A1–3, a loop is opened which does not extend above the solar wind formation height. Magnetic tension applies dominantly to the kink in the newly-opened magnetic field line, such that it moves rapidly in response to this force and generates an Alfvén wave. In B1–3 a similar reconnection event occurs, with a loop which now extends above the solar wind formation height. Here the plasma dynamics dominate over the magnetic field, and so the kink propagates outwards, embedded in the solar wind.

open otherwise closed flux, but can not be inferred from the remote sensing data employed in this study. At such heights it is not clear what configuration of reconnection might be taking place. The polarities inferred by HMI data correspond to the photosphere only, and so with increasing height many different loops may encounter CH open flux and reconnect. In particular, for large loops reconnecting at these heights, a kink may be produced in the IMF, but no reconnection signatures will be observed by EIS.

Typically, inverted magnetic field (with Sunward strahl signatures) is used *in situ* to identify instances of interchange reconnection near the Sun (e.g., Crooker et al.,

2004; Owens et al., 2013). Owens et al. (2013) in particular point out that for a reconnection event to manifest *in situ* as a kink or inversion in the IMF, it needs to occur with a loop which extends higher than, or is of comparable height to, the height of solar wind formation. A schematic of reconnection for a loop both extending above and confined below the solar wind formation height is shown in Figure 6.12. We suggest an estimate of this height as similar to the source surface; say heliocentric distances of 1.5–3.5 $R_{\odot}$. In PFSS models, below the source surface the magnetic energy density dominates over the plasma energy density. In this region then, the magnetic field in the corona responds to and dissipates a perturbation before it is carried out into the solar wind, instead producing an Alfvén wave which propagates into the heliosphere (Owens et al., 2013).

Reconnection observable by EIS could also lead to kinked IMF, by opening taller loops at their base. Examining Figures 6.10 and 6.11, for reconnection occurring so low down, only antiparallel reconnection should lead to a kinked IMF. Component reconnection instead will keep the apex of the loop connected at both ends; preventing a kink from forming.

Kinks in the field created by reconnection may or may not fully invert. Also, for a kink which propagates out into the solar wind, the magnetic field will evolve to remove the kink at the order of the local Alfvén speed (Gosling et al., 2005). Depending on the loop and reconnection height, reconnection geometry, and solar wind evolution, initially inverted field may straighten to the point of no longer exhibiting a full inversion when finally encountered at the spacecraft. Instead the observed magnetic field may simply be deflected from the nominal (or background) Parker spiral direction, while still remaining in the same sector, and exhibiting antisunward strahl. Reconnection thus might not always manifest as a local inversion of the IMF. It appears that it often does, however, due to the common observations of inverted IMF in the solar wind (around 5% of the time, as measured by Owens

et al., 2013).

We can consider specific field orientations to infer some details of reconnection geometry. We expect kinks in the field to primarily lie in the plane in which the magnetic field footpoint moves during interchange. For example, a reconnection event in which an open field line's footpoint moves to the east or west, should manifest primarily as a kink in the ecliptic east-west plane, rather than the north-south. *In situ* observations should thus be able to distinguish this aspect of the reconnection geometry.

For reconnection which occurs at higher altitudes than can be seen in the AIA or EIS observations, the affected loops, and their compositions and structure, cannot be determined from the observations in this study. Loops and open flux rooted in locations which are distant in the low corona can conceivably converge at greater heights, making reconnection between structures which appear isolated in the low coronal observations possible. The closed loop footpoints, which become open following reconnection, might then lie well outside of the EIS fields of view, and so their compositional properties cannot be directly measured, even if they were reliably located with magnetic field modelling. Robust statements on the precise source locations of streams which exhibit signatures of this reconnection are thus not possible in such a case. At best we can suggest candidate source regions from the available data and the mapped sourcepoints.

6.4.3 Solar Wind from a CH-QS Boundary

In this section we will offer explanations for the *in situ* properties observed for the solar wind during R1. The primary tool for distinguishing solar wind sources is composition; in this case C^{6+}/C^{5+} and Fe/O as plotted in Figure 6.9. The C^{6+}/C^{5+} variations revealed 3 distinct periods, which we labelled as CH, CHB and QS, in order of increasing charge state. Changes in Fe/O do not match perfectly with

these periods, but the CH appears to feature the lowest Fe/O, while the CHB and QS periods are comparable (CHB has slightly higher Fe/O on average). This is not perfectly in line with the expectations of Fe/O evolution for a CHB suggested by McComas et al. (2002), who found FIP bias to hold at the lower coronal hole values in wind originating from the CHB. It is more similar to the observations for abundance by Wang et al. (2009).

We examine the EIS remote sensing results for R1 (Figure 6.5) to see if this *in situ* compositional configuration can be explained through measurements of relative abundance around the source. As previously stated, due to lack of counts in the EIS data we assume a base FIP bias of 1 for the CH plasma measured remotely. However, the FIP bias inferred for the CH-associated stream, from Fe/O values measured *in situ*, appears to be significantly larger than this. We assume that this lowest FIP bias region we observe *in situ* is in fact truly from the CH (as supported by C^{6+}/C^{5+} and v_{sw} data) and that there is some scaling between the EIS Si X/S X biases of 1 to ≥ 3 and the *in situ* Fe/O-derived biases of $\sim$ 2–7. Outside the CH, the *in situ* Fe/O values are on the higher end of those generally observed for both QS and AR in statistical studies (Kilpua et al., 2016; Fu et al., 2017). We thus assume that they correspond to the regions which display FIP biasing of ≥ 3 (roughly the maximum which can be observed with this EIS dataset).

Having argued that the *in situ* Fe/O values seen in the CHB and QS periods of R1 are associated with regions of EIS-derived FIP bias of ≥ 3, we consider what regions around the eastern boundary of the CH could possibly produce them in the solar wind. The change in C^{6+}/C^{5+} between CHB and QS regions measured *in situ* suggests that the sources of these two regions are different, despite the similarity of the Fe/O abundance values. From C^{6+}/C^{5+} values we might expect that the CHB source should lie closer to the CH than the QS source, considering expansion factor models of Wang and Sheeley Jr (1990). In Section 6.3.4 we noted two particular

regions which exhibited strong upflows, non-thermal velocity, FIP bias around ≥ 3 and are situated close to regions of open flux predicted by the PFSS model; these were contained in Boxes 1 and 2 of Figure 6.5. We thus offer the explanation that the CH portion of the R1 stream originates in the CH-proper, while the CHB and QS streams could reasonably originate in locations similar to these FIP-enhanced upflow locations at Boxes 1 and 2.

Boxes 1 and 2 of Figure 6.5 appear to reasonably match with the CHB and QS periods during R1. These locations are in an area of the corona where we expect the magnetic field to be predominantly closed, as evidenced by the brightness of emission there (e.g., in Figure 6.5a) and the predicted open flux locations from the PFSS model (Figure 6.8). For plasma to escape from these regions and produce the compositional signatures observed *in situ*, it must make its way onto open magnetic field lines. A straightforward way to allow this is through component interchange reconnection of the closed field rooted in these regions with the adjacent open magnetic field of the CH, as was found in numerous configurations by Fazakerley et al. (2016) and others. Component-type reconnection is favoured here due to the like-polarity of these two regions. Following a reconnection event, open field lines are rooted in the previously closed-off region, and plasma is permitted to flow into the heliosphere. Two distinct locations in the FIP-enhanced source region show signatures of v_{nt} which may indicate plasma motions associated with reconnection. Both of these locations are coincident with pronounced upflows, which if the field were opened would likely form outflows into the heliosphere. This reconnection occurs low down in the corona, and is probably continuously transferring footpoints of open flux from the CH to the neighbouring QS region. Since this is most likely component reconnection, we do not expect it to be responsible for the kinks in IMF observed *in situ*.

There are further signatures consistent with reconnection to consider for R1. In

Figure 6.9a we observe fluctuations in $\Delta\phi_P$ which are stronger during the period of *in situ* observations which we associate with the CHB and QS than that during mapping to the CH. Conversely, θ_{el} is more steady in the CHB and QS periods than in the CH. The large deflections, and one inversion, of $\Delta\phi_P$ are consistent with expectations of interchange reconnection. Such reconnection occurs with large loops, and is likely at higher altitudes than that inferred from the EIS observations above. *In situ* evidence for interchange reconnection with loops of varying sizes has been previously reported by Fazakerley et al. (2016). The variation which we observe in $\Delta\phi_P$, although limited by the 2-hour resolution we apply to the data, occurs on scales of around 6–12 hours. This is larger than the typical scales of solar wind magnetic flux tubes inferred by Borovsky (2008), indicating that if this is a signature of some near-Sun reconnection processes, they likely involve extended bundles of flux tubes.

The change in IMF alignment for R1 does not clearly and consistently line up with changes in plasma compositional signatures. We thus cannot, for example, associate each of the two non-CH regions we have identified with one instance of reconnection. This is unsurprising given the difficulty in interpreting these deflections as reconnection signatures described in the previous section. In the simplest terms we see larger, and more numerous, deviations from Parker angle alignment in the CHB and QS periods, which we would also expect if interchange reconnection had occurred in the corona with loops of sufficient height to produce interplanetary kinks. The reconnection process itself must also occur at a sufficient height so as not to be detected by EIS. There is one instance during R1 in which the field orientation crosses the point of inversion, relative to the radial direction, for around 4 hours at DoY $\sim$ 92. Given the above arguments, this is the reconnection signature for R1 in which we have most confidence.

We next consider the field orientation to infer details of the reconnection geometry.

The kinks in the field primarily lie in the east-west (ecliptic) plane, rather than north-south. This signature of reconnection primarily transports open flux footpoints to the east or west. Since this is solar wind which trails the main CH stream, the most likely configuration is reconnection between open CH flux and loops which lie to the east. Since this stream falls adjacent to the HCS, these loops probably make up the streamer belt.

The possibility that reconnection occurs at a range of heights complicates the process of identifying source regions. Reconnection may occur at higher altitudes than can be observed by EIS or AIA. The loops which are available for this reconnection, their orientation, and their composition, are thus not known. Thus, while the EIS fractionation data could be matched reasonably well with the *in situ* measurements, some or all of the solar wind we observe may originate in other locations. This unfortunately increases the ambiguity of the origins of the CHB and QS wind for R1. This may explain why e.g., the CHB and QS periods have slightly different compositional signatures while appearing to be from approximately the same region (Box 1 and 2 of Figure 6.5). It may be the case that one or both of these streams in fact originates in some larger closed loop, which may be rooted outside of the EIS field of view, and which contains plasma of distinct composition.

To summarise this section, for solar wind associated with a CH-QS boundary during R1, combined *in situ* and remote sensing data suggest that interchange reconnection occurs between open CH field and eastward loops, allowing plasma from these loops to escape into the solar wind. Further, it seems likely that this reconnection occurs at, and with loops of, a range of heights. Low-altitude reconnection results in the plasma motions which are detected through $v_{\rm nt}$ by EIS. Reconnection with large loops results in kinks in magnetic field orientation which are observable at 1 au. The reconnection observed at lower altitudes appears to be component reconnection. Unobserved reconnection higher up can not be classified here, but could

arise from many different geometries, and produce the kinks which are observed. Good candidate source regions can be seen near the coronal hole boundary in the EIS observations, but these are not necessarily the only relevant source regions for this period. In the following section, we contrast these explanations and observations for R1 with those for R2 to investigate how solar wind origins change once an AR has emerged nearby.

6.4.4 Solar Wind from a CH-AR Boundary

Active Region Influence *In Situ*

We now discuss of the solar wind observed during R2, which is associated with a trailing CH-AR boundary. Before exploring the origins of the *in situ* observations which arise for this period, we first contrast them with some *in situ* results from the equivalent CH-QS boundary in R1, and explore why differences and similarities arise. Given the evidence summarised in Section 6.4.1, we present with confidence that the differences are a result of the changes to the source region caused by the emergence of AR-12532.

Obvious differences between R1 and R2 manifest in the durations of equivalent streams. The first of these is in the CH stream in both cases (also labelled S1 for R2) which was found to persist for ~ 3 days in R1 but only ~ 1.2 days in R2. Given that the mapped sourcepoint locations (and size of the CH in EUV imagery around these locations) are approximately preserved between R1 and R2, we suggest that this is a result of the AR influence on the CH. It is possible that in R2 there is more open magnetic flux associated with source regions of non-CH composition plasma than there is in R1. In R2, this would both decrease the size of the CH-composition stream, and increase the size of the non-CH-composition streams which follow it. This is again consistent with open magnetic flux being transferred from the CH to previously closed locations through interchange reconnection.

The streams which follow the CH stream, (CHB and QS for R1; S2–10 for R2) are also clearly different between R1 and R2. The CHB and QS periods are both around one day in length. S2–10 in R2 are very different to their counterparts in R1, each lasting around 8–12 hours. The values of C^{6+}/C^{5+} and Fe/O in these structures do not increase monotonically as they do for R1; instead they fluctuate between values characteristic of different sources. The different combinations of Fe/O and C^{6+}/C^{5+} values within these structures also suggest at least five distinct sources, as opposed to the three suggested in R1. This too is consistent with an increased occurrence of interchange reconnection resulting from the presence of AR-12532 at the CH boundary in R2; releasing plasma from different regions to the heliosphere. It also suggests that the CH-AR boundary, or the AR itself if this is also opened, features diversity in its composition between plasma populations. This is consistent with the perceived variability of plasma composition within an AR (as found e.g., by Baker et al., 2013).

In Section 6.3.5, we reported that R2 features more large ($\geq 45°$) deviations in IMF angle $\Delta\phi_P$ than R1 during the periods of interest; 4 of which constitute inversions relative to the radial direction. R2 also exhibits more strong deviations from 0° in θ_{el} of the IMF. Following the same reasoning as for R1, we can interpret these deviations as kinks in the IMF due to reconnection. As there are more large deviations for R2 than in R1, this would indicate more instances of this reconnection during R2. Further, since the deviations also occur more strongly in θ_{el} than in R1, this reconnection might also be occurring in the north-south plane, as well as the east-west.

Some similarities between R1 and R2 are also worth highlighting. Across the entire S2–11 portion of R2, there are no C^{6+}/C^{5+} or Fe/O measurements which are greater than the maximum measured C^{6+}/C^{5+} and Fe/O during the CHB and QS periods of R1. This is somewhat unexpected, given the higher possible fractiona-

tion observed for ARs compared to QS (Fu et al., 2017) and observations that AR plasma might experience greater FIP biasing, particularly at loop footpoints, than other closed field regions (Baker et al., 2013). This does agree with the observations of Widing and Feldman (2001), however, who reported that active regions often display weaker fractionation than the quiet Sun; particularly when newly-emerged. If FIP-bias is greatest in the AR core (which from EIS observations in Figure 6.7 appears to be the case) then the similarity of Fe/O between R1 and R2 may indicate that plasma from the AR core does not reach ACE.

Another similarity during the periods of interest for both R1 and R2 is that the strahl remains mostly unidirectional (Figure 6.9). We have already noted that Sunward strahl is often evidence of reconnection, while bidirectional strahl is usually evidence of a loop, still closed at both ends. Solar wind from active regions may exhibit both of these phenomena, given the loop expansion mechanism discussed in Section 6.1. The observed strahl however remains unidirectional for most of the observations of R2, giving no unique evidence of the existence of these loops. We cannot fully exclude their existence, however, as closed loops may still exist which do not display bidirectional strahl, e.g., due to the strahl travelling from one end of the loop being highly scattered (Owens et al., 2013).

Sources of Solar Wind from the CH-AR Boundary

We now turn to discussing the possible origins of the solar wind during the period of interest for R2 - which we have associated with the emergence of AR-12532- through remote sensing data. We focus on the structures highlighted in Figure 6.9: S1–10. For these 0.5–1 day periods, *in situ* composition data imply more distinct source region states (at least five) than in R1 (at most 3), related to multiple instances of interchange reconnection in R2. 'Distinct source region states' for the periods S1–10 may refer to multiple source locations, repeating source locations

with time varying properties, varying release processes, or some combination of these. We shall compare *in situ* observations to EIS data, as we did for R1 in Section 6.4.3, to search for viable sources. In Section 6.3.4 we presented EIS data for both the CH and AR-12532. Based on the mapping we default to the CH and CH-AR boundary being the most likely region for solar wind sources, and will only consider the active region or other sources if strong evidence exists in *in situ*-remote sensing comparisons. Given the evidence of interchange reconnection at greater heights in the corona already noted above, there is reason enough to believe that the AR-proper, and potentially other regions, might contribute to the solar wind. Candidate source regions identified below are therefore only suggestions which can reasonably explain the observed *in situ* properties.

We first consider the structures with CH-like composition: S1, S6 and S8. These all feature low FIP bias, as is consistent with the presumed FIP bias of ~ 1 for the CH as seen by EIS in Figure 6.6. Since upflows and open flux also reside in the CH, it is a viable source of solar wind of this composition. We are confident that S1 originates in the CH-proper, although this is not as certain for S6 and S8, as they fall between clearly non-CH sourced *in situ* streams. If S6 and S8 do also originate in the CH, this suggests a mapped sourcepoint path which crosses the CH boundary multiple times. There is some support for this in the mapped sourcepoints, which fall very much along the CH boundary. This could also arise as a result of interchange reconnection processes leading to open flux which is rooted in a non-CH source region being interspersed with flux which is predominantly rooted in the CH.

We now turn to the remaining periods which do not exhibit CH composition. First we consider those with CH-like Fe/O measurements, which nevertheless coincide with C^{6+}/C^{5+} measurements which are greater than those for the source CH. These structures, S2, S4, and S5, have intermediate (and indeed possibly high) charge

state values associated with low-FIP bias. This is similar to the case of coronal hole boundary region from McComas et al. (2002). Examining the EIS FIP maps for the CH-AR boundary during R2, regions of both low and high FIP bias exist along the boundary with the coronal hole. These regions are coincident with solar wind sourcepoints, and upflows are also seen in Doppler velocity measurements. Other areas of the CH-AR boundary exhibit FIP bias of ~ 1 also, although these are not obviously open to the heliosphere, and would likely require some reconnection to occur to allow this. Most of the low-FIP regions coincide with the low-$v_{\rm nt}$ area of the CH-AR region, so for reconnection to open these regions it would need to occur at heights above those detectable by EIS in Fe XII. It is thus likely that at least some of this low-FIP bias plasma is contributed from the over-expanding CH boundary, and the rest can be explained by the opening of closed loops which lie further from this boundary. For reconnection above heights observed by EIS, we note again that sourcepoints of opened loops may fall outside of the EIS FOVs available in this study.

Finally we consider the 4 high-Fe/O structures which correspond to intermediate and high C^{6+}/C^{5+} measurements; S3, S7, S9 and S10. Their composition is characteristic of closed loops which possess both higher electron temperatures and stronger fractionation than coronal holes. S3, S7 and S9 are all of intermediate charge state while S10 displays high charge state. S3 is somewhat anomalous in that it lies very close to the low-intermediate cutoff. Considering first the intermediate charge state structures, one explanation is that they may originate from the CH boundary, at a region of enhanced FIP bias of 2–3. One such region is evident in Box 1 in the EIS maps in Figure 6.6, near the west-most boundary crossing of the mapped solar wind sourcepoints out of the CH. This also coincides with regions of strong upflows, and enhanced $v_{\rm nt}$, consistent with escape of solar wind from this region via interchange reconnection. Other, smaller, enhancements of all three of

these parameters are found further east along the coronal hole boundary. These are possible sources for streams S3, S7 and S9.

Considering now S10, we might expect a FIP-enhanced source which lies away from the CH boundary (to explain the higher C^{6+}/C^{5+}). A large region meeting this description can be found in Box 2 of Figure 6.6d. However, there are no strong upflows at this location, and also no enhancements in v_{nt}, which renders this region a questionable solar wind source. Other possibilities are that this plasma may originate from the AR itself, but given that there are no other particularly unusual characteristics compared to the rest of the CH-AR boundary (e.g., very high C^{6+}/C^{5+} or Fe/O), this does not appear to necessarily be the case either.

Turning from an explanation of charge state based on CH-proximity, we consider the origins of different composition signatures more generally. There is no expectation that electron temperature and FIP bias should vary 1-to-1 in the corona (see Chapter 2). As such, the higher Fe/O values during S3, S7, S9 and S10 could be due to origins in closed loops, which for some reason have different relationships between fractionation and C^{6+}/C^{5+} than those from which S2, S4, and S5 originate. This is consistent with reconnection opening multiple different loops, of different sizes and properties, as we have already suggested. Further, these different combinations could also arise from opening similar coronal loops at different heights; another scenario suggested above. Heavy ions upflowing from a loop which has opened below the charge state freeze-in height will continue to evolve in ionisation based on electron collisions in the CH plasma environment (see e.g., Landi et al., 2011, and Chapters 1 and 2). Typically coronal holes are cooler than closed field regions in terms of T_e, and so the charge states would freeze-in at a lower state than if this were not occurring. This might explain observations of intermediate and low-C^{6+}/C^{5+} during periods of high-Fe/O. Further again, as the temperature across a coronal loop is not necessarily constant (e.g., Huang et al., 2012) reconnection at

different heights may also allow plasma of different characteristic ionisation states to escape into the heliosphere from the loop itself.

Our observations contain no compelling evidence from compositional comparisons that any of the solar wind within S1–10 necessarily originates from outside of the CH or AR-connected boundary. This is not surprising, because in the EIS observations there is no level of fractionation which is unique to the AR, whose presence in the *in situ* data would thus unambiguously be from that location. Most of the composition signatures, and other observations, appear to be readily explained by having their origins in the CH itself or in the CH-AR boundary; the region connected by loops to the core of the AR. We expect component reconnection at this AR-connected boundary, at least for heights observable by EIS, since reconnection signatures are observed adjacent to the like-polarity open CH flux. As for R1, this means that reconnection at the heights observed by EIS is not likely the cause of kinks in the IMF. While it thus certainly seems likely that solar wind is being released from the AR-connected region, again the possible contribution from other regions cannot be ruled out.

Active Region-Associated Interchange Reconnection

We shall now discuss what reconnection configurations are suggested by the *in situ* magnetic field observations. Previously we noted the increased number, and size, of IMF deflections during R2, in both the azimuthal and elevation planes, relative to R1. We interpret this as evidence of more instances of interchange reconnection occurring as a result of the presence of AR-12532 during R2. The *in situ* signatures of this reconnection suggest that it is with large loops, above EIS observation heights, as established above. Given that reconnection is also a good explanation for the many different structures which are encountered *in situ*, these results support one another. The interchange reconnection occurring during R2 appears to create larger

kinks in the field than that for R1, although this could be a factor relating to the one-dimensional nature of *in situ* observations or evolution of kinks during propagation through the heliosphere. Due to the increased number of true inversions, which are less likely to be a product of turbulence or velocity shear, we have confidence in a larger number of reconnection signatures for R2 than R1.

The strong north-south, as well as east-west, oriented deflections in the field suggest interchange reconnection is not confined only to occur between structures which are at similar latitudes. This is consistent with the likely reconnection geometry; open flux footpoints, such as those indicated by the mapping, reconnecting with closed field associated with the active region to the north. A similar process is shown in Figure 6.11. We have already observed evidence of this occurring between the CH and CH-AR boundary, although low in the corona through EIS observations. Since we argue that the effects of the AR on the solar wind are isolated in R2 when compared to R1, it follows that this additional north-south reconnection should be a consequence of the emergence of AR-12532. Thus it seems likely that this reconnection should occur between open flux and AR-connected loops. AR-connected loops include those connecting the CH-AR boundary to the negative core of the AR. Reconnection between open CH flux and these loops would constitute component reconnection, and open the CH-AR boundary to the heliosphere.

Another possibility is reconnection occurring with loops extending southward from the AR-proper. This would make anti-parallel reconnection possible, and open up the positive polarity side of the AR to the heliosphere at ecliptic latitudes (analogous to the process in Figure 6.10). From a simplistic viewpoint, we might argue that the stronger inversions we observe are more likely to be a result of antiparallel than component reconnection (as exampled by comparing the post-reconnection schematics of Figures 6.10 and 6.11). However we cannot conclude either way with certainty. We note that footpoints of open flux predicted by PFSS modelling (Figure

6.8) appear to the north and north-east of the AR. Such open flux is conceivably that being opened by such an interchange process.

Solar wind might also emerge from the AR itself, but be unobserved in the ecliptic plane. There is evidence that reconnection resulting in plasma escaping to the solar wind occurs at AR-12532. This was described in Section 6.3.4 based on the EIS observations in Figure 6.7. In Box 1 of this figure, strong upflows coincide with reconnection signatures in v_{nt}, at a location adjacent to open flux. This suggests component interchange reconnection is taking place, opening the field at this part of the AR. Since this open flux is rooted quite far to the north of the mapped solar wind sourcepoints, it appears unlikely that this plasma would make its way into wind which is observed in the ecliptic. We thus argue, with some confidence, that plasma from this location is able to escape into the solar wind, but we cannot confirm if it reaches the ecliptic to be observed at L1.

To summarise, the precise source regions for most of the structures S1–10 for R2 are somewhat ambiguous, although identifying likely sources is possible. There are multiple separate source locations and mechanisms of release which are likely at play, and it is not clear how plasma in any individual structure (excepting perhaps those with CH composition) comes to enter the solar wind. We are confident that solar wind escapes from the CH-proper, and from the AR-connected CH boundary, due to component interchange reconnection certainly at low altitudes and also possibly at higher ones, through configurations which are not present in the non-AR case. It also appears likely that antiparallel interchange reconnection allows the escape of plasma nearer to the core of the AR into the heliosphere. We can state with more confidence that solar wind escapes from the positive polarity region of the AR-proper, through component reconnection, but that the plasma released in this way is probably not observed *in situ*.

Solar Wind from the Negative AR Footpoints?

We now turn to examining the origins of S11 - the period of unknown origins during R2. S11 likely originates either in the negative QS region, or around the negative AR footpoint. It is tempting to favour the latter origin for S11, simply because the solar wind conditions following the HCS in R1 are very different from those in R2. Examining AIA data corresponding to the backmapped release times for the solar wind in which HCS crossings are embedded for both R1 and R2 (further east around the disk than the observations shown in e.g., Figure 6.1) reveals that a small CH is present in R1 but not in R2. This alone can explain the higher velocity, and lower C^{6+}/C^{5+} and Fe/O following the crossing in R1 as a fast stream originating in this CH. The fact that the two periods are different *in situ* is thus not strong enough evidence for an AR origin for S11.

During S11 we observe enhanced strahl intensity (although in Section 6.3.5 we note that data are missing) in Figure 6.3.5. Enhanced strahl flux however is not typical of slow solar wind, which is usually associated with far weaker strahl than fast (e.g., Pagel et al., 2005). Elsewhere in our observations, increases in strahl flux appear to occur primarily during fast streams, or the compression regions which precede them. This increase is therefore unique, as the stream here is neither fast, nor apparently compressed. This might suggest that S11 does not originate in typical QS, and is instead from flux rooted in the AR. Examining the literature however, we find no studies on whether the enhancement of strahl from ARs relative to QS is expected.

Given the above evidence, we maintain the position that it is quite possible, although unconfirmed, that S11 plasma might originate in AR-12532 itself. If this is true then it requires some process to allow plasma to escape from the AR. Given that there does not appear to be adjacent open negative flux, X-point interchange reconnection of negative flux with the positive AR footpoint is more likely than

component reconnection. Another explanation is the expansion of an AR loop into the solar wind. (The monodirectional strahl during S11 could be explained by the loop disconnecting from the Sun at the positive end.) Possible AR-origins for S11 thus exist, although we have not examined them deeply. Without more detailed modelling of the AR and surrounding regions, the true source of S11 remains unknown. We leave this to future work, as the origin of S11 does not have strong bearing on the overall conclusions of this study.

6.4.5 Results in Context of AR Solar Wind Models

In Section 6.1 we described 3 suggested mechanisms for solar wind to escape from an AR. These can be summarised as loop expansion beyond the source surface, interchange reconnection with open CH flux, and complex reconnection with multiple steps. Now we shall discuss our results as they relate to each of three models.

There are no obvious instances where only loop expansion could explain any of the structures S1–10 during R2. The most obvious *in situ* signature of a closed loop, bidirectional strahl, does not occur in R2. Loop expansion may however still be taking place. The loop might disconnect at one end before reaching the observer, or have extended far enough into the heliosphere that strahl from one of the footpoints is highly broadened (e.g., as described by Crooker and Owens, 2012). Since we infer interchange reconnection with loops of comparable height to the height of solar wind formation (Section 6.4.4) it seems plausible for these to in fact be expanded AR loops. Without a more precise estimate of the height of these reconnecting loops, we cannot conclude this with certainty.

Multiple pieces of evidence have been found for interchange reconnection being responsible for the non-CH solar wind during R2. This reconnection appears to occur across a range of heights, with loops of different sizes, and releases plasma from multiple regions of distinct composition. Component reconnection is most

likely, and antiparallel reconnection also appears possible. It is unsurprising that this is the primary explanation for the observed solar wind, given that this observational period was chosen because of the emergence of an AR adjacent to a CH.

For R2, it is difficult to unambiguously detect instances of multi-step reconnection processes as a solar wind mechanism because the more simple interchange reconnection with CH open flux is so readily available as an explanation. However, since interchange reconnection seems to occur at multiple heights, it appears that plasma could travel along multiple reconnected field lines while making its way into the heliosphere. Thus, although only one instance of interchange reconnection is strictly required to open a given loop to the heliosphere, multiple steps might take place. This is not as compelling a case as that of Culhane et al. (2014); Mandrini et al. (2014), where only through multiple steps could AR plasma reach the solar wind.

6.4.6 Prospects for Solar Orbiter and Parker Solar Probe

The findings of this study present multiple challenges and opportunities for upcoming heliospheric missions to study the origins of solar wind from ARs, and the origins of solar wind in general. Here we describe some challenges, while opportunities will be described as future work in Chapter 7. The difficulty in identifying the source location for the AR-associated solar wind, and conclusion that many different regions contribute, will make choosing targets for Solar Orbiter's remote sensing observations ahead of time more difficult. Some of the solar wind for R2 likely originates outside of the two regions observed by EIS, as a result of high-altitude coronal reconnection. The FOV of many instruments might thus be too narrow to observe all of the regions contributing to the solar wind. A choice must therefore be made on which region should make the most significant contribution to the wind reaching the spacecraft. Making this choice would require more detailed modelling of the corona and solar wind.

Since the only certain source region for the wind in structures S2–10 was the AR-connected CH boundary, the observations of this region are the most important to the study. The most obvious remote sensing target for Solar Orbiter might otherwise be the core of the AR, which we have not confirmed as a solar wind source. The better target from the perspective of linked observations, the CH-AR boundary, is only apparent because of the mapped sourcepoint locations which are nearby. This again highlights the importance of solar wind backmapping, or forward modelling as will be the case when choosing remote sensing targets for Solar Orbiter.

6.5 Conclusions

In this chapter, we have isolated the effects of an active region on the solar wind produced from the trailing edge of a coronal hole. We have done so by contrasting *in situ* and remote sensing observations between two consecutive Carrington rotations, occurring before and after the emergence of the active region AR-12532. We conclude through ballistic backmapping techniques and remote sensing observation that the primary source of variation in the *in situ* parameters between the two rotations is the influence of AR-12532. This study thus uniquely allows the isolation of AR influence on the solar wind from other effects. To our knowledge, it is the first study to do so in this way. Our results show that the emergence of an AR to the east of a CH significantly modulates the solar wind from the CH and CHB.

The effects of AR-12532 on the solar wind detected from the coronal hole boundary are primarily on the structure and composition of the wind. While the CH-QS boundary produces solar wind which is separable into three distinct periods (probably from two or three distinct source regions) the CH-AR boundary here leads to many more (10 or 11) structures manifesting *in situ*, with at least 5 distinct origins responsible for them. These are associated, although not perfectly coincident, with strong deviations in the magnetic field from its expected orientation both in azimuth

and elevation. Considering these IMF deflections, and EIS observations which allow us to diagnose properties and processes at the source region, we conclude that the structural and compositional properties are a result of increased instances of interchange reconnection. This reconnection occurs at the CH-AR boundary, and possibly other locations.

EIS $v_{\rm nt}$ and Doppler velocity measurements, combined with *in situ* magnetic field, provide the evidence that interchange reconnection is the most likely dominant mechanism by which the AR-associated plasma escapes into the heliosphere. EIS-observed reconnection signatures are suggestive of component reconnection. Observing *in situ* signatures thus suggests that reconnection occurs with loops of a range of sizes, across a range of heights in the corona. It is not possible to conclude this using EIS on-disk observations alone. The complexity thus suggested for the reconnection configuration highlights the difficulty of unambiguously linking a given stream in the solar wind to a precise source location, while understanding all of the possible steps the plasma went through to escape the corona.

We find no conclusive evidence for the loop expansion and multi-step reconnection processes described in Section 6.1. These may be occurring, but are not easily proven in a configuration where interchange reconnection should dominate. To isolate and test these mechanisms, we suggest further study of unique AR-solar wind configurations such as this one, chosen to be most likely to isolate the particular process of interest.

Our results suggest that modelling the coronal magnetic field, and solar wind propagation to the spacecraft, in advance of observations will be necessary to fully exploit data from Solar Orbiter and Parker Solar Probe. This is particularly true when aiming to improve understanding of the origins of the solar wind associated with ARs. If successful, then many of the assumptions and ambiguities in this study and others like it stand to be be overcome by these missions.

Chapter 7

Conclusions and Future Work

In the three original studies of this thesis we have investigated the origins of the solar wind through both *in situ* and remote sensing approaches. In the first study, suprathermal strahl and halo electron populations were tested for signatures of coronal electron temperature. In the second study, the origins of transitional composition features in solar wind rarefaction regions were identified. In the third study, the *in situ* effects of an active region on solar wind from a coronal hole boundary were isolated and explained. In this chapter we summarise the key conclusions for each study. We then outline the future work which could be carried out using existing data. Finally, we describe follow-on studies which will shortly be possible using data from Solar Orbiter and Parker Solar Probe.

7.1 Key Conclusions

In Chapter 4, comparing the energy content of halo and strahl electrons to an established proxy for coronal electron temperature, we found only very weak correlations. This result holds across a solar cycle's worth of observations, and contrasts with earlier results which used a more limited data set and less vigorous method. The most consistent, although not yet confirmed, explanation for the weak correla-

tion is that processing in the interplanetary medium, rather than coronal effects, is responsible. Under this conjecture, suprathermal electron energy content is initially related to coronal electron temperature, but this relationship is eroded through processing in the heliosphere. Alternatively, the initial relationship between core and halo electron temperature in the corona, as predicted by Che and Goldstein (2014), may be incorrect.

In Chapter 5 we found, for a group of low-latitude coronal hole streams, that intermediate composition in the associated rarefaction regions observed *in situ* was primarily intrinsic to the source region; the trailing coronal hole boundaries. The size of any intermediate composition region which could be reasonably explained through an alternative process, such as footpoint motion and interplanetary mixing (as in Schwadron et al., 2005), was found to be very small. This is a consequence of the near ecliptic latitude and heliocentric distance (~ 1 au) of the measurements. This result supports the viewpoint that intermediate composition in solar wind measured at L1 is representative of some aspect of the source; either its physical properties, or mixing in the corona. This conclusion is positive for the prospects of successful *in situ* components of Sun-heliosphere connection studies; particularly with Solar Orbiter, which will rely on solar wind composition as a tracer of source region properties.

Further results were obtained testing the widely-applied two-step backmapping procedure, through comparison of mapped *in situ* properties with EUV coronal observations. We found that for a majority of events studied, mapping accuracy was improved by applying a ballistic propagation time which explicitly accounts for solar wind acceleration. The reason for this, as was originally suggested by Neugebauer et al. (1998), is likely the non-cancellation of mapping errors resulting from solar wind acceleration and corotation. This cancellation was suggested first by Nolte and Roelof (1973), who assumed that corotation should persist out to significantly

greater heliospheric distances than is assumed in this work, and that of Neugebauer et al. (1998).

In Chapter 6, we report the changes to solar wind from a trailing coronal hole boundary which arose due to the emergence of an active region. The influence of the active region primarily resulted in the presence of many short-lived solar wind structures, linked to numerous, distinct, source region states. From these observations, plus evidence of reconnection in remote sensing non-thermal velocity and *in situ* IMF observations, we concluded that solar wind from this CH-AR boundary was most likely produced by interchange reconnection. This reconnection appears to take place over a range of heights and orientations in the corona, releasing plasma from many regions of the CH-AR system into the heliosphere.

7.2 Immediate Future Work

How Coronal are Suprathermal Electrons?

Coronal signatures in suprathermal electron populations should be studied further. Several Carrington rotations reported as part of the work in Chapter 4 did feature reasonable correlations between suprathermal electron properties and O^{7+}/O^{6+}, which may be the result of reduced processing during their propagation to 1 au. Analysing these periods more closely might reveal details on the coronal relationship which is otherwise smeared-out during solar wind transport. Such details would help to answer the question of how suprathermal solar wind electron populations are energised.

While some data selection was carried out in Chapter 4, this was primarily to remove ICMEs. Stream interaction regions are locations where electron populations are most likely to be scattered, so a future study may also wish to remove these periods. Further, as commented in the chapter, it would be informative to test for

correlations within isolated fast and slow streams. Taking these steps would open the possibility of finding stronger correlations between suprathermal electrons and ion charge states, if they exist for certain types of solar wind. Finding stronger correlations in such a case would provide stronger evidence that processing is in fact eroding an initial relationship in the corona, and would provide evidence for the energisation of suprathermal electrons, as suggested by Che and Goldstein (2014).

Some drawbacks in the use of O^{7+}/O^{6+} as a tracer parameter were noted in Chapter 2, although in Chapter 4 we found that the use of C^{6+}/C^{5+} or C^{6+}/C^{4+} did not lead to different conclusions. The differences that do exist between the results for oxygen, carbon, and other charge states should be studied, and would reveal information about the formation heights of suprathermal electron populations in the corona, since these ions all freeze-in at different heights. Future work, including that with Solar Orbiter, would likely benefit from using a carbon charge state instead of oxygen, or a combination of several species.

Coronal and Heliospheric Boundaries

The conclusions drawn based on the 18 events studied in Chapter 5 could be made more robust if a more rigorous and methodical procedure were used to select the events. We believe that the current list covers most of the suitable periods in the 2012-2016 interval, and is likely representative, but a rigid set of selection criteria may lead to a small number of further events being introduced, or removed. A rigorous selection process would also allow us to draw conclusions based on statistical arguments, which would then be more readily extended to other, more general cases. Extending the selection criteria to be less restrictive regarding e.g., source coronal hole properties would help to improve the statistical relevance of the study by introducing more events.

In Chapter 5 we tested the effects of footpoint switching resulting from AR emer-

gence at a CH boundary, using our simple solar wind model (Appendix B). In this work, we simply used a reconnection rate derived from the case study of Baker et al. (2007), without considering additional instances. Obtaining further reconnection rates from additional observations of a similar type would allow for a better representation of the mixed charge state regions which might arise from interchange reconnection. Knowledge of the extent, in space and time, of such regions would thus improve studies which seek to explain the origins of solar wind from ARs; one of the candidate sources for the slow solar wind.

Footpoint motions and differential streaming could also explain instances where rapid *in situ* changes in velocity appear to correspond to more smeared-out changes in composition; a feature we have observed for the *in situ* components of many of the events in Chapter 5. It is unlikely that this smoothness results from the existence of some coronal boundary layer, or else we would expect it to also be smooth in velocity - at least at the trailing edge where rarefactions are prone to form. It may also be however that this is an artefact of the extensive time-averaging which has been applied to produce significant counts in composition data from ACE. A future study (particularly with Solar Orbiter, which will have improved time resolution in charge state measurements over ACE) would be to investigate the possible roles of differential streaming in creating these features. This knowledge would be critical for studies which seek to locate the source regions of such features using composition data.

Two-Step Backmapping Technique

Results from both Chapters 5 and 6 would benefit from a similarly simple, but more physically realistic, mapping technique. Improving upon PFSS modelling is difficult for a multi-event study, since more complex non-potential models require more complex boundary conditions. More straightforwardly, we could in future

improve the solar wind portion of the mapping by replacing the ballistic step with MHD modelling. MHD models of the solar wind are publicly available (e.g., the ENLIL model, available from NASA's Community Coordinated Modeling Center at `https://ccmc.gsfc.nasa.gov/models/`) and so are approaching the accessibility of the PFSS models used for the corona. A major advantage of MHD models is that they account for stream interactions. This would reduce the occurrence of dwells in the mapped data, a major issue for the mapping in Chapter 5 in particular, and improve the reliability of the results derived from mapping.

As detailed in Section 5.5.1, errors for the PFSS component of the present mapping technique could be quantified by mapping down from an ensemble of points at the source surface, rather than a single point. We could thus produce a 'most-likely' mapping location for each sourcepoint. The robustness of the results could also be tested by repeating the mapping with PFSS models with a range of source surface heights, and possibly using different flux transport models to produce the inner boundary.

In Section 5.5.1, comparisons between PFSS field polarity, and mapped *in situ* magnetic field polarity, implied an offset between the mapped longitude and the true source longitude of the solar wind. This offset, which is primarily an offset in the mapped location of the HCS, was typically opposite to that reported by Neugebauer et al. (1998) using the same approach. Both sets of observations were made over a limited number of Carrington rotations, and for two different solar cycles. A modern statistical study of these alignments, spanning the observational periods of both studies and the intervening periods, might help to explain this discrepancy; particularly if it is a result of solar cycle effects. Understanding, and correcting for, the discrepancy would improve solar wind mapping for connection studies. It would also yield information on the acceleration/corotation relationship for the slow solar wind (as typically the HCS is contained in slow streams) which might help to

constrain its origins.

Solar Wind from a CH-AR Boundary

Further examination of the event from Chapter 6 could also be fruitful. Additional analysis of the *in situ* data should include considering the velocity associated with the different composition structures. Reconnection at different heights may, for example, affect the solar wind acceleration process for individual structures. This could be tested through considering simultaneously velocity, magnetic field direction, and composition for each structure.

Detailed modelling of the AR magnetic field (similar to that in e.g., Harra et al., 2008; Culhane et al., 2014; Mandrini et al., 2014) would provide more information on the most-likely locations at which solar wind outflow takes place. Especially valuable would be indication of the existence of QSLs, at which reconnection might occur. It may also be possible through additional modelling to determine if solar wind from the negative polarity part of the AR footpoint in this event might somehow reach ecliptic latitudes. Similarly to Chapter 5, repeating this study with a more sophisticated backmapping technique, e.g., an MHD model, would again improve the accuracy of the mapping. Mapped sourcepoint locations could be more accurately determined, increasing the reliability of the results.

The event studied in Chapter 6 is particularly rare due to the preservation of coronal hole features, compared to the previous rotation during which the AR was not present. Repeating this case study with more such events, if they could be found, would help to generalise the results, and contribute to a more broad understanding of how AR solar wind originates at the Sun. However, we note that in the period 2012–2016, there do not appear to be any comparable events. Such periods may exist outside of this range (although SDO data are only available from June 2010), but we believe these to be uncommon.

While the precise configuration found in Chapter 6 appears to be quite uncommon, ARs are frequently present at trailing coronal hole boundaries. This can be seen in the collection of events for Chapter 5 in Table 5.1; 8 out of 18 events include an AR near the trailing boundary. (Note however that 3 of these also exhibit ICME signatures.) An informative study might collect examples of CH-AR boundaries such as these, and contrast their *in situ* properties with solar wind from CH-QS boundaries. The appearance of reconnection signatures in the *in situ* data, and distinct compositional structures, would be good points of comparison between these two groups. Such a study would help to answer the question: "How does solar wind originate from a CH-AR boundary?" in a more general sense than is possible with the single case study of Chapter 6.

Another avenue for further studies on the origins of AR solar wind might be examining the loop expansion and multi-step reconnection models of AR solar wind. These could take the form of case studies of particular AR configurations, where the solar wind is not likely to be produced by the simpler interchange reconnection mechanisms found in Chapter 6. Such case studies stand to verify these AR solar wind models with *in situ* measurements. An example of such a case study for multi-step reconnection processes is the AR studied by Culhane et al. (2014); Mandrini et al. (2014).

7.3 Prospects for Future Missions

In this section we discuss how the work in this thesis might be extended using Solar Orbiter, as well as Parker Solar Probe. First, however, we highlight some relevant information about Solar Orbiter.

Solar Orbiter Mission Profile

Solar Orbiter is equipped with *in situ* and remote sensing instrumentation which offer comparable, and often enhanced, observation capabilities to those which supply the data for this thesis. Electron, proton and alpha, and heavy ion populations will be characterised using the Solar Wind Analyser (SWA) instruments; EAS, PAS and HIS respectively. Crucially, HIS (the Heavy Ion Sensor) will provide compositional information in a similar manner to ACE-SWICS, but at enhanced cadence of 5 min in standard operation. This is an order of magnitude improvement on the 1–2 hour resolution SWICS data which are used in this thesis.

Remote sensing instruments include the Extreme Ultraviolet Imager (EUI) which will provide full disk EUV observations; serving a similar purpose to SDO-AIA in this thesis. Also onboard is an EUV imaging spectrometer, SPICE, which will remotely measure physical properties in a limited FOV; in a similar fashion to Hinode-EIS in this thesis. Due to limited remote sensing FOVs, particularly at perihelion, co-observations of *in situ* solar wind and its source will require a change in pointing of the spacecraft onto the target source region. To identify these targets, accurate predictive solar wind modelling will be necessary.

A crucial aspect of the Solar Orbiter mission is that it will travel to heliocentric distances of ~ 0.28 au. At such distances, solar wind processing (such as at stream interactions, as detailed in Chapter 1) is expected to be significantly reduced. Mapping of solar wind back to the Sun should therefore be more reliable at these distances. Solar Orbiter therefore stands to make far better-connected *in situ* and remote sensing measurements than have been possible to date, with *in situ* data which are also more 'pristine' relative to the source. In the later stages of the mission, Solar Orbiter will also shift orbit out of the ecliptic plane by $\sim 25°$, allowing for the first remote observations of the Sun's polar magnetic field.

How Coronal are Suprathermal Electrons?

SWA-HIS and SWA-EAS will measure ions and electrons within 0.3 au which are still relatively pristine with respect to their coronal source. An extension to the study in Chapter 4 with Solar Orbiter could thus answer whether coronal conditions or transport effects are the primary mechanism responsible for the weak strahl/halo-charge state relationship reported in Chapter 4. Should we see correlations increase with proximity to the Sun, then this would confirm that there is an initial state created in the corona in which the energy content of suprathermal electrons is related to core electron temperature, and which is then eroded during the transport to 1 au. This would provide valuable insight into the origins of suprathermal electrons in the corona and their scattering in the heliosphere.

Coronal and Heliospheric Boundaries

We expect that observations of rarefactions with Solar Orbiter will make the boundary between fast and slow streams, as studied in Chapter 5, more clear. When observing solar wind nearer to the Sun with less developed compressions and rarefactions, properties at the trailing (and likely leading) boundaries of fast streams should be more pristine. By identifying the original stream boundary more precisely, we might test whether intermediate composition regions in fact lie on one or both sides of the boundary. This will reveal the processes at the Sun (e.g., evolving expansion factor, intermediate loop size/temperature) which produce wind of this composition. Further, by contrasting the composition in the leading and trailing edges, we might identify whether the two originate from the same processes.

Solar Wind Mapping Improvements

The close approach of Solar Orbiter and Parker Solar Probe will allow sampling of solar wind with a reduced travel time. The ballistic backmapping will in such a

case be more sensitive to timing offsets due to the balance between corotation and acceleration. Comparing EUV and PFSS magnetic field alignment with mapped *in situ* features as in Chapter 5 might then allow for more detail to be uncovered on the corotation and acceleration profiles of the solar wind. This will further our understanding of a fundamental question in heliophysics: How is the solar wind accelerated?

PFSS models are currently built up from near-Earth measured synoptic maps, and must rely on flux transport models to predict the magnetic field on the opposite side of the Sun (Chapter 3). The PFSS step in the mapping of solar wind measured by Solar Orbiter may therefore prove less accurate than in present studies, at times when the spacecraft location is in opposition to the Earth. This is because the relevant PFSS field lines will depend heavily on modelled, rather than observed, photospheric flux. This issue might be resolved in the future, by combining near-Earth-observed magnetograms with those from Solar Orbiter-PHI itself. This will only be possible however once this instrument is successfully cross-calibrated with existing magnetographs.

Solar Wind from Active Regions

The findings in Chapter 6 present multiple challenges and opportunities for upcoming heliospheric missions to study the origins of solar wind from ARs, and the origins of solar wind in general. Some of the observed AR-associated wind likely originated from outside of the two regions observed by EIS, as a result of high-altitude coronal reconnection. This presents a problem for limited-FOV instruments; it may not be possible to observe all of the key solar wind sources simultaneously. A choice must therefore be made ahead of time on which region should make the most significant contribution to the wind reaching the spacecraft. Making this choice would require detailed modelling of the corona and solar wind.

In Chapter 6 we also found that the most obvious region for remote sensing study (the AR core) was not in fact the best region to observe to link with *in situ* observations (the CH-AR boundary). This highlights the importance of prioritising solar wind sources, rather than traditional solar observing targets (e.g., eruptive ARs) when trying to establish linked observations. It also again highlights the importance of solar wind backmapping, or forward modelling as will be the case when choosing remote sensing targets for Solar Orbiter.

Improvements to the link between source and solar wind offered by Solar Orbiter and Parker Solar Probe will be invaluable to studies (e.g., that of Chapter 6) which aim to understand the origins of AR solar wind. Features at the interaction regions between streams (e.g., corresponding to CH-AR boundaries) will be less distorted by propagation, and ballistic mapping is expected to be more reliable. The problem of producing reliable magnetograms of off-disk photospheric flux, however, is particularly severe when studying the solar wind from newly emerged ARs (such as AR-12532 in Chapter 6). This is because newly-emerging complex magnetic structures present instances where we must rely more strongly on flux transport models than data.

Observation of kinked and highly-deflected IMF was used as evidence of interchange reconnection in Chapter 6, although we could not infer it with absolute certainty. For these future missions, observing solar wind at <1 au will mean that kinks resulting from interchange reconnection should be more pronounced than in this study, as they gradually 'unkink' over the course of solar wind propagation. This would be very helpful in making inferences of reconnection occurrence based on *in situ* data. Also, magnetic field deviations caused by other processes, such as stream shears and turbulence, may be relatively less pronounced as these will not yet have had the chance to develop. Loop expansion models can also be tested further by searching for bidirectional strahl, since at these lower heliocentric distances,

observed loops will be more likely connected to the Sun at both ends. These points apply in particular to Parker Solar Probe, because it will reach perihelion distances drastically closer to the Sun than those of Solar Orbiter. These observations may thus provide *in situ* evidence for the range of suggested AR solar wind processes, with greater reliability than is currently available.

In this section we have outlined ways in which connected *in situ* and remote sensing observations with Solar Orbiter, and additionally inner-heliosphere observations with Parker Solar Probe, can be immediately put to use to understand the origins of the solar wind. Specific studies into the origins of suprathermal electrons and compositional features; solar wind in the boundaries between better-understood streams; and solar wind from complex active regions, all contribute to an overall picture of how the solar wind is produced at the Sun. We expect that in the near future these forthcoming cutting-edge missions will fill in gaps, and add details to, the studies presented in this thesis.

Appendices

Appendix A

Coordinate Systems

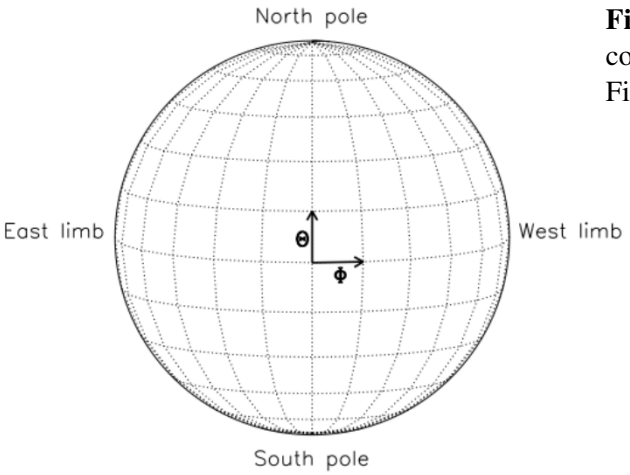

Figure A.1: θ and ϕ in heliographic coordinates, shown on the solar disk. Figure from Thompson (2006).

Heliographic Coordinates

Sun-centric coordinate system; example in Figure A.1. r: distance from the centre of the Sun, θ: latitude angle out of ecliptic plane, ϕ: longitude angle in east-west direction. Note that the Sun rotates from east to west. $\phi = 0°$ is defined by the specific coordinate system. **Stonyhurst coordinates:** $\phi_s = 0°$ on the Earth-Sun line. **Carrington coordinates:** $\phi_{Carr} = 0°$ moves at the sidereal solar rotation rate. Some notes on Carrington coordinates:

1. The Earth-Sun line at the J2000.0 epoch was at $\phi_{Carr} = 84.10°$.

2. A “Carrington rotation” is defined as the time between consecutive instances of the Earth-Sun line aligning with $\phi_{\text{Carr}} = 0°$. Carrington rotations are numbered, with the first commencing on 1853/11/09.

3. Since the Sun rotates east-west, the Carrington longitude of the Earth-Sun line decreases from 360° to 0° over the course of a Carrington rotation.

Helioprojective Cartesian Coordinates

Observer-centric coordinate system; typically used for remote imagery. θ_y: elevation angle, θ_x: azimuthal angle in clockwise direction. [0°, 0°] is located at disk centre. When presenting solar imagery, θ_x and θ_y are often simply referred to as x and y.

Appendix B

Simple Solar Wind Model

We have developed a simple 1-dimensional solar wind model to assist in the interpretation of *in situ* composition results in Chapter 5. This model captures the key footpoint motion and differential streaming elements of a related model developed by Schwadron et al. (2005) (see Chapter 2) but applied to solar wind observed at ecliptic latitudes at 1 AU. Our model thus places sensible constraints on the size of a region where compositional signatures of solar wind from different source regions have been mixed, by the process of footpoint motion across a coronal hole boundary in the corona, followed by differential streaming of minor ions in the solar wind. This model is applied to complement our results in Chapter 5 and shall be described in this appendix. First we detail how the model treats the propagation of the bulk solar wind, and includes the processes of footpoint motion and minor ion differential streaming. We then go on to describe how the model treats the change in connectivity occurring from footpoint motions.

B.1 Modelling Bulk Solar Wind

Our model treats the solar wind as a collection of "super-particles" moving radially outwards at constant velocity from an inner boundary of $30\,R_{\odot}$. This is chosen

to match the inner boundary in the model of Schwadron et al. (2005). This inner boundary is expected to lie beyond the Alfvén point, and as such the assumption of a radially propagating solar wind is reasonable. It is important to note that these super-particles each represent a collection of solar wind parameters at a location in the model heliosphere, and are not individual solar wind particles, or collections of particles. Given solar wind parameters as functions of longitude along the inner boundary, the model iterates the nature of the outflow over time. At each time step, every super-particle is allowed to move outwards at its assigned velocity, and a new super-particle is generated at the inner boundary. We use the solar rotation rate to evolve the inner boundary with time, and create solar wind super-particles of appropriate properties as required. The magnetic field is scaled with radial distance as:

$$B(r) = B_0 \left(\frac{r_0}{r}\right)^2 \sqrt{\frac{1+(\Omega_\odot r \sin(\alpha)/v)^2}{1+(\Omega_\odot r_0 \sin(\alpha)/v)^2}} \tag{B.1}$$

where $B(r)$ is the magnetic field strength at distance r, B_0 is the magnetic field strength at distance r_0, $\Omega_\odot$ is the solar rotation rate, α is heliospheric colatitude ($\alpha = 90^\circ$ at the equator), and v is the solar wind velocity. Other assigned properties are proton density (scaling as $1/r^2$), a charge state/composition flag, and the longitude of the particle's creation at the inner boundary (henceforth "source longitude"). The model operates in a frame which is static relative to the Sun's rotation, such that the corona is moving from east to west, and subsequent emitted particles are assigned decreasing source longitudes.

Under the constant solar wind velocity assumption, a 'gap' will naturally form between any two initially-neighbouring super-particles where the leading particle has greater speed than the trailing. To ensure that no large gaps form in the model domain, two new super-particles are created between any pairs of super-particles which exceed a threshold distance apart. These new particles are evenly spaced, and are assigned speeds such that there is a linear transition in speeds across them

and between the original pairs of particles. Other properties such as composition flag and source longitude are set to be identical to the original particle they are nearest. This preserves any discontinuous transitions in composition.

In the true solar wind, the gap described above is not truly empty, as the pressure gradient created causes the plasma from the initially fast and slow streams to expand into it. A pressure wave propagates from the gap into the initial fast (slow) stream at the magnetosonic speed in that region, and any regions which are reached by this wave are decelerated (accelerated) towards the gap (Borovsky and Denton, 2016). This leads to the degradation of discontinuous speed boundaries at the trailing edges of fast streams, not only in the gap, but extending into initially fast and slow regions, so that they too make up part of the rarefaction. To approximate this effect, we model a perturbation wave which propagates radially in both directions, initiating from a velocity discontinuity (specifically here the fast-slow discontinuity). For simplicity, we propagate the wave at the Alfvén speed, which we expect to be on the order of the magnetosonic speed in the solar wind. This is the case as long as $v_A \gg c_s$, where v_A is the Alfvén speed and c_s is the sound speed. Any super-particles which this wave reaches are subject to a change in velocity. Again for simplicity, we aim to produce a velocity profile in the rarefaction which is smoothly varying. To do so, we modify the velocity of all the 'perturbed' super-particles, such that their velocity evolves linearly with radial distance, from the initially lowest to highest value. Changing the velocities in this way broadly has the effect of accelerating initially slow, and decelerating initially fast, regions.

B.2 Modelling of Differential Streaming with Footpoint Motion

We wish to apply our model to a situation similar to that modelled by Schwadron et al. (2005); a solar wind rarefaction with a CHBL, and differential streaming to mix disparate ion populations across stream boundaries. We allow the solar wind to be produced at the inner boundary and expand out in time. In addition to each super-particle's source longitude, we also continually track the longitude of the magnetic footpoint linked to that particle. This is done by starting with the source longitude, and evolving it at a differential footpoint motion rate, ω_{fp}, which is a fraction of the solar rotation rate $\Omega_\odot$, opposed to the direction of rotation: $\omega_{fp} = -D\Omega_\odot$ ($0 < D < 1$). A schematic of this footpoint motion is shown in Figure B.1, in the frame corotating with the corona, and thus corotating with the source longitudes of the solar wind super-particles. We find ω_{fp} by calculating the photospheric differential rotation rate, ω, at given heliospheric latitude, b, using the empirical formula derived from observations by Lamb (2017):

$$\omega = 14.296 - 1.847\sin^2(b) - 2.615\sin^4(b) \tag{B.2}$$

ω_{fp} is then found with the expression:

$$\omega_{fp} = -(\Omega_\odot - \omega) \tag{B.3}$$

Equations B.2 and B.3 produce a footpoint motion rate of $\omega_{fp} = -0.27\Omega_\odot$ at a heliospheric latitude of 75°, which is very similar to the factor of -0.25 applied at 75° by Schwadron et al. (2005). A particle with footpoint originally in a coronal hole, at longitude angle ϕ from the boundary between low and high charge state, will therefore after a time $t_{\text{cross}} = \phi/\omega_{fp}$ have its footpoint cross that boundary.

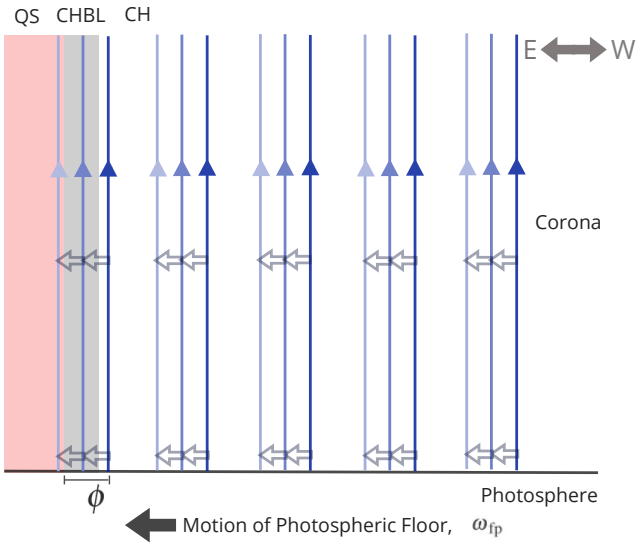

Figure B.1: Schematic representation of the footpoint motion of open field lines resulting from differential photospheric rotation, as implemented in the model. The corona, photosphere, and magnetic field lines are represented in a frame corotating with the corona. Due to photospheric differential rotation, in this frame the photospheric floor moves eastward at the rate ω_{fp}. The open field lines all extend out into the heliosphere at greater heights than those shown. Coronal hole (CH), coronal hole boundary layer (CHBL) and quiet Sun (QS) regions of the corona are labelled. The rigid rotation of the corona means that these boundaries remain static in this frame. Magnetic field lines are drawn which extend from the photosphere up through the corona; lighter field lines represent the field at later points in time. The footpoints of these field lines move eastward with the photospheric floor, and so decrease in longitude with time. In the corona, the field lines are dragged eastward due to the footpoint motion. Above the corona, in the solar wind, the motion of these field lines relative to the rigidly-rotating frame leads to the sub-Parker spiral introduced in Section 2.4. For the most easterly field line, initially located an angle ϕ from the QS region, the footpoint moves such that it becomes rooted in the QS region; a different source to its original location.

At this point the super-particle in the solar wind is considered to be magnetically connected to a different source region than that of its origin. This configuration is shown for the most easterly field line in Figure B.1.

Following Schwadron et al. (2005), we model the differential streaming of minor ions along magnetic field lines from the inner boundary at $30\,\text{R}_\odot$. Our model thus assumes that differential streaming onsets and reaches the limit of v_A, as described in Section 1.3.7, at approximately this height. If this assumption deviates strongly from reality then there may be significant consequences for the final results. How-

ever, modelling the effects of differential streaming at heights much below $30\,R_\odot$ would require also modelling the bulk solar wind at such heights, where simplifying assumptions such as radial solar wind propagation are unlikely to hold, and so the task of modelling becomes far more complex.

We model minor ion streaming only for those super-particles whose footpoints we judge to have crossed from the coronal hole (or CHBL) into some other high charge state source region. We do not model the streaming of ions from footpoints which are yet to cross the boundary, there is no compositional difference between the solar wind and the current source footpoint. We model the propagation of ions at a differential speed, which is in addition to that of the background solar wind, anti-sunward along the magnetic field. For each super-particle, i, whose footpoint crosses the boundary, a differentially streaming particle is created which represents the minor ions "i, ion". This new particle leaves the Sun and propagates out at the local differential streaming rate, which is comparable to the local Alfvén speed v_A (Marsch et al., 1982). We use the streaming speed found observationally for heavy ions at 1 AU by Berger et al. (2011):

$$v_{\text{diff}} = (0.55 \pm 0.15) v_A \tag{B.4}$$

This is less than the streaming speed of exactly v_A applied by Schwadron et al. (2005). We calculate v_A for the streaming ion particle based on its radial distance from the Sun, $r_{i,\text{ion}}$, and radially-scaled magnetic field strength and proton density. The streaming speed therefore follows the Alfvén speed in being significantly higher in near-Sun space. As the differential streaming is directed along the field, the minor ions move out radially at a rate $v_{r\text{-diff}} = v_{\text{diff}} \cos\theta$ relative to the bulk solar wind, where θ is the angle of the local magnetic field from the radial direction. We calculate θ based on the sub-Parker spiral magnetic field, which results from differential footpoint motion as detailed in Section 2.4 and illustrated in Figure 2.5,

using the expression:

$$\theta = \tan^{-1}\left(\frac{(1-D)\Omega.r_{i,ion}}{v}\right) \tag{B.5}$$

where v is the bulk solar wind speed at $r_{i,\mathrm{ion}}$.

We measure at each time step whether or not streaming minor ions from the source have reached a given super-particle, i, in the model; $r_{i,\mathrm{ion}} > r_i$. When this condition is met the composition of minor ions at that super-particle is considered to be mixed.

Bibliography

H Alfvén. Existence of electromagnetic-hydrodynamic waves. *Nature*, 150:405–406, 1942.

SK Antiochos, CR DeVore, JT Karpen, and Z Mikić. Structure and dynamics of the Sun's open magnetic field. *The Astrophysical Journal*, 671(1):936, 2007.

SK Antiochos, Z Mikić, VS Titov, R Lionello, and JA Linker. A model for the sources of the slow solar wind. *The Astrophysical Journal*, 731(2):112, 2011.

CN Arge, CJ Henney, J Koller, CR Compeau, S Young, D MacKenzie, A Fay, and JW Harvey. Air force data assimilative photospheric flux transport (ADAPT) model. In *AIP Conference Proceedings*, volume 1216, pages 343–346. AIP, 2010.

M Asplund, N Grevesse, AJ Sauval, and P Scott. The chemical composition of the Sun. *Annual Review of Astronomy and Astrophysics*, 47, 2009.

RG Athay. *The solar chromosphere and corona: Quiet Sun*, volume 53. Springer Science & Business Media, 2012.

D Baker, L van Driel-Gesztelyi, and GDR Attrill. Evidence for interchange reconnection between a coronal hole and an adjacent emerging flux region. *Astronomische Nachrichten*, 328(8):773–776, 2007.

D Baker, L van Driel-Gesztelyi, CH Mandrini, P Démoulin, and MJ Murray. Mag-

netic reconnection along quasi-separatrix layers as a driver of ubiquitous active region outflows. *The Astrophysical Journal*, 705(1):926, 2009.

D Baker, DH Brooks, P Démoulin, L van Driel-Gesztelyi, LM Green, K Steed, and J Carlyle. Plasma composition in a sigmoidal anemone active region. *The Astrophysical Journal*, 778(1):69, 2013.

W Baumjohann and RA Treumann. *Basic space plasma physics*. World Scientific, 1997.

L Berger, RF Wimmer-Schweingruber, and G Gloeckler. Systematic measurements of ion-proton differential streaming in the solar wind. *Physical review letters*, 106(15):151103, 2011.

P Bochsler. Minor ions in the solar wind. *The Astronomy and Astrophysics Review*, 14(1):1–40, 2007.

PL Bornmann, D Speich, J Hirman, LO Matheson, R Grubb, HA Garcia, and R Viereck. GOES X-ray sensor and its use in predicting solar-terrestrial disturbances. In *GOES-8 and Beyond*, volume 2812, pages 291–299. International Society for Optics and Photonics, 1996.

JE Borovsky. Flux tube texture of the solar wind: Strands of the magnetic carpet at 1 AU? *Journal of Geophysical Research: Space Physics*, 113(A8), 2008.

JE Borovsky. The plasma structure of coronal hole solar wind: Origins and evolution. *Journal of Geophysical Research: Space Physics*, 121(6):5055–5087, 2016.

JE Borovsky and MH Denton. The trailing edges of high-speed streams at 1 AU. *Journal of Geophysical Research: Space Physics*, 121(7):6107–6140, 2016.

RJ Bray and RE Loughhead. Sunspots, the international astrophysics series. *London: Chapman Hall*, 1964, 1964.

DH Brooks and HP Warren. Establishing a connection between active region outflows and the solar wind: Abundance measurements with EIS/ Hinode. *The Astrophysical Journal*, 727(1):L13, 2011.

L F Burlaga. Anisotropic diffusion of solar cosmic rays. *Journal of Geophysical Research*, 72(17):4449–4466, 1967.

RC Carrington. *Observations of the Spots on the Sun from November 9. 1853, to March 24, 1861, Made at Redhill*. Williams and Norgate, 1863.

JW Chamberlain. Interplanetary gas. II. Expansion of a model solar corona. *The Astrophysical Journal*, 131:47, 1960.

P Charbonneau. Dynamo models of the solar cycle. *Living Reviews in Solar Physics*, 7(1):3, 2010.

H Che and ML Goldstein. The origin of non-Maxwellian solar wind electron velocity distribution function: Connection to nanoflares in the solar corona. *The Astrophysical Journal*, 795(2):L38, 2014.

H Che, ML Goldstein, and AF Vinas. Bidirectional energy cascades and the origin of kinetic Alfvénic and whistler turbulence in the solar wind. *Physical Review Letters*, 112(6):1–5, 2014.

SR Cranmer. Coronal holes. *Living Reviews in Solar Physics*, 6(1):1–66, 2009.

SR Cranmer, AA van Ballegooijen, and RJ Edgar. Self-consistent coronal heating and solar wind acceleration from anisotropic magnetohydrodynamic turbulence. *The Astrophysical Journal Supplement Series*, 171(2):520, 2007.

NU Crooker and MJ Owens. Interchange reconnection: Remote sensing of solar signature and role in heliospheric magnetic flux budget. *Space science reviews*, 172(1-4):201–208, 2012.

NU Crooker, JT Gosling, and SW Kahler. Reducing heliospheric magnetic flux from coronal mass ejections without disconnection. *Journal of Geophysical Research: Space Physics*, 107(A2):SSH–3, 2002.

NU Crooker, SW Kahler, DE Larson, and RP Lin. Large-scale magnetic field inversions at sector boundaries. *Journal of Geophysical Research: Space Physics*, 109(A3), 2004.

JL Culhane, LK Harra, AM James, K Al-Janabi, LJ Bradley, RA Chaudry, K Rees, JA Tandy, P Thomas, MCR Whillock, et al. The EUV imaging spectrometer for Hinode. *Solar Physics*, 243(1):19–61, 2007.

JL Culhane, DH Brooks, L van Driel-Gesztelyi, P Démoulin, D Baker, ML DeRosa, CH Mandrini, L Zhao, and TH Zurbuchen. Tracking solar active region outflow plasma from its source to the near-earth environment. *Solar Physics*, 289(10): 3799–3816, 2014.

P Debye and E Hückel. De la theorie des electrolytes. I. abaissement du point de congelation et phenomenes associes. *Physikalische Zeitschrift*, 24(9):185–206, 1923.

CE DeForest, WH Matthaeus, NM Viall, and SR Cranmer. Fading coronal structure and the onset of turbulence in the young solar wind. *The Astrophysical Journal*, 828(2):66, 2016.

P Démoulin. Where will efficient energy release occur in 3-D magnetic configurations? *Advances in Space Research*, 39(9):1367–1377, 2007.

KP Dere, E Landi, HE Mason, BC Monsignori Fossi, and PR Young. CHIANTI-an atomic database for emission lines-I. Wavelengths greater than 50 Å. *Astronomy and Astrophysics Supplement Series*, 125(1):149–173, 1997.

KP Dere, E Landi, PR Young, G Del Zanna, M Landini, and HE Mason. CHIANTI–an atomic database for emission lines-IX. Ionization rates, recombination rates, ionization equilibria for the elements hydrogen through zinc and updated atomic data. *Astronomy & Astrophysics*, 498(3):915–929, 2009.

L-G Ding, G Li, G-M Le, B Gu, and X-X Cao. Seed population in large solar energetic particle events and the twin-CME scenario. *The Astrophysical Journal*, 812(2):171, 2015.

JF Dowdy, D Rabin, and RL Moore. On the magnetic structure of the quiet transition region. *Solar Physics*, 105(1):35–45, 1986.

JK Edmondson, SK Antiochos, CR DeVore, BJ Lynch, and TH Zurbuchen. Interchange reconnection and coronal hole dynamics. *The Astrophysical Journal*, 714 (1):517, 2010.

HA Elliott, CJ Henney, DJ McComas, CW Smith, and BJ Vasquez. Temporal and radial variation of the solar wind temperature-speed relationship. *Journal of Geophysical Research: Space Physics*, 117(A9), 2012.

E Endeve, T E Holzer, and E Leer. Helmet streamers gone unstable: Two-fluid magnetohydrodynamic models of the solar corona. *The Astrophysical Journal*, 603(1):307, 2004.

R Esser and RJ Edgar. Reconciling spectroscopic electron temperature measurements in the solar corona with in situ charge state observations. *The Astrophysical Journal*, 532(1):L71–L74, 2000.

AN Fazakerley, LK Harra, and L van Driel-Gesztelyi. An investigation of the sources of Earth-directed solar wind during Carrington rotation 2053. *The Astrophysical Journal*, 823(2):145, 2016.

U Feldman and KG Widing. Elemental abundances in the solar upper atmosphere derived by spectroscopic means. *Space Science Reviews*, 107(3-4):665–720, 2003.

U Feldman, KG Widing, and HP Warren. Morphology of the quiet solar upper atmosphere in the $10^4 < T_e < 10^6$ K temperature regime. *The Astrophysical Journal*, 522(2):1133, 1999.

U Feldman, HP Warren, CM Brown, and GA Doschek. Can the composition of the solar corona be derived from Hinode/Extreme-ultraviolet Imaging Spectrometer spectra? *The Astrophysical Journal*, 695(1):36, 2009.

WC Feldman, JR Asbridge, SJ Bame, M. D. Montgomery, and S. P. Gary. Solar wind electrons. *Journal of Geophysical Research*, 80(31):4181, 1975.

LA Fisk. Acceleration of the solar wind as a result of the reconnection of open magnetic flux with coronal loops. *Journal of Geophysical Research: Space Physics*, 108(A4), 2003.

LA Fisk, NA Schwadron, and TH Zurbuchen. On the slow solar wind. *Space science reviews*, 86(1-4):51–60, 1998.

LA Fisk, NA Schwadron, and TH Zurbuchen. Acceleration of the fast solar wind by the emergence of new magnetic flux. *Journal of Geophysical Research: Space Physics*, 104(A9):19765–19772, 1999.

V Formisano, F Palmiotto, and G Moreno. α-particle observations in the solar wind. *Solar Physics*, 15(2):479–498, 1970.

JW Freeman. Estimates of solar wind heating inside 0.3 AU. *Geophysical research letters*, 15(1):88–91, 1988.

H Fu, B Li, X Li, Z Huang, C Mou, F Jiao, and L Xia. Coronal sources and in situ properties of the solar winds sampled by ACE during 1999–2008. *Solar Physics*, 290(5):1399–1415, 2015.

H Fu, MS Madjarska, L Xia, B Li, Z Huang, and Z Wangguan. Charge states and FIP bias of the solar wind from coronal holes, active regions, and quiet Sun. *The Astrophysical Journal*, 836(2):169, 2017.

J Geiss and P Bochsler. Rapports isotopiques dans filesysteme solaire. *Cepadues-Editions, Paris*, 213, 1985.

J Geiss, G Gloeckler, R von Steiger, H Balsiger, LA Fisk, AB Galvin, FM Ipavich, S Livi, JF McKenzie, and KW Ogilvie. The southern high-speed stream: results from the SWICS instrument on Ulysses. *Science (New York, N.Y.)*, 268(5213): 1033–1036, 1995a.

Johannes Geiss, G Gloeckler, and R Von Steiger. Origin of the solar wind from composition data. *Space Science Reviews*, 72(1-2):49–60, 1995b.

SE Gibson, JU Kozyra, G de Toma, BA Emery, T Onsager, and BJ Thompson. If the Sun is so quiet, why is the Earth ringing? a comparison of two solar minimum intervals. *Journal of Geophysical Research: Space Physics*, 114(A9):A09105, 2009.

G Gloeckler, J Geiss, H Balsiger, P Bedini, JC Cain, J Fischer, LA Fisk, AB Galvin, F Gliem, DC Hamilton, et al. The solar wind ion composition spectrometer. *Astronomy and Astrophysics Supplement Series*, 92:267–289, 1992.

G Gloeckler, J Cain, FM Ipavich, EO Tums, P Bedini, LA Fisk, TH Zurbuchen, P Bochsler, J Fischer, RF Wimmer-Schweingruber, J Geiss, and R Kallenbach. *The Advanced Composition Explorer Mission*, pages 497–539. Springer Netherlands, Dordrecht, 1998.

G Gloeckler, T Zurbuchen, and J Geiss. Implications of the observed anticorrelation between solar wind speed and coronal electron temperature. *Journal of Geophysical Research*, 108(A4):1158, 2003.

L Golub and JM Pasachoff. *The solar corona*. Cambridge University Press, 2010.

N Gopalswamy, P Mäkelä, S Akiyama, H Xie, S Yashiro, and AA Reinard. The solar connection of enhanced heavy ion charge states in the interplanetary medium: Implications for the flux-rope structure of CMEs. *Solar Physics*, 284(1):17–46, 2013.

JT Gosling. Large-scale inhomogeneities in the solar wind of solar origin. *Reviews of Geophysics*, 13(3):1053–1058, 1975.

JT Gosling, RM Skoug, DJ McComas, and CW Smith. Direct evidence for magnetic reconnection in the solar wind near 1 AU. *Journal of Geophysical Research: Space Physics*, 110(A1), 2005.

GE Hale. On the probable existence of a magnetic field in sun-spots. *The astrophysical journal*, 28:315, 1908.

LK Harra, SA Matthews, and JL Culhane. Nonthermal velocity evolution in the precursor phase of a solar flare. *The Astrophysical Journal Letters*, 549(2):L245, 2001.

LK Harra, Taro Sakao, CH Mandrini, H Hara, S Imada, PR Young, L van Driel-Gesztelyi, and D Baker. Outflows at the edges of active regions: contribution to solar wind formation? *The Astrophysical Journal Letters*, 676(2):L147, 2008.

S Hefti, TH Zurbuchen, LA Fisk, G Gloeckler, D Larson, and RP Lin. The transition from slow to fast solar wind: Charge state composition and electron observations. In *AIP Conference Proceedings*, volume 471, pages 495–497. AIP, 1999.

V Heidrich-Meisner, T Peleikis, M Kruse, L Berger, and R Wimmer-Schweingruber. Observations of high and low Fe charge states in individual solar wind streams with coronal-hole origin. *Astronomy & Astrophysics*, 593: A70, 2016.

JT Hoeksema, JM Wilcox, and PH Scherrer. The structure of the heliospheric current sheet: 1978–1982. *Journal of Geophysical Research: Space Physics*, 88 (A12):9910–9918, 1983.

Z Huang, RA Frazin, E Landi, WB Manchester, AM Vásquez, and TI Gombosi. Newly discovered global temperature structures in the quiet Sun at solar minimum. *The Astrophysical Journal*, 755(2):86, 2012.

AJ Hundhausen, HE Gilbert, and SJ Bame. The state of ionization of oxygen in the solar wind. *The Astrophysical Journal*, 152:L3, apr 1968a.

AJ Hundhausen, HE Gilbert, and Bame SJ. Ionization state of the interplanetary plasma. *Journal of Geophysical Research*, 73(13):5485–5493, 1968b.

JD Jackson. *Classical electrodynamics*. John Wiley & Sons, 2012.

S Kahler and RP Lin. The determination of interplanetary magnetic field polarities around sector boundaries using $E > 2\,\mathrm{keV}$ electrons. *Geophysical research letters*, 21(15):1575–1578, 1994.

S Kahler, NU Crooker, and JT Gosling. Properties of interplanetary magnetic sector boundaries based on electron heat-flux flow directions. *Journal of Geophysical Research: Space Physics*, 103(A9):20603–20612, 1998.

SW Kahler and A Vourlidas. Solar energetic particle events in different types of solar wind. *The Astrophysical Journal*, 791(1):4, 2014.

NV Karachik and AA Pevtsov. Solar wind and coronal bright points inside coronal holes. *The Astrophysical Journal*, 735(1):47, 2011.

L Kepko, NM Viall, SK Antiochos, ST Lepri, JC Kasper, and M Weberg. Implications of L1 observations for slow solar wind formation by solar reconnection. *Geophysical Research Letters*, 43(9):4089–4097, 2016.

EKJ Kilpua, MS Madjarska, N Karna, T Wiegelmann, C Farrugia, W Yu, and K Andreeova. Sources of the slow solar wind during the solar cycle 23/24 minimum. *Solar Physics*, 291(8):2441–2456, 2016.

Y-K Ko, LA Fisk, G Gloeckler, and J Geiss. Limitations on suprathermal tails of electrons in the lower solar corona. *GRL*, 23(20):2785–2788, 1996.

Y-K Ko, K Muglach, Y-M Wang, PR Young, and ST Lepri. Temporal evolution of solar wind ion composition and their source coronal holes during the declining phase of cycle 23. I. Low-latitude extension of polar coronal holes. *The Astrophysical Journal*, 787(2):121, 2014.

M Kojima, K Fujiki, T Ohmi, M Tokumaru, A Yokobe, and K Hakamada. Low-speed solar wind from the vicinity of solar active regions. *Journal of Geophysical Research: Space Physics*, 104(A8):16993–17003, 1999.

T Kosugi, K Matsuzaki, T Sakao, T Shimizu, Y Sone, S Tachikawa, T Hashimoto, K Minesugi, A Ohnishi, T Yamada, et al. The Hinode (Solar-B) mission: an overview. In *The Hinode Mission*, pages 5–19. Springer, 2007.

AS Krieger, AF Timothy, and EC Roelof. A coronal hole and its identification as the source of a high velocity solar wind stream. *Solar Physics*, 29(2):505–525, 1973.

DA Lamb. Measurements of solar differential rotation and meridional circulation from tracking of photospheric magnetic features. *The Astrophysical Journal*, 836 (1):10, 2017.

J M Laming, JJ Drake, and KG Widing. Stellar coronal abundances. 3: The solar first ionization potential effect determined from full-disk observation. *The Astrophysical Journal*, 443:416–422, 1995.

JM Laming. On collisionless electron-ion temperature equilibration in the fast solar wind. *The Astrophysical Journal*, 604(2):874–883, 2004.

JM Laming. The FIP and inverse FIP effects in solar and stellar coronae. *Living Reviews in Solar Physics*, 12(1):2, 2015.

E Landi and ST Lepri. Photoionization in the solar wind. *The Astrophysical Journal Letters*, 812(2):L28, 2015.

E Landi, RL Alexander, JR Gruesbeck, JA Gilbert, ST Lepri, WB Manchester, and TH Zurbuchen. Carbon ionization stages as a diagnostic of the solar wind. *The Astrophysical Journal*, 744(2):100, 2011.

E Landi, JR Gruesbeck, ST Lepri, TH Zurbuchen, and LA Fisk. Charge state evolution in the solar wind. Radiative losses in fast solar wind plasmas. *The Astrophysical Journal Letters*, 758(1):L21, 2012a.

E Landi, JR Gruesbeck, ST Lepri, TH Zurbuchen, and LA Fisk. Charge state evolution in the solar wind. II. Plasma charge state composition in the inner corona and accelerating fast solar wind. *The Astrophysical Journal*, 761(1):48, 2012b.

E Landi, PR Young, KP Dere, G Del Zanna, and HE Mason. CHIANTI–an atomic database for emission lines. XIII. Soft x-ray improvements and other changes. *The Astrophysical Journal*, 763(2):86, 2013.

E Landi, R Oran, ST Lepri, TH Zurbuchen, LA Fisk, and B Van der Holst. Charge state evolution in the solar wind. III. Model comparison with observations. *The Astrophysical Journal*, 790(2):111, 2014.

I Langmuir. Oscillations in ionized gases. *Proceedings of the National Academy of Sciences*, 14(8):627–637, 1928.

B Lavraud and DE Larson. Correcting moments of in situ particle distribution functions for spacecraft electrostatic charging. *Journal of Geophysical Research: Space Physics*, 121(9):8462–8474, 2016.

JR Lemen, DJ Akin, PF Boerner, C Chou, JF Drake, DW Duncan, CG Edwards, FM Friedlaender, GF Heyman, NE Hurlburt, et al. The atmospheric imaging assembly (AIA) on the solar dynamics observatory (SDO). In *The Solar Dynamics Observatory*, pages 17–40. Springer, 2011.

RP Lepping, MH Acũna, LF Burlaga, WM Farrell, JA Slavin, KH Schatten, F Mariani, NF Ness, FM Neubauer, YC Whang, et al. The Wind magnetic field investigation. *Space Science Reviews*, 71(1-4):207–229, 1995.

Ø Lie-Svendsen, VH Hansteen, and E Leer. Kinetic electrons in high-speed solar wind streams: Formation of high-energy tails. *Journal of Geophysical Research: Space Physics*, 102(A3):4701–4718, 1997.

RP Lin. Energetic particles in the solar wind and at the Sun. In *AIP Conference Proceedings*, volume 385, pages 25–40. AIP, 1997.

RP Lin, KA Anderson, S Ashford, C Carlson, D Curtis, R Ergun, D Larson, J McFadden, M McCarthy, GK Parks, H Rème, JM Bosqued, J Coutelier, F Cotin, C D'Uston, KP Wenzel, TR Sanderson, J Henrion, JC Ronnet, and G Paschmann. A three-dimensional plasma and energetic particle investigation for the Wind spacecraft. *Space Science Reviews*, 71:125–153, 1995.

JA Linker, RM Caplan, C Downs, P Riley, Z Mikic, R Lionello, CJ Henney, CN Arge, Y Liu, ML DeRosa, et al. The open flux problem. *The Astrophysical Journal*, 848(1):70, 2017.

G Livadiotis and DJ McComas. Understanding kappa distributions: A toolbox for space science and astrophysics. *Space Science Reviews*, 175(1-4):183–214, 2013.

AR Macneil, CJ Owen, and RT Wicks. Tests for coronal electron temperature signatures in suprathermal electron populations at 1 AU. *Ann. Geophys*, 35:1275–1291, 2017.

M Maksimovic, I Zouganelis, J-Y Chaufray, K Issautier, EE Scime, JE Littleton, E Marsch, DJ McComas, C Salem, RP Lin, et al. Radial evolution of the electron distribution functions in the fast solar wind between 0.3 and 1.5 AU. *Journal of Geophysical Research: Space Physics*, 110(A9), 2005.

CH Mandrini, FA Nuevo, AM Vasquez, P Démoulin, D van Driel-Gesztelyi, Land Baker, JL Culhane, GD Cristiani, and M Pick. How can active region plasma escape into the solar wind from below a closed helmet streamer? *Solar Physics*, 289(11):4151–4171, 2014.

E Marsch, K-H Mühlhäuser, H Rosenbauer, R Schwenn, and FM Neubauer. Solar wind helium ions: Observations of the Helios solar probes between 0.3 and 1 AU. *Journal of Geophysical Research: Space Physics*, 87(A1):35–51, 1982.

JC Maxwell. A dynamical theory of the electromagnetic field. *Proceedings of the Royal Society of London*, 13:531–536, 1863.

DJ McComas, SJ Bame, P Barker, WC Feldman, JL Phillips, P Riley, and JW Griffee. *The Advanced Composition Explorer Mission*, pages 563–612. Springer Netherlands, Dordrecht, 1998.

DJ McComas, HA Elliott, and R von Steiger. Solar wind from high-latitude coronal holes at solar maximum. *Geophysical research letters*, 29(9), 2002.

DJ McComas, HA Elliott, NA Schwadron, JT Gosling, RM Skoug, and BE Goldstein. The three-dimensional solar wind around solar maximum. *Geophysical research letters*, 30(10), 2003.

J-P Meyer. Solar-stellar outer atmospheres and energetic particles, and galactic cosmic rays. *The Astrophysical Journal Supplement Series*, 57:173–204, 1985.

N Meyer-Vernet. *Basics of the solar wind*. Cambridge University Press, 2007.

H Morgan, L Jeska, and D Leonard. The expansion of active regions into the extended solar corona. *The Astrophysical Journal Supplement Series*, 206(2):19, 2013.

HM Mott-Smith. History of "plasmas". *Nature*, 233:219, 1971.

D Müller, RG Marsden, OC St. Cyr, and HR Gilbert. *Solar Orbiter*, volume 285. 2013.

N Murphy, EJ Smith, and NA Schwadron. Strongly underwound magnetic fields in co-rotating rarefaction regions: Observations and implications. *Geophysical research letters*, 29(22):23–1, 2002.

K Mursula, L Holappa, and R Lukianova. Seasonal solar wind speeds for the last 100 years: Unique coronal hole structures during the peak and demise of the grand modern maximum. *Geophysical Research Letters*, 44(1):30–36, 2017.

AG Nash, NR Sheeley, and Y-M Wang. Mechanisms for the rigid rotation of coronal holes. *Solar physics*, 117(2):359–389, 1988.

M Neugebauer, RJ Forsyth, AB Galvin, KL Harvey, JT Hoeksema, AJ Lazarus, RP Lepping, JA Linker, Z Mikic, JT Steinberg, et al. Spatial structure of the solar wind and comparisons with solar data and models. *Journal of Geophysical Research: Space Physics*, 103(A7):14587–14599, 1998.

M Neugebauer, PC Liewer, EJ Smith, RM Skoug, and TH Zurbuchen. Sources of the solar wind at solar activity maximum. *Journal of Geophysical Research: Space Physics*, 107(A12), 2002.

JT Nolte and ECs Roelof. Large-scale structure of the interplanetary medium. *Solar Physics*, 33(2):483–504, 1973.

KW Ogilvie and MD Desch. The WIND spacecraft and its early scientific results. *Advances in Space Research*, 20(Results of the IASTP Program):559–568, 1997.

KW Ogilvie, DJ Chornay, RJ Fritzenreiter, F Hunsaker, J Keller, J Lobell, G Miller, JD Scudder, EC Sittler, RB Torbert, D Bodet, G Needell, AJ Lazarus, JT Steinberg, JH Tappan, A Mavretic, and E Gergin. SWE, a comprehensive plasma instrument for the WIND spacecraft. *Space Science Reviews*, 71:55–77, 1995.

MJ Owens and RJ Forsyth. The heliospheric magnetic field. *Living Reviews in Solar Physics*, 10(5), 2013.

MJ Owens, NU Crooker, and NA Schwadron. Suprathermal electron evolution in a Parker spiral magnetic field. *Journal of Geophysical Research: Space Physics*, 113(11):1–8, 2008.

MJ Owens, NU Crooker, and M Lockwood. Solar origin of heliospheric magnetic field inversions: Evidence for coronal loop opening within pseudostreamers. *Journal of Geophysical Research: Space Physics*, 118(5):1868–1879, 2013.

SP Owocki, TE Holzer, and AJ Hundhausen. The solar wind ionization state as a coronal temperature diagnostic. *The Astrophysical Journal*, 275:354–366, 1983.

C Pagel, NU Crooker, DE Larson, SW Kahler, and MJ Owens. Understanding electron heat flux signatures in the solar wind. *Journal of Geophysical Research: Space Physics*, 110(A1), 2005.

EN Parker. Sweet's mechanism for merging magnetic fields in conducting fluids. *Journal of Geophysical Research*, 62(4):509–520, 1957.

EN Parker. Dynamics of the interplanetary gas and magnetic fields. *The Astrophysical Journal*, 128:664, 1958.

EN Parker. Dynamical theory of the solar wind. *Space Science Reviews*, 4(5-6): 666–708, 1965.

GK Parks. *Physics of space plasmas – an introduction*. Redwood City, CA; Addison-Wesley Publishing Co., 1991.

G Paschmann and PW Daly. Analysis methods for multi-spacecraft data. 1998.

WD Pesnell. *Solar dynamics observatory (SDO)*. Springer, 2015.

V Pierrard, M Maksimovic, and J Lemaire. Electron velocity distribution functions from the solar wind to the corona. *Journal of Geophysical Research*, 104(A8): 17021, 1999.

V Pierrard, M Maksimovic, and J Lemaire. Core, halo and strahl electrons in the solar wind. *Astrophysics and Space Science*, 277(1-2):195–200, 2001.

WG Pilipp, K-H Muehlhaeuser, H Miggenrieder, MD Montgomery, and H Rosenbauer. Characteristics of electron velocity distribution functions in the solar wind derived from the Helios plasma experiment. *Journal of Geophysical Research*, 92(5):1075–1092, 1987.

JG Porter, JM Fontenla, and GM Simnett. Simultaneous ultraviolet and x-ray observations of solar microflares. *The Astrophysical Journal*, 438:472–479, 1995.

ER Priest and P Démoulin. Three-dimensional magnetic reconnection without null points: 1. Basic theory of magnetic flipping. *Journal of Geophysical Research: Space Physics*, 100(A12):23443–23463, 1995.

F Reale. Coronal loops: Observations and modeling of confined plasma. *Living Reviews in Solar Physics*, 11(1), 2014.

IG Richardson and HV Cane. Near-Earth interplanetary coronal mass ejections during solar cycle 23 (1996–2009): Catalog and summary of properties. *Solar Physics*, 264(1):189–237, 2010.

P Riley, JA Linker, Z Mikić, R Lionello, SA Ledvina, and JG Luhmann. A comparison between global solar magnetohydrodynamic and potential field source surface model results. *The Astrophysical Journal*, 653(2):1510, 2006.

H Rosenbauer, R Schwenn, E Marsch, B Meyer, H Miggenrieder, MD Montgomery, K-H Mühlhäuser, W Pilipp, W Voges, and SM Zink. A survey on initial results of the Helios plasma experiment. *Journal of Geophysics Zeitschrift Geophysik*, 42:561–580, 1977.

R Rosner, WH Tucker, and GS Vaiana. Dynamics of the quiescent solar corona. *The Astrophysical Journal*, 220:643–645, 1978.

T Sakao, R Kano, N Narukage, J Kotoku, T Bando, EE DeLuca, LL Lundquist, S Tsuneta, LK Harra, Y Katsukawa, et al. Continuous plasma outflows from the edge of a solar active region as a possible source of solar wind. *Science*, 318 (5856):1585–1588, 2007.

E Sanchez-Diaz, AP Rouillard, B Lavraud, K Segura, C Tao, R Pinto, NR Sheeley Jr, and I Plotnikov. The very slow solar wind: Properties, origin and variability. *Journal of Geophysical Research: Space Physics*, 121(4):2830–2841, 2016.

KH Schatten, JM Wilcox, and NF Ness. A model of interplanetary and coronal magnetic fields. *Solar Physics*, 6(3):442–455, 1969.

PH Scherrer, J Schou, RI Bush, AG Kosovichev, RS Bogart, JT Hoeksema, Y Liu, TL Duvall, J Zhao, CJ Schrijver, et al. The Helioseismic and Magnetic Imager

(HMI) investigation for the Solar Dynamics Observatory (SDO). *Solar Physics*, 275(1-2):207–227, 2012.

K Schindler, M Hesse, and J Birn. General magnetic reconnection, parallel electric fields, and helicity. *Journal of Geophysical Research: Space Physics*, 93(A6): 5547–5557, 1988.

J Schou, PH Scherrer, RI Bush, R Wachter, S Couvidat, MC Rabello-Soares, RS Bogart, JT Hoeksema, Y Liu, TL Duvall, et al. Design and ground calibration of the Helioseismic and Magnetic Imager (HMI) instrument on the Solar Dynamics Observatory (SDO). *Solar Physics*, 275(1-2):229–259, 2012.

CJ Schrijver and ML DeRosa. Photospheric and heliospheric magnetic fields. *Solar Physics*, 212(1):165–200, 2003.

CJ Schrijver and GL Siscoe. *Heliophysics: Plasma Physics of the Local Cosmos*. Cambridge University Press, 2009.

H Schwabe. Sonnenbeobachtungen im jahre 1843. von herrn hofrath schwabe in dessau. *Astronomische Nachrichten*, 21:233, 1844.

NA Schwadron. An explanation for strongly underwound magnetic field in co-rotating rarefaction regions and its relationship to footpoint motion on the the Sun. *Geophysical research letters*, 29(14), 2002.

NA Schwadron and DJ McComas. The sub-Parker spiral structure of the heliospheric magnetic field. *Geophysical research letters*, 32(3), 2005.

NA Schwadron, LA Fisk, and TH Zurbuchen. Elemental fractionation in the slow solar wind. *The Astrophysical Journal*, 521(2):859, 1999.

NA Schwadron, DJ McComas, HA Elliott, G Gloeckler, J Geiss, and R Von Steiger. Solar wind from the coronal hole boundaries. *Journal of Geophysical Research: Space Physics*, 110(A4), 2005.

R Schwenn. *Large-Scale Structure of the Interplanetary Medium*, pages 99–181. Springer Berlin Heidelberg, Berlin, Heidelberg, 1990.

J Seough, Y Nariyuki, PH Yoon, and S Saito. Strahl formation in the solar wind electrons via whistler instability. *The Astrophysical Journal*, 811(1):L7, 2015.

CW Smith, J LHeureux, NF Ness, MH Acuña, LF Burlaga, and J Scheifele. The ACE magnetic fields experiment. In *The Advanced Composition Explorer Mission*, pages 613–632. Springer, 1998.

EJ Smith. The heliospheric current sheet. *Journal of Geophysical Research: Space Physics*, 106(A8):15819–15831, 2001.

EJ Smith and JH Wolfe. Observations of interaction regions and corotating shocks between one and five AU: Pioneers 10 and 11. *Geophysical Research Letters*, 3 (3):137–140, 1976.

JT Steinberg, AJ Laxarus, KW Oglivie, and J Byrnes. Differential flow between solar wind protons and alpha particles: First WIND observations. *Geophysical Research Letters*, 23(10):1183–1186, 1996.

EC Stone, AM Frandsen, and RA Mewaldt. The Advanced Composition Explorer. *Space Science*, 86:1–22, 1998.

S Stverak, M Maksimovic, PM Travinicek, E Marsch, AN Fazakerley, and EE Scime. Radial evolution of nonthermal electron populations in the low-latitude solar wind: Helios, Cluster, and Ulysses Observations. *Journal of Geophysical Research: Space Physics*, 114(5):1–15, 2009.

J Tao, L Wang, Q Zong, G Li, CS Salem, RF. Wimmer-Schweingruber, J He, C Tu, and SD Bale. Quiet-time suprathermal ($\sim$ 0.1–1.5 keV) electrons in the solar wind. *The Astrophysical Journal*, 820(1):22, 2016.

WT Thompson. Coordinate systems for solar image data. *Astronomy & Astrophysics*, 449(2):791–803, 2006.

L Tonks. The birth of plasma. *American Journal of Physics*, 35(9):857–858, 1967.

Y Uchida, A McAllister, KT Strong, Y Ogawara, T Shimizu, R Matsumoto, and HS Hudson. Continual expansion of the active-region corona observed by the Yohkoh soft X-ray telescope. *Publications of the Astronomical Society of Japan*, 44:L155–L160, 1992.

L van Driel-Gesztelyi and LM Green. Evolution of active regions. *Living Reviews in Solar Physics*, 12(1):1, 2015.

L van Driel-Gesztelyi, JL Culhane, D Baker, P Démoulin, CH Mandrini, ML DeRosa, AP Rouillard, A Opitz, G Stenborg, A Vourlidas, et al. Magnetic topology of active regions and coronal holes: implications for coronal outflows and the solar wind. *Solar Physics*, 281(1):237–262, 2012.

D Verscharen, BDG Chandran, S Bourouaine, and JV Hollweg. Deceleration of alpha particles in the solar wind by instabilities and the rotational force: implications for heating, azimuthal flow, and the parker spiral magnetic field. *The Astrophysical Journal*, 806(2):157, 2015.

AF Viñas, C Gurgiolo, T Nieves-Chinchilla, SP Gary, and ML Goldstein. Whistler waves driven by anisotropic strahl velocity distributions: Cluster observations. In *AIP Conference Proceedings*, volume 1216, pages 265–270. AIP, 2010.

C Vocks, C Salem, RP Lin, and G Mann. Electron halo and strahl formation in the solar wind by resonant interaction with whistler waves. *The Astrophysical Journal*, 627(1):540, 2005.

Y-M Wang and NR Sheeley Jr. Solar wind speed and coronal flux-tube expansion. *The Astrophysical Journal*, 355:726–732, 1990.

Y-M Wang and NR Sheeley Jr. Solar implications of Ulysses interplanetary field measurements. *The Astrophysical Journal Letters*, 447(2):L143, 1995.

Y-M Wang, NR Sheeley Jr, JL Phillips, and BE Goldstein. Solar wind stream interactions and the wind speed-expansion factor relationship. *The Astrophysical Journal Letters*, 488(1):L51, 1997.

Y-M Wang, JB Biersteker, NR Sheeley Jr, S Koutchmy, J Mouette, and M Druckmuller. The solar eclipse of 2006 and the origin of raylike features in the white-light corona. *The Astrophysical Journal*, 660(1):882, 2007.

Y-M Wang, Y-K Ko, and R Grappin. Slow solar wind from open regions with strong low-coronal heating. *The Astrophysical Journal*, 691(1):760, 2009.

EJ Weber and L Davis Jr. The angular momentum of the solar wind. *The Astrophysical Journal*, 148:217–227, 1967.

KG Widing and U Feldman. On the rate of abundance modifications versus time in active region plasmas. *The Astrophysical Journal*, 555(1):426, 2001.

T Wiegelmann and T Sakurai. Solar force-free magnetic fields. *Living Reviews in Solar Physics*, 9(1):5, 2012.

JM Wilcox. The interplanetary magnetic field. solar origin and terrestrial effects. *Space Science Reviews*, 8(2):258–328, 1968.

LB Wilson. Wind-3DP caveats, 2015. `https://spdf.gsfc.nasa.gov/pub/data/wind/3dp/wind3dp_caveats.pdf` Accessed: 2017-03-03.

GL Withbroe. The temperature structure, mass, and energy flow in the corona and inner solar wind. *The Astrophysical Journal*, 325:442–467, 1988.

L Zhao and LA Fisk. Understanding the behavior of the heliospheric magnetic field and the solar wind during the unusual solar minimum between cycles 23 and 24.

Solar Physics, 274(The Sun-Earth Connection Near Solar Minimum):379–397, 2011.

L Zhao, TH Zurbuchen, and LA Fisk. Global distribution of the solar wind during solar cycle 23: ACE observations. *Geophysical Research Letters*, 36(14):L14104, 2009.

JB Zirker. Coronal holes and high-speed wind streams. *Reviews of Geophysics*, 15 (3):257–269, 1977.

TH Zurbuchen. The solar wind composition throughout the solar cycle: A continuum of dynamic states. *Geophysical Research Letters*, 29(9):1–4, 2002.

TH Zurbuchen, S Hefti, LA Fisk, G Gloeckler, and R Von Steiger. The transition between fast and slow solar wind from composition data. In *Coronal Holes and Solar Wind Acceleration*, pages 353–356. Springer, 1999.